Universitá degli Studi di Parma

Dottorato di ricerca in Scienza e Tecnologia dei Materiali Innovativi

Ciclo XXVII (2012-2014)

Local structure and dynamics of hydrogen in carbon nano-materials: a neutron scattering and DFT approach

Coordinatore:
Chiar.mo Prof. Enrico Dalcanale
Tutors:
Chiar.mo Prof. Mauro Riccó
Dr. Stéphane Rols

Dottorando:
Chiara Cavallari

January 2015

Declaration of Authorship

I, Chiara Cavallari, declare that this thesis titled, 'Local structure and dynamics of hydrogen in carbon nano-materials: a neutron scattering and DFT approach' and the work presented in it are my own. I confirm that:

- This work was done wholly or mainly while in candidature for a research degree at this University.
- Where any part of this thesis has previously been submitted for a degree or any other qualification at this University or any other institution, this has been clearly stated.
- Where I have consulted the published work of others, this is always clearly attributed.
- Where I have quoted from the work of others, the source is always given. With the exception of such quotations, this thesis is entirely my own work.
- I have acknowledged all main sources of help.
- Where the thesis is based on work done by myself jointly with others, I have made clear exactly what was done by others and what I have contributed myself.

Signed: _____

Date: _____

"Run rabbit run. Dig that hole, forget the sun. And when at last the work is done, don't sit down it's time to dig another one."

Breathe (*The Dark Side of the Moon*, Pink Floyd)

UNIVERSITÁ DEGLI STUDI DI PARMA

Abstract

Scienze MM.FF.NN.
Dipartimento di Fisica e Scienze della Terra

Dottorato di Ricerca in Scienza e Tecnologia dei Materiali Innovativi

Local structure and dynamics of hydrogen in carbon nano-materials: a neutron scattering and DFT approach

by Chiara Cavallari

The study of the interaction between hydrogen and carbon monolayers has attracted a remarkable interest in different scientific domains, from interstellar chemistry, to nano-electronics and energy storage just to name a few. The debate about the peculiar state of hydrogen at the graphene surface is still open and active and has important fundamental and technological issues. It is evident that the behavior of a chemically absorbed H atom at the graphene surface depends on different parameters, like the chemical bonds and the local atomic environment. The latter properties are specific to the graphene samples studied, namely to their preparation and further processing, as well as to the hydrogenation stage. Recently, the development of chemical methods, which exploit the thermal exfoliation of graphite oxide for producing gram-scale amount of graphene (TEGO), has opened the routes towards the experimental investigations of graphene using techniques that are usually reserved to bulk systems, like neutron scattering. In this work, macroscopic amount of graphene are studied using neutron scattering (neutron diffraction and spectroscopy). We show that the hydrogen local environment can be efficiently characterized, both qualitatively and quantitatively, thanks to its influence on the dynamics of the chemisorbed hydrogen atoms. The combination of experimental data and *ab-initio* DFT calculations allows to identify the spectral fingerprints of the specific C-H configurations located at in-plane defects onto the graphene plane. The temperature dependence of the neutron spectra, coupled to ^{1}H-NMR investigations, reveals an activated evolution of the structure of the in–plane voids, with a surprisingly low activation barrier. Finally, we extend the neutron studies to other type of carbon nanostructures, in particular to Nickel-decorated graphenes and to Lithium-intercalated fullerides, all of them being material relevant to hydrogen storage.

Acknowledgements

I would like to express my special thanks and appreciation to my advisors Dr. Stéphane Rols and Prof. Mauro Riccó for having always encouraged my research and for having allowed me to grow as a person and research scientist. Your enthusiasm, advices and friendship have been really priceless for me.

I would also like to thank my committee members and Dr. Pascale Launois and Prof. Jean-Louis Bantignies for serving as referees for the "Doctor Europeaus" label. I would especially like to thank Dr. Daniele Pontiroli and Dr. Mattia Gaboardi for samples synthesis and preparation, help in PDF data treatment and your always sharp suggestions. I shared some neutron beamtimes also with Dr. Gina Vlachopoulou and Dr. Matteo Aramini, former Carbon Nanostructures Laboratory members: thanks for your precious help and nice company!

A lot of people helped me during these three years at the Institut Laue Langevin: Dr. Michela Brunelli, Dr. Mark Johnson and all the CS lab, Dr. Monica Jimenez-Ruiz, Dr. Henry Fischer, Dr. Peter Fouquet, Dr. Emmanuelle Suard, Dr. Mohamed Zbiri, Dr. Gabriel Cuello, Dr. Alexander Ivanov, Dr. Hannu Mutka, Dr. Thomas Hansen, Dr. Marie-Bernadette LePetit, Dr. Elena Cannuccia, Olivier Meulien, Alain Bertoni, David Hess, Simon Baudoin, Olivier Losserand, Alain Daramsy, Stéphane Armanet, Remy Mudingay and many others. All of you have been there to support me when I collected, treated and analyzed data for my Ph.D. thesis. I would like to express my special gratitude to Dr. Claudia Mondelli, who introduced me to the ILL and neutron scattering, already 4 years ago. I thank also all the ILL not-scientific staff, in particular Laurence Tellier, Martine Cedile, Regine Olinger, Travel Office, Bureau Paie, Health Physics and storehouse staff, for their kindness and willingness. This work was financed by an ILL Ph.D. studentship grant. I am really grateful to the ILL for fundings and beamtime allocations. I enjoyed a lot working at the ILL! A big big big thank you to you all (and to anyone I have forgotten)!

Thanks to all who have contributed, directly or indirectly, to this thesis: Dr. Brian Pauw (NIMS, Tsukuba, Japan), Dr. Elsa Callini, Dr. Philippe Mauron, Dr. Andreas Borgschulte (EMPA, Dübendorf, Switzerland), the H2FC platform for IR beamtime allocation at EMPA, Dr. Chiara Milanese (Universitá di Pavia, Italy), Prof. David Keen and Dr. Tristan Youngs (ISIS - Rutherford Appleton Laboratory, Didcot, UK), Dr. Simon Kimber (ESRF, Grenoble, France), Prof. Petra Rüdolf (University of Groninger,

Netherlands), Dr. Kazutomo Suenaga and Dr. Hiromichi Kataura (AIST, Tsukuba, Japan), Dr. Rozenn LeParc (Université de Montpellier II, France).

A special thanks to my family. Words cannot express how grateful I am to my mother and my father. I would also like to thank all of my old and new friends, who I have met on my way to physics, who has made my french life so sweet, who has always supported me ... And, last but definitely not least, I would like to thank N., for being always my best friend.

List of Figures

Notes

Useful quantities in Neutron Scattering

E(meV) = 81.8/ λ^2 where λ is in Å

1 meV = 11.6 K

1 meV = 8.065 cm^{-1}

1 meV = 0.2418 THz

$\sigma = 4\pi b^2$

$\Delta t[ps] = \frac{0.66}{\Delta E[meV]}$

Atomic species	Coh. XS (barn)	Inc. XS (barn)
1H	1.7583	80.27
2H	5.592	2.05
C	5.551	0.001
Li	0.454	0.92
Ni	13.3	5.2
V	0.0184	5.08
Al	1.495	0.0082

from http://www.ncnr.nist.gov/resources/n-lengths/

note: Li Abs. XS 70.5 barns

Notes

List of Samples studied in this thesis and their abbreviations

Samples	**Short description**	**Other Names**
TEGO	Thermal Exfoliated Graphite Oxide	Graphene
H-TEGO	Hydrogenated Thermal Exfoliated Graphite Oxide	H-Graphene
D-TEGO	Deuterated Thermal Exfoliated Graphite Oxide	D-Graphene
BMG	Ball-Milled Graphite	Nanographite
H-BMG	Hydrogenated Ball-Milled Graphite	H-Nanographite
Graphite	Graphite (powder)	-
GC	Glassy Carbon	-
GO	Graphite Oxide	-
$Li_{12}C_{60}$	Li-intercalated fulleride $Li_{12}C_{60}$	-
$H_yLi_{12}C_{60}$	Hydrogenated Li-intercalated fulleride $Li_{12}C_{60}$	-
Li_6C_{60}	Li-intercalated fulleride Li_6C_{60}	-
$H_yLi_6C_{60}$	Hydrogenated Li-intercalated fulleride Li_6C_{60}	-
Ni–TEGO	Nickel decorated thermal exfoliated GO NiC_{80}	Ni–Graphene
H–NiTEGO	Hydrogenated Ni–decorated thermal exfoliated GO	H–NiGraphene

To my dearly beloved Mum and Pippo for their love, endless support and encouragement. I love you!

Chapter 1

Introduction

1.1 Carbon nanostructures for applications: General Introduction

A large variety of carbon-based nanomaterials, from fullerenes through carbon nanotubes to graphene, have stimulated the scientific community thanks to their exceptional properties, spanning a very wide range of potential applications, like electronics [1], sensors [2], biology [3], energy storage [4] and structural engineering [5], just to name a few.
Graphene is a monatomic layer of carbon atoms with sp^2 hybridization arranged on a honeycomb lattice with lattice constant a = 1.42 Å. It stands as a perfect two-dimensional material [6]. As illustrated in Fig. 1.1, graphene can be imagined as the building block of graphite, fullerene and nanotubes, populating the nanocarbon bestiary with structures of variable dimensionality and physico-chemical properties.
C_{60} was the first carbon nanostructure invented in 1985 by H. Kroto, R. Curl and R. Smalley, who were awarded in 1996 by the Nobel Prize in Chemistry [7]. It has a cage-like fused-ring molecular structure (truncated icosahedron, which possesses a very high symmetry I_h) resembling a soccer-ball and composed of sixty carbon atoms forming twenty hexagons and twelve pentagons with a carbon atom at each vertex of each polygon and a bond along each polygon edge. The molecules of C_{60} stick together in the solid state via van-der-Waals forces and assume a face centered cubic lattice (at room temperature[1]). The synthesis and stability of macroscopic amount of C_{60} has stimulated a variety of studies on fullerites and their intercalation compounds (fullerides) [9–12]. In particular, this latter family of compounds discloses a rich and fascinating field of research: if

[1] At room temperature, in pure crystalline C_{60}, the fullerene molecules are orientationally disordered and the corresponding crystal structure can be described as a face centered cubic (fcc) lattice of C_{60} spheres. At low temperatures (below 249 K) the individual molecules are locked against rotation, they become orientationally ordered resulting in a simple cubic structure [8].

at the beginning they appeared particularly attractive for their superconducting character [13, 14], they recently showed interesting properties as ionic conductors and gas absorbers [15, 16].

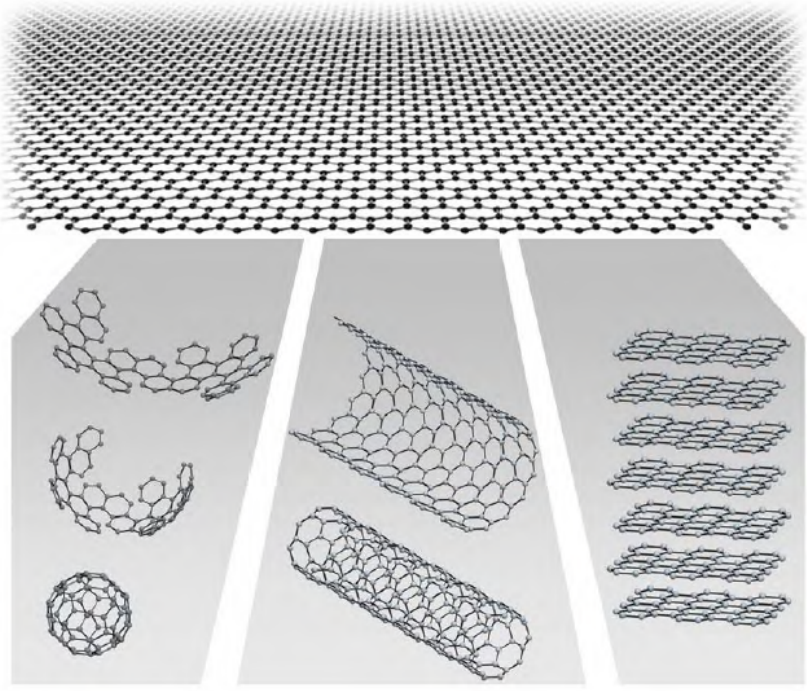

FIGURE 1.1: Graphene is a 2D building material for carbon materials of all other dimensionalities. It can be wrapped up into 0D C_{60} buckyballs, rolled into 1D nanotubes or stacked into 3D graphite. Taken from [17].

Macroscopic single graphene layers were successfully isolated from graphite through mechanical exfoliation in 2004 [17] and A. Geim and K. Novoselov won the Nobel Prize in Physics in 2010 for this invention. Graphene was discovered due to the optical interference it creates on top of a SiO_2 substrate, which rendered its observation with an ordinary optical microscope possible. In addition, it was found to be stabilized by the presence of local roughness and ripples, when freely suspended, as predicted for a 2D lattice[2]. The out-of-plane deformations can attain 1 nm [19, 20].

Among all carbon allotropes, graphene is remarkable for its exceptional electronic properties. Since the discovery of graphene mono–layer, important progresses have been made in producing both single and multi–layers. Most of the techniques currently employed are not new and are modified versions of those conceived to grow different carbon nanostructures and graphitic materials. As we will describe in the following, the "graphenes" synthesized by these techniques are inhomogeneous in terms of quality, purity and amount. The mechanical exfoliation remains the method of choice for producing graphene of the highest quality. However, epitaxial growth and chemical synthesis have

[2] According to the Mermin-Wagner theorem [18], long-wavelength fluctuations are expected to destroy the long-range order of 2D crystals.

recently become well established methods. Graphene based compounds appear not only interesting for electronic applications but also for other fields of technological relevance, thanks in particular to their large surface area and low weight.
The current interest in graphene is remarkable, as evidenced by the large number of articles published in the last few years. A tremendous number of excellent reviews can be found on graphene over the internet [21].

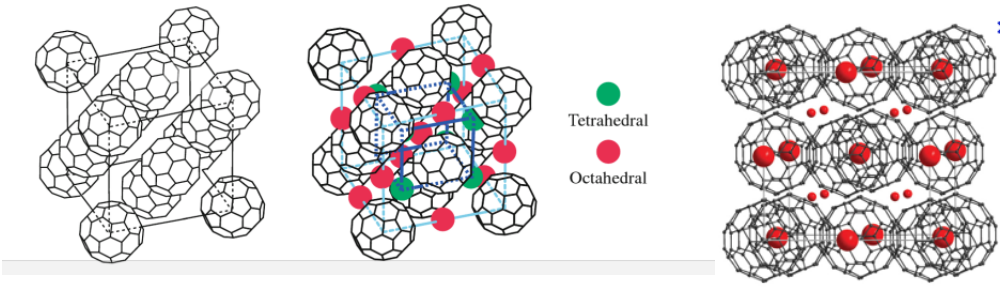

FIGURE 1.2: *Left:* A-intercalated A_3C_{60}. C_{60} has a face centered cubic structure with large voids between the molecules which can accommodate cations, to form A_nC_{60}. Taken from [22]. *Right:* Polymorphism was found to control the superconductivity and magnetism in Cs_3C_{60}. Here the fcc phase has been reported. Taken from [23].

The applications and implications of carbon nanostructures in science and technology are extremely broad and would deserve a much more detailed description, which is not in the scope of this introduction[3].

In this thesis, we report on the characterization of defective graphene–based compounds and alkali–metal intercalated fullerides, which are materials with potential applications in the field for energy storage. The next sections aim at providing the reader with a general background. Since a particular attention is put on to the study of hydrogenated defective graphene, this introductory chapter is devoted especially to contextualise the "graphenes" and to give an overview on the interest in hydrogen interaction with carbon and its possible implications. The introduction on Lithium intercalated fullerides will be given in a dedicated section in Chap. 8. We refer the interested reader to [24] and [25] for more complete reviews on the synthesis and physical properties of metal-intercalated fullerides.

[3] A lot of different form of carbonaceous materials like amorphous carbon, nanonions, nanodiamonds, nanofibers, nanorods ... have been attracting an increasing interest in research. They are not treated in this manuscript.

1.2 Hydrogen and Carbon Materials

"The Hydrogen Economy" has stimulated the interest from both the technical and scientific community over the last decade. In the perspective of providing a long–term solution to many of our transport and energy needs, which are nowadays strongly dependent on fossil fuels, it comprises:

- The production of molecular hydrogen.
- The transport and storage of hydrogen.
- The use of hydrogen in fuel cells, which combine oxygen and hydrogen to produce electricity (and some heat).

Hydrogen has the best ratio of valence electrons to protons (and neutrons) of all the periodic table and the energy gain per electron is very high. Moreover, hydrogen is the most abundant element on Earth. Once produced, it is a clean synthetic fuel: when burnt with oxygen, the only exhaust gas is water vapour. However, before a hydrogen economy can become a reality, there are significant technological, economic and institutional barriers that need to be addressed. In particular, for on-board energy storage applications, vehicles need compact, light, safe and affordable tanks and suitable materials with high volumetric and gravimetric storage capacity, able to operate in mild conditions have to be found [4]. Carbonaceous materials are attractive candidates for solid–state hydrogen storage because of the combination of adsorption ability, high specific surface area, microporous structure and low-mass density [26–28]. The capture of H may rely either on van–der–Waals attractive forces (**physisorption** of molecular hydrogen) or on the overlap of the highest occupied molecular orbital of carbon with the occupied hydrogen electronic wavefunction. This necessitates forming new C-H bonds, after overcoming the activation energy barrier for hydrogen dissociation (**chemisorption** of atomic hydrogen). Physisorbed hydrogen has a very small binding energy, normally of the order of 10-100 meV, while chemisorbed hydrogen has conversely a strong C–H covalent bonding, with a binding energy of more than 1-2 eV.

Many theoretical and experimental works have reported the study of hydrogen storage capacity of carbon nanostructures. The efforts in this field were not always successful and consequently, the obtained results were often controversial. It appears clear that high hydrogen storage capacity at ambient conditions, which should meet the US. Department of Energy DOE targets [29], cannot occur in bare carbon nanostructures. The recent proposed guidelines to enhance the hydrogen storage capacity in carbon-based compounds involve the decoration of the material with alkali, alkali–earth and transition

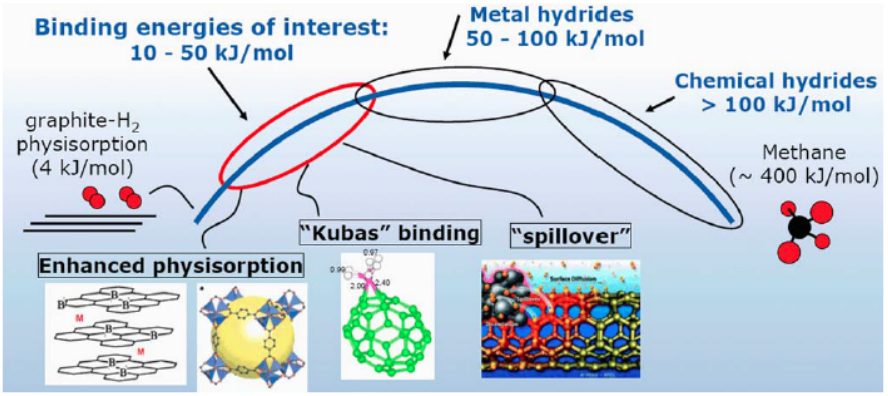

FIGURE 1.3: Overview of the binding energies of different hydrogen adsorption materials. Taken from [28].

metals. These latter can promote new type of interactions and absorption mechanism, as Kubas–binding or spillover [30–33] which could improve the hydrogen uptake or induce the formation of intermediate steps, with increased hydrogen affinity [16, 34–37]. The nature of the interaction between hydrogen and the host nano–materials can help the understanding of the basic mechanisms of hydrogen storage. More details on the study of the hydrogen interaction with metal–decorated graphene and metal–intercalated fullerides are reported in Chap. 7 and Chap. 8, respectively.

1.2.1 Hydrogen and Graphene

The understanding of hydrogen interaction with graphene and its possible implications has clearly polarized the attention of the scientific community in diverse valuable fields. If at the beginning of the last decade, absorption of hydrogen on graphitic surfaces was investigated mostly in conjunction with hydrogen storage, therefore focusing on physisorbed molecular hydrogen, atomic hydrogen chemisorbed at the surface of carbonaceous materials has been recently theoretically and experimentally investigated [38–40].

Particularly simple and elegant in this context is the idea of attaching atomic hydrogen to each site of the graphene lattice, which changes the C hybridization from sp^2 to sp^3, therefore removing the conducting π-bands and opening an energy gap in the electronic density of states. A predicted example for this is graphane [41], a wide-gap semiconductor, in which hydrogen is bonded to each carbon site of graphene. This idea opened the concept of chemical modification of graphene, which promises a whole range of new two-dimensional crystals with designed nanoscale magnetic and spin properties [42, 43]. While ideal graphene is in itself nonmagnetic, simple defects as single-atom vacancies and chemisorbed hydrogen bring a magnetic moment. The adsorption of atomic H is

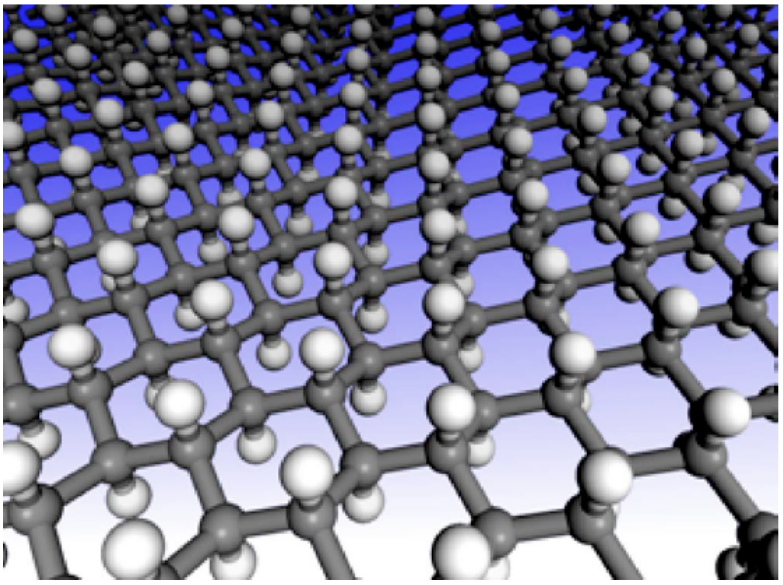

FIGURE 1.4: The structure of graphane, in the chair conformer. C is represented in gray and H in white. The figure shows the hexagonal network with carbon in sp^3 hybridization. Taken from [41].

accompanied by the appearance of a magnetic moment of $1\mu_B$ localized on the orbitals surrounding each H atom. These magnetic moments are calculated to interact with one another either ferromagnetically or antiferromagnetically, depending on whether their respective adsorption site are localized [44].

The interest of hydrogen on graphene is not only fueled in connection with nano-electronics, nano-spintronics and hydrogen storage. In the area of interstellar chemistry of example, it has been suggested that hydrogen atoms stored in the chemisorbed state on graphitic media might be an energy source for future space applications, due to the high energy release in molecular hydrogen formation from atomic recombination on this surface [45]. In spite of the continuous destruction by UV radiation and cosmic rays, H_2 is the most abundant molecule in the interstellar medium (ISM). However, no efficient gas-phase route exists for H_2 formation at the low H-atom densities of the ISM. Thus, efficient formation of H_2 in interstellar carbonaceous dust and molecular clouds is believed to proceed via diffusive atomic recombination of hydrogen atoms adsorbed on sidereal graphene-like surfaces in the very cold regions below 20 K [46]. At these temperatures, hydrogen atoms are absorbed on the dust particles but can still easily move on the surface. Once two atoms meet, they react to form molecular hydrogen. If the surface temperature becomes too high, the residence time of atoms on the surface becomes very short and the chance of two atoms to meet up becomes negligible. A proposed recombination mechanism is the Eley-Rideal reaction, where an incoming hydrogen atom reacts with another H atom that is chemically bound at the surface [47].

Since a considerable fraction of the interstellar grains is expected to consist of carbonaceous material, a popular laboratory model is the hydrogen abstraction from graphite bombarded with a hot (2000 K) atomic hydrogen beam [45, 48] or coronene [49, 50]. These systems are used to investigate the energy landscape and the dynamical behavior of hydrogen atoms absorbed on carbons. The possibility of atomic hydrogen to diffuse onto the graphene plane is at the center of a large and quite controversial debate. A very rich literature is devoted to this issue and although several different theoretical approaches have been used for predicting H–diffusion and even tracking its pathway onto the graphene plane, up to now the precise microscopic mechanism of diffusion and recombination is still missing. It appears evident from experiments and literature that the H state at the graphene surface, as well as the stability of H aggregates, strongly depends on its chemical state and the hydrogenation treatment. It is therefore extremely sensitive to the graphene synthesis, manipulation and history [51–57].

1.3 Graphene: synthesis and properties

As stated in the first section, not all graphenes are equivalent and they are subsequently addressed to different fundamental and technological targets. This section gives a very general overview, providing the reader with details and references about the synthesis methods, physical properties and potentiality of graphene in a very general conception.

1.3.1 Introduction

As already mentioned in the previous section, graphene has focused the interest of science and technology thanks to its unusual properties as high carrier concentration and mobility, good mechanical and thermal properties and extraordinary optoelectronics properties [58–63]. Several reviews have been published in the last few years, focusing on single and multilayer graphene sheets. Complete overviews of the electronic properties of graphene, its synthesis, characterization and potential applications can be found in [64, 65].

There are nowadays several different techniques that are suited for manufacturing various quality of graphene. Making high-quality graphene inexpensively and in bulk is an absolutely necessary first step for the material to ever live up to its promise in commercial applications. Basically one can distinguish two different approaches. On the one hand graphene can be detached from an already existing graphite crystal, using the so-called exfoliation methods. On the other hand the graphene layers can be grown directly on a substrate surface, like in epitaxial growth and chemical vapor deposition CVD. In the next paragraphs, the most common synthetic methods will be reviewed on

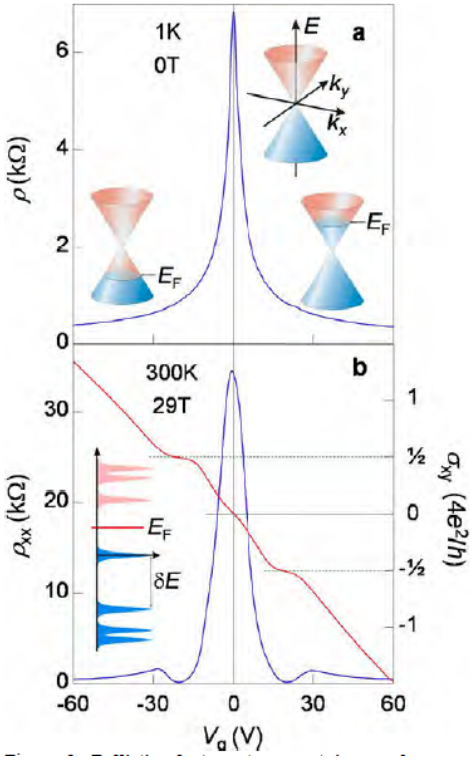

FIGURE 1.5: Ballistic electron transport in graphene. Taken from [17].

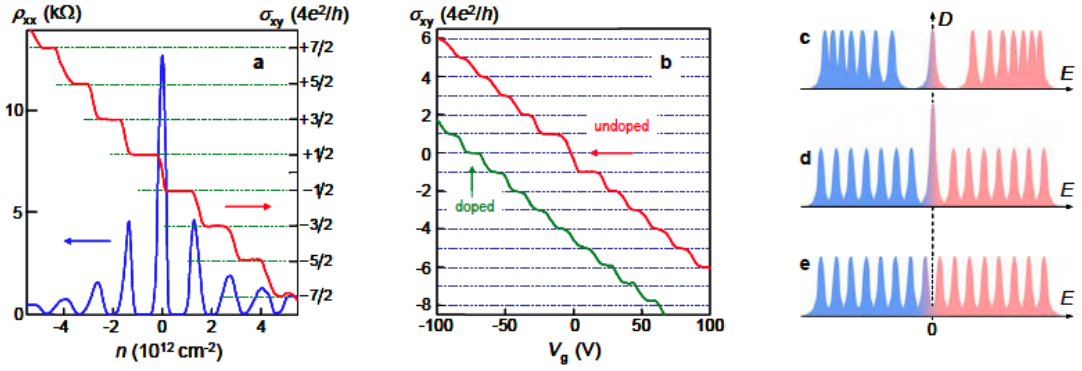

FIGURE 1.6: Chiral quantum Hall effects. Taken from [17].

the bases of different requirements: the quality of the graphene, which is defined by the purity of the product and the lack of intrinsic defects, the size of the obtained flakes and complexity. Another important aspect, that has been crucial for the research conducted in this work, is the amount of graphene which can be produced simultaneously. It is important to remark that only "monocrystalline" graphene has the remarkable properties introduced above. Monocrystalline graphene can however only be produced through what are known as mechanical cleavage techniques, in which the graphene is pulled off

in single layer flakes from graphite (known also as the Scotch–Tape method and its successive refinements). These techniques tend to be unscalable for manufacturing large quantities of the material: producing one gram of high quality material typically takes about 10 days, rendering these methods not applicable for industrial applications.
The development of a method for producing high-quality graphene in large quantities is therefore essential for further investigations and possible concrete technological applications.

1.3.2 Graphene production

The first method reported for obtaining single-layer graphene has been conceived by Novoselov and Geim in 2004. The exfoliation of graphite is achieved using a simple adhesive tape (Scotch–Tape peeling technique). After the micromechanical exfoliation of graphite, multiple-layer graphene remains on the tape. By repeating the peeling, multiple-layer graphene is cleaved into various flakes of few-layers graphene. Afterwards the tape is attached to a substrate and the glue dissolved, *e.g.* by acetone, in order to detach the tape from the material. Finally one last peeling with an unused tape is performed. The critical ingredient for the successful discovery was the observation that graphene becomes visible with an optical microscope if placed on top of a Si wafer with a carefully chosen thickness of SiO_2, owing to a feeble interference-like contrast with respect to an empty wafer [17]. The flakes obtained in this way differ considerably in size and thickness, where the sizes range from nanometers to several tens of micrometers for single-layer graphene depending on the preparation of the wafer. The quality of the graphene is found to be very high with almost no defects.

A totally different approach for obtaining graphene is to grow it directly on a surface. The size of the layers are not dependent on the initial graphite crystal. The growth can occur in two different ways. Either the carbon atoms already exist in the substrate or it has to be added from a source/crucible. Graphene can be prepared by epitaxial growth on silicon carbide or on a transition metal substrate, by simply heating and cooling it down. The results, in terms of single or bi-layer graphene formed, are highly dependent on the growth parameters, like temperature, heating rate and/or pressure. In fact, if temperature and pressure are too high, the growth of nanotubes can occur. The graphitization of SiC was discovered in 1955, but it was regarded for a long time as an unwelcome side effect and was used as a method for producing graphene only recently.
The Ni(111) surface has a lattice structure very similar to the one of graphene, with a mismatch of the lattice constant at about 1.3 %. For this reason, a thin Ni layer can be evaporated onto a SiC crystal. Upon heating the carbon atoms diffuse through the Ni layer and form a graphene or graphite layer on the surface, depending on the heating

FIGURE 1.7: Sticky tape can be used to peel off powdered graphite, leaving a single layer of graphene. Taken from lostinscience.wordpress.com.

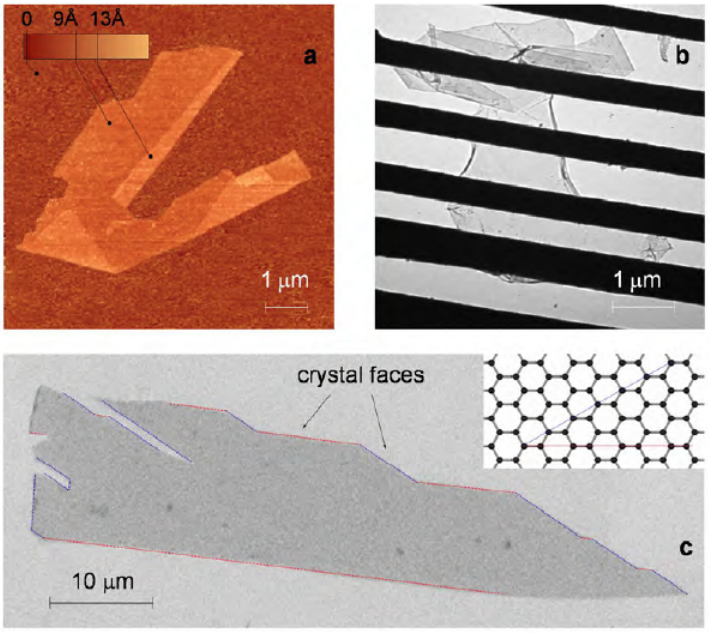

FIGURE 1.8: (a) Graphene produced by micro mechanical cleavage visualized by atomic-force microscopy (b) A TEM image of a graphene sheet freely suspended on a micron-size metallic scaffold. (c) Scanning Electron Micrograph of a relatively large graphene crystal, which shows that most of the crystal's faces are zigzag and armchair edges as indicated by blue and red lines and illustrated in the inset. Taken from [66].

rate. The so–produced graphene is easier to detach from the surface than the graphene produced by the growth on a simple SiC crystal without Ni. Other metal substrates, like the (0001) surface of ruthenium (Ru), have been explored for graphene epitaxial growth. The growth of graphene starts at several locations on the crystal simultaneously and these graphene islands grow together, as shown in Fig. 1.9. Therefore, epitaxial graphene is not perfectly homogeneous, due to topological defects or grain boundaries. Its quality therefore is not as good as that of mechanically exfoliated graphene.

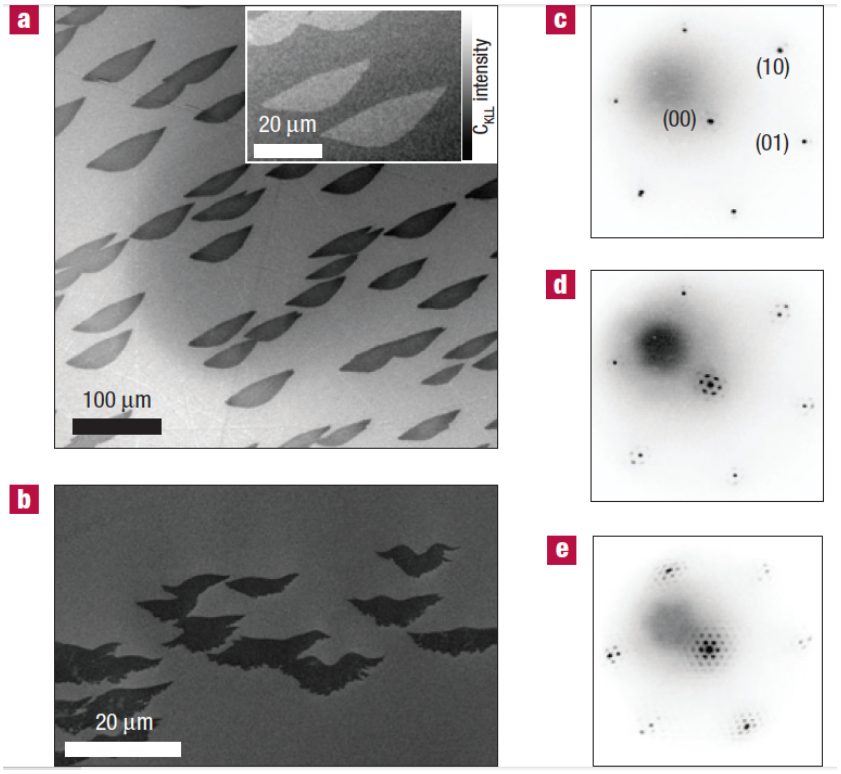

FIGURE 1.9: The morphology of epitaxial graphene grown on Ru(0001). (a-b) The UHV-SEM image of a large area of the Ru(0001) surface after first-layer graphene growth. In the Inset: a scanning Auger microscopy image, obtained on the sample. (c) Selected-area low-energy electron diffraction pattern of the Ru(0001) substrate. (d) Diffraction pattern of one-layer epitaxial graphene on Ru(0001). (e) Diffraction pattern of two-layer epitaxial graphene. Taken from [67].

Chemical vapor deposition (CVD) is a well known process in which a substrate is exposed to gaseous compounds. These compounds decompose on the surface in order to grow a thin film, usually by heating the sample with a filament or with plasma, whereas the by-products evaporate. Graphene can be grown by exposing a foil (usually Ni or Cu or transition metals) to a gas mixture of H_2, CH_4 and Ar at about 1000^oC. The methane decomposes on the surface and hydrogen atoms evaporate. Then, carbon diffuses into the Ni substrate. After cooling down in an Ar atmosphere, a graphene layer grows on the surface. The shape of the resulting material can also be controlled by patterning

the substrate. These graphene layers can be subsequently transferred by the use of a polymer support, which will be attached onto the top of the graphene. After etching the Ni substrate, the graphene can be stamped onto the required substrate and the polymer support gets peeled off or etched away. Using this method, several layers of graphene can be stamped onto one another. The optical and electrical performance of graphene prepared by CVD is very high but the purity is not optimal. On the other hand, the so–produced graphene layers can be very large and are easily obtained in large batches. The complexity is rather low, since CVD is a well-known method and often used in industry. Therefore the bottom-up approach of CVD is proving to be by far the best method for the large–production of single graphene sheets.

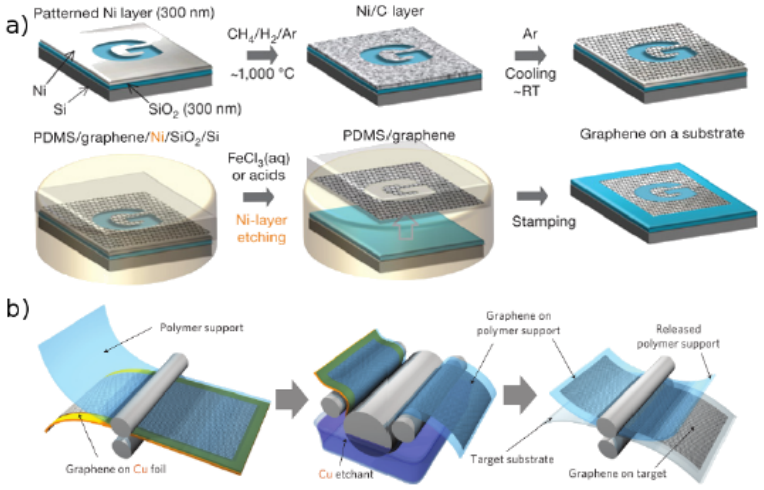

FIGURE 1.10: (a) Scheme of preparation of graphene by CVD and transfer via polymer support. The carbon solves into the Ni during the CVD and forms graphene on the surface after cooling. With a polymer support the graphene can be stamped onto another substrate, after etching of the Ni layer. An appropriate patterning of the Ni foil allows a control of the shape of the graphene. (b) Roll-to-roll process of graphene films grown on copper foils and transferred on a target substrate. Taken from http://www.physik.fu-berlin.de.

Beside the methods already described to produce graphene monolayers, many other methods have been developed in view of its massive production, like Liquid Phase Exfoliation (LPE) [68] and chemical methods. They include a large class of chemical routes, including solvothermal synthesis [69] and the exfoliation of graphite oxide [70]. The latter represents the most successful top–down approach. It is based on a wet chemical synthesis: in the most common procedure, pure graphite powder is oxidized by the reaction with strong acids, to yield Graphite Oxide (GO). This material can eventually undergo a partial reduction with $NaBH_4$ or hydrazine, which help obtaining a less defective graphene. A flash thermal treatment at 1050^o C completes the graphite exfoliation, producing a material, so–called Thermal Exfoliated Graphite Oxide (TEGO), which is

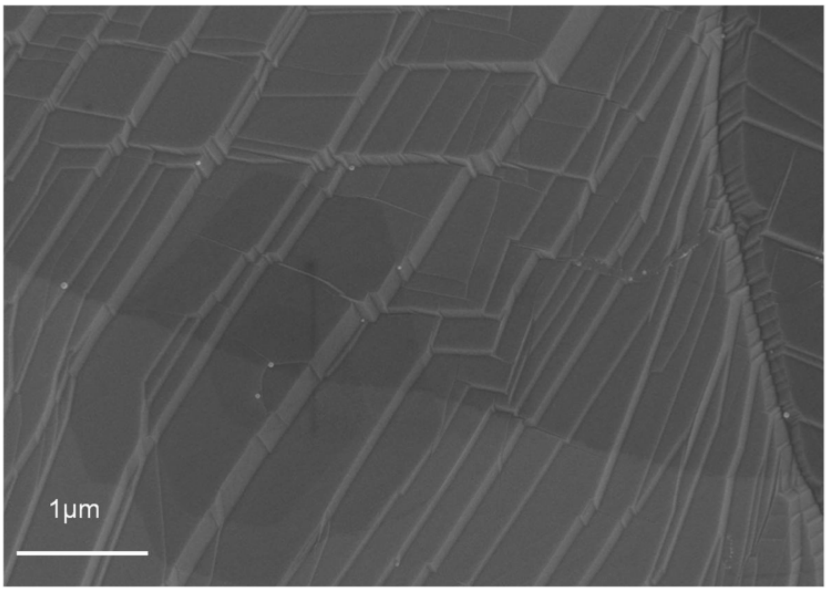

FIGURE 1.11: Graphene grown by Chemical Vapor Deposition (CVD) method on a copper surface

largely composed of single graphene layers. This method has been used for producing the graphene samples studied in this work. A more detailed description will be given in Chap. 4. The main advantages of the chemical route lie in its ease, low–cost, low–impact and effectiveness in producing scalable quantities of graphene (grams of graphene can be produced in few hours). However, an important drawback of this method lie in the variable quality and defectiveness of the product, which limit its usefulness to certain applications requiring a pure product, *i.e.* in nanoelectronics. However it results good for domains requiring large specific area.

As a closing remark, it is noteworthy to observe that this family of wet chemical methods is often intended to include also some minor but emerging techniques, that are not discussed here: in particular the production of graphene Langmuir-Blodgett films [72] and the electrochemical method [71]. Although the research in the field is very dynamic and could certainly open new fascinating scenarios in the near future, producing defect-free graphene in large quantities via chemical route has remained a challenge.

The work presented in this thesis was focused on the study of defective graphene samples produced by the thermal exfoliation of graphite oxide (TEGO). This graphene is intrinsically rich in defects and as we will see in the next section, the defects characterization is of paramount importance for a deep understanding of its physico-chemical properties and eventually to designing and engineering new applicative materials. Moreover, the

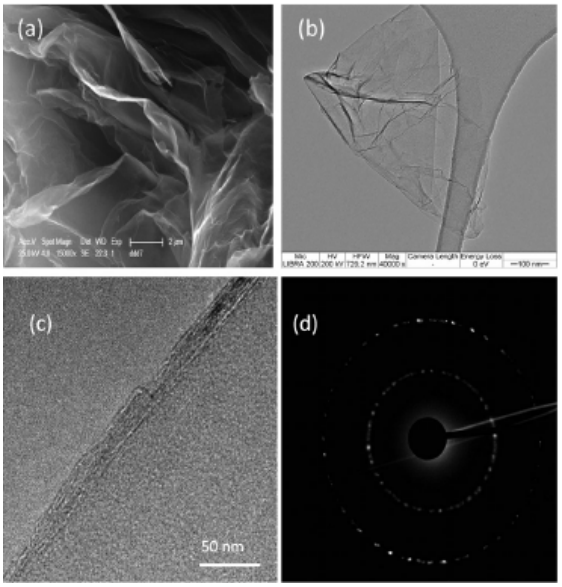

FIGURE 1.12: (a) SEM, (b) TEM, (c) HRTEM images and (d) SAED pattern of few layer graphene sheets prepared by electrochemical method from graphite. Taken from [71].

peculiarity of disposing of samples in gram-scale allows the characterization using experimental techniques, which are not conventionally applied to graphene, like solid–state spectroscopies (Neutron Scattering, NMR, μSR).

1.3.3 Defects in Graphene

Atomic-scale defects in graphene could alter the physical and chemical properties of carbon nanostructures and therefore their investigation and understanding are relevant for both fundamental and technological issues. Defects are usually seen as imperfections that could significantly degrade the performances of a material: for instance, clean and pure materials may be required in electronic devices, in order to minimize the scattering centers density and get uniform transport properties. However, at the nanoscale, the control and even the maximization of defects concentration is sometimes extremely useful for engineering a specific device.

In addition, defects do exist in real systems and are unavoidable in growth processes. Defects can also be deliberately introduced into the materials during the crystal growth or by irradiation with energetic particles (electrons or ions) and/or chemical treatment. Hence their effects, together with their possibilities to enrich the functionalities of carbon nanostructures, should be carefully investigated. Topological defects as pentagon-heptagon pairs, mono-vacancies and multi-vacancies, ad-atoms and edges are typical stable graphene defects, already predicted and experimentally detected. Several experimental works have shown the occurrence of either native or physically introduced

defects in graphene. Tansmission electron microscopy (TEM) and scanning tunneling microscopy (STM) have been used to obtain images of defective graphene with atomic resolution [73]. Even though, the theory of defects has already been developed to some extent in the context of carbon nanotubes and graphite, defects in graphene are still surprisingly not completely understood [74, 75]. In the following paragraphs different types of defects commonly present in graphene will be shortly reviewed.

Point defects and topological distortions: One of the unique properties of graphene is its ability to reconstruct by forming non-hexagonal rings. The simplest example is the Stone–Wales (SW) defect, which does not involve any removed or added atoms. Four hexagons are transformed into two pentagons and two heptagons [SW(55-77) defect] by rotating one of the C-C bonds by 90^o, as shown in Fig. 1.13. The defected structure retains the same number of atoms as pristine graphene and no dangling bonds are introduced. The density of Stone–Wales defects is usually small due to the high activation barrier of several eV for the bond rotation.

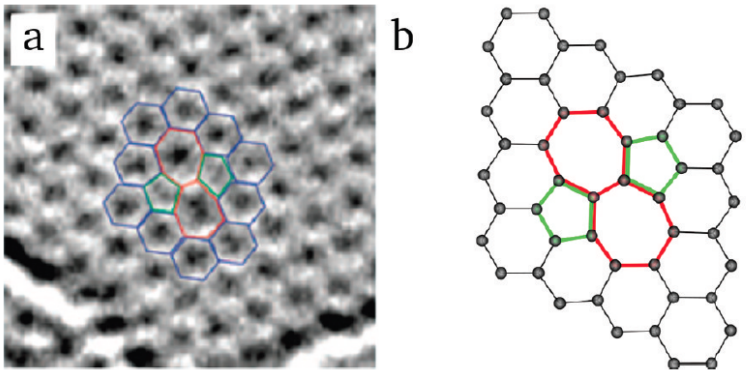

FIGURE 1.13: Stone–Wales defects in graphene. A Stone–Wales defect is the rearrangement of the six-membered rings of graphene into pentagons and heptagons. This rearrangement is a result of $\pi/2$ (90^o) rotation of a C–C with respect to the midpoint of the bond. Taken from [74].

Topological defects in graphene, like dislocations and grain boundaries, introduce nonlocal disorder into the crystalline lattice. Generally, these line defects are tilted boundaries which separate two domains with different lattice orientations, with the tilt axis normal to the plane. High barriers must be overcome (> 6 eV) for the formation of these distortions. Their formation has been theoretically predicted and experimentally observed within the thermal spike of an irradiation (ions or electrons) event or under extreme conditions. It is well-known that the properties of polycrystalline materials are often dominated by the size of their grains and by the atomic structure of the grain boundaries, but the role of these structures is more pronounced in two-dimensional materials such as graphene where even a line defect can divide and disrupt a crystal. In

particular, dislocations and grain boundaries govern the electronic transport in graphene and may eventually be used for engineering graphene-based nanomaterials and functional devices [76].

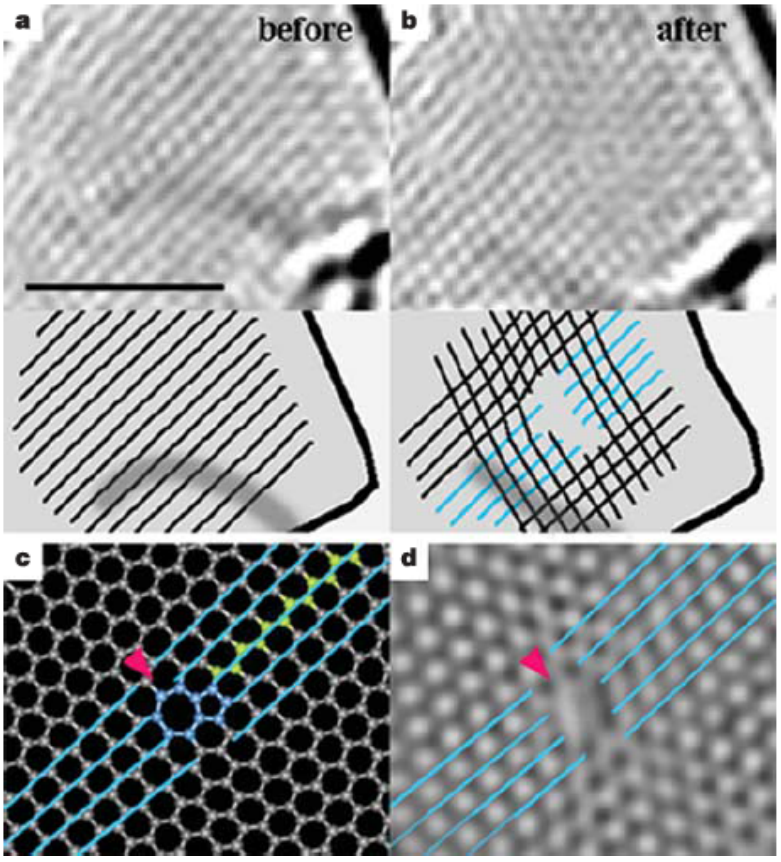

FIGURE 1.14: In situ observation of a topological defect in a graphene layer, induced by an electron beam, after several tens of seconds of irradiation. HR-TEM images show of a single graphene layer before (a) and after (b) the electron beam irradiation. The scale bar is 2 nm. Taken from [73].

Carbon vacancies and edges: The simplest "vacancy-type" defects on the graphene plane show structure with voids created by removing one or several. The Single Carbon Vacancy (SAV) undergoes a Jahn-Teller distortion which leads to the saturation of two of the three dangling bonds towards the missing atom. This leads to the formation of a five-membered and a nine-membered ring ((5-9) defect) and one dangling bond. STM images show SAVs as a protrusion, due to an increase of the local density of states at the Fermi energy, which is spatially localized on the dangling bonds. It is intuitively clear that the formation energy of this defect is high because of the presence of an under-coordinated carbon atom.

Double vacancies (DAV) can be created either by the coalescence of two SAVs or by removing two neighboring C atoms. Similar to the creation of a Stone-Wales defect,

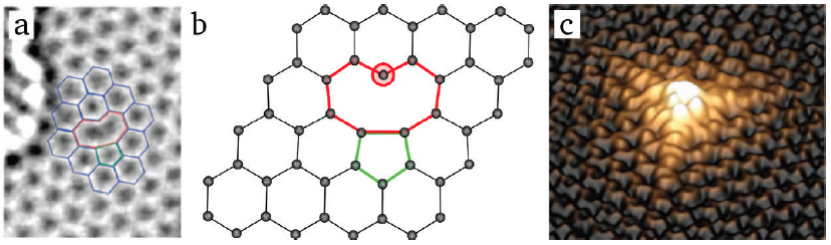

FIGURE 1.15: Single Atom Vacancy SAV (5-9): (a) an experimental TEM image. (b) its atomic structure obtained from our DFT calculations. (c) an experimental STM image, appearing as a protrusion due to an increase in the local density of states at the dangling bond (marked with a circle in panel (b). Taken from [74]

the rotation of one of the bonds could lead to the creation of different arrangement of reconstructed rings instead of hexagons like perfect graphene, like *e.g.* (5-8-5), (555-777) and (5555-6-7777) defects. The atomic network remains coherent with minor perturbations in the bond lengths around the defect. Some images of the atomic structures of reconstructed double vacancy defects in graphene are reported in Fig. 1.16.

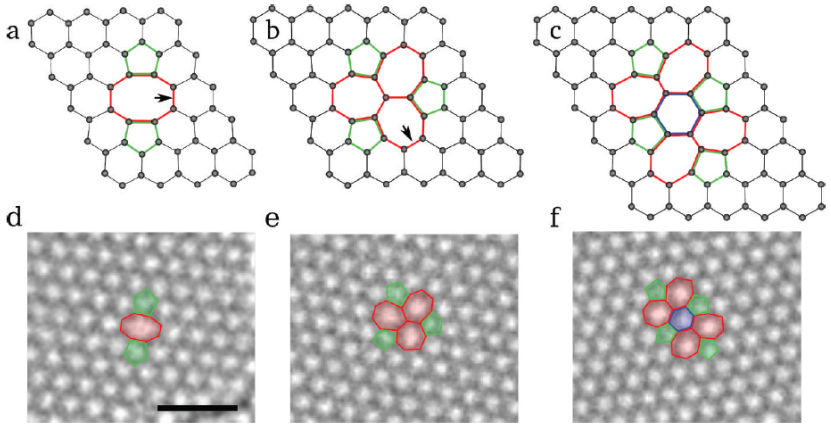

FIGURE 1.16: Atomic structures of reconstructed double vacancy defects in graphene as obtained from DFT calculations (a-c). Experimental TEM images of the same structures (d-f). Taken from [74].

The removal of more than two atoms may lead to larger and more complex defect configurations. Generally, as an even number of missing atoms allows a full reconstruction (complete saturation of the dangling bonds), these vacancies are energetically favored over structures with an odd number of missing atoms, where an open bond remains. If a larger number of atoms is instantaneously removed from a small area, a reconstruction requires bending or warping the layer, its surface area being considerably reduced. In these cases, the formation of a hole with unsaturated bonds around its peripheral border may be more likely. Intuitively, one may expect to obtain a more-or-less random set of carbon vacancies. In general there is no reason for excluding the presence of

dangling bonds also in even-atoms vacancies formed during out-of-equilibrium processes.

Edges themselves can be considered as defects with respect to the ideal graphene plane. The simplest edge structures are the armchair (AC) and the zigzag (ZZ) orientations.

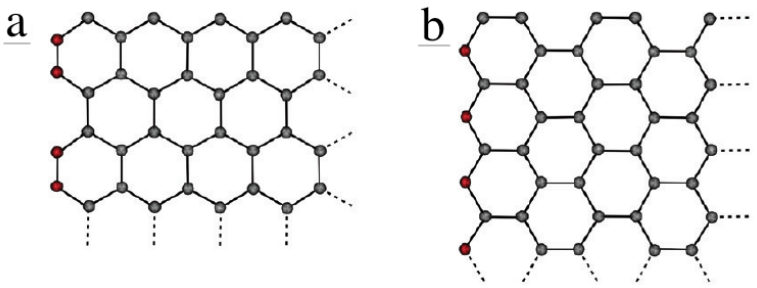

FIGURE 1.17: Different edge orientations in graphene: (a) armchair (AC) edge; (b) zigzag (ZZ) edge

Edges of finite size in graphene, particularly nanographene or nanoribbons, play an important role in giving unconventional electronic structures depending on their AC or ZZ shape. The creation of non–bonding localized electronic states that co-exist with the itinerant electrons gives rise to a plethora of intriguing phenomena. For instance, dangling bonds or vacant atoms were suggested to be responsible of ferromagnetism in some impurity-free carbon materials, like amorphous carbon samples and irradiated highly oriented pyrolitic graphite [77–80]. In this context, in order to explain both the electronic properties and surface (re)activity and the recently observed ferromagnetism in some carbon materials, it has been proposed that under ambient conditions a significant fraction of the oxygen-free edge sites are neither H-terminated nor unadulterated free radicals, the zigzag sites assuming a carbene-like ground state and the armchair ones a carbyne-like structure [81].

Adsorbed molecules and functionalization of graphene: Placing an atom to any in-plane position within the plane would require a prohibitively high energy. For this reason, rather than straining the local structure in two dimensions, additional atoms, like interstitial impurities or more complex chemical groups tend to use the third dimension and bind to C as ad-atoms. The effect of a foreign (non-carbon) atom on the properties of graphene depends on the bonding between the atom and graphene itself. If the bond is weak, only physisorption due to van–der–Waals interaction can occur. If the interaction is stronger, covalent chemical bonding between the foreign atom and the nearest carbon atoms leads to chemisorption. In samples derived from wet chemical methods a great variety of functional groups can be bound to the carbon network. A particular example

of defect is the chemical doping. Oxidation is the one of most common reaction of carbon atoms in a graphene layer with other species. After treatment in an oxidizing acid (HNO_3 or H_2SO_4), it is possible to attach oxygen and hydroxyl (-OH) or carboxyl (-COOH) groups to graphene. When graphene is covered more or less uniformly with hydroxyl or carboxyl groups, the material is called graphene oxide, which is essentially a highly defective graphene sheet functionalized with oxygen groups. It is intuitively clear that defects associated with dangling bonds should locally enhance the reactivity of graphene. Indeed, numerous simulations indicate that hydroxyl, carboxyl, other groups or atoms can easily be attached to vacancy-type defects or graphene edges.

The controlled creation of defects with a high spatial selectivity can be used for the local functionalization of graphene samples and the development of graphenes with the designed properties. Plasma treatment and adsorption of atomic hydrogen on a graphene surface followed by its self-organization and hydrogen island formation can also be referred to in the context of graphene functionalization [82].

1.4 General motivation of the thesis

Over the last few years, thanks to the development of new chemical methods, the massive fabrication of graphene has opened the route towards the experimental investigations using characterizations and hydrogen detection techniques that are not usual for 2D systems. Prof. M. Riccó and coworkers of the Carbon Nanostructures Laboratory (CNL) at the University of Parma (Italy) have applied muon spectroscopy (μSR) to investigate the hydrogen interaction with Thermal Exfoliated Graphite Oxide (TEGO). These studies have shown that TEGO has a particular affinity with hydrogen. This property has an interest at both the fundamental and technological levels. As discussed at the beginning of this chapter, in the context of a growing demand of renewable fuels hydrogen has been identified as a possible replacement to the current gasoline for automotive application and as the cornerstone of a more general conception towards the "hydrogen economy". Considerable interest has been stimulated by carbon nanostructures for their relatively low weight and the possibility to modify their interaction energy with the hydrogen molecule. In the case of graphene, the interaction with hydrogen finds an additional and more fundamental echo: from the controversial rising of magnetism in carbons, to nano–electronics and astrophysics. In the astrochemistry discipline, the role of Polycyclic Aromatic Hydrocarbons (PAHs) on the synthesis of complex molecules (including H_2) in the interstellar medium is a current topic. The fundamental issue in this thematic is the understanding of the dynamics of hydrogen at the surface of a carbonaceous support. μSR suggested the formation of CH-μ groups (analogue to CH_2) at graphene

in-plane vacancies (SAV) when TEGO is bombarded with muons (analogue to H atoms). Moreover, this process seems to be supported by a thermally activated muon capture mechanism [83, 84]. The mobility of chemisorbed hydrogen at the graphene (TEGO) surface was also proved by ^{1}H-NMR. These studies evidenced that the H-mobility is active already at low temperature and it is associated with a surprisingly low activation energy of about only 30 meV [85]. Despite the use of several characterization techniques, the localization of H in the complex carbon structure appears very difficult. In particular, a comprehensive picture of the hydrogen behavior at the graphene surface as well as a detailed study of the defects revealed to be very challenging but essential for getting a very deep insight into the hydrogen behavior. On the other hand, thanks to the high neutrons' sensitivity to hydrogen, neutron scattering represents the ideal probe for investigating either the structure or the dynamics of hydrogenous materials [86, 87]. In particular, Inelastic Neutron Scattering (INS) can provide detailed informations about the dynamical properties of the matter, as vibrations, rotational and diffusional motions in a very wide energy range. In contrast to optical spectroscopy, INS is not restricted to the central point in the Brillouin Zone and subject to symmetry selection rules. Its high sensitivity to all types of atomic movements makes it the technique of choice to extract the Vibrational Density of States (VDOS). Moreover, INS spectra can be accurately modeled and first principle calculations provide then an ideal complement to the experiment, allowing to assign the experimental features to specific vibrational modes. The hydrogen atoms are quantum particles, therefore their properties are subject to subtle variations depending on their local environment. As the molecular vibrations appear to be very sensitive to the local environment, INS can even indirectly provide, support and complement structural information about chemical environment at a very local scale.

In the next chapter we will show how neutron scattering and *ab-initio* simulations have contributed to gain a deeper insight into the local structure and dynamics of some selected carbon nanostructures, with a special attention to Thermal Exfoliated Graphite Oxide (TEGO). The last part of the thesis has been devoted to the dynamical and structural characterization of Nickel–decorated graphene and Alkali-metal intercalated fullerides (mainly A_xC_{60}, A=Li, x=6,12). These studies are not as complete as the one carried out for TEGO and H-TEGO, since they were performed at the end of this PhD project and are still in progress at the time of writing.

This work has been carried out at the Institut Laue Langevin (Grenoble, France) to extend and complement the investigations conducted by Dr. M. Mazzani, Dr. M. Gaboardi and Dr. M. Aramini, during their PhD at the Carbon Nanostructures Laboratory (CNL) in Parma from the neutron perspective.

1.5 How the thesis is organized

The thesis is articulated as follows.

- The experimental techniques (Neutron Scattering), including the instrumentation and data treatment, are presented in Chap. 2. The computational methods are given in Chap. 3.
- In Chap. 4 several characterizations of Thermal Exfoliated Graphite Oxide (TEGO) and nanographite are discussed. In particular we detail the sample synthesis and the morphological (HR-TEM and SEM), structural (diffraction and direct space analysis) and spectroscopic (XPS, UPS, Raman and IR spectroscopy) studies.
- Inelastic Neutron Scattering (INS) experiments and the computational work on Hydrogenated TEGO are discussed in Chap. 5. The experimental results, together with DFT simulations, have allowed to efficiently assign the vibrational lines in the neutron spectra to specific C-H configurations at the graphene surface.
- Chap. 6 treats the thermal evolution of the C-H bending modes and its connection with H mobility in TEGO, as probed by NMR. The possible implication of quantum tunneling effects in this dynamical process is discussed.
- Chap. 7 and Chap. 8 are devoted to Nickel–decorated TEGO and Alkali–Intercalated fullerides, respectively. The neutron scattering characterizations, with a particular emphasis to INS, are presented.
- The general conclusions and future prospects are summarized in Chap. 9

Chapter 2

Neutron Scattering

2.1 Introduction

This chapter will discuss the principal aspects of the neutron scattering based experimental techniques that have been used in this work for characterizing our carbon nanostructured samples. It is organized as follows: the first part will briefly summarized the specificities of the neutron-matter interaction, underlying the advantages/disadvantages of the neutron radiation with regards to others scattering techniques (X-Ray, visible light...). The second and third part will deal with elastic and inelastic scattering respectively, giving an overview of the theory and the description of the instruments used. We will refer as frequently as possible to the well-known neutron scattering textbooks [88, 89], and restrict the technical descriptions of the data treatment and analysis to the minimum.

2.2 Why using neutron scattering?

Neutrons are particles which are very abundant in nature, but which are only found stable when confined inside the nucleus part of the atoms. Together with the protons, they participate to the stability of matter linked together by strong nuclear interactions. This is why the production of neutrons either necessitates or releases a large amount of energy. They are produced at large scale facilities, either using steady state reactor or pulsed sources. The principle of production differs from one type of source to another: the steady state reactor use the fission of an ^{235}U enriched core to produce high energy neutrons, while the pulsed sources send compressed pulses of an intense beam onto a heavy target, subsequently producing intense pulses of high energy neutrons. The latter (of several hundreds of MeV) are thermalized, *i.e.* slowed down to the meV energy range

to be usable in common scattering experiments on the different instruments.
The as-produced thermal neutrons have characteristic wavelength of $\sim$ 1 Å which corresponds to typical energies of $\sim$ 10 meV, which is comparable to the elementary excitations found in solids and liquids (phonons, molecular vibrations...). These peculiar properties make neutron scattering a very natural and powerful probe for studying both the structure and the fluctuations of the atomic positions in condensed matter. By comparisons, the energy of $\sim$ 1 Å X-photons are typically of the keV range, rendering the detection of meV large energy transfers very difficult (but feasible in recent synchrotron beamlines). In the other direction, the typical wavelength for lasers is several hundreds of nanometers, which restricts Raman scattering investigation to the center of the Brillouin zone, *i.e.* making difficult (when feasible) the measurement of dispersion curves. However, neutron scattering is a low flux techniques, which is one of the most important limiting factor. As a consequence, the resolution of a beamline in terms of energy or momentum transfer is in general much less than what can be done in equivalent instruments using X-rays or optical spectroscopies. Also, the sample quantity required for neutron investigations is much larger than the other spectroscopic techniques, making the experiments on single graphene layers for example, totally impossible at the moment. As usually stated, it is the complementarity of the different techniques, *e.g.* IR, neutron, X-ray, Raman and NMR which allowed deriving a coherent picture of the samples we studied.

2.3 Basics of neutron scattering

In this section, there is no question of developing the whole theory of neutron scattering, but simply to provide the reader with the basics to understanding the rest of the manuscript. All the concepts treated in the following sections are developed extensively in the general textbooks of condensed matter physics and neutron scattering [88–90].

The neutron observable when doing a neutron scattering measurement is called the scattering cross section $\frac{\partial^2\sigma}{\partial\Omega\partial\omega}$. It represents the flux of neutrons with incident wavevector (energy) $\mathbf{k}_i$ (E_i) which have been scattered with wavevector $\mathbf{k}_f$ (E_f) in the solid angle $\mathbf{\Omega} \pm \partial\mathbf{\Omega}$, *i.e.* with energy transfer $\hbar\omega = E_i - E_f$ and momentum transfer $\hbar\vec{Q} = \vec{k_i} - \vec{k_f}$ to the sample. This quantity can be separated into a *coherent* and an *incoherent* part as a consequence of the peculiar neutron-nuclei interactions so that it can be written in the following form:

$$\frac{\partial^2\sigma}{\partial\Omega\partial\omega} = \left(\frac{\partial^2\sigma}{\partial\Omega\partial\omega}\right)_{coh} + \left(\frac{\partial^2\sigma}{\partial\Omega\partial\omega}\right)_{inc} = \frac{k_f}{k_i}\, S(\vec{Q},\omega) \tag{2.1}$$

with

$$S(\vec{Q},\omega) = S_{coh}(\vec{Q},\omega) + S_{inc}(\vec{Q},\omega) \tag{2.2}$$

$S(\vec{Q},\omega)$ is called the total dynamical structure factor of the system, and contains the complete information of the sample state. Alike the cross section, it can be separated into a coherent ($S_{coh}(\vec{Q},\omega)$) and an incoherent ($S_{inc}(\vec{Q},\omega)$) part. As we will see, each of these latter quantities can be divided into an elastic and an inelastic part. In particular, the understanding of the *coherent part of the elastic scattering* will allow deriving information on the structure of the sample. By contrast, the *inelastic part of the incoherent scattering* will be analysed to derive the spectroscopic signatures of the different hydrogen atoms at the carbon surface, *i.e.* to derive information about their local environment. We will discuss briefly these notions in the following paragraphs.

2.3.1 Coherent and incoherent scattering cross sections

The notions of coherence and incoherence are the building blocks of neutron scattering. The different materials we have studied during this thesis are mostly composed of carbon, a purely coherent scatterer, and hydrogen which is mostly incoherent. It is therefore useful to precise the meaning of these notions.

When a neutron interacts with a nucleus, it can be either absorbed or scattered, in the latter case its energy and/or trajectory can be affected. The relatively weak energy of the thermal neutrons used in a neutron scattering experiment (in the order of few meV) prevents the excitations of the internal nuclei levels and core electronic states, but is responsible for the sensitivity of the neutrons to the global dynamics of the nuclei, *i.e.* to the instantaneous structure of the material under study. The neutron-nucleus interaction is characterized by a *scattering length* b, which can be a complex quantity for an absorbing material and which quantifies the capacity of an isotope to interact with the neutron beam. This interaction depends on the total spin state $\mathbf{J} = \mathbf{I} + \mathbf{S}$ of the neutron-nucleus system (with $\mathbf{I}$ the nucleus spin and $\mathbf{S}$ that of the neutron). The scattering length therefore varies from one chemical species to another, but also from one isotope to another within the same species: for a given isotope i the statistic average of the scattering length over all the spin states $b_i^{coh} = \overline{b_i}$ is called the *coherent* scattering length. The coherent part of the scattering therefore approximates the ensemble of isotopes i to be all in the same average spin state.

The deviation of the real state of the system from this ideal situation is characterized by the *incoherent* scattering length, $b_i^{inc} = \sqrt{\overline{b_i^2} - \overline{b_i}^2}$, defined as the mean squared of the scattering lengths b_i. The coherent and incoherent cross sections are defined by $\sigma_i^{coh} = 4\pi(b_i^{coh})^2$ and $\sigma_i^{inc} = 4\pi(b_i^{inc})^2$ respectively. For a pure isotope, we will refer

to the *spin* origin of the incoherent scattering. Spin incoherence vanishes for isotopes which have the peculiarity that $\overline{b_i^2} = \overline{b_i}^2$. This happens when the atomic numbers Z and A have even values, which is the case for ^{4}H, ^{12}C, ^{16}O, ^{20}Ne... their nucleus having a nuclear spin equal to 0. This is why the scattering for an isotopically pure material made of ^{12}C has no incoherent scattering.
Another source of incoherent scattering originates from the natural distribution of the isotopes of one atomic species. In that case, the scattering lengths have to be calculated in order to account for this distribution, and this is why a natural material made of carbon, *i.e.* containing 1.1% of ^{13}C with $b_{^{13}C}^{inc}$ = -0.52 10^{-15} m has a small but finite incoherent cross section of 0.001 barns. In the rest of this manuscript, we will consider that pure carbon nanostructures scatter neutron purely coherently, with a coherent cross section $\sigma_C^{coh} = 5.554$ barns. The situation is entirely reversed for a hydrogen containing material. The neutron cross section of H (82.02 barns) is the largest among the periodic table of the elements. In particular, its incoherent cross section amounts σ_H^{inc}=80.26 barns which makes this elements mostly incoherent scatterer. By contrast, the coherent and incoherent scattering cross section for a deuterium atom are $\sigma_D^{coh} = 5.592$ barns and $\sigma_D^{inc} = 2.05$ barns respectively. A solution for controlling the relative proportion of coherent and incoherent scattering is to monitor the ratio H/D in the sample, via deuteration of the hydrogenated parts in the system under study.

2.3.2 Elastic and inelastic scattering – The van Hove correlation functions

In the introduction part of this chapter we have indicated that the scattering (either coherent or incoherent) can also be qualified as a function of the energy transfer between the neutron probe and the sample:

$$S_{coh}(\vec{Q},\omega) = S_{coh}^{el}(\vec{Q}) + S_{coh}^{inel}(\vec{Q},\omega) \quad (2.3)$$

$$S_{inc}(\vec{Q},\omega) = S_{inc}^{el}(\vec{Q}) + S_{inc}^{inel}(\vec{Q},\omega) \quad (2.4)$$

Following van Hove citevanhove54 the dynamical structure factors are linked to the space and time correlation function via the following double Fourier transforms:

$$S_{coh}(\vec{Q},\omega) = \frac{1}{2\pi\hbar}\int dt e^{-i\omega t}\int d^3\vec{r}K(\vec{r},t)e^{i\vec{Q}\cdot\vec{r}} \quad (2.5)$$

$$S_{inc}(\vec{Q},\omega) = \frac{1}{2\pi\hbar}\int dt e^{-i\omega t}\int d^3\vec{r}K_s(\vec{r},t)e^{i\vec{Q}\cdot\vec{r}} \quad (2.6)$$

where $K(\vec{r},t)$ and $K_s(\vec{r},t)$ are the pair and self time–and–space correlation functions respectively. They give the probability of finding an atom located at $\vec{r}$ at time t if this

atom strictly (for the self) or any atom (for the pair) is located at the origin at time $t = 0$.

Elastic scattering

In case of no energy transfer (the neutron is scattered without any change of its initial speed/wavelength) the scattering is elastic and the pertinent variable to consider is the momentum transfer $\vec{Q}$ between the neutron wave and the sample. $S^{el}_{coh}(\vec{Q})$ provides information on the atomic structure of the sample at *long* time. Here the adjective *long* refers to the maximum correlation time provided by the instrument, *i.e.* it depends on the energy resolution of the neutron spectrometer used in the experiment: the sharper the instrumental resolution, the longer the correlation time. For a diffractometer, the energy resolution is extremely broad by construction (there is no energy analyser for a diffractometer), so that the scattered intensity is integrated *over the complete energy transfer range*, and we qualify the scattering as *total scattering* with the (total) structure factor:

$$S_{coh}(\vec{Q}) = \int_{-\infty}^{+\infty} d\omega S_{coh}(\vec{Q},\omega) \tag{2.7}$$

According to the equation 2.5 one can easily show that

$$S_{coh}(\vec{Q}) = \int d^3\vec{r} K(\vec{r},0) e^{i\vec{Q}\cdot\vec{r}} \tag{2.8}$$

with $K(\vec{r},0) = \delta(\vec{r}) + \rho_0 g(\vec{r})$ [89], ρ_0 the average density of the material and $g(\vec{r})$ *the static pair distribution function*, one can rewrite Eq. 2.8 in the form:

$$S_{coh}(\vec{Q}) = 1 + \rho_0 \int g(\vec{r}) exp(i\vec{Q}\cdot\vec{r}) d^3r \tag{2.9}$$

If one wants to make visible the forward scattering at Q=0, $\rho_0\delta(\vec{Q})$, then one can write:

$$S_{coh}(\vec{Q}) = 1 + \rho_0 \int g(\vec{r}) exp(i\vec{Q}\cdot\vec{r}) d^3r + \rho_0\delta(\vec{Q}) - \rho_0\delta(\vec{Q}) \tag{2.10}$$

$$S_{coh}(\vec{Q}) = 1 + \rho_0 \int [g(\vec{r}) - 1] exp(i\vec{Q}\cdot\vec{r}) d^3r + \rho_0\delta(\vec{Q}) \tag{2.11}$$

In an experiment, the forward scattering at Q=0 is not measured, so that the experimental quantity accessible is:

$$S_{coh}(\vec{Q}) = 1 + \rho_0 \int (g(\vec{r}) - 1) exp(i\vec{Q}\cdot\vec{r}) d^3r \tag{2.12}$$

For isotropic samples, one has $g(\vec{r}) = g(r)$, and the previous equation can be further reduced to:

$$S_{coh}(Q) - 1 = \int G(r)\frac{sin(Qr)}{Q}dr \tag{2.13}$$

with the reduced atomic pair distribution function $G(r) = 4\pi r\rho_0(g(r)-1)$. By using the properties of the inverse Fourier transform, one can show that the reduced PDF $G(r)$ can be expressed by:

$$G(r) = \frac{2}{\pi}\int Q[S(Q) - 1]sin(Qr)dQ \tag{2.14}$$

The total scattering therefore provides an instantaneous picture of the atomic correlations in the sample, *i.e.* its instantaneous structure. The reduced PDF function $G(r)$ provides an excellent way of characterizing the atomic structure of materials containing a considerable amount of disorder or reduced coherent length.

The elastic incoherent scattering appears as a background in the diffraction measurements. It can be expressed as:

$$S^{el}_{inc}(\vec{Q}) = \sum_{j\in H} exp(-2W_j(\vec{Q})) \tag{2.15}$$

with $W_j(\vec{Q})$ the Debye-Waller term of the hydrogen atom j in the sample.

Eq. 2.16 is valid for an oriented (crystalline) sample. The powders we have studied are isotropic, so that the latter expressions have to be averaged over all the directions of the $\vec{Q}$ vector. The structure factor then depends only on the amplitude of $\vec{Q}$ so that we will write:

$$S^{el}_{inc}(Q) = \overline{\sum_{j\in H} exp(-2W_j(\vec{Q}))} \tag{2.16}$$

with $\overline{X}$ denoting the orientation average of the quantity X.
It is usual for an isotropic sample to approximate the Debye-Waller term $W_j(\vec{Q})$ by its isotropic expression $W_j(Q) = \frac{1}{6}Q^2U_j^2$, with U_j being the mean squared displacement of the hydrogen atoms j. If U_j are not too different from one type of hydrogen to another, U_j can be replaced by an atomic averaged mean square displacement U, so that 2.16 can be written as:

$$S^{el}_{inc}(Q) = N_H exp(-\frac{1}{3}Q^2U^2) \tag{2.17}$$

The latter expression shows that the intensity of the elastic line is proportional to the quantity of H atoms in the sample and has a very smooth dependence with the momentum transfer Q. It provides a very useful mean for deriving the number of hydrogen

atoms present in the sample, as well as an estimation of their averaged mean square displacement.

In the Chap. 5 we used Eq. 2.17 to derive the quantity of hydrogen present in several samples. For that, we have measured the time-of-flight spectrum of a calibrated mass of Vanadium, which is an almost pure incoherent scatterer ($\Sigma_V^{coh} = 0.0184$ barn; $\Sigma_V^{coh} = 5.08$ barn). The integrated elastic line of the spectrum, over a limited range in Q to reduce the effect of the Debye–Waller term, is therefore proportional to the known number of V atoms (N_V) in the sample. A particular care was taken to keep the vanadium sample measurements in strictly the same geometry as the carbon sample measurements. The elastic intensity of the vanadium standard (I_V) and of the H-containing sample (I_H) was evaluated in a common range of Q, avoiding some non-negligible coherent contributions from the carbon framework. If we make the assumption that the Debye - Waller factor in both estimations is a second order correction to the quantity derived, the number of H atoms in the H-containing sample (N_H) is derived from:

$$N_H = \left(\frac{I_H}{I_V}\right)\left(\frac{sigma_V}{sigma_H}\right) N_V \tag{2.18}$$

with σ_V and σ_H being the V and H incoherent neutron scattering cross-section, respectively.

Inelastic scattering

By contrast to elastic scattering, a subsequent part of the kinetic energy of the neutrons is transferred to the sample for inelastic scattering. The analysis of the resulting *inelastic spectrum* $S(\vec{Q},\omega)$ provides information on the energy levels of the sample under study. These levels can be magnetic (crystal field, spin waves), and/or nuclear. In the latter case they reflect the fluctuations of the atomic positions in the system, which vary with the thermodynamics conditions (P, T ...) of the sample. The time (and space) periodic variations of the atomic positions will reflect the interactions at stake in the sample. They will be revealed by their corresponding (eigen) frequency ω_λ, either characteristic of stiff molecular vibrations, or soft lattice (phonon) modes. The energy distribution of these modes will be the main subject of this thesis.

In this part, we give the expressions of the coherent and incoherent structure factors for inelastic scattering. As developed in the textbooks [88, 89], we consider here that the movement of the atoms is limited to short range fluctuations, *i.e.* vibrations around their

equilibrium positions. In particular, we do not consider here any long range diffusion of the atoms nor anharmonic terms in the interatomic potential. We restrict therefore the development of the inelastic structure factor in power of the displacement of the atoms to the first order, *i.e.* to *one phonon events*. We will consider that the coherent part of the scattering originates essentially from carbon contributions and will develop the incoherent term as if originating uniquely from hydrogen atoms. If this approach is valid for pure hydrogenated carbon nano–structures, one has to bear in mind that hydrogen atoms have a non negligible coherent scattering cross section. Also, when metal decorated graphene or metal intercalated fullerides are considered, the contribution of the metallic particles should be included. In particular, Ni, Li and Na atoms have coherent and incoherent cross sections which should be taken into account in the interpretation of their spectra. However, the extrapolation of the proposed formalism to the real cases is straightforward, and therefore we will restrict our discussion here to a pure carbon framework host containing hydrogen atoms as guests.

The development of the expressions of the dynamical structure factors is based on the knowledge of the atomic positions $\vec{r_n}$ in the sample and of the normal modes $|\lambda\rangle$ and normal frequency ω_λ. The latter are respectively the eigenvector and the eigenvalues of the 3N $\times$ 3N dynamical matrix (or Hessian matrix, N being the total number of atoms in the structure) which is constituted of the force constant elements of the system calculated from the derivatives of the harmonic interatomic potential of the system around its equilibrium state [90, 91].

In case of coherent scattering, simplifications arise if one can describe the structure of the carbon structure as the periodical arrangement of unit cells. The latter can be derived from the simple graphene cell (*i.e.* composed of only two inequivalent C atoms) or constructed from the symmetry inequivalent parts of a more complex structure if one consider the case of the fulleride crystals for example. For such crystals, the atoms are indexed according to the cell l they belong to, and are given a type d, so that N_d denotes the number of inequivalent atoms in the carbon unit cell and N_l the number of cells in the sample. Thanks to the translational symmetry of the structure, the 3N $\times$ 3N problem is reduced to the evolution of the eigenvalues $\omega_j(\vec{q})$ and eigenvectors $|j\vec{q}\rangle$ of a $3\mathrm{N}_d \times 3\mathrm{N}_d$ matrix as a function of wavevectors $\vec{q}$ belonging to the first Brillouin zone of the crystal. The quantum number λ of the total hamiltonian is therefore replaced by the couple $(j, \vec{q})$.

In phonon creation (Stokes), the coherent dynamical structure factor in the one phonon process approximation [88, 89] $S_{coh}(\vec{Q},\omega)$ can be written:

$$S_{coh}(\vec{Q},\omega) = N_l \frac{n(\omega,T)+1}{2\omega} \sum_j F_j(\vec{Q})\delta(\omega-\omega_j(\vec{Q})) \tag{2.19}$$

with the one phonon form factor:

$$F_j(\vec{Q}) = \| \sum_{d=1}^{N_d} \frac{b_d^{coh} e^{-W_d(\vec{Q})}}{\sqrt{(M_d)}} \vec{Q}\cdot\vec{e_j}(\vec{Q} \mid d))\|^2 \tag{2.20}$$

and the Bose thermal population factor $n(\omega,T) = (exp(\hbar\omega/k_\beta T)-1)^{-1}$. Index d refers to the dth atom among the N_d atoms in the unit cell, with mass M_d and coherent scattering length b_d^{coh}. $W_d(\vec{Q})$ is the Debye-Waller factor of atom d, and $\vec{e_j}(\vec{Q} \mid d))$ is the displacement of atom d in the normal mode $|j\vec{Q}\rangle$.

For a powder the isotropic averaging of the expression $S_{coh}(\vec{Q},\omega)$ is given by

$$S_{coh}(Q,\omega) = \frac{1}{4\pi}\int d^2\Omega S(\vec{Q},\omega) \tag{2.21}$$

The one phonon incoherent cross section writes:

$$S_{inc}(\vec{Q},\omega) = \frac{n(\omega,T)+1}{2\omega}\frac{b_H^{inc}}{M_H}\sum_{d\in H} e^{-2W_d(Q)} \sum_{j,\vec{q}} \|\vec{Q}\cdot\vec{e_j}(\vec{q} \mid d))\|^2 \delta(\omega-\omega_j(\vec{q})) \tag{2.22}$$

which in the case of a powder can be approximated to:

$$S_{inc}(Q,\omega) = \frac{n(\omega,T)+1}{2\omega}\frac{3NQ^2}{2}\frac{b_H^{inc}}{M_H}\sum_{d\in H} e^{-2W_d(Q)} g_d(\omega) \tag{2.23}$$

with $g_d(\omega)$ being the partial phonon density of state of atom d:

$$g_d(\omega) = \frac{1}{3N}\sum_\lambda \|\vec{e_\lambda}(d)\|^2 \delta(\omega-\omega_\lambda) \tag{2.24}$$

In case that only one type of hydrogen atoms exists in the sample (or if we make the assumption that their dynamics is not significantly different), one can further simplifies the previous expression as:

$$S_{inc}(Q,\omega) = \frac{n(\omega,T)+1}{2\omega}\frac{3NQ^2}{2}\frac{b_H^{inc}}{M_H} e^{-2W_H(Q)} g_H(\omega) \tag{2.25}$$

with $g_H(\omega)$ being the hydrogen partial phonon density of states, and resulting from the statistical averaging of the different atomic hydrogen types in the sample:

$$g_H(\omega) = \sum_{d \in H} g_d(\omega) \tag{2.26}$$

From the expressions 2.19 and 2.22 one clearly sees that coherent scattering has a condition that ensures - in addition to the conservation of energy - the conservation of the total momentum of the neutron-sample system. This appear as an additional condition over the $\vec{Q}$ vector in the expression 2.19. This condition has made the success of neutron scattering in condensed matter science, providing an experimental mean of the measurement of the dispersion curves, *e.g.* sound waves or spin waves. In the data, this conditions and *i.e.* the strong Q dependence of the coherent form factor $F_j(\vec{Q})$ of expression 2.19 makes possible the distinction between a coherent and an incoherent signal: while the former possesses a rather complex dependence with Q, the latter is rather monotonous in Q, resulting from the competition between an increasing Q^2 term and an exponentially decreasing Debye-Waller (see Fig. 2.1).

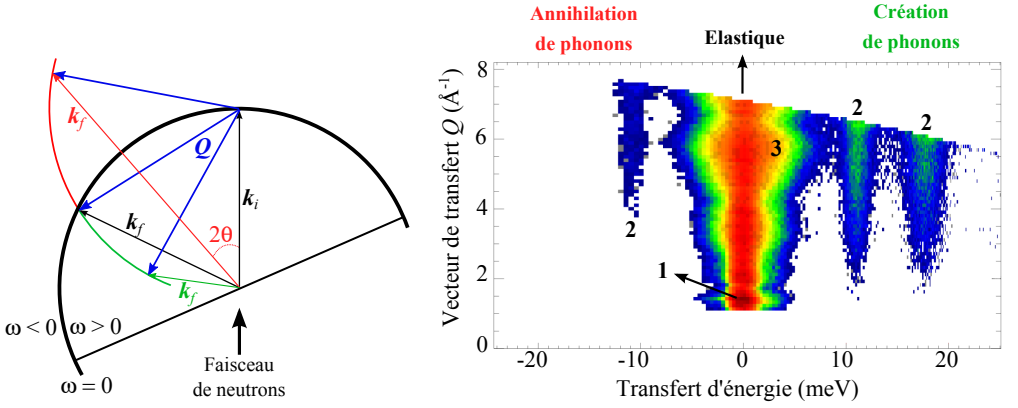

FIGURE 2.1: *Left:* Characteristic set up of an inelastic neutron scattering experiment. *Right:* Dynamical structure factor $S(\vec{Q},\omega)$ of a powder composed of fullerene-cubane $C_{60}{\cdot}C_8H_8$ measured on the IN4C spectrometer at the ILL. The incoming neutron beam with wavevector $\vec{k}_i$ is scattered with wavevector $\vec{k}_f$. If $k_i = k_f$, the scattering is elastic ($\omega = 0$) giving rise to the intense vertical band in the $S(\vec{Q},\omega)$ map, showing intense Bragg spots at specific Q. In case $k_f > k_i$, neutrons are accelerated through the annihilations of some phonons (anti-Stokes scattering). At the contrary, the energy released by the neutrons to the sample when $k_f < k_i$, permits the creation of phonons (Stokes scattering). The region of $S(\vec{Q},\omega)$ indicated by **2** localizes inelastic features whose monotonous Q dependence (and strong intensity) suggests they arise from phonons implying vibrations of a strong incoherent scatterer *i.e.* from the H atoms attached to the cubane molecules in this case. The region marked by **3** is called "quasielastic" scattering and represents low frequency modes, *i.e.* Debye modes or relaxations (free rotations...). Here, the strong Q modulation of the latter scattering indicates a coherent nature of the signal: it characterizes the free rotations of the C_{60} molecules in the structure [92].

Inelastic neutron scattering data handling and representations

In the rest of this manuscript, the inelastic neutron scattering data will be presented and discussed using several representations. When the coherent nature of the signal has to be highlighted or when a global view of the scattering is desired, the $S(\vec{Q},\omega)$ maps will be showed. When the energy dependence is essentially discussed, we will either use the generalized density of state $G(\bar{\theta},\omega)$ or susceptibility $\omega^{-1}\chi''(\bar{\theta},\omega)$ representations. They are defined as:

$$G(\bar{\theta},\omega) = \frac{S(\bar{\theta},\omega)}{Q(\bar{\theta},\omega)^2}\frac{\omega}{n_B^{\pm}(\omega,T)} \tag{2.27}$$

$$S(\bar{\theta},\omega) = \frac{1}{\pi}\frac{1}{1-e^{-\hbar\omega/k_BT}}\chi''(\bar{\theta},\omega) \tag{2.28}$$

where $S(\bar{\theta},\omega)$ represents the dynamical structure factor $S(\theta,\omega)$ at a fixed angle θ averaged over a certain angular width[1]. The scattering is further considered as originating from an averaged set of mean angles $\bar{\theta}$, *i.e.* implying effective momentum transfers $Q(\bar{\theta},\omega)$ expressed as:

$$Q(\bar{\theta},\omega) = k_i^2 + k_f^2 - 2k_ik_fcos(\bar{\theta}) \tag{2.29}$$

In the expressions 2.27 and 2.28, the term $n_B^{\pm}(\omega,T)$ is the population factor (also called Bose factor) with $n_B^+ = \frac{1}{e^{\beta\hbar\omega}-1}+1$ for positive $\hbar\omega$ (Stokes) and $n_B^- = \frac{1}{e^{\beta|\hbar\omega|}-1}$ for negative $\hbar\omega$ (anti-Stokes).
In the hight temperature approximation one can consider that $\omega^{-1}\chi''(\omega) \propto \omega^{-2}G(\omega)$ [10]. As a consequence, the susceptibility of the system does not depend on temperature for harmonic crystals. Any departure from this constant behavior would reflect the onset of anharmonicity in the material under investigation.

When a quantitative comparison between the data and the simulations is required, we further corrected the as-obtained generalized density of states $G(\theta,\omega)$ in Eq. 2.27 from the Debye-Waller decrease at high Q. The method employed is called the "interpolation at low Q" an is valid only for incoherent scattering, *i.e.* was used only for hydrogenated samples. This is based on the fact that $G(\bar{\theta},\omega)$ contains the term $exp(-2W_H)$ as part of the structure factor $S_{inc}(\bar{\theta},\omega)$ (see 2.25), with $W_H = \frac{Q(\bar{\theta},\omega)^2u_H^2}{3}$. The method consist of a linear fit of the quantity $ln(G(\bar{\theta},\omega))$ plotted as a function of $Q(\bar{\theta},\omega)^2$ for each value of the energy transfer ω: $ln(G(\bar{\theta},\omega)) = A(\omega)*Q(\bar{\theta},\omega)^2 + K(\omega)$. $K(\omega)$ therefore stands

[1] If statistics is required, one can even sum up the scattered intensity at fixed energy transfer over the total range of angles allowed by the spectrometer geometry.

for the the generalized density of states interpolated to $Q = 0$, *i.e.* should be free from any Q dependence in the case of an incoherent scatterer[2].

We will as well discuss the *mean square displacement* that we derive from the data by:

$$\langle u_H^2 \rangle = 3\frac{\ln[I(Q)]}{Q^2} \tag{2.30}$$

I(Q) is obtained by fitting the (incoherent part of the) elastic contribution of the scattering at each Q (or scattering angle θ) to a gaussian function.

2.4 Diffraction and PDF analysis

We have used high energy neutron diffraction to derive structural informations about the carbon nanostructures and their hydrogenated (deuterated) counterpart. The use of high energy neutrons beams (or short wavelength in the case of Xrays) to derive the atomic pair distribution function (PDF) of compounds organized at the nanoscale is getting more and more popular [93]. It provides an efficient way of characterizing a structure when traditional Bragg analysis (*i.e.* Rietveld refinement methods) is limited by the lack of Bragg peaks in the diffraction pattern due to disorder and/or limited coherent domain. Note than in the following chapters (in particular in Chap. 4) dedicated to the discussion of the PDF, we will also present data obtained on the High Energy Diffraction Beamline ID15 at the European Synchrotron Facility ESRF.

2.4.1 The diffractometer D4C

D4C is a two-axis diffractometer, which uses short-wavelength neutrons from the hot source and measures then diffraction patterns over a large Q-range. This allows the characterisation of local atomic order of non-crystalline materials (glasses, liquids, amorphous solids and solutions) with excellent accuracy [94].

Principle: An incident wavelength is provided by a crystal monochromator. The scattered neutrons are recorded over a large scattering range by a large array of microstrip detectors, making the machine very efficient and very stable for difference measurements on small samples.

[2] This is a valid assumption as far as multiphonon scattering is negligible. In case of high temperatures and/or scattering processes involving large Q transfers, it is often better to let the data uncorrected from the Debye–Waller contribution as the latter and that from the multiphonon scattering often compensates each other to a large extend.

Instrument description: D4C is built on the H8 hot beam at the ILL. The monochromator take-off angle is $2\theta_M \sim$ 20-40° variable. The available monochromators are all horizontally and vertically focusing: Cu (220) for $\lambda = 0.7$ Å , Cu (220) for $\lambda = 0.5$ Å , Cu (331) for $\lambda = 0.35$ Å. All three monochromators faces are 20 cm high and 23 cm wide. Filters are used for $\lambda/2$ harmonic contamination. A high-transmission monitor located between the monochromator and the beam-defining slits is used for normalisation to incident beam intensity.

The sample is mounted in an evacuated cylindrical bell jar with a wide-angle thin aluminum exit window. The samples are contained in cylindrical vanadium cans (see Fig. 2.3). Vertical and horizontal slits allow defining a maximum illuminated cross-section of 5 cm (Vert.) and 2 cm (Horiz.).

The instrument is equipped with 9 ^3He-gas 1D position-sensitive detectors, with distance between sample and detection surface of 1146 mm. Each detector of 64 cells covers 8° in 2θ. Since there is a 7° gap between two detectors, at least 2 angular positions of the 9-detector ensemble are required to produce a complete diffractogram, and normally scans of 5 or 6 angular positions are used in order to equilibrate counting statistics. The final available 2Θ-range of the diffractogram is 1.5° to 140° [94].

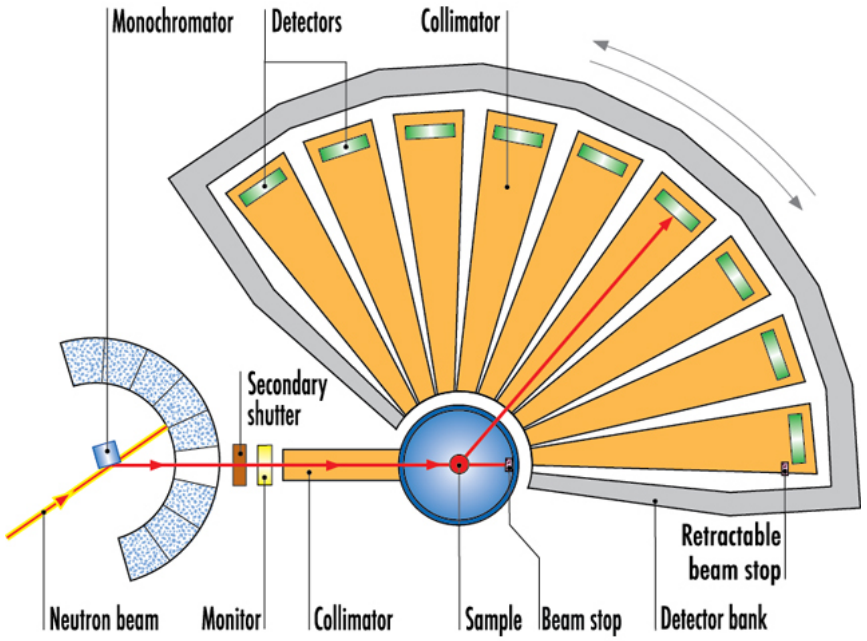

FIGURE 2.2: Layout of the D4 diffractometer [94].

Data treatment: The data reduction consisted of the following operations and were performed using a software procedure developed by the D4C team.

FIGURE 2.3: Image of a typical 7mm Vanadium cylindrical sample holder used during the experiment on D4C.

1. Grouping repeated scans of the D4C detectors over the available range of scattering angles in the reciprocal space.

2. Appropriate background (a linear combination of the vanadium sample holder and empty bell jar contribution) subtraction from the raw data, taking into account absorption effects [95] as well as the incoherent-scattering contribution.

3. Standard multiple-scattering [96] and Placzeck [97] corrections were applied.

4. Fourier transform was performed to produce the reduced PDF G(r) described in § 2.3.2.

2.5 Neutron spectroscopy – Inelastic neutron scattering

In this section, we describe the principle of the two neutron spectrometers that were used during this thesis: the thermal time of flight spectrometer IN4C and the hot filter-analyser spectrometers IN1BeF/LAGRANGE.
The first cited instrument belongs to the direct, crystal monochromator, category of the time of fight instruments (*i.e.* hybrid TOF). This means that the incident neutrons have their wavelength (energy E_i) chosen by a crystal monochromator and that the final

energy E_f of the scattered neutrons is analysed by measuring their time of flight. IN4C is built on the thermal beam H12 at the ILL, therefore allowing the investigation of energy and momentum transfer range from [0, 100] meV and [0.5, 10] $Å^{-1}$ respectively. This instrument is very well suited to the measurement of lattice excitations (phonons, rotations, librations...) and molecular vibrations up to 100 meV. Its large sensitivity to molecular rotations (either free quantum rotors levels or hindered rotations) makes it very useful to probe the quantity of residual molecular hydrogen or hydrogenated molecular units (-CH3) in the sample, *e.g.* in hydrogenated graphene. IN4C was largely employed also to probe the change of the C_{60} dynamics upon intercalation with metal atoms, as we will see in Chap. 8.
The inverse analyser spectrometer IN1BeF (which was recently replaced by LAGRANGE) has a different principle. It uses also a crystal monochromator to vary the incident neutron energy E_i, while the scattered energy E_f is fixed by, either the Bragg cut-off of a Be filter for the IN1BeF instrument, or by the (002) Bragg reflexion of a monocrystal block of HOPG in the case of LAGRANGE. IN1 is an instrument built on the hot source at the ILL. It delivers neutrons from several tens of meV to several eV, *i.e.* covering a very large range of energy transfer. It is very useful for measuring the molecular vibrations like the periodic local deformation of the C-H bonds in the hydrogenated samples. These modes can be separated into the so-called bending and stretching components, which have intense signatures in the 100-150 meV and 350 meV range respectively. These modes give the spectral signature of the C-H local environment.

2.5.1 Time of Flight principle and the spectrometer IN4C

For the inelastic neutron scattering measurements that were performed on the time of flight spectrometer IN4C, the sample were constituted of powders (about 500 mg) filled in air tight aluminum cells (transparent to neutrons), of dimensions ($4 \times 3 \times 0.02$ cm^3) (see Fig. 2.4 and 2.5). The sides of the cell was covered during acquisition by cadmium, absorbing neutrons in order to reduce the background noise. As we will show in this paragraph, the measurements of vibrational excitations in powders using time of flight spectrometry proved suitable. We explain below the principles of this technique.

Principle: The principle of the time of flight method is to measure the number of neutrons scattered in a certain solid angle as a function of time. The kinetic energy of each scattered neutron is evaluated by its time of flight t, *i.e.* the time it takes for the neutrons to cover the sample to detector distance, which can be traced back to its speed. Knowing its initial energy - chosen by the crystal monochromator - one can access to

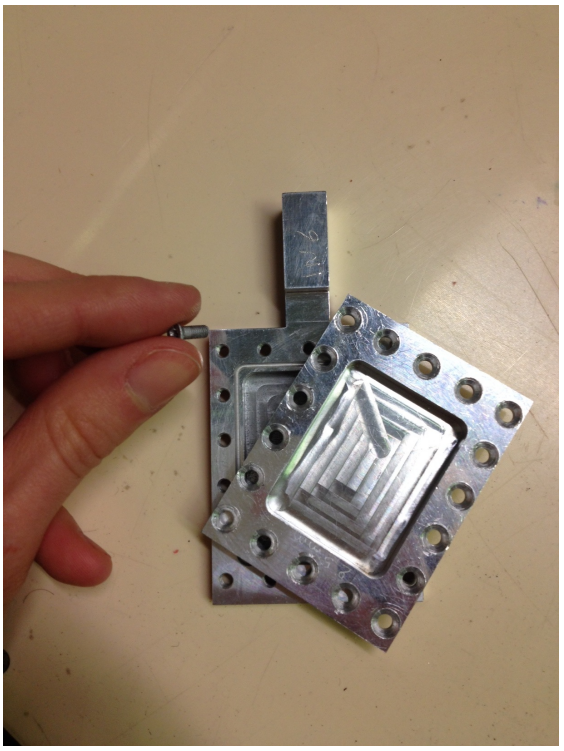

FIGURE 2.4: Image of a flat Aluminium sample holder used during the experiment on IN4C.

FIGURE 2.5: Image of vial containing TEGO powder for an the experiment on IN4C. Sample handling and manipulations were done inside a glovebox in order to prevent any possible oxygen moisture contamination of the samples.

the energy transfer $\hbar\omega$ between the neutron and the sample. Fig. 2.6 shows the layout of the IN4C time of flight spectrometer (ILL, Grenoble) used for our investigations.

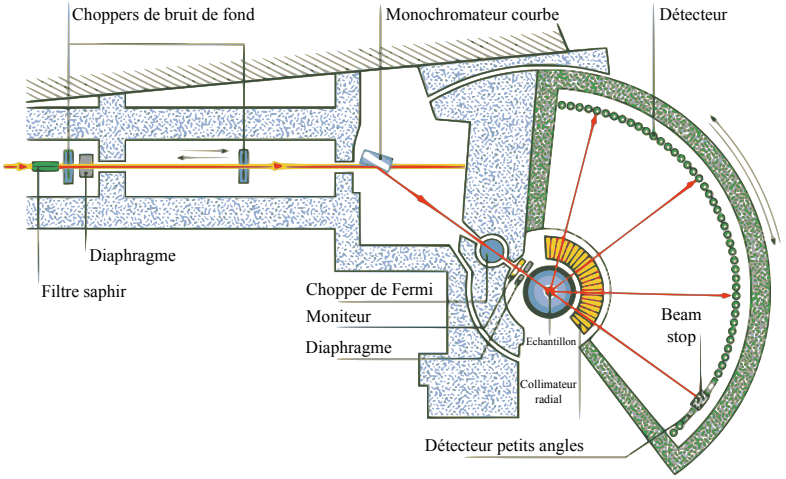

FIGURE 2.6: Layout of the IN4C spectrometer (ILL, Grenoble) [98]. Background choppers are neutron opaque discs and drilled of holes, through which only selected neutrons can pass. They are placed perpendicularly to the incident beam and rotate with a typical speed of about 1000 rpm. The curved monochromator consists of an assembly of 55 graphite or copper single crystals, forming an angle with the incident neutron beam determined by the choice of the incident wavelength. The Fermi chopper is formed by an aluminum cassette containing an assembly consisting of a succession of layers of aluminum blades glued together using a ^{10}B enriched epoxy resin. This optical element ensures a sharp chopping of the incident beam into short time pulses and defines the origin of time t = 0. It also provides a way to tune the resolution of the instrument using the time focusing principle [99].

Instrument description: A "white" beam of neutrons comes from the neutron beam tube H12, whose aperture is located in the core neighborhood at the position of the maximum thermal neutron density. These neutrons are produced by the enriched uranium core and further thermalized by the heavy water moderator at ambient temperature.
A set of two "wheels" type steel choppers, with their horizontal axis of rotation and made of eight windows each, provides a long pulse and a rough selection of the wavelength. It also prevents higher or lower orders of the incident wavelength contaminating the measurements. They role mostly is to ensure protection against fast epithermal neutrons of the direct beam which can add a significant contribution to the background, in addition to the action of a sapphire filter positioned far upstream of the instrument. This beam is then made monochromatic by a double-curved monochromator Fig. 2.7 (*i.e.* having a variable horizontal and vertical curvature). It consists of a set of 55, 2 × 4 cm single crystals mounted on a mechanism that allows to obtain a nearly spherical surface, geometrically focussing much of the divergent incident beam on a small sample volume. Bragg's law is used to select the wavelength of the incident neutrons:

$$2\frac{d_{mono}}{p}sin(\Theta_B) = \lambda_i \tag{2.31}$$

where d_{mono} is the inter-reticular distance of the selected monochromator Θ_B the angle between the lattice planes and the incident neutron beam, p an integer indicating the order of reflection and λ_i the desired wavelength.

FIGURE 2.7: *Left:* Photo of the IN4C monochromator. *Right:* Photo of the IN4C Time-Of-Flight path (a view from the inside). *Reproduction not authorized.*

The resulting monochromatic beam is finally "chopped" by a Fermi chopper. This latter consists of a horizontal rotor whose function is to run an assembly of aluminum slats glued together by epoxy glue[3] enriched in ^{10}B atoms[4] at high speed (up to 40 000 rpm). In this way, the monochromatic beam can only pass through the slats when the latter ones are positioned parallel to the beam. Their fast rotation therefore transforms the long pulses into sharp monochromatic flashes of neutrons. The Fermi chopper is connected to an electronic counting device that will trip with some delay compared to the top of the Fermi. This moment, denoted t_0 is the time reference for measuring the travel time of the neutron from the Fermi chopper down to the ^{3}He detectors through the sample: it is the *time of flight* of the neutrons (see Fig. 2.7).

Neutrons scattered by the sample are therefore recorded as a function of their time of arrival (and therefore energy transfer) at the detector located at an angle 2θ. Neutrons having gained energy from the sample will arrive first at the detectors (anti-Stokes region), followed by those elastically scattered arriving in the *elastic channel*. Finally neutrons that have transferred their energy to the sample reach the detectors the last

[3]This optical component is called *slit pack*

[4]This component is highly absorbent to thermal neutrons

(Stokes region).

The energy resolution $\frac{\Delta E}{E}$ of the IN4C spectrometer varies between 4 and 6% (at elastic scattering). Its best performances are found for incident wavelengths between 0.7 and 4 Å. The multidetector is composed of 396 ^3He gas tubes covering scattering angles ranging from 3° to 135°. This large detector coverage allows one to measure a large domain in $(Q, \bar{\omega})$ for a single setup (see Fig. 2.8).

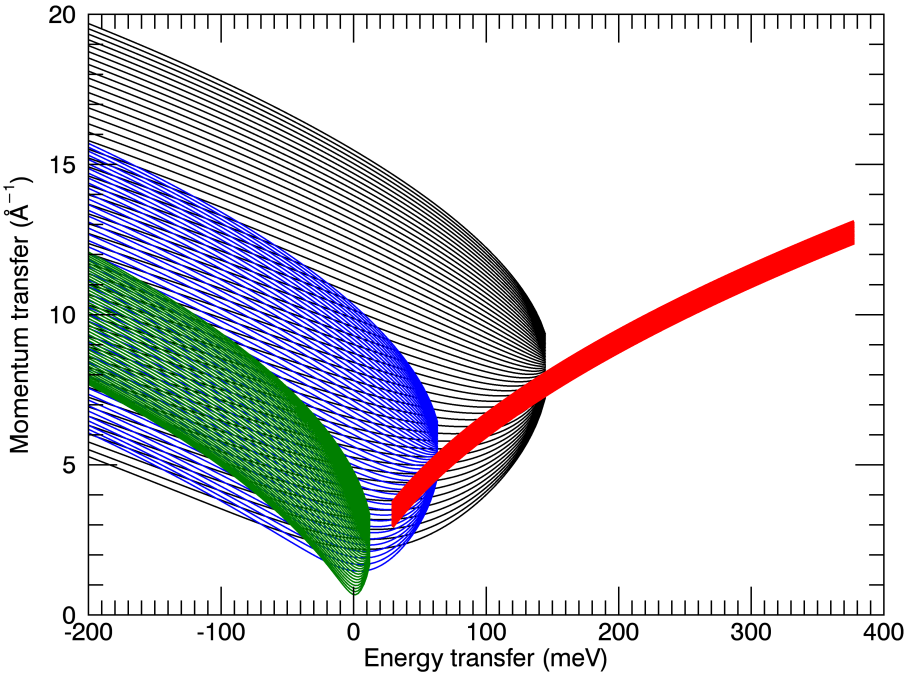

FIGURE 2.8: $(Q, \hbar\omega)$ regions covered during the INS experiments: on IN4C using the incident wavelength 0.74 Å (black), 1.11 Å (blue) and 2.41 Å (green) - on IN1BeF-LAGRANGE (red line).

Data treatment: There are multiple ways of doing the data treatment. This mainly depends on the physical quantity one wants to highlight. Several softwares are available at the ILL to perform the different data reductions. We have used the suite of TOF routines available in the LAMP platform, developed by the CS group at the ILL. Its native language is IDL (see Fig. 2.9).

A classical basic treatment consists of:

1. Normalization of the data to the monitor counts (*i.e.* to the number of incident neutron).

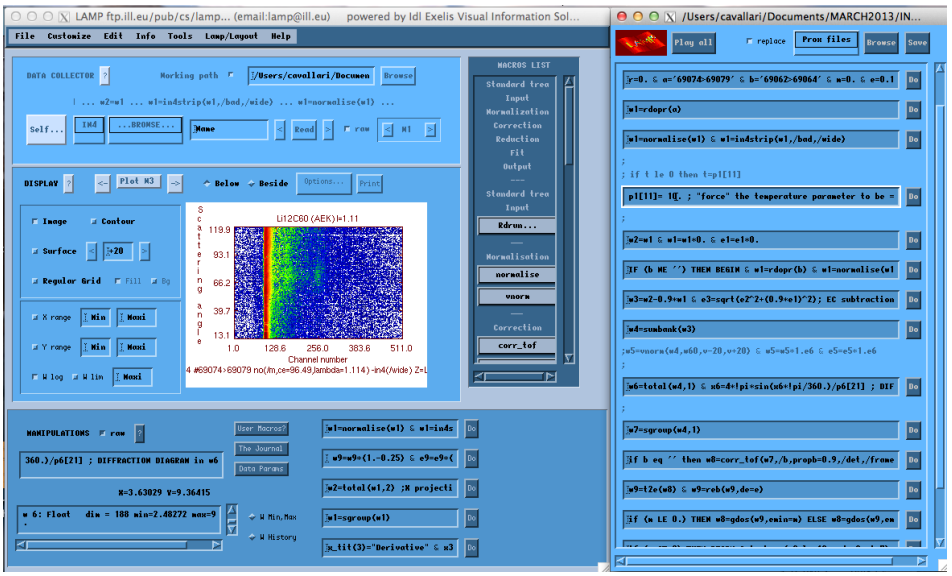

FIGURE 2.9: LAMP graphical interface.

2. Subtraction of the contribution of the sample holder - particular care should be taken for sample transmission.

3. Normalization of the data to a Vanadium standard. Vanadium being an almost purely incoherent scatterer, the elastic intensity (*i.e.* integration of the signal over the elastic channels) of its spectrum should be independent of the scattering angle. Hence, it provides a correct account for the sole Debye-Waller decrease at high Q.

4. Correction of the data from the neutron speed dependent efficiency of the detector.

5. Detector grouping of the data: this allows to improve the statistics of the signal (the new "average list of scattering angle are denoted $\bar{\theta}$).

6. Time of flight to energy conversion. At this stage, the $S(\bar{\theta}, \omega)$ spectrum is obtained.

7. $S(\bar{\theta}, \omega)$ spectrum can be further treated in order to provide the Generalised Density Of States $G(\bar{\theta}, \omega)$ given by the relation 2.27 or the susceptibility $\chi''(\bar{\theta}, \omega)$ given by equation 2.28.

8. At a final stage, a triangulation and interpolation scheme is used to convert the $S(\bar{\theta}, \omega)$ maps into the more physical $S(Q, \omega)$.

We have reported the input files for data reduction (.prox files) in the Appendix B.

2.5.2 The inverse graphite analyser spectrometers IN1-LAGRANGE

The IN1-LAGRANGE (former IN1BeF) instrument, simply called "LAGRANGE" in the rest of this manuscript, was chosen to investigate high-frequency vibrations in a wide energy range (50-450 meV), where the internal modes of H in graphene are expected. Due to its analyzing set-up, it provides a relatively higher energy resolution (approximately 2% in the energy range probed, from 50 to 450 meV). This, together with a high flux, allows for short acquisition times at various temperatures, making it particularly suitable to inspect fine features in the spectra and follow their evolution with temperature in great details. The samples (about 0.5 mg) were held at 10K within a cylindrical aluminum can (see Fig. 2.10) using a standard Displex cryostat.
LAGRANGE is the unique option for studying the high frequency excitations in materials at the ILL. It is installed on the hot beam H8 and constitutes the secondary spectrometer of the IN1. This instrument shares the primary spectrometer, constituted of a monochromator, with the IN1-TAS triple axis spectrometer option and the D4 diffractometer (described in [94]). LAGRANGE has been recently commissioned [100]. It replaces the IN1-Be filter option. During this thesis, we have used both, but we will focus the description of the instrument on the LAGRANGE option.

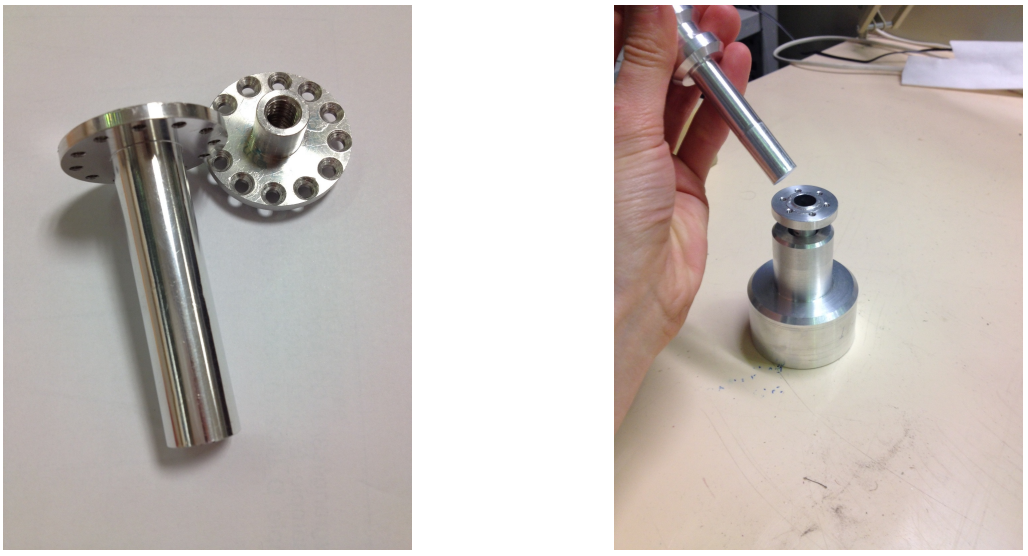

FIGURE 2.10: *Left:* Photo of a cylindrical Aluminium sample holder used during the experiment on IN1-Lagrange. *Right:* Photo of a cylindrical Aluminium sample holder, placed into an apposite metal support for gently pressing the sample inside.

Principle: By contrast to IN4C, where the incident wavelength of the neutron is prepared and the scattered energy is analysed by TOF, the principle on LAGRANGE resides on scanning the incident energy E_i for a fixed scattered energy E_f set by the

crystal analysers. This is a continuous "point by point" instrument, *i.e.* the instrument changes its configuration at each energy step (at each E_i), alike what is generally done on triple axis spectrometers.

Owing to the relatively large scattered angles defined by the LAGRANGE geometry, the spectrometer probes a relatively thick region in (Q,ω), as described in Fig. 2.8. However, the Q domain available to the instrument at each energy transfer is integrated at the detector, so that no Q dependence on the scattering can be analysed, but the integration results in a very intense signal.

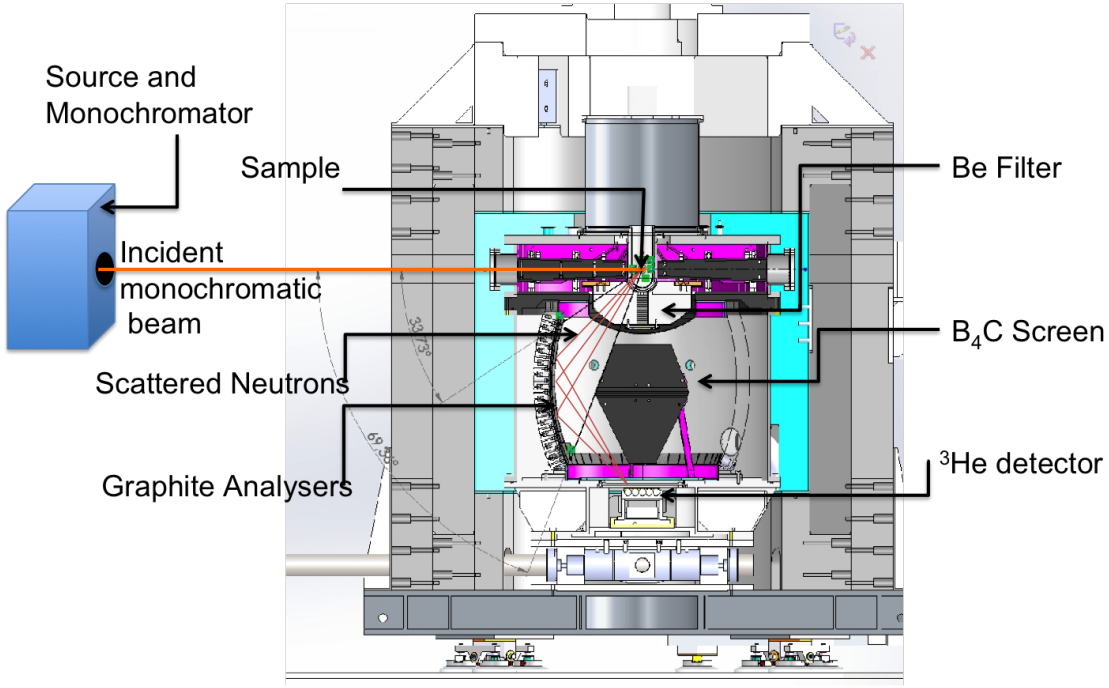

FIGURE 2.11: Vertical cut of the LAGRANGE insert (or secondary spectrometer): the scattered neutrons with final energy of 4.5 meV are focussed to the ^3He detector by the arrangement of HOPG analyser mounted on an ellipsoidal surface, with the sample located at one of its locus. The spectra are obtained by varying the incident neutron energy. This is achieved by scanning the Bragg take-off angle of several crystal monochromators. A cooled block of polycrystalline Be is used as a large band low pass filter, reducing the background. The direct view of the secondary source (the sample) is avoided by placing a container filled with B_4C powder between the sample and the detector, *i.e.* significantly reducing the background [100].

Instrument description: IN1-LAGRANGE is installed on the hot beam H8, having a direct view of the ILL hot source, made of a graphite block heated at high temperature. A large double-focussing multi-face crystal monochromator supplies the secondary spectrometer LAGRANGE with a monochromatic beam in the intermediate and high neutron energy ranges (mosaic Cu220 and Cu331 crystal faces) as well as in the lower energy range (elastically bent Si111 and Si311 reflections). The incident energy E_i is

fixed by the Bragg angle between the monochromator face and the sample.

The IN1-Lagrange uses the combination of a cooled Be-filter and a large area, space focussing crystal analyzer, to collect the 4.5 meV energy scattered neutrons over a large solid angle of 2.5 steradian. The focussed scattered neutron are all recorded with a relatively small single counter (a He3 gas detector). This permits, contrary to typical TOF instruments, to decouple large solid angle detections from counting volume which results in a substantial lowering of the corresponding background.

The focussing reflecting surface of 1 m^2 is built around the vertical sample-detector axis from 612 pyrolytic graphite (PG) crystals set to reflect neutrons with a fixed average energy of 4.5 meV. The appropriately shaped beryllium filter, cooled at a temperature of 20 K, is installed immediately after the sample in order to remove higher-order harmonics in the analyser reflections.
The carefully designed screen of boron-containing absorber is installed on the sample-detector axis in order to suppress the intense elastic scattering from the sample. Further reduction of the instrument background, contaminated by the high neutron energy components, is achieved through massive polyethylene shielding built around the whole analyser. The whole instrument can be considered as a variant of a classical three-axis spectrometer with a very large barrel-like fixed-energy analyser. There are no mutually moving parts within the secondary spectrometer which is positioned as a whole around the monochromator in order to record the inelastic scattering spectra changing step-by-step the incident energy similarly to a typical experiment on a three-axis spectrometer. The energy transfer, which corresponds to excitation energy in the sample, is obtained by a subtraction of the analyser energy of 4.5 meV from the energy of incident monochromatic neutrons.

Data treatment: The following data treatment was performed:

1. Subtraction of the contribution of the sample holder and instrument global contributions to the measured signal.
2. Calibration of the intensity to that of a liquid water standard.
3. Subtraction of a sample and energy dependent background, originating from *e.g.* multiphonon contributions at large energy transfer.
4. Normalization of the integrated signal to unity.

Note that the measurements were performed at a constant monitor value for each incident energy. This prevents the monitor normalization and detector efficiency steps of the TOF reductions to be performed.

The as corrected scattered intensity measured $S(\bar{\theta},\omega)$ (with $\bar{\theta}$=51.54°)is linked to the generalised density of states given by Eq. 2.27. In the extent that k_f is much smaller than k_i, and that $E_i \sim \hbar\omega$ one can make the approximation that $Q^2 \sim \hbar\omega$. If the measurements are done at temperatures not too high, so that $\hbar\omega \ll k_\beta T$, then the use of Eq. 2.27 indicates that the intensity $S(\bar{\theta},\omega)$ is directly proportional to $G(\bar{\theta},\omega)$.
To further obtain the hydrogen partial density of states (in the case of hydrogenated materials), one has however to correct the signal from the Debye-Waller contribution given by:

$$W(Q) = \frac{\hbar Q^2}{4M_H}\int_0^{\omega_{max}} \frac{g_H(\omega)}{\omega} coth(\frac{\hbar\omega}{2k_\beta T})d\omega \tag{2.32}$$

where Q is the modulus of the scattering vector, ω the frequency, $g_H(\omega)$ and M_H the partial density of states and the mass of the H atoms respectively. In the practical calculation, we used the experimental GDOS $G(\bar{\theta},\omega)$ collected at 5K on Lagrange and completed in the low frequency range by those measured on IN4C, as $g_H(\omega)$ to calculate $W(Q)$ at the different temperatures.

Chapter 3

Theoretical Methods and Computational Modeling

Spectroscopic techniques are the ideal probe to investigate the dynamical properties of a system at the atomic level. In parallel with the technological development of spectroscopic instruments with improved resolution and sensitivity, the ever growing computer capacities and performances have rendered possible the simulations of complex molecular systems with extreme precisions. Nowadays the experimental data are quasi-systematically analysed and discussed on the basis of the results of numerical modelling, simulations and theoretical approaches with various degree of complexity, the latter being dependent on the physical-chemistry of the system and/or the number of degree of freedom to be simulated.

In the context of this thesis, the essential goal of the numerical simulations is to calculate the neutron observables[1] of an hypothetical model and to confront it to the experimental data. In case of a good match, the atomic model will be considered as valid and further physical properties can subsequently be predicted.

The neutron observables are completely determined by the knowledge of the phonon spectrum of the system, *i.e.* the vibration frequency of the ensemble of atoms in the material under study. This latter reflects the interactions between the atoms from which the interatomic forces, or force constants can be derived. Therefore, the simulations aim at probing the Potential Energy Surface (PES) $V = V(R)$ of a given arrangement of atoms R. The knowledge of this PES enables the minimum energy structure to be calculated. The interatomic forces can subsequently be obtained by calculating the variation of the PES with regards to the atomic displacements. In the harmonic approximation one can further derive the matrix dynamics which, after diagonalization, provides the eigenfrequencies and eigenvectors (phonons) of the molecular system. This technique,

[1] that we introduced in Chap. 2.

well-established in lattice dynamics [91] was used to study the metal fullerides crystalline phases, as discussed in Chap. 8. In the case of hydrogenated graphene, we used Molecular Dynamics (MD) which consists on calculating the time evolution of the atomic positions, *i.e.* their trajectory being based on the derivation of the interactomic forces at each time step.

Nowadays a large set of computation techniques are efficiently implemented and can be easily used. The Quantum Mechanical *ab-initio* methods, have the specific atomic positions as unique input. The Hartree-Fock, post Hartree-Fock and **Density Functional Theory (DFT)** methods belong to this category. They give the best level of precision on the physical properties calculated. However, they necessitate a significant computational power, which limits these techniques to the study of models made up of several hundreds of atoms at the maximum. For larger systems, semi empirical Tight Binding (TB) techniques or parametrized empirical force fields (FF) have to be used, however giving less precise or reliable results. The choice of the more appropriate technique depends therefore on the level of required accuracy, timescale, nature and size of the system.

The computational work in this thesis has been carried out using the *ab-initio* method of Density Functional Theory. DFT is free of adjustable parameters and treats the electrons explicitly: this makes it one of the most successful and employed methods for solid state physics and quantum chemistry. Nowadays almost 3000 scientific publications about DFT appear every year (statistics from ISI Web of Science). As it will be discussed later on in the next Chapters 5, 6 and 7, we made an extensive use of Inelastic Neutron Scattering (INS) for investigating the dynamical properties of selected carbon nano–structures. In Neutron Scattering (NS), the spatial and time scales match very well those accessible to the simulations, the experimental observables correlate therefore directly with the properties obtained from the numerical approaches. This, added to the relatively simple expression of the neutron scattering cross section, makes NS an ideal technique to confront experiments and atomistic simulations.

As it will be continuously developed along this manuscript, the deep understanding of the complex features observed in the experimental data could not disregard the use of computational tools. In particular, the combination between simulations and experiments have demonstrated to be a unique tool for probing the H behaviour at the graphene surface.

This chapter aims at giving a general understanding of the computational methods which have been used throughout the rest of this work. We shall describe the theoretical basis behind the DFT and the principles grounded in the theory which lead to extract functions directly comparable to the experimental data. We will start from the description of the total Hamiltonian of a molecular system and its simplification by using the Born-Oppenheimer approximation. This will allow to deriving the expression of the electronic

Hamiltonian which is at the heart of the problem. We will then introduce very briefly the theorems and approximations at the origin of DFT. The last part of this chapter will introduce the Molecular Dynamics (MD) simulations.

3.1 The Total Hamiltonian and the Born–Oppenheimer Approximation

The Hamiltonian $\mathcal{H}$ of a molecular system constituted of K ions and N electrons in interaction is defined as the sum of their kinetic energy and their potential energy. The kinetic energy is composed of two contributions T_e and T_n, corresponding respectively to the movements of the N electrons and to the K ions. The potential energy comprises three Coulomb terms V_{ee}, V_{nn} and V_{en}, corresponding respectively to the electrostatic forces between electrons, between ions, and between electron and ions. We have:

$$\mathcal{H} = T_n + T_e + V_{en} + V_{nn} + V_{ee} \tag{3.1}$$

The Schrödinger equation of the stationary states of the systems is of the form:

$$\mathcal{H}\Psi(\{\vec{r}\},\{\vec{R}\}) = E\Psi(\{\vec{r}\},\{\vec{R}\}) \tag{3.2}$$

with $\{\vec{r}\} = \vec{r}_1, ..., \vec{r}_N$ and $\{\vec{R}\} = \vec{R}_1, ..., \vec{R}_K$ the ensemble representing respectively the electrons and ions coordinates of the system. Ψ is the wavefunction associated to the stationary state with energy E. It depends on the $3N$ electron and $3K$ ions coordinates, if one neglects the spin degree of freedom of the electron.
The solution of Eq. 3.2 allows in principle to derive the wavefunction Ψ of the system and its associated energy E, *i.e.* to calculate all the physico-chemical properties of the atomic system. However, owing to the very large number of variable in this equation ($[3N+3K]$–body problem), this is not possible for systems in condensed matter. Approximations have to be introduced, the first one being the so–called **Born-Oppenheimer** approximation.
The Born-Oppenheimer approximation decouples the electronic degrees of freedom from the ionic coordinates, an approximation justified by the difference of mass between these two entities. One therefore makes the assumption that the timescale associated with the ionic motion is much slower than the one associated with the electronic motions, *i.e.* electrons follow *adiabatically* the motion of the nuclei. The wavefunction Ψ can therefore be expressed as the product of an electronic wavefunction Ψ_{elec} and a nuclear wavefunction

Ψ_{nucl} such as:

$$\Psi(\{\vec{r}\},\{\vec{R}\}) = \Psi_{elec}(\{\vec{r}\};\{\vec{R}\})\Psi_{nucl}(\{\vec{R}\}) \tag{3.3}$$

where the sign ";" underlines the parametric dependence of Ψ_{elec} on the ionic coordinates $\{\vec{R}\}$.

In that case, the Schrödinger equation 3.2 can be decomposed into two interdependent equations via the $E_{elec}(\{\vec{R}\})$ term, related to the electronic energy of the system:

$$[T_e + V_{ee} + V_{en}]\,\Psi_{elec}(\{\vec{r}\};\{\vec{R}\}) = E_{elec}(\{\vec{R}\})\Psi_{elec}(\{\vec{r}\};\{\vec{R}\}) \tag{3.4}$$

$$\left[T_n + V_{nn} + E_{elec}(\{\vec{R}\})\right]\Psi_{nucl}(\{\vec{R}\}) = E\Psi_{nucl}(\{\vec{R}\}) \tag{3.5}$$

The electronic and nuclear Hamiltonian H_{elec} and H_{nucl} are defined as:

$$H_{elec} = T_e + V_{ee} + V_{en} \tag{3.6}$$

$$H_{nucl} = T_n + V(\{\vec{R}\}) \tag{3.7}$$

with $V(\{\vec{R}\}) = V_{nn} + E_{elec}(\{\vec{R}\})$ being the potential energy (hyper)surface PES that we introduced earlier. Therefore, our problem of calculating the neutron observables is equivalent to solving Eq.3.5, where the electronic degrees of freedom only appear as parameters in the PES expression. Considering the large mass of the ions, the classical equivalent of Eq. 3.5 is often used and leads to the theory of phonon. The goal of the *ab-initio* DFT is to solve the electronic Schrödinger equation Eq. 3.4 and to express the term $E_{elec}(\{\vec{R}\})$ which appears in the expression of the PES. The first and last term of the electronic hamiltonian H_{elec} in Eq. 3.6 are mono–electronic and therefore do not raise any problem in the resolution of the electronic Schrödinger equation Eq. 3.4. All the difficulty is actually concentrated in the electron–electron interaction V_{ee} which prevents the many body hamiltonian H_{elec} to be expressed as the sum of single electron hamiltonians. This term renders impossible the analytical determination of the electronic ground state and energy. Approximations and/or new approaches to the problem are therefore required to go further. DFT as a whole provides a very efficient way of approaching the real solutions of the electronic problem.

3.2 Density Functional Theory

Density functional theory[2] is one of the most popular and successful quantum mechanical approach to matter and has proven very powerful since its foundations in the sixties. Its

[2]The literature on DFT is large and rich in excellent reviews and overviews. We refer the interested reader to the following books and papers [101], [102], [103] and [104] for a more complete introduction about DFT and its applications.

high efficiency and good scaling with a relatively high accuracy are the main reasons for its important and still growing success. In many–body quantum theory, the wavefunction is the fundamental variable that contains all the informations on the state of a system and from which the expectation values of the observables of interest are calculated. The main idea beyond DFT is that the electronic density $n(\vec{r})$ is used as the basic variable of the problem and that all the properties can be calculated from it. The use of the density as the basic variable, instead of the many–body wavefunctions is a great advantage. If the latter depends on $3N$ degrees of freedom (actually $4N$ if one considers the electron spin), the former is a function of only 3 variables. This renders the electronics problem solvable for systems containing more than few atoms.
The basis of DFT were put already by L. Thomas and E. Fermi in 1928 (Thomas–Fermi model) but the real formulation was proved by P. Hohenberg and W. Kohn in 1964, who founded the formalism, introducing the approximations to model the interaction between the electrons.

First Theorem The first Hohenberg-Kohn theorem states that[3] *the external potential* v *is uniquely determined by the electronic charge density* $n(\vec{r})$. This is a univocal correspondence: conversely, *the total energy is a unique functional of the density* $E[n(\vec{r})]$. In other words every ground–state property, and in particular the ground–state energy, is a functional of the electron density:

$$E[n] = F[n] + \int n(\vec{r})v dr \tag{3.8}$$

with $F[n] = T_e[n] + V_{ee}[n]$ the Hohenberg and Kohn *universal functional* and $V_{ext}[n] = \int n(\vec{r})v(\vec{r})d^3\vec{r}$.

Second Theorem The second theorem relates the non-degenerated ground-state density n_0 to the ground-state energy E_0 by stating that the energy functional $E[n]$ is universal for $n = n_0$. By minimizing $E[n]$ with respect to n, the exact ground-state density is obtained: $Min_n[E(n)] = E_0$ [105]. However the expression of the universal functional $F[n]$ is unknown.
DFT became practical when Kohn and Sham proposed to replace the fully interacting many-body system by an ensemble of independent fictitious particle in a modified external potential $v_s(\vec{r})$, and characterized by the same density as that of the real electronic system [106]. In the Kohn-Sham approach, the total energy functional can be written as:

$$E[n] = T_s[n] + V_{ext}[n] + E_H[n] + E_{XC}[n] \tag{3.9}$$

[3] as usual in DFT, we will write v the ion–electron potential.

where $T_s[n]$ is the non-interacting kinetic energy, $V_{ext}[n]$ is the external potential. $E_H[n]$ is Hartree energy and represents the classical Coulomb interaction of an interacting charge density $n(\vec{r})$. $E_{XC}[n] = (T_e[n] - T_s[n]) + (V_{ee}[n] - E_H[n])$ is the exchange–correlation functional.

Conceptually the exchange energy of a system of electrons is associated with the Pauli exclusion principle: because two electrons with the same spin must have a spatial separation, the electron-electron repulsion energy is reduced. The *correlation* energy is defined as the difference between the correct many-body energy and the Hartree energy, without corrections. The exact ground state and energy could be obtained in principle by finding $n(\vec{r})$ such that:

$$\frac{\delta E[n]}{\delta n} = 0 \tag{3.10}$$

with the condition that:

$$\int n(\vec{r}) d^3\vec{r} = N \tag{3.11}$$

Formally this can be realized by introducing the Lagrange parameter μ such that:

$$\frac{\delta}{\delta n}\left[T_s[n] + E_H[n] + E_{XC}[n] + \int n(\vec{r}) v(\vec{r}) d^3\vec{r} - \mu \int n(\vec{r}) d^3\vec{r}\right] = 0 \tag{3.12}$$

One can develop this equation and obtain the Kohn-Sham equations [106] which can be solved by an iterative self-consistent procedure. At this stage, DFT is an exact theory. The problem remains in that we don't know the exact expression of the exchange–correlation functional $E_{XC}[n]$. To go further, this term has to be approximated.

3.2.1 Approximations and pseudopotentials

The simplest approach used to approximate the exchange–correlation functional is the Local Density Approximation (LDA) [106]: the value of $E_{XC}[n(\vec{r})]$ is approximated by the exchange-correlation energy of an electron in an homogeneous electron gas of the same density $n(\vec{r})$ (see Fig. 3.1) :

$$E_{XC}^{LDA}[n(\vec{r})] = \int \varepsilon_{XC}[n(\vec{r})] n(\vec{r}) d\vec{r} \tag{3.13}$$

The exchange-correlation energy is usually interpolated analytically by Quantum Monte Carlo methods [107]. LDA is often surprisingly accurate and for systems with slowly varying charge densities generally gives very good results. Despite the remarkable success of the LDA, its limitations mean that care must be taken in its application. For instance, in strongly correlated systems LDA is very inaccurate. Moreover it does not account for

van der Waals interactions at all and gives a very poor description of hydrogen bonding systems.

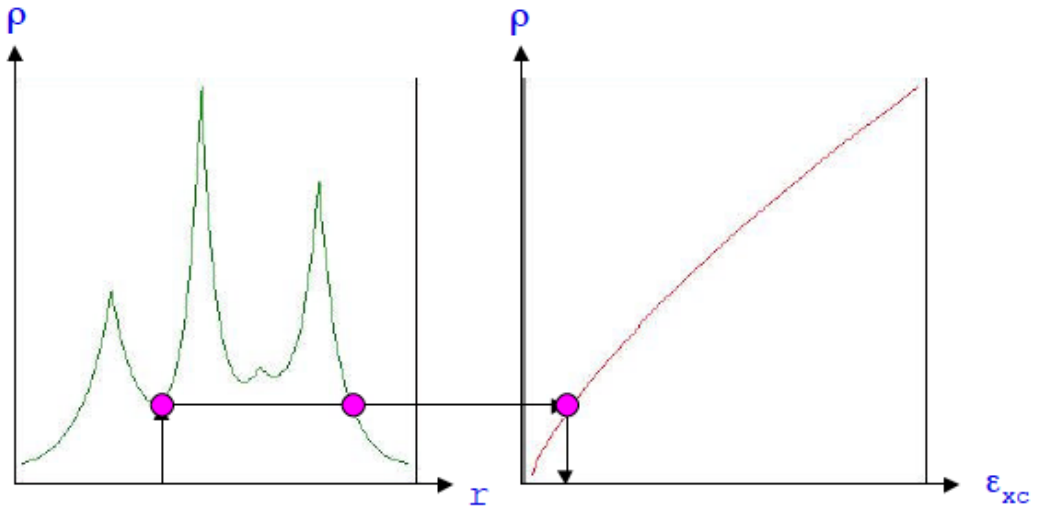

FIGURE 3.1: In the LDA, the exchange-correlation energy per particle of a uniform electron gas is transferred locally to the inhomogeneous system of interest. By courtesy of A. Savin (unpublished).

An first step to improving the LDA is to include its local variation. This is done by rendering E_{XC} a functional of the density $n(\vec{r})$ and of its gradient $\nabla n(\vec{r})$.
The functionals of the general form:

$$E_{XC}^{GGA}[n(\vec{r})] = \int f_{GGA}(n(\vec{r}), \nabla n(\vec{r}) d^3\vec{r} \tag{3.14}$$

are known as GGA (Generalized Gradient approximation) functionals. For many properties, for example optimized geometries, ground state energies of molecules and solids, covalent bonds and weakly bonded systems, GGAs often yields better results than LDAs. Several GGA functionals have been developed so far and depending on the system under study a wide variety of results can be obtained. Among them, a few of the most popular gradient corrected correlation functionals are PBE [108], which has been widely used in this thesis, PW91 [109], Lee-Yang-Parr [110] and Perdew86 [111].
A number of new f_{GGA} functionals include a third generation which uses the second derivative of the density and/or kinetic energy densities as additional degrees of freedom (meta-GGAs functional) and a forth generation which adds "exact exchange" calculated from the Hartree-Fock exchange (as for instance hybrid functionals mixing a portion of the exact Hartree-Fock exchange to a LDA- or GGA-type functionals).
Basis sets are necessary to practically solve the Kohm-Sham equations. Essentially, almost all electronic structure methods today rely on an expansion of the unknown

wavefunction/density in terms of a set of basis functions. Any type of basis function may in principle be used, like exponential functions, Gaussians, polynomial, plane-wave, spline, Slater type orbitals and numeric atomic orbitals. The choice of the basis set should allow for an accurate description of the problem with a computational cost as low as possible and reflect some of the physics of the system under investigation. For example, for bounded atomic or molecular systems, functions should go to zero when the distance between the nucleus and the electron becomes large. Atom centered orbitals like Gaussian functions have become very popular in the calculations of chemical problems. In condensed matter physics, basis functions with a periodicity matching the crystal lattice are mostly employed. Thus, plane waves (PW) are the natural choice for systems with periodic boundary conditions (PBC).
Calculating the total electronic wavefunction for a relatively large system is an extremely hard task. The outer wavefunctions must be orthogonal to the inner ones due to the Pauli exclusion principle. This introduces nodes into the wavefunctionswhich therefore require a very high plane wave cutoff and a large number of basis set for being accurately expressed. In addition, the majority of the physical properties of a system depends on its valence electrons. To make the calculation easier and avoid large and useless computational effort, pseudo–potentials are introduced, which are simple energy correction to account for contributions of the core electrons and nucleus. Pseudopotential are atom-specific and method-specific and they can be mainly classified in norm-conserving, ultra-soft [112] and PAW pseudo potentials [113], [114]. The general and common idea behind the use of pseudo–potential is to remove the need to consider explicit orbitals for inner electrons and replace a nodal function with a smoother one, which is more computationally convenient and ultimately to provide a way to calculate all-electron properties from these smooth wavefunctions.

In conclusion, DFT presents a formally exact framework, where the complicated part of physics is incorporated in E_{XC}. The above described eigenvalue problem is solved using an iterative method (self-consistent loop). The energy of a configuration can be minimized with respected to the atomic coordinates. Mathematically, this corresponds to finding the stationary point of a function whose exact form is generally unknown. This task is solved employing iterative methods, such as quasi-Newton methods or the conjugate gradient method for instance. The obtained energy minima corresponds to stable configurations.

3.2.2 A plane wave DFT code: VASP

The plane-waves VASP code (Vienna Ab-Initio Simulation Package) was used in all DFT simulations performed in this thesis. VASP is a complex package for performing

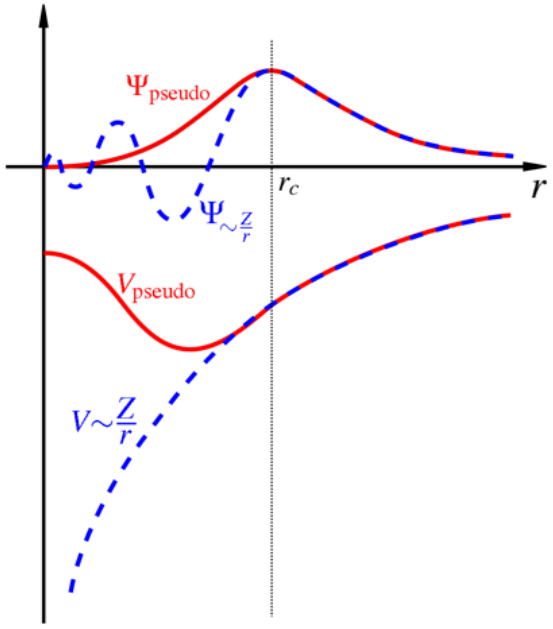

FIGURE 3.2: Comparison of a wavefunction in the Coulomb potential of the nucleus (blue) to the one in the pseudopotential (red). The real and the pseudo wavefunction and potentials match above a certain cutoff radius r_c. Taken from Wikipedia.

ab-initio quantum-mechanical DFT simulations with a plane wave basis set [115]. The interaction between ions and electrons can be described using either Ultrasoft Pseudo Potentials (USPP) or the Projector Augmented Wave (PAW) method, both allowing a considerable reduction of the necessary number of plane–waves per atom (this is particularly useful for transition metals and first row elements).
VASP was firstly conceived in parallel with the CASTEP code [116], which had a distinct development. Since 1989, progressive and continuous progresses and improvements (including parallelization, conversion to Fortran, implementation of new potentials and algorithms) have been done, making VASP one of the most known and employed DFT code in the world.
VASP uses a relatively large number of input and output files. However, the minimal set of input files needed for a simulation is the following one:

- POSCAR: Bravais-lattice cell shape and size and initial atom positions.
- POTCAR: The pseudo potentials for every atomic species, in the order it is reported in POSCAR.
- KPOINTS: Integration grid over k-space (as single Γ point or Monkhorst-Pack grid [117], [118]).
- INCAR: Details about the job to perform (*i.e.* algorithm choices).

The interested reader can refer to Appendix A for the input files used in this work.

3.3 Molecular Dynamics

Molecular dynamics (MD) simulates the time-dependent behaviour of a N particles system, by producing a phase space trajectory obtained through the integration of the classical Newton's equations of motions.
A particle, initially at position $\vec{r_0}$ and velocity $\vec{v_0}$ and subject to a force $\vec{F}$ during the time interval t, is moved to a new position $\vec{r}(t)$ according to the classical relation:

$$\vec{r}(t) = \vec{r_0} + (\vec{v_0}t + \frac{1}{2}\vec{a}t^2) \tag{3.15}$$

where $\vec{a} = \frac{\vec{F}}{m}$ and $\vec{F} = \frac{-dU}{d\vec{r}}$. The acceleration $\vec{a} = \frac{\vec{F}}{m}$ is assumed constant in the time interval t.
Traditionally, MD simulations use (semi)empirical interatomic potentials, allowing nowadays to treating efficiently large scale structures and macromolecular systems. In 1985, Car and Parrinello presented a scheme to efficiently combine Molecular Dynamics and Density Functional Theory, then expanding the potentialities of DFT to dynamical properties of different systems, as disordered (liquids for examples) materials [119]. In DFT-MD the atoms are moved according to the classical Newton's mechanics but the interatomic forces acting between the atoms are computed according to quantum mechanics, solving from first-principles the electronic structure for a given set of atomic positions and then calculating the resulting forces on each particles. The development of *ab-initio* molecular dynamics (AIMD or DFT-MD in this context) has proceeded and different computational algorithms have been successfully improved and implemented. Nowadays DFT-MD allows to treat systems composed by hundreds of atoms and achieve times scales of hundreds of ps. It has become the preferred choice for a lot of problems requiring high level of electronic accuracy, including chemical reactions, excitations and charge transfer.
VASP implements a method derived from the original Car-Parrinello based on the evaluation of the instantaneous electronic ground state at each MD integration step. Once the initial conditions (positions and velocities of each atom) are set, the model to represent the forces acting of each particle, the classical equations of motion have to be solved:

$$m_i \frac{d^2\vec{r}_i(t)}{dt^2} = \vec{f}_i = -\frac{\partial}{\partial \vec{r}_i} U(\vec{r}_i) \tag{3.16}$$

where $U(\vec{r}_i) = U(\vec{r}_1, \vec{r}_2, \cdots, \vec{r}_N)$ is the potential energy depending on the coordinates of the N particles. This is a set of non-linear coupled equations which has to be solved using an appropriate integration algorithm. The trajectory is discretized by an integrator to advance over small time steps (at least, small enough for allowing a correct sampling of the phase–space for the required properties of the system of interest) [120]

3.3.1 Thermodynamical ensembles

In classic molecular dynamics, simulations are usually done in the microcanonical ensemble (NVE): the number of particles, volume and energy have a constant value. The total energy is constant, but not the kinetic and potential energy contributions, so that the temperature will fluctuate a lot. The microcanonical ensemble does not correspond to the conditions under which most experiments are carried out. In real experiments, the temperature (or pressure) is generally controlled instead of the energy. It is then desirable to have a control over the temperature (or pressure) and work at constant T (or P) to compare the experimental data to the simulations. If one is interested in the behavior of the system at a specific T, the use of thermostat to control the temperature is required. The thermodynamical ensemble corresponding to this situation is the canonical ensemble (NVT). In this case, the temperature is related to the particle velocities via the equipartition of energy principle:

$$K = \sum_{i}^{N} \frac{1}{2} m_i v_i^2 = \frac{3}{2} N k_\beta T \tag{3.17}$$

The instantaneous temperature of a system during a MD simulation is therefore directly related to its kinetic energy as follows :

$$T = \sum_{i=1}^{N} \frac{m_i \|v_i\|^2}{k_\beta N_{df}} \tag{3.18}$$

where N_{df} is the total number of degrees of freedom. The average temperature $\langle T \rangle$ is identical to the macroscopic temperature.
The simplest way to alter the temperature of the system is by **velocity scaling** [121] which is based on tuning the atomic velocities until the desired temperature is reached. If the temperature at time t is $T(t)$ and the velocities at the time $t + 1$ are multiplied by a scaling factor λ, then the associated temperature change can be calculated as

$$T(t) = \sum_{i=1}^{N} \frac{m_i \|v(t)_i\|^2}{k_\beta N_{df}} \tag{3.19}$$

$$T(t+1) = \sum_{i=1}^{N} \frac{m_i \|v(t+1)_i\|^2}{k_\beta N_{df}} = \sum_{i=1}^{N} \frac{m_i \|\lambda v(t)_i\|^2}{k_\beta N_{df}} = \lambda^2 T(t) \tag{3.20}$$

and then

$$\Delta T = T(t+1) - T(t) = \lambda^2 T(t) - T(t) = (\lambda^2 - 1)T(t) \tag{3.21}$$

$$\lambda = \sqrt{\frac{T_0}{T(t)}} \tag{3.22}$$

This algorithm controls the temperature by multiplying the velocities at each time step by the factor $\lambda = \sqrt{\frac{T_0}{T(t)}}$, where T (t) is the temperature at the time step t as calculated from the kinetic energy and T_0 is the desired temperature. One problem with this approach is that it does not allow fluctuations of the temperature which are present in a canonical ensemble. However this technique can be useful to force a system to reach the desired temperature in a view to preparing it into its initial state prior the production step. A *softer* formulation of this approach is the **Berendsen thermostat** [122]. To maintain the temperature, the system is coupled to an external heat bath with fixed Temperature T_0. The velocities are scaled at each step, such that the rate of temperature change is proportional to the difference:

$$\Delta T = \frac{\Delta t}{\tau}(T_0 - T(t)) \tag{3.23}$$

$$\lambda^2 = \frac{\Delta t}{\tau}\left(\frac{T_0}{T(t)} - 1\right) + 1 \tag{3.24}$$

In practice, τ is used as an empirical parameter to adjust the strength of the coupling between the system and the bath. In the limit $\tau \to \infty$ the Berendsen thermostat is inactive and the run is sampling a microcanonical ensemble. The temperature fluctuations will grow until they reach the appropriate value of a microcanonical ensemble. On the other hand, too small values of τ will cause unrealistically low temperature fluctuations. If τ is chosen the same as the time step of the simulation t, the Berendsen thermostat is nothing else than the simple velocity scaling. Typical values for τ used in MD simulation of condensed phase systems are in the order of ≈ 0.1 ps. The Berendsen thermostat is extremely efficient for relaxing a system to the target temperature, but once the system has reached the equilibrium, it is important to probe a correct canonical ensemble. The **extended system method** was originally introduced by Nose (1984)

and subsequently developed by Hoover (1985). Nosé proposed an extended Lagrangian containing additional fictitious coordinates and momenta. The idea behind the **Nose-Hoover** thermostat is to allow thermal fluctuations, employing a friction coefficient χ and a heat bath Q. The heat bath is considered as an integral part of the system by addition of an artificial degree of freedom S which acts as an external parameter on the simulated system. S is associated with an effective mass and a velocity $\vec{s}$. The magnitude of S determines the coupling between the reservoir and the real system and so influences the temperature fluctuations [123], [124].

In this thesis, the velocity scaling and Nose thermostat methods, as implemented in the VASP code, have been used. The SMASS parameter controls the choice of the ensemble and relative algorithms during MD runs. When a canonical ensemble using the algorithm of Nosé is simulated, the Nose mass controls the frequency of the temperature oscillations during the simulation. It should be set so that the induced temperature fluctuations show approximately the same frequencies as the typical 'phonon'-frequencies for the system under investigation. The input files of the MD jobs have been reported as well in the Appendix A.

3.3.2 Running the simulation

In order to propagate a physical system following the equations of motions detailed above, there are three specific stages[4]:

- **Setting up the starting configuration**
  The input structure has to be geometrically relaxed to the minimum of its potential energy. This ensure a reliable starting geometry at 0 K and 0 bar.

- **Equilibration**
  Normally, the initial configuration is not representative of the conditions one wants to explore. It is important to ensure that an equilibrated state has been achieved; during this phase one should follow the temperature (or pressure and density) and the different energy components, until they fluctuate around some average value without showing any drift.

- **Trajectory production**
  Once one has attained the equilibrium at the desired temperature (or pressure), the production run can be performed. This run has to last for a time much longer than the relaxation time of the property of interest and then ensure the validity

[4]Historically DFT-MD simulations are run for liquids or amorphous materials. In this chapter, references to simulation procedures are, even when not specified, related to condensed matter.

of the ergodic hypothesis, *i.e.* that the time average of a given property coincides with the ensemble average.

Finally the simulated trajectory has to be analyzed to extract the desired properties. One can have access to the atomic positions, velocities and even forces as a function of time, so any statistical mechanical property that can be expressed in terms of those variables can be computed.

3.4 Getting closer to the experiments: Phonons and Density of States

As introduced in Chap. 2, the important dynamical function to be extracted from the simulations is the phonon density of states. In a system vibrating harmonically around a configuration of stable equilibrium, the density of states represents the spectrum of the normal modes' frequencies. The energies and entropies of vibrations contribute importantly to finite temperature thermodynamics of crystals and can be calculated by integrating the phonon density of states itself. A common approach[5] is to use DFT to calculate the vibrational modes of a crystal and then post-processing the outputs to calculate the phonon density of states and other thermodynamical functions of interest. Different methods are currently implemented in most DFT codes and several post-processing software compatible with DFT output are available as well. One way to implement the theory of crystal vibrations in a practical way is to explicitly calculate the forces between every atom in the crystal and construct the force constant matrix of the crystal. Each atom i is displayed along the crystallographic directions and the forces are calculated by the DFT implementation of the Hellman-Feynman theorem [127]. Finally, the force constant matrix allows to calculate the normal modes at any particular wavevector $\vec{q}$. This technique, consisting in calculating the force constant matrix (dynamical matrix) by explicitly displacing the atoms in the supercell is called the **direct method** [128]. A brief description of the application of this method for extracting neutron variables will be given in Chap. 8, as it has been employed for phonon calculations of the Li-intercalated fulleride $Li_{12}C_{60}$.

An alternative method, which not implies the explicit calculation of the interatomic force constants matrix, is based instead on Molecular dDynamics. The vibrational spectra can

[5]Other common methods, based on the calculation of the vibrational modes via interatomic force constants are the frozen-phonon technique [125], where a monochromatic perturbation with a finite amplitude is frozen in the system and the finite differences of the forces induced on all the atoms of the supercell by the perturbation are then evaluated and the Linear Response method, which utilizes density functional perturbation theory for a direct calculation of second order derivatives of the energy [126].

be extracted from Molecular Dynamics trajectories, via the Time- Fourier Transform of the velocity-velocity autocorrelation function:

$$g(\omega) = \sqrt{\frac{1}{2\pi}} \int_{-\infty}^{\infty} e^{i\omega t} \sum_i \frac{\langle \vec{v_i}(t)\vec{v_i}(0)\rangle}{\langle \vec{v_i}(0)\vec{v_i}(0)\rangle} dt \tag{3.25}$$

where the function $\frac{\langle \vec{v_i}(t)\vec{v_i}(0)\rangle}{\langle \vec{v_i}(0)\vec{v_i}(0)\rangle}$ is the velocity-velocity autocorrelation function (VAF), calculated from a chosen initial time (t=0) for the MD trajectory and for each atom of the system i, along all three components of the velocity $\vec{v_i}$.

3.4.1 nMOLDYN

nMOLDYN is a software for post-processing and analyzing MD trajectories computed through a wide variety of *ab-initio* and classical molecular dynamics codes (including VASP) [129]. The program nMOLDYN has been mainly conceived in connection with neutron scattering experiments, allowing the computation and decomposition of neutron scattering spectra, mainly through the computation of time or space correlation functions (TCF). This permits a detailed analysis of the structure and dynamics of the system under consideration, as the calculation of incoherent and coherent dynamic structure factors, elastic incoherent structure factors (EISFs), mean-square displacements, the atom-averaged velocity autocorrelation function (VACF) (in isotropic average or along a given direction):

$$C_{vv}(t) = \sum_{\alpha 1}^{N} w_\alpha C_{vv\alpha}(t) \tag{3.26}$$

and the cartesian density of states as cosine Fourier transform of the VACF:

$$g(\omega) = \int_0^{\infty} C_{vv}(t) cos(\omega\ t) \tag{3.27}$$

nMoldyn provides two user interfaces, a Graphical Interface (see Fig. 3.3) and a Command-Line Interface, based on python. Input trajectories have to be converted from netCDF format to Molecular Modeling Toolkit (MMTK) format and, by specifying the parameters for the calculations the user wishes to perform, one can straightforward starts the calculation itself.

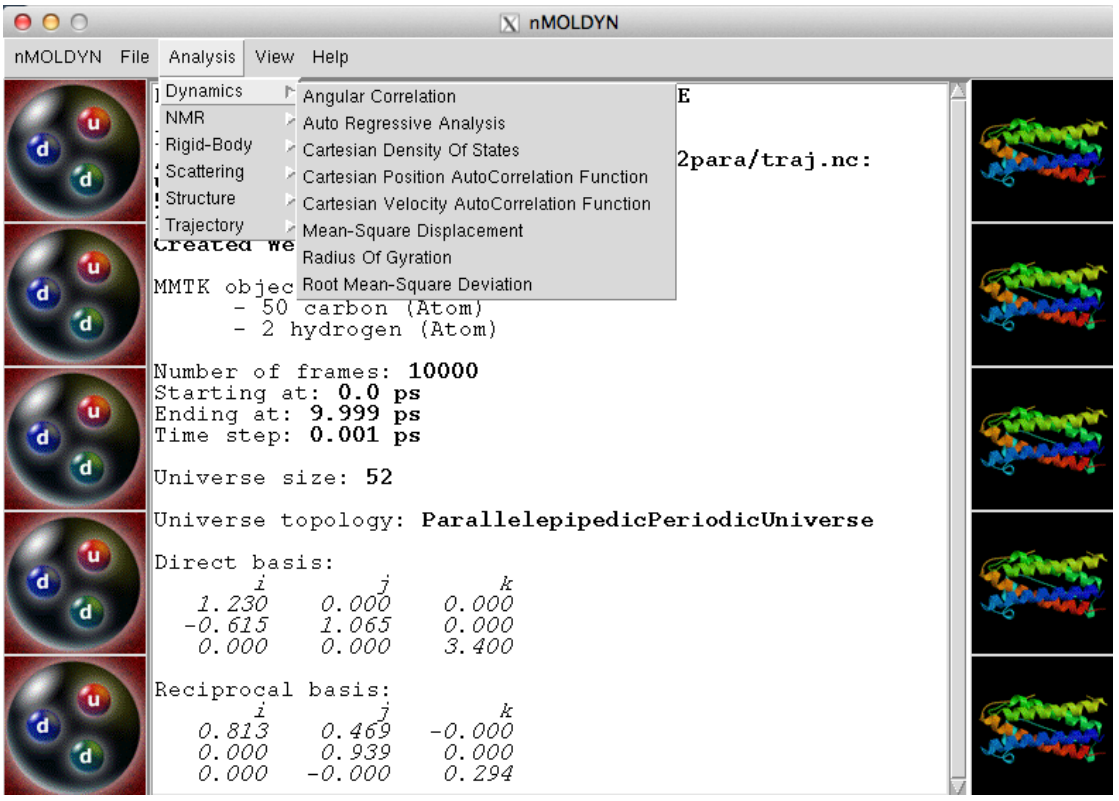

FIGURE 3.3: nMOLDYN 3.0 - Graphical interface

nMOLDYN user guide provides a complete overview about the theory and the computational implementation of the neutron functions [130].

3.5 Computational modeling: Summary

The simulations of the H-graphene systems were performed using the frozen-core all-electron wave (PAW) method, as implemented in the Vienna *ab-initio* DFT code VASP. The electron exchange and correlation were treated within the generalized gradient approximation (GGA) in the Perdew-Burke-Ernzerhof (PBE) form. We used a plane-wave cut-off energy of 500 eV and the relaxation of the atomic positions was performed until the Hellmann-Feynmann forces acting on each atom were smaller then 10^{-4} eV/Å. Electronic convergence was achieved when the difference between the total energy of two successive steps in the self-consistent electronic loop was less then 10^{-4} eV. Only the Gamma point in the Brillouin zone was considered for Geometry Optimization (GO). The optimized structures were used as input for the computation of Molecular Dynamics (MD) trajectories. After a first thermal equilibration of the system at 300 K in the NVT ensemble (lasting 2 ps with a time step of 1.0 fs and using the Berendsen thermostat with a velocity scaling each 2 steps), a production run of 10 ps was performed for each

model. The temperature of 300 K was controlled using the Nose thermostat, with a coupling constant of 96 THz. Finally, the Density of States (DOS) was computed as Time Fourier Transform of the Velocity AutoCorrelation Function (VACF), as implemented in the nMOLDYN program. The computation of the VACF from each step of the MD trajectory and using an incoherent weight allows the extraction of the *partial Density of States* pDOS of the H atoms directly. H-DOS were normalized to the number of H atoms in each considered model and convoluted with a Gaussian function, to account for the instrumental resolution.

All the graphene calculations performed in this thesis were done using a multiple of the unit cell, applying periodic boundary conditions. More details about the models will be given in Chap. 5.

Chapter 4

Experimental data: preliminary characterization

In the next three Chapters 4, 5 and 6, we will present and discuss the results of the experimental characterizations and data analysis of Thermal Exfoliated Graphite Oxide (TEGO) and Hydrogenated Thermal Exfoliated Graphite Oxide (H-TEGO), with particular emphasis to its intrinsic defects, hydrogen chemical environment and local dynamics. We will review here the samples synthesis, post-production treatments and preliminary elemental and structural characterizations. Sample synthesis and post-treatments have been carried out at the Carbon Nanostructures Laboratory, at the Physics and Earth Sciences Department of the University of Parma (Italy). The following characterizations have been mostly performed in the context of fruitful collaborations, which will be mentioned and detailed in the text.

4.1 Sample synthesis and preparation

Graphene samples were synthesized through the thermal exfoliation of graphite oxide. **The term "graphene" will be used as a synonym of "thermal exfoliated graphite oxide (TEGO)" at different places throughout of this manuscript, such that graphene will refer to the particular carbon product containing defective graphene, which is produced by thermal exfoliation of graphite oxide**. This chemical method appeared for the first time in 2009, when S. Park and R.S. Ruoff proposed the use of colloidal suspensions to produce graphene flakes [70, 131]. This approach is both versatile and scalable and therefore adaptable to a wide variety of applications requiring bulk amount of material. Obviously, the use of wet chemical routes in graphene synthesis has opened the door towards the production of chemically

modified graphenes. Since then, the development of chemical methods for producing graphene has grown in importance. Nowadays, the thermal exfoliation of graphite oxide still remains one of the most qualified methods for producing gram quantities of graphene.

The synthesis procedure, which leads to the final production of graphene, is composed of two fundamental steps: 1) the oxidation of graphite, with the formation of graphite oxide as intermediate product and 2) the exfoliation of graphite oxide through chemical reduction and/or flash thermal treatment. In the next paragraphs, we will describe these specific synthetic procedures. Further details can also be found in the supplementary informations of [84] and in a dedicated chapter of [83].

Several chemical methods of **Graphite Oxidation** have been proposed and applied since the middle of 19^{th} century. Among them, the most famous are the Brodie [132] and the Staudenmaier methods [133], which essentially differ from the oxidation mixture employed. Many other procedures have been proposed for producing graphitic oxide, nearly all dependent upon strong oxidizing mixtures containing one or more concentrated acids. The method employed to produce the graphene samples studied in this work is the original Brodie synthesis. A commercial pure graphite powder with RW-A purity grade (purchased from the SGL Carbon company) has been oxidized in concentrated nitric acid HNO_3 and HCl at mild temperatures. The product of these oxidation reactions, known as Graphite Oxide (GO), is an expanded and functionalized graphite, whose general structure is represented in Fig. 4.1. Graphite oxidation leads to the presence of many functional groups like oxygen epoxide groups, carbonyl (C=O), hydroxyl (-OH) and phenol moieties attached to the graphite planes [134]. Well reacted samples of graphitic oxide will have a carbon to oxygen atomic ratio lying between 2.1 and 2.9. The color of the product when suspended in water may be used as a criterion for the degree of oxidation of graphite: a product rich in graphitic oxide will have a bright yellow color whereas poorer samples with higher carbon-to-oxygen ratios will have a green to black hue. GO retains the layered structure of graphite but with a much larger interlayer spacing of about 0.7 nm. Moreover GO is hydrophilic and an insulator [135]. The detailed structure of GO is still not completely understood due to the strong disorder and irregular packing of the layers. Several structural models have been proposed so far. GO appears mainly composed of aromatic islands of variable size which have not been oxidized and well separated from each other by aliphatic rings containing phenol (or aromatic diol), C-OH , epoxide groups and double bonds. The layers of GO terminate with C-OH and -COOH groups (Lerf-Klinowski model) [136]. Slight modified versions of this model structure have been proposed, although maintaining the dominance of epoxides and alcohols on the basal plane.

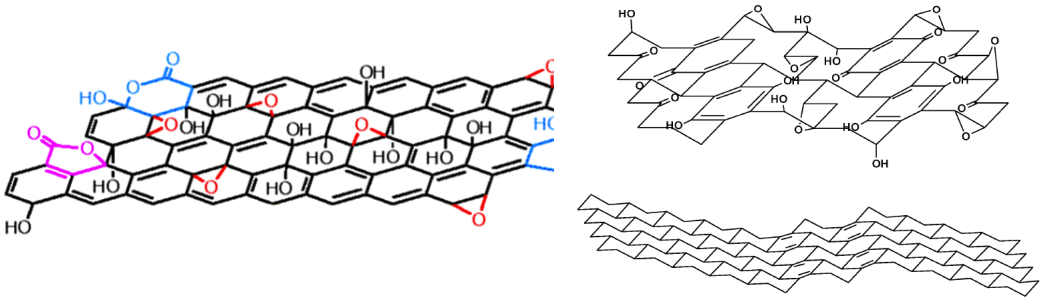

FIGURE 4.1: *Left:* Structural model for GO proposed by Lerf-Klinowski (1998). The model indicates only the chemical connectivity and not the spatial orientation of the functional groups. Hydroxyl groups are perpendicular to the graphitic plane and the interplanar space contains also water molecules. Taken from [136]. *Right:* Structural model for GO proposed by Dékány (2008) [137], including single ketones and/or quinones. Taken from [138].

The Laboratory X-Ray Diffraction patterns, displayed in Fig. 4.2, shows the (002) reflection shifted towards a lower angle corresponding to an interplanar distance which is almost doubled [83] with respect to that of graphite. These results are consistent with previous XRD studies found in the literature. In addition GO has been extensively characterized by a number of different techniques, including XPS, NMR, Raman Spectroscopy, Electron Microscopy and Electron Diffraction [138, 139]. The most important chemical transformation of graphite oxide is its reduction to graphene-like materials. The reduction can be achieved chemically through the use of strong reductants (such as hydrazine or sodium boro-hydride), electrochemically or thermally, as done in this work.

The most important chemical transformation of graphite oxide is its reduction to graphene-like materials. The reduction can be achieved chemically through the use of strong reductants (such as hydrazine or sodium boro-hydride), electrochemically or thermally, as done in this work.

GO was placed inside a quartz tube and then abruptly heated to 1300 K under dynamic high vacuum conditions (10^{-5} mbar). It was kept to this temperature for 30 minutes before been quickly cooled down to room temperature. The flash thermal treatment of GO forces the chemical groups decorating the carbon planes to detach suddenly from the plane, generating an internal overpressure, mainly composed of CO_2 and CO, that separates the graphene layers. This **Thermal Exfoliation** increases the sample volume by more than 1000 times, as it appears evident in Fig. 4.3. An illustrative video about

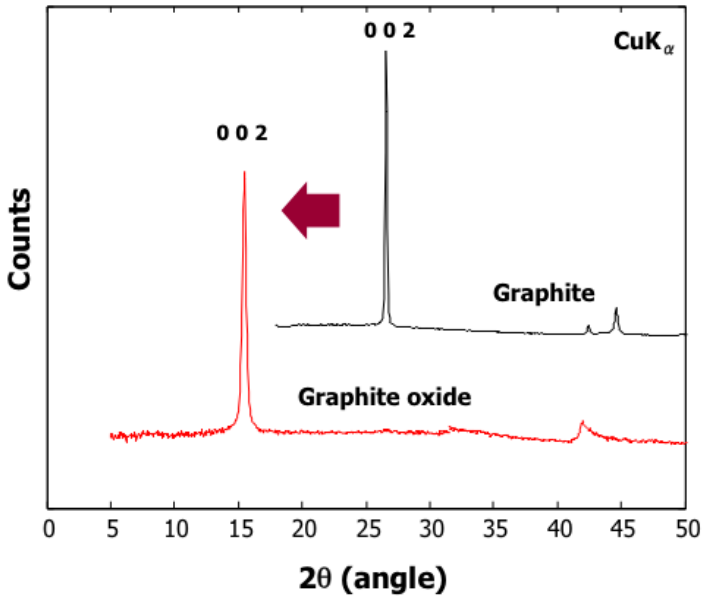

FIGURE 4.2: X-Ray diffraction pattern of graphite oxide.

the exfoliation of GO can be also found on youtube [140]. This process yields a black carbon powder made of extremely fluffy, soft, expanded graphene flakes, with a very low density.

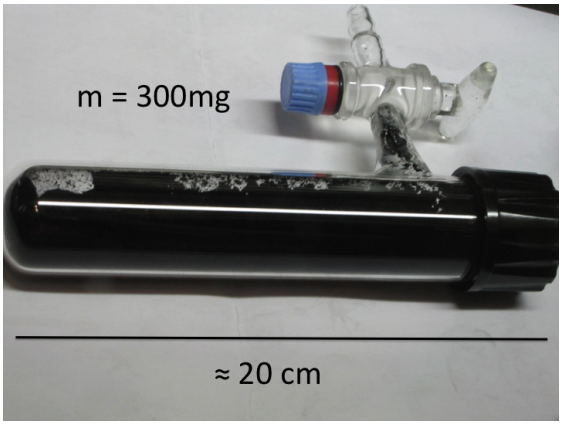

FIGURE 4.3: Thermal exfoliated graphite oxide (around 300 mg) in a glass vial under controlled atmosphere.

The morphological characterization, reported in the next sections, proved that a consistent part of the sample is made out of single layer graphene. It is worth noting that

the formation of CO_2 and CO causing the exfoliation implies that when the functional groups are disrupted from the plane, most of the times they presumably bring away the carbon atom they were attached to. Hence, graphene samples obtained by this route still has many chemical and structural defects, especially carbon vacancies. This chemical method provides compounds with a certain level of disorder, such as chemically reactive defects (mainly carbon vacancies and edges) and corrugations of the planes. Thermally expanded graphite oxide (TEGO) can be produced in large amount and the synthesis is in principle scalable at industrial level, becoming attractive for large scale applications. The amount of sample available was several hundreds of mg.

4.1.1 Ball-milled graphite

Mechanically **ball-milled graphite (or nanographite)** has been measured as reference material as well. Nano-sized graphite samples were prepared from commercial graphite powder of high purity (of purity grade RW-A, purchased from SGL Carbon company), after a preliminary annealing in vacuum at high temperatures (> 1100 K). This thermal treatment was introduced with the aim of removing eventual surface contaminants that could be irreversibly inserted inside the structure during the ball-milling process. Graphite was placed inside a ZrO_2 grinding bowl and ball-milled in Ar atmosphere (< 1 ppm O_2 and H_2O) for 1 hour at 50 Hz with a Fritsch Mini-mill pulverisette. Due to the extreme reactivity of the dangling bonds at graphite edges, particular care was taken that ball-milled graphite (BMG) samples were not exposed to air at any stage of preparation or subsequent handling. It is well known that this mechanical treatment leads to the reduction of the graphite grain size down to the few nanometers range, leading to the formation of nanocrystalline phases. However it introduces also several structural deformations. At moderate milling time, no relevant damage of the honeycomb intra-layer order was observed, however with increasing milling time, turbo-static disorder, planes cleavage, planes breaking and reduction of the crystal grain size were observed, up to the stage where the material gradually gets amorphous. Raman, SEM and TEM investigations indicate that our as-produced ball-milled graphite sample is composed of nano-sized graphite platelets and elongated nano-grains with an average thickness of 6 nm [80, 83].

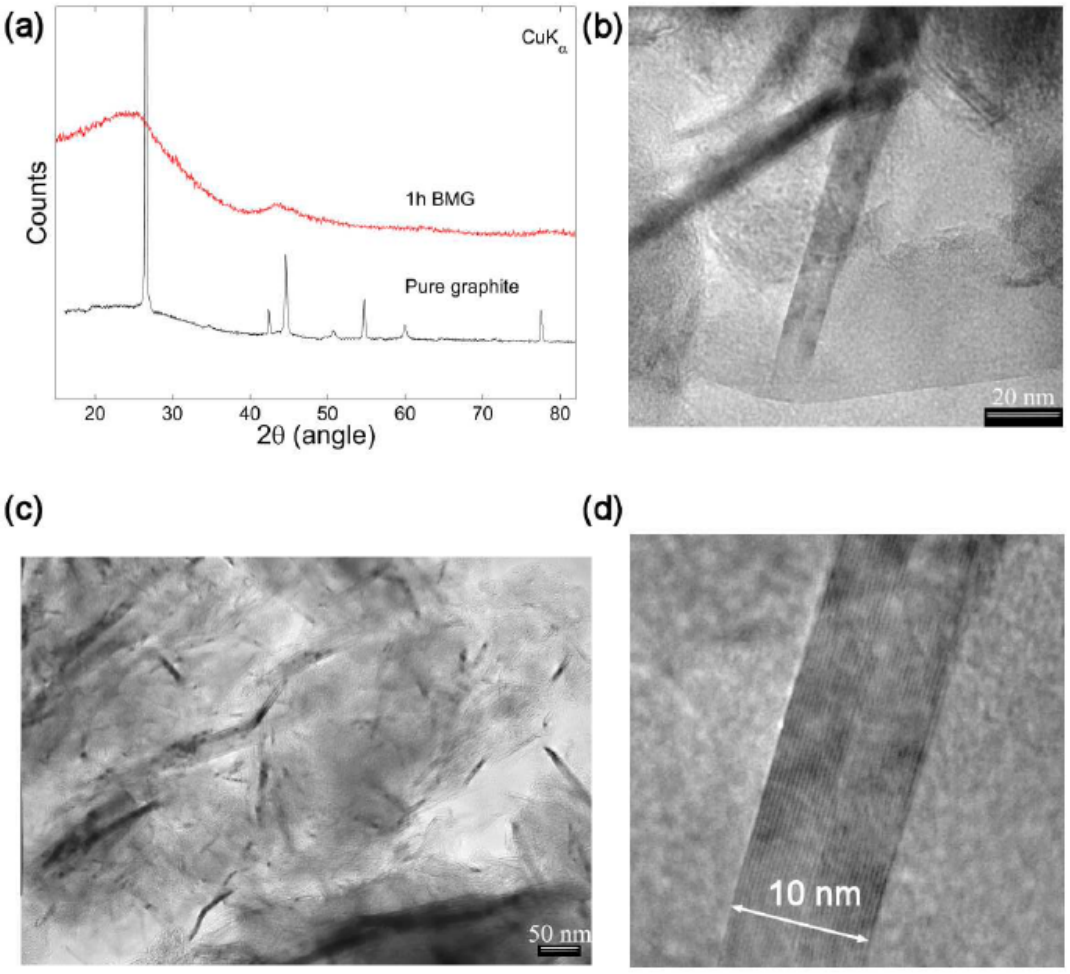

FIGURE 4.4: (a) Comparison between the X-Ray powder Diffraction patterns of graphite (bottom in black) and ball-milled graphite (top in red). (b) TEM images of ball milled graphite show that the sample consists of graphite nano-sized platelets and graphite nanoribbons. (c,d) Nanoribbons, whose mean dimensions along the stacking c-axis is 6-7 nm, appear crystalline and preserve the initial graphite stacking distance of 0.35 nm. Taken from [80].

4.1.2 Hydrogenation

The **hydrogenation** of TEGO and nanographite (Ball-Milled Graphite) was performed by annealing the samples at 1273 K under 100 ml/min H_2 flux at ambient pressure for one hour in a quartz vial. The hydrogenated materials will be called H-TEGO and H-nanographite (H-BM graphite), respectively in the rest of the manuscript. A similar process under D_2 flux led to the formation of deuterated graphene (D-TEGO), employed in the neutron scattering investigations. It is important to highlight that all TEGO and H-TEGO synthesis, post-treatments and consequent handling including preparation and execution of experimental measurements, where not differently specified, have been

carried out under controlled atmosphere, in order to avoid any possible oxygen moisture contamination of the samples.

4.2 Preliminary characterization

In this section several characterizations of the samples under investigation are presented.

4.2.1 Morphological characterization

The samples have been firstly characterized with respect to their morphology using electron microscopy and diffraction, which are among the most common techniques for graphene structural characterization.
Characterization of TEGO with High Resolution Transmission Electron Microscopy (HR-TEM), Selected Area Electron Diffraction (SAED) and Scanning Electron Microscopy (SEM) (Fig. 4.6) clearly demonstrated that the samples contain both single and few layers of sp^2 carbon [141]. For TEM analysis, a small amount of TEGO was exposed to air and quickly dispersed in isopropanol. A droplet of the suspension was deposited onto carbon coated copper grids, for recording the images. The use of an electron beam with low power density (80 kV) assured no beam damage or modification in the morphology of the sample and witnessed the presence of very thin planar areas surrounded by thicker defective domains, as depicted in Fig. 4.5.
This morphological characterization has been performed thanks to fruitful collaboration with Dr. Mohammad Choucair of the University of Sidney (Australia) and Dr. Chiara Milanese of the University of Pavia (Italy) for SEM measurements and Dr. Giovanni Bertoni of the Instituto Materiali per l'Elettronica e Magnetismo IMEM-CNR in Parma (Italy) for HR-TEM and SAED analysis.

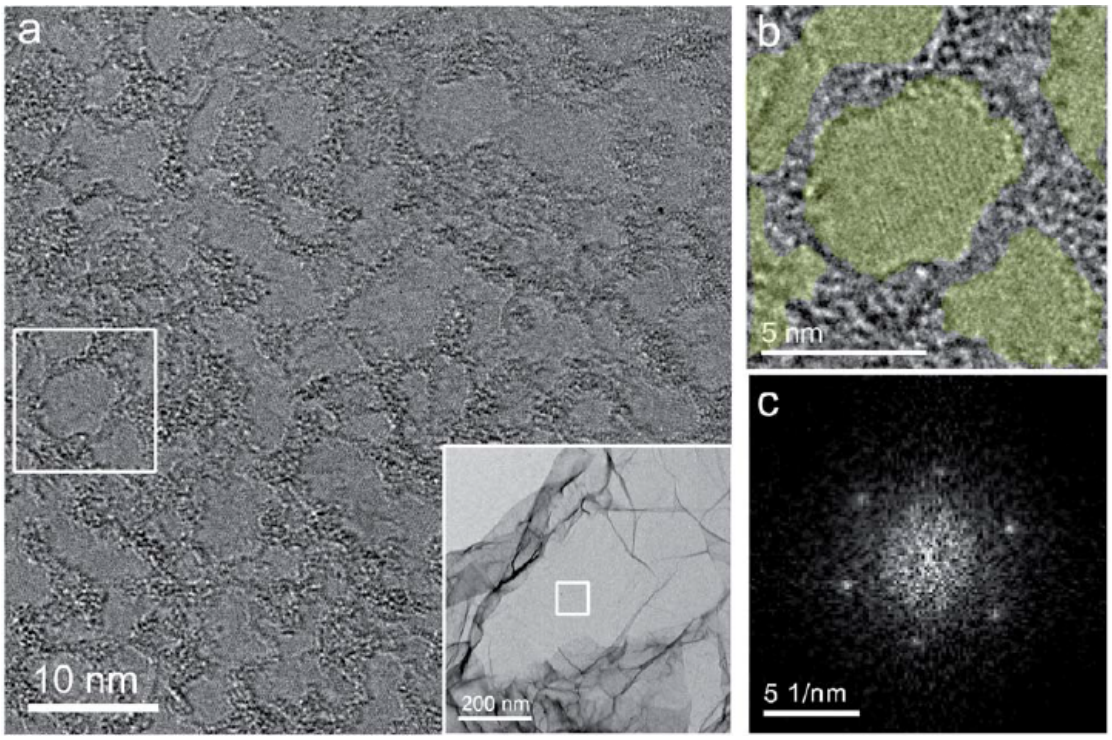

FIGURE 4.5: TEM images of TEGO (a) 80 kV HRTEM image from a flat TEGO region. Small very thin domains are surrounded by thicker areas, probably due to residual GO after exfoliation. (b) Zoom of a portion of the film, in which the thin domains (mostly single layers) are highlighted in yellow. (c) FFT from the central domain, with sharp (1100) spots from an ordered hexagonal graphene pattern. Taken from [142].

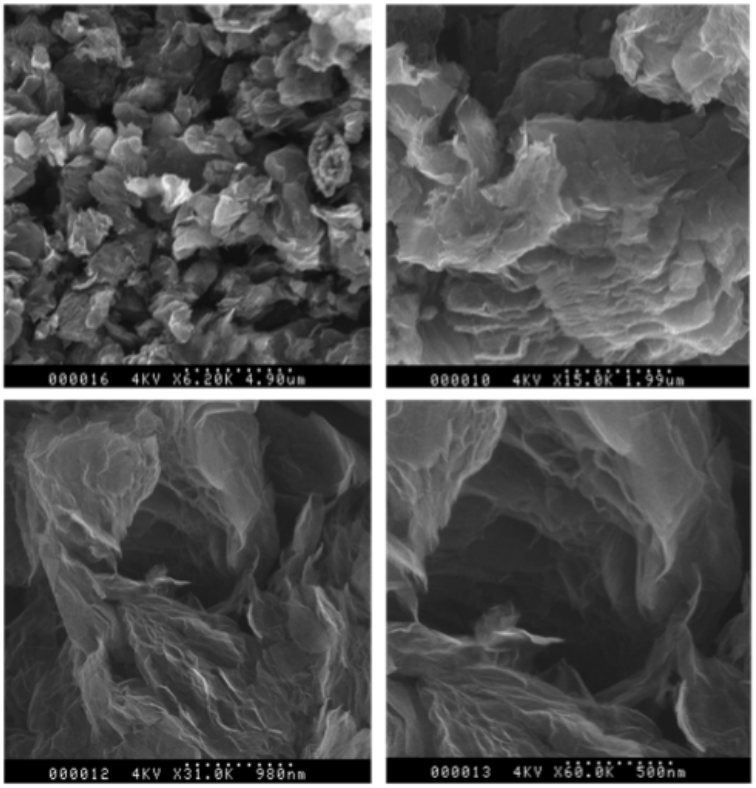

FIGURE 4.6: SEM images showing that the exfoliated TEGO is formed by 2 μm fluffy flakes, each one consisting of stacked sheets.

4.2.2 Structural Characterization

X-Ray and Neutron diffraction were used for characterizing the samples on the structural point of view. In this section we will present Neutron and X-Ray data, either in the form of $I(Q)$ or Pair Distribution function $G(r)$, whose theoretical background has been presented in Chap. 2. The Pair Distribution Function $G(r)$ has been experimentally determined via sine Fourier transform of a properly corrected total scattering function $S(Q)$:

$$G(r) = \left(\frac{2}{\pi}\right) \int_{Q=0}^{Q_{max}} Q[S(Q) - 1] sin(Qr) dQ \tag{4.1}$$

where r is the radial distance.

The Neutron Diffraction experiments have been performed on the High-resolution two-axis diffractometer D2B [143] and on the Liquids and Amorphous Diffractometer D4C (ILL, Grenoble) while the X-Ray Powder Diffraction data have been collected on the High Energy Scattering Beamline ID15B [144] at the European Synchrotron Radiation

Facility (ESRF, France). Experimental details and results will be discussed in this subsection.

For such poorly crystalline compounds, diffraction data may provide qualitative but useful structural informations, like the number of layers and the characteristic size of spatial sp^2 coherence. The peaks on the diffraction pattern are broadened by an amount inversely proportional to the crystallite size and measuring this broadening gives a way to estimate this size through the Scherrer equation [145]:

$$L = \frac{K_s \lambda}{\beta cos\theta} \tag{4.2}$$

where L is the crystallite size, λ is the wavelength of the radiation, β[1] is the peak broadening (in radians) and θ is the Bragg angle. K_s is a dimensionless constant of the order of unity, known as the Scherrer constant [146]. Warren showed that the constant K_s is 1.86 for two-dimensional peaks and it is 0.89 for three diminutional peaks [147]. It should be pointed out that this formula for the two-dimensional particle size has exactly the same form as the equation for the crystalline particle size expect for a numerical coefficient about twice as large. For carbonaceous materials, the lateral extent of the graphene layers and the number of stacked layers can be estimated using the Scherrer equation 4.2 with the appropriate shape constant. Usually, the (002) (or (004)) reflection is used to estimate the carbon crystallite dimension perpendicular to the basal graphene layer L_c and the (100) (or (110)) reflection is used to estimate the lateral dimension of the graphene layers L_a.

Data sets have been collected on D2B (λ=1.594 Å, around 2 hours per scan at room temperature, in air) using standard neutron diffraction vanadium cells (see §2.4.1 in Chap. 2), sealed with an Indium o-ring and containing around 100 mg of samples each. Data were converted from 2θ to Q scale, normalized for the sample mass and corrected from a polynomial background. The strong intensity observed for Q values below 1 $Å^{-1}$ does not provide any reliable structural information, being mainly attributed to elastic scattering from air. The range in Q is therefore limited to [1-7 $Å^{-1}$].

The neutron diffraction patterns of graphite (measured as reference), nano-graphite (ball-milled graphite) and graphene (TEGO) are reported in Fig. 4.7. The crystalline reflection (002), located $\approx$ 1.8 $Å^{-1}$, is still present in both nanographite and TEGO, indicating the permanence of some out-of plane stacking. It appears shifted towards lower Q values, with respect to graphite, because of an increased interlayer distance and the introduction of turbostraticity. The two-dimensional reflections (10) and (11),

[1]Eventual resolution effects should be taken into account

with the three-dimensional (004) reflection superimposed on (10) appear around Q = 3 $Å^{-1}$ and Q = 5 $Å^{-1}$, respectively [147–149]. As expected for typical two-dimension reflections, they feature a clearly asymmetric peak shape, with a sharp increase in the intensity at the low Q side and a slow decay at larger Q [148], D2B has been designed to achieve a very good resolution, limited only by the particle size ($\frac{\Delta d}{d} \approx 5 \cdot 10^{-4}$). From a fit of the first reflection (002), one could extract the averaged domain size L_c by applying the Scherrer equation 4.2. The layer dimension L_a can be determined as well, from the breadth of the two-dimensional (10) reflection at half maximum intensity. The calculated L_a and L_c are about 100 Å and 38 Å respectively. In particular, this corresponds to an averaged number of 10 layers in both TEGO and nanographite.

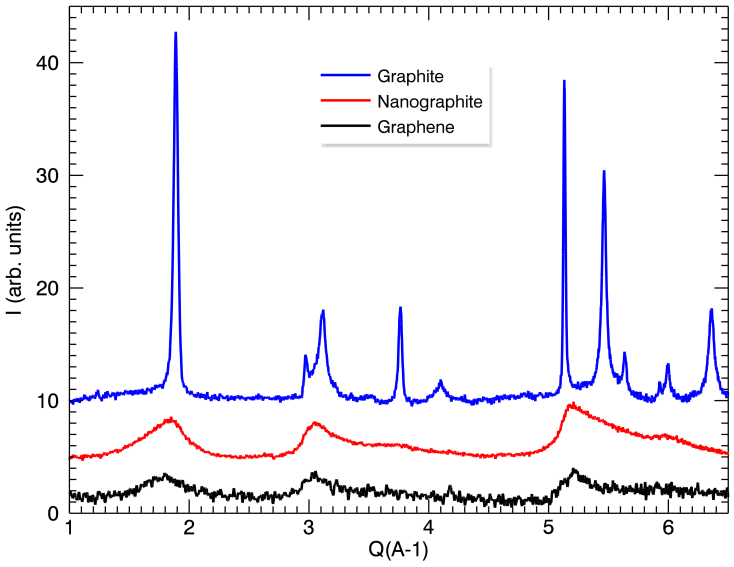

FIGURE 4.7: Neutron diffraction pattern of graphite, nano graphite and graphene (TEGO) collected on D2B.

It should be pointed out that a standard structural approach - like Rietveld refinement - is not possible for such poorly crystalline samples and the quantities discussed above should be interpreted as mean qualitative informations about the averaged domain size.

Nanocarbon produces an extremely strong small angle scattering, rapidly increasing with decreasing Q, as shown in Fig. 4.8. A material consisting of "nano-to-micro" large scale structures, as clusters, pores and flakes will give rise to small angle scattering. From the shape of the small angle intensity one can roughly make hypothesis about the nanostructure geometry and dimensions. Dedicated Small angle studies should be

addressed to unravel the large scale morphological information contained in the small angle scattering observed in the graphene and nanographite samples. Preliminary Small Angle X-Ray Scattering (SAXS) and Small Angle Neutron Scattering (SANS) data have been collected on TEGO and nanographite at the National Institute for Materials Science (NIMS, Tsukuba, Japan) by Dr. Brian Pauw and on the Near and InterMediate Range Order Diffractometer NIMROD at the ISIS neutron facility (Didcot, UK). These data sets will not be discussed in this thesis.

High energy diffraction data, implying short-wavelength neutrons from the hot source, allow measuring the diffraction diagram over a large Q-range. This provides a way to characterise the local atomic order of disordered or non-crystalline materials (see Chap. 2). We used the high energy two-axis diffractometer D4C at the ILL with incident wavelength λ=0.5 Å, corresponding to a maximum Q of 23.5 Å^{-1}, with a Q-dependent resolution $\Delta Q/Q$ below 0.05. Samples were sealed inside a 7 mm diameter Vanadium cylindrical cell, sealed with Cu-rings (see §2.4.1 in Chap. 2). Measurements lasted around 6 hours each and have been performed at 20 K in view of reducing the thermal excitations and the corresponding dynamical disorder.

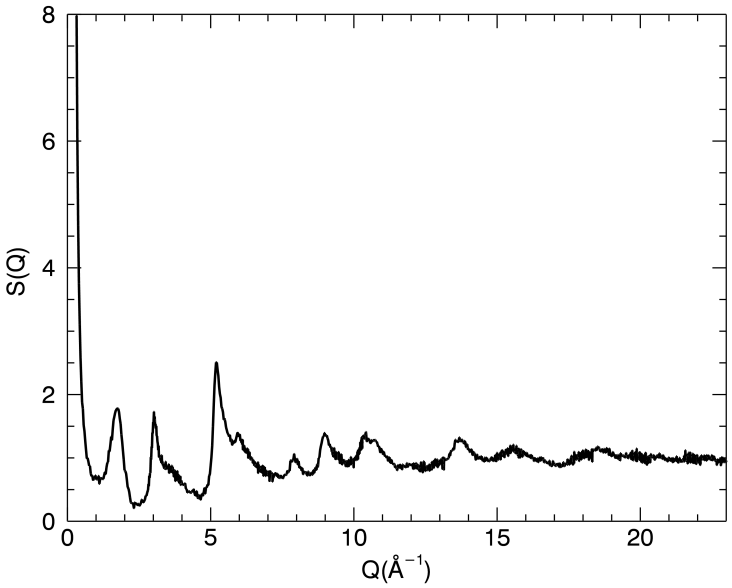

FIGURE 4.8: Neutron diffraction $S(Q)$ of graphene (TEGO) collected on D4C.

The $G(r)$ of graphite and graphene, extracted from D4 neutron data, are reported in Fig. 4.10. Similar data sets were collected on the High Energy Scattering Beamline ID15B (see Fig. 4.9), dedicated to applications using very high energy X-ray radiation.

The option ID15B uses a large area detector (Perkin-Elmer flat panel detectors), making it particularly suitable to data collection at wide angles. For the synchrotron experiments, the samples were loaded and sealed in 2 mm kapton capillary (TEGO) or 1 mm quartz capillary (graphite and nanographite), whose signal was subtracted from the sample data by measuring a background. Measurements were performed at room temperature, using an incident wavelength $\lambda = 0.22235$ Å (calibrated on a Ceria standard). Raw data were converted to 1D-diffraction pattern using the Fit2D software [150] and then to $G(r)$ ($Q_{max} = 22.2$ Å $^{-1}$) using the PDFgetX3 software suite [151].

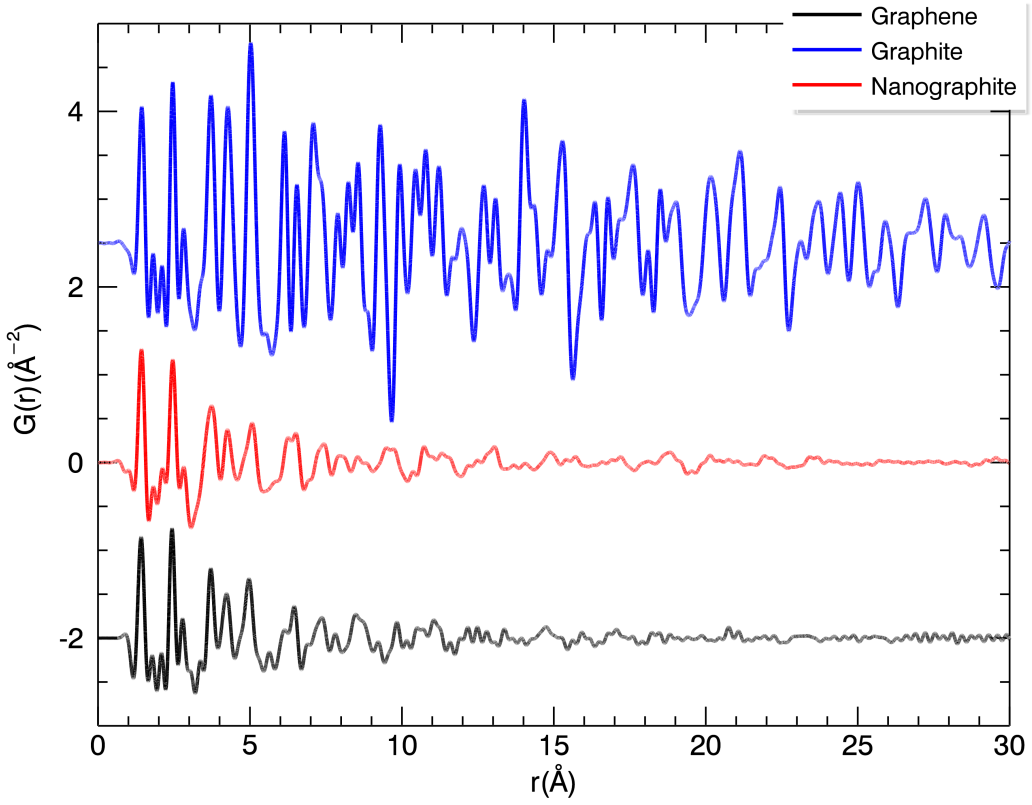

FIGURE 4.9: $G(r)$ of graphite, nano graphite and graphene (TEGO) extracted from X-rays diffraction data, collected on ID15B.

$G(r)$, as already discussed in Chap. 2, displays peaks which correspond to the neighbors distances from an arbitrary fixed origin. Atomistic modeling should complement the data analysis [152, 153]. In particular, through a full-profile fitting of the experimental atomic pair distribution function, one can ultimately extract lattice constants, atomic positions, anisotropic atomic displacement parameters, correlated atomic motion, exponential damping and experimental factors that may affect the data. In this context we

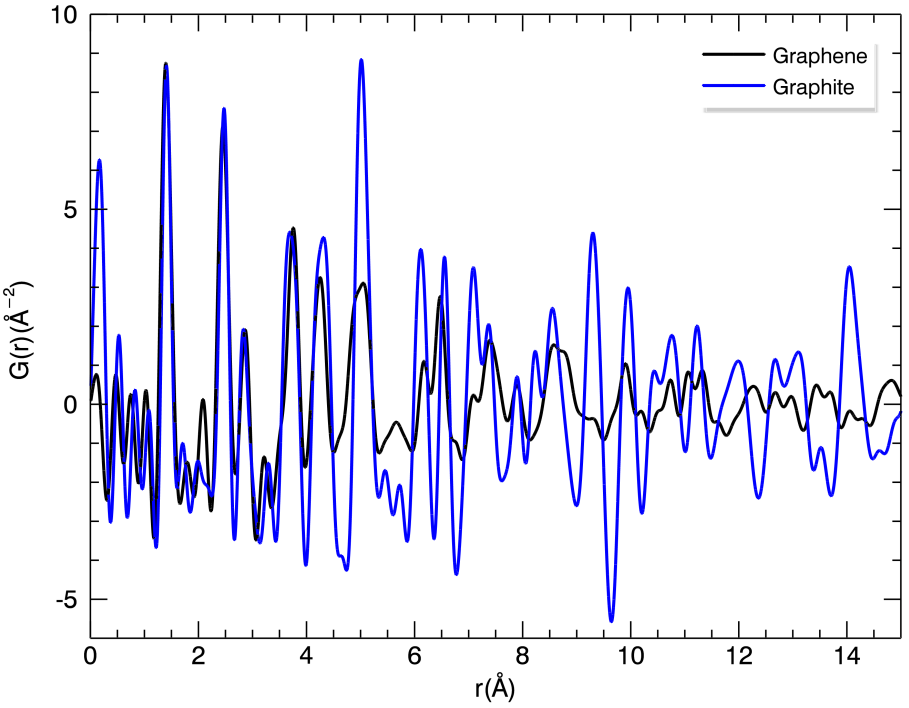

FIGURE 4.10: Pair Distribution Function of graphite and graphene (TEGO) extracted from neutron diffraction data, collected on D4C.

will discussed only qualitatively the general features of the $G(r)$, lingering on the first C-C peak, which strongly depends on the very local carbon environment and hybridization.

In graphite the C-C distance appears at 1.42 Å ± 0.1%, which is the expected value for pure aromatic C sp^2 systems. In graphene one can note a slight distortion of this C-C distance, due to the presence of at least two other different contributions and suggesting hence the presence of other C hybridization states (not aromatic Csp^2, Csp^3 ...). In particular, by fitting this first peak with three gaussian functions, beside the aromatic Csp^2 component around 1.42 Å, we observe clearly two other peaks localized at 1.33 Å ± 0.6% and at 1.50 Å ± 0.09%. This suggests the presence of at least two additional C-C distances, which appear compatible with sp^2 not aromatic and sp^3 C-C bonds in the proportion of 30 % and 18 % respectively and most likely ascribable to defective regions.

Features at higher r maintain a clear correspondence with their counterpart in graphite, indicating the conservation of the local structure over the first neighbor wheels and then the signal is dumped already above 15 Å. The correlations in space are lost. Note that the peaks around and below r = 1 Å were not taken into account in the analysis, the

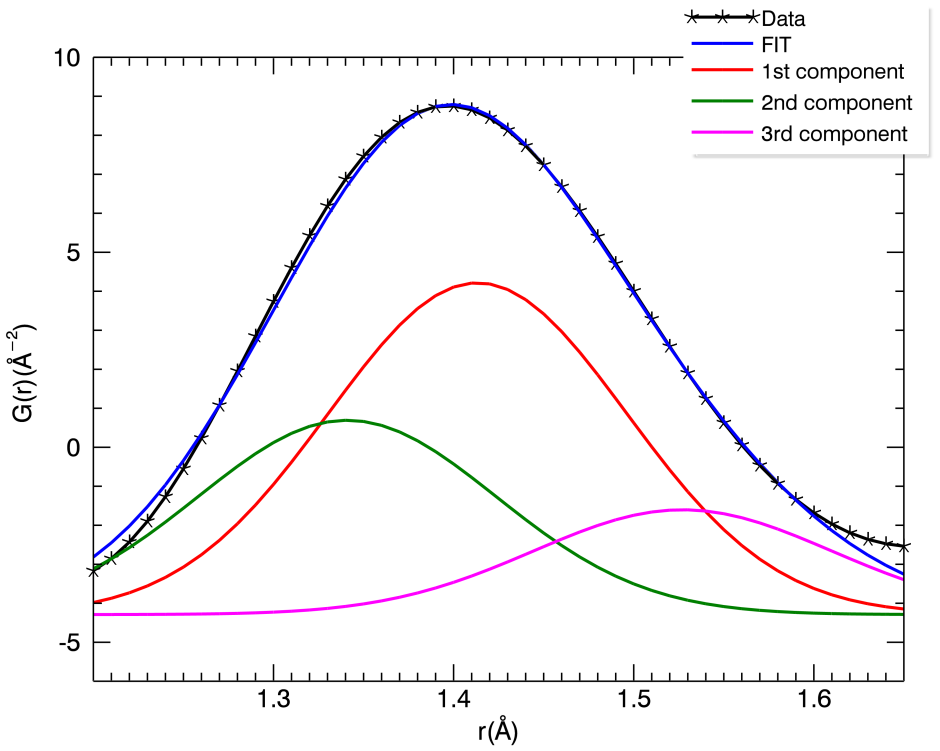

FIGURE 4.11: Detail of the first peak - located ≈ 1.4 Å - in the $G(r)$ of TEGO, together with the deconvolution in three different components (from D4C data, shown at the left)

latter corresponding to unphysical interatomic distance.

In Fig. 4.12, we report the $G(r)$ of D-graphene, that we compare to that of TEGO. The hydrogenation (deuteration) process should introduce a supplementary set of interatomic distances, corresponding to C-H(D) neighbors, with a first peak in the $G(r)$ expected around 1.09 Å (typical value for the C-H bond distance). The D-graphene structural response appears very similar to that of TEGO. This suggests that $G(r)$ is more sensitive to the averaged carbon network, than to its fine structure, *i.e.* to the very local modifications induced by H. There is no clear evidence of the presence of C-D distances (expected around 1 Å). As we will show in Chap. 5, the amount of H(D) in the sample was certainly too low for being directly appreciated through Direct Space Analysis (PDF).

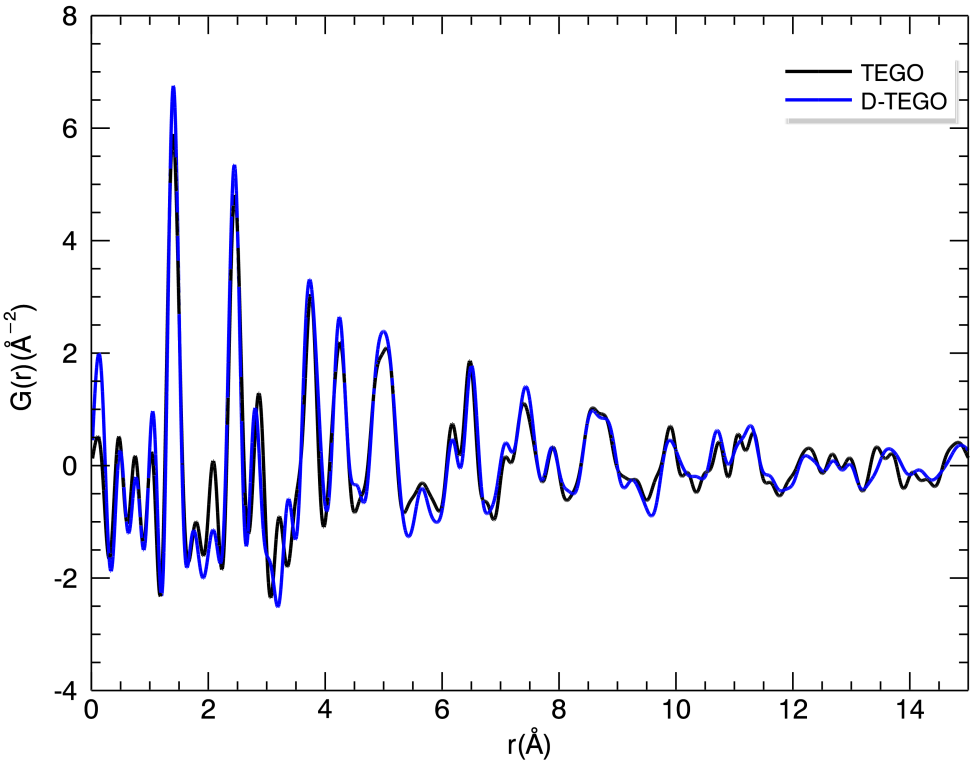

FIGURE 4.12: Pair Distribution Function of graphene (TEGO) and deuterated graphene (D-TEGO) extracted from D4 data

4.2.3 Other techniques

Several techniques, as X-ray and UV photoemission spectroscopy (UPS/XPS), Raman and Infrared (IR) Spectroscopy, SQuID Magnetometry, Nuclear Magnetic Resonance (NMR) and Muon Spin Rotation (μSR), have been employed as characterization tools, in order to identify the nature and concentration of defects. They were also used to study the hydrogen interaction with TEGO as a function of temperature and track its behavior at the graphene surface.

In the following paragraphs, some of the most relevant complementary investigations are discussed in order to complete the graphene chemical-physical characterization and to help the reader having a more global panoramic of this complex system. One could refer to the original works or technical books for more specific details about the techniques and instrumentations used. In particular, several of these analysis have been already extensively discussed in the following papers [83], [84], [154], [142] and [85].

X-ray and UV photoemission spectroscopy (XPS and UPS) experiments have

been performed on both TEGO and H-TEGO by Dr. Verrucchi and collaborators at Istituto dei Materiali per l'Elettronica e il Magnetismo, IMEM-CNR in Povo (Trento, Italy). Graphene samples were first dispersed in a solution of isopropanol and collected on a polyethylene foil, after solvent evaporation. XPS analysis showed the presence of carbon (C) and oxygen (O) in the samples, with relative atomic percentage for TEGO and H-TEGO of around 97%/3% in both cases. The amount of oxygen appears very low, thus indicating that the thermal exfoliation process has been effective in removing almost the totality of the oxygenated groups, which are present in the precursor (GO), as discussed in the first section of this chapter.

The core level analysis, performed on the C1s core level, allowed to extracting the percentage presence of the different C hybridization. The C1s core level in TEGO appears as a structured peak, whose main component is associated to sp^2 C, as expected for a graphenic structure. Both UPS and XPS measurements suggested that the majority of graphene sheets in TEGO are stacked to form few-layered structures and there is a clear presence of defects onto and between planes, as confirmed also by HR-TEM investigations. The C 1s peak in H-TEGO shows essentially the same four components and an additional peak ascribable to carbon bound to hydrogen, which represents about 6.6% of the C 1s emission [155]. This suggests that hydrogenation induces the formation of C-H bonds and this involves mainly defective graphene regions [85]. Moreover the hydrogenation procedure appears not to increase the amount of C-O group. As a final remark, it is noteworthy to observe that these are surface probes, therefore the data are strongly affected by the condition of the sample near the surface.

Raman spectroscopy is one of the most common techniques for graphene characterization. Its large use in the physics of graphene and carbon materials relies on the high sensitivity to the carbon network's structure and dynamics and therefore its capability of providing useful informations as the average sp^2 domain size, the number of layers [156] and disorder degree within the plane [157, 158]. Raman spectroscopy experiments on TEGO have been performed at the Empa - Swiss Federal Laboratories for Materials Science and Technology in Dübendorf (Switzerland) using a Bruker Senterra Raman spectrometer with a 532 nm laser as incident excitation [142]. Samples were placed into 0.7 mm diameter quartz capillaries. The Raman spectrum of TEGO, reported in Fig. 4.13 shows several remarkable features, as expected for a defective graphene sample: the D band, at about 1350 cm^{-1}, the G (graphitic) band at around 1570 cm^{-1}, the D' band at about 1620 cm^{-1} and the 2D band at around 2710 cm^{-1}. The D and D' bands are associated to structural defects and disorder. The integrated area of the D and G bands can be used to determine the degree of disorder. It has been shown that the inverse ratio of I_D/I_G is proportional to the crystallite size for nanographitic materials [159]:

$$L_a(nm) = (2.4 \cdot 10^{-10})\lambda_{laser}^4 \left(\frac{I_D}{I_G}\right) \tag{4.3}$$

The average sp^2 domains of L_a results to be around 12 nm, in good agreement with the one imaged by HRTEM (10-15 nm). This value is much higher than the one found in $G(r)$, the latter being sensitive to punctual defects, which could break the aromaticity inside sp^2 regions.

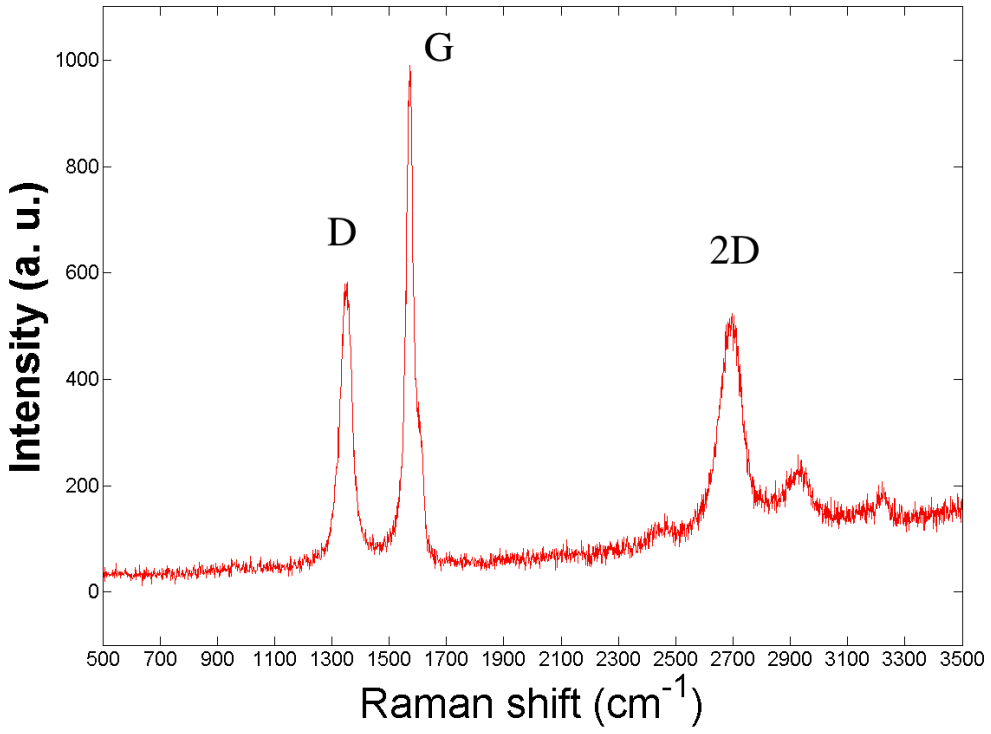

FIGURE 4.13: Raman spectrum of TEGO.

InfraRed (IR) spectroscopy measurements have been performed at the Empa - Swiss Federal Laboratories for Materials Science and Technology in Dübendorf (Switzerland) as well, thanks to a fruitful collaboration with Dr. Elsa Callini, Dr. Andreas Borgschulte and Dr. Philippe Mauron of the Hydrogen and Energy group.

An ALPHA's Platinum ATR single reflection diamond FT-IR spectrometer (Bruker), operating under Argon atmosphere has been used, in order to avoid the exposition of the samples to air. Several small graphene flakes have been investigated, by placing gradually a very small amount of sample onto a diamond crystal and then pressing it down with a pressure applicator. Measurements were collected in reflection mode. Every

spectrum was recorded as $I_T = \frac{I_s}{I_b}$ where I_b is the background measurement (obtained by measuring the empty instrument inside the glove box atmosphere) and I_s is the sample measurement. A polynomial baseline has been subtracted to I_T, in order to render possible the observation the signal coming from the sample. Data have been acquired by summing 64 scans, each scan taking 5s. Instrument control, data acquisition and treatment were done using the OPUS software (Bruker).

IR spectroscopy is a very appropriate technique for the identification of functional groups. It registers the molecular and atomic vibrational frequencies, characteristic of each functional group. As standard routine, one could identify a functional group of a molecule by comparing its vibrational frequency to an IR stored data bank or a known reference.

In Fig. 4.14 the IR spectra of graphene (TEGO) and H-graphene (H-TEGO) are reported. Data from 1800 cm^{-1} to 2800 cm^{-1} correspond to the diamond cut-off. For this reason they are excluded from the data interpretation. TEGO spectrum features several intense peaks located at 1050 cm^{-1} and 1600 cm^{-1}, ascribable to C-O stretching modes and C=C aromatic bending modes respectively and some minor components at 1700 cm^{-1} and 3700 cm^{-1}, which appear compatible with C=O carbonyl stretching and O-H alcoholic stretching modes. The H-TEGO spectrum is strongly modified: only the intense feature around 1600 cm^{-1} is observed. Below 1000 cm^{-1}, a series of peaks is observed, *i.e.* in a region where C-H bending modes appear in hydrocarbon.

This suggest that the treatment in hydrogen flux leads to the removal of the oxygenated chemical group and induces the formation of C-H bonds. However the C-H vibrational signature is very poor and unclear in these data, likely due to the structural non homogeneity of the samples, the very local nature of the probe and absorption phenomena of the IR light by carbonaceous materials. As we will see in the next chapters, the latter features appear very clearly in the corresponding neutron spectra.

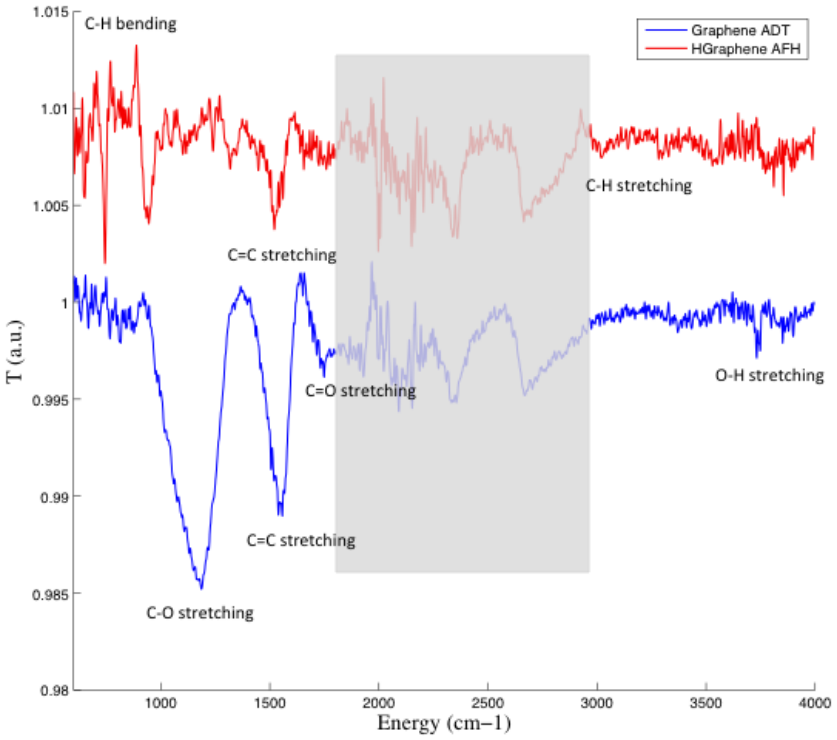

FIGURE 4.14: IR spectra of TEGO and H-TEGO. This latter one has been shifted along y-axis for clarity. The shaded region corresponds to the diamond cut-off.

4.3 Partial conclusions

The principle considerations of this chapter can be summarized in the following lines:

- We have describe the bulk synthesis of defective graphene (TEGO).
- The carbon network is non homogenous on the structural point of view and appears very difficult to be precisely characterized.
- On the structural point of view (direct space analysis) there is not clear indication of the effect of hydrogenation.
- Optical spectroscopies (in particular Raman and IR) provide useful information about the level of disorder and the functional groups characterizing the as-prepared graphene surface. In particular IR evidences the appearance of complex vibrational features ascribable to C-H modes.

Chapter 5

Neutron spectroscopy: analysis and results

Beside the large set of instrumental techniques used to characterize the TEGO and BMG samples at a local scale, the results being reported in Chap. 4, no real difference is observed between those two graphitic samples. In particular they give very similar diffraction response, either performing classical Bragg analysis, or using PDF approaches, the later being better suited to ill crystalline samples or nano-crystals powders. This is rather surprising as the macroscopic aspect of both samples is very different with a much lower density for TEGO.

In this chapter, we present the results obtained from Inelastic Neutron Scattering (INS) investigations, whose analysis have been performed on the basis of *ab-initio* molecular dynamics simulations (AIMD) described in Chap. 3. The theoretical and data results are presented in the form of the Generalized Density of States (GDOS) $G(\omega)$ that we defined in Chap. 2.

In the first part of this chapter, we will discuss the features observed in the GDOS of graphene (TEGO), based on the comparison with those observed in the spectra of a Nanographite and a Graphite sample. The GDOS reflects the lattice dynamics of the carbon framework and the comparison between the different samples' spectra reveals the effect of the reduction of dimensionality and increase of disorder on the dynamical properties.

In the second part, we will present a detailed neutron spectroscopy study of the hydrogenated graphene and nano-graphite. As already discussed in Chap. 2, since the scattering cross section is much greater for hydrogen ($\sigma_H = 82$ barns) than for carbon [1] ($\sigma_C = 5.55$ barn), any displacements involving hydrogen atoms will produce an intense feature in the GDOS. In an hydrogenated sample, the GDOS spectrum is assimilable to

[1] or any other element in the periodic table.

the partial density of state of hydrogen in the material. We show that the main features of the GDOS measured for H-TEGO and H-BMG can be ascribed to C-H bending and stretching modes, having strong similarities with those typical of Polycyclic Aromatic Hydrocarbons (PAHs). We use AIMD simulations to calculate the partial density of states of H atoms located on specific sites on the carbon framework. These simulations show that the detailed shape of the neutron spectra in the bending mode range of the GDOS, can be used as a fingerprint of the local environment of the H atoms, *i.e.* the C hybridization, bond lengths and arrangement of the first neighbours strongly influence the spectra in this range.
The neutron derived GDOS spectrum provides an efficient way of characterizing the in–plane defects of an hydrogenated graphitic sample, the latter being very difficult to observe with other techniques.

5.1 Inelastic neutron scattering data

This section is divided into two parts: the first part aims at characterizing the raw samples. The goal is to probe the dynamic of the carbon framework of each sample before hydrogenation. It is followed by a extensive discussion on the effect of hydrogenation on the dynamics response of these material.

The INS data were collected on the thermal neutron time-of-flight spectrometer IN4C at the ILL. Two types of investigations were performed. At the relatively high temperature of 320 K, the GDOS was derived in the [0-180 meV] energy range using an incident neutron wavelength $\lambda = 2.41$ Å (which corresponds to an incident energy of 14.08 meV) in up-scattering mode (anti-Stokes scattering). The instrument was set in the inelastic time focusing mode, which consists of spinning the rotating Fermi chopper at high speed, in order to achieve the best resolution in the inelastic range. The elastic resolution was $\Delta E \sim 0.8$ meV. The dynamics was also measured at low temperature (T = 5 K) in down-scattering mode (Stokes scattering) using the wavelengths $\lambda = 1.5$, 1.1, and 0.74 Å which correspond to incident energies of 36.35, 66.39 and 149.38 meV respectively. The use of several incident energies allows probing an extended energy range (up to 120 meV) with the best resolution. The different spectra were assembled by rescaling their intensity so that they match in overlapping areas.
We used also the IN1-BeF and IN1-LAGRANGE hot neutron spectrometers (see Chap. 3) in order to:

- extend the investigated frequency range to a maximum energy of 500 meV;

- better resolve the details of the GDOS spectra in the bending mode region around $\sim$ [80-200 meV] thanks to its better resolution compared to IN4C in this range (around 4% and 2% of $E_i \approx \hbar\omega$ for IN1-BeF and IN1-LAGRANGE respectively).

The powder (a mass of several hundreds of mg) was placed inside a standard flat or cylindrical Al-cell, sealed with an Indium ring. All sample manipulations and handling, as well as sample-holder filling were done under the controlled Argon atmosphere (O_2 and H_2O content below 0.1 ppm) of a glove box, in order to avoid any air or oxygen moisture contamination prior to the INS experiments.

5.1.1 The dynamics of the carbon framework

The GDOS of graphite, nanographite (BMG) and graphene (D-TEGO) are reported in Fig. 5.2. The graphite GDOS shows some characteristic features: a first singularity at $\sim$ 17 meV, followed by a more or less constant GDOS up to $\sim$ 60 meV where a peak is observed. A clear pseudo-gap is found, followed by a complex feature with a maximum intensity at 75 meV. Each of these remarkable features corresponds to a well known van Hove singularity (VHS), the latter corresponding to regions in the reciprocal space where the phonon dispersion curves have flat dependence (see Fig. 5.2), *i.e.* giving intense contributions to the density of states [160–162]. The profile of these features reflects indirectly the lattice structure, as the VHS appears in high symmetry points of the first Brillouin zone. A perfect crystal with long range order will therefore be characterized by a well defined lattice and a reciprocal lattice with sharp spots. The corresponding VHS will be sharp and one expects well defined profiles in the GDOS. At the contrary, a disordered material (like a glass) or a crystal with limited extension (in the *nm* scale) share the same GDOS characteristics [163]: large features associated to ill defined VHS and a transfer of the GDOS spectral weight to low frequency. The origin of the smoothed features in a glass can be understood as resulting from the folding of some parts of the Brillouin zone when one introduces disorder in the lattice. This flattens the dispersion curves in many places, resulting in an broadening of the crystalline features. Local modes are also created which participate to the increased complexity of the GDOS. As for crystals of reduced dimensions, the limited extent of the grain enlarges the spots in the Brillouin zone accordingly, resulting in more diffuse VHS, *i.e.* larger singularities in the GDOS.

The reduced dimensions of the grains in nanographite and graphene have strong effects not only on the structure, as discussed in Chap. 4, but also on the GDOS profile: the peaks are found to be broader when observable and an increased intensity in the low frequency part of the spectrum is observed. In particular, the features at 60 and 75 meV are present but much less defined in the BMG GDOS, with a vanishing pseudo gap

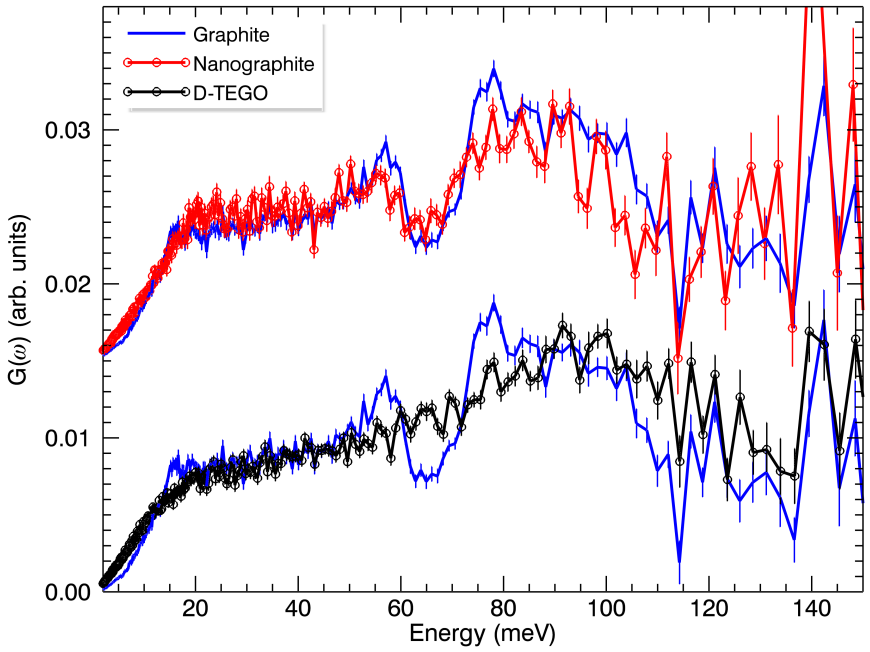

FIGURE 5.1: Experimental GDOS of graphite, nanographite and graphene measured on IN4C, at 320K and $\lambda = 2.41$ Å in up-scattering mode.

in between. In the same range, the GDOS appears essentially featureless in defective graphene. These observations suggests that the in–plane carbon structure is significantly more perturbed for the D-TEGO sample than for the BMG sample. By contrast, both spectra show the same smooth, linear dependence of the GDOS in the lowest energy range, up to a frequency larger than the first feature of graphite at 17 meV. This linear dependence suggests that it originates from the acoustic modes propagating inside the plane, *i.e.* revealing the stronger 2D character of the systems with regards to graphite, certainly due to the reduced number of planes per grain.

5.1.2 The dynamics of the hydrogenated materials

Fig. 5.3 shows the neutron GDOS of as-prepared TEGO, deuterated TEGO[2] and hydrogenated TEGO[3]. All the spectra were normalized to the mass of carbon (≈ 250 mg) in the neutron beam. Additional measurements of the GDOS were performed at 10 K on the H-TEGO sample (blue circles).

The intensity enhancement observed from TEGO to H-TEGO denotes an increased

[2]D-TEGO was obtained by thermal treatment of TEGO under D_2 flux.
[3]H-TEGO was obtained after thermal treatment under H_2 flux.

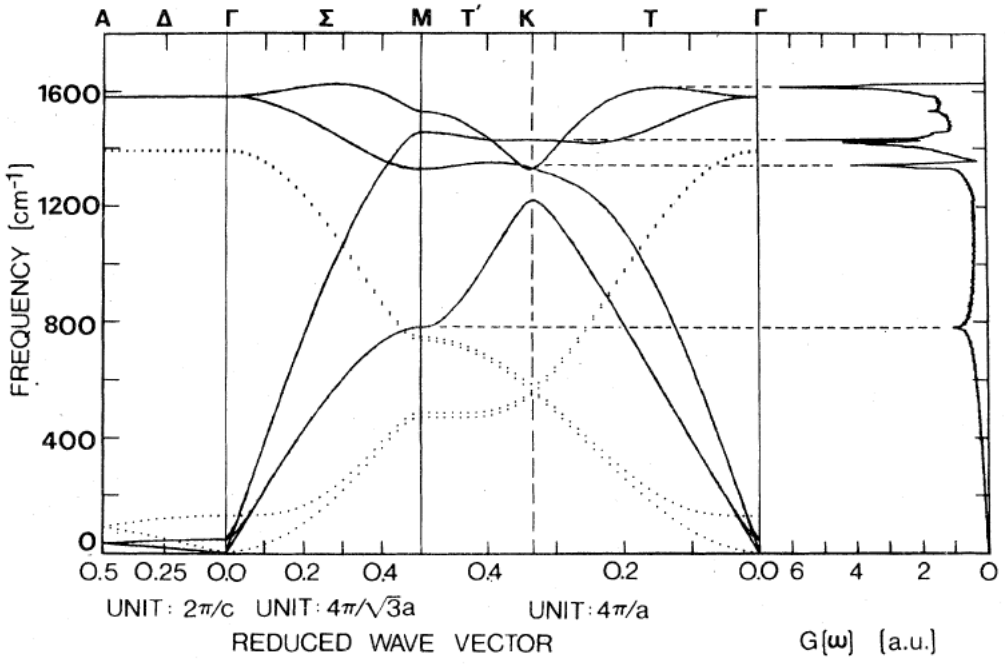

FIGURE 5.2: Graphite phonon dispersion curves and density of states G(ω), calculated from the lattice-dynamics model of Nicklow, Wakabayashi and Smith. The solid lines correspond to in-plane displacements, while the dotted ones represent out-of-plane displacements. The dashed horizontal lines are guide to the eye to show the k-space regions which contribute to the Van Hove singularities [164] in the density of states. Taken from [161].

quantity of hydrogen in the H-TEGO sample. The same observation can be done for the Nanographite sample (BMG and H-BMG GDOS are shown in Fig. 5.4). The larger intensity observed in the TEGO sample compared to that of D-TEGO, especially in the region around 100 meV suggests the presence of hydrogen in as-prepared TEGO, *i.e.* prior to hydrogenation. It also validates the thermal treatment in Deuterium atmosphere to promote H/D exchange.

From the neutron TOF data it was possible to estimate the amount of hydrogen in TEGO before and after hydrogenation as well as in H-BMG, by rescaling the elastic scattered intensity to that of a reference vanadium sample of calibrated mass, according to Eq. 2.18 in Chap. 2. We found that the H amount in TEGO is 0.17(2) wt %, while after hydrogenation it increases by a factor of 4, reaching 0.69(2) wt % in H-TEGO. A similar estimation for HBM graphite gives the value of 0.21(8) wt %. This has evidenced a particular capability of graphene in dissociating the molecule of H_2 and trapping atomic hydrogen in covalent C-H bonds.

The H-TEGO (and H-BMG) GDOS measured on IN4 feature different domains:

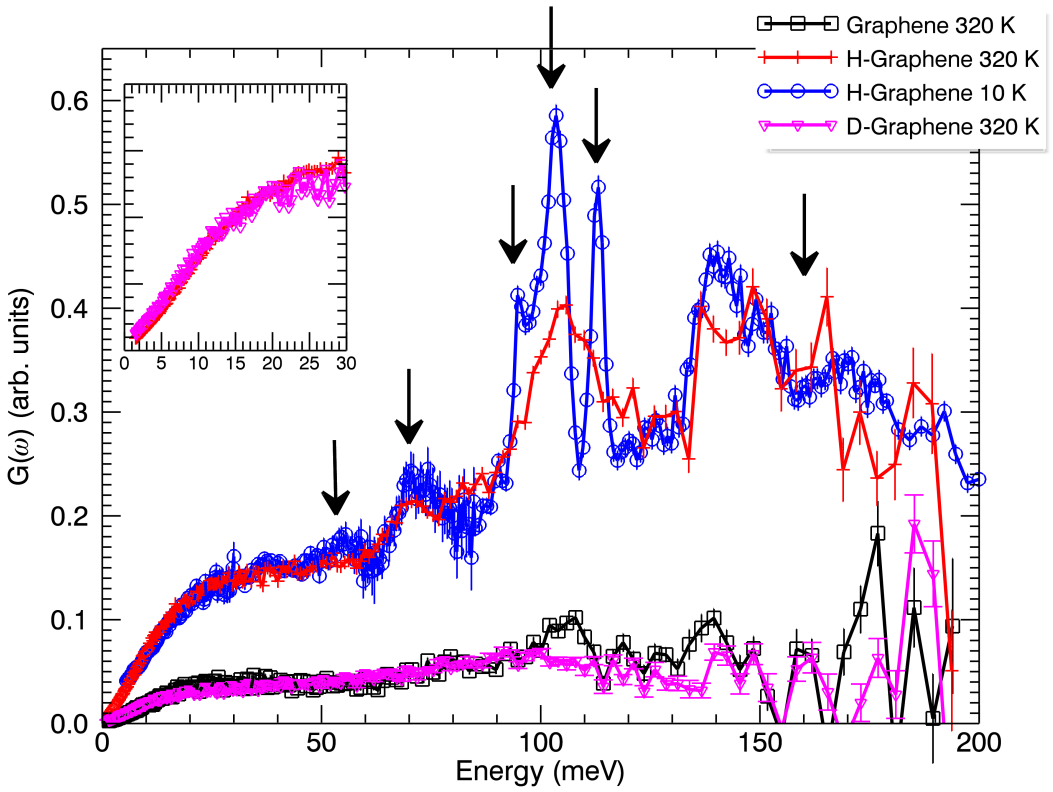

FIGURE 5.3: Inelastic neutron spectra obtained on IN4 at 320 K with incident wavelength of 2.41 Å on as-prepared TEGO (squares), D-TEGO (triangles), and H-TEGO (crosses). Squares: INS spectra obtained on H-TEGO at 10 K using Lagrange. Black arrows indicate the main features due to H localized modes in the H-TEGO. Inset: The D-TEGO GDOS has been rescaled for a factor $\alpha = 3.91$ to match the GDOS of H-TEGO in the so–called *riding modes* range.

- a low-medium energy range (E $\gtrsim$ 50 meV), which appears essentially featureless. In this low frequency region of the spectra, no sharp feature and no important temperature evolution is observed.

- a high energy range (E $\gtrsim$ 50 meV) characterized by the presence of localized bands centred at $\sim$ 55, 75, 110 and 150 meV. In particular, the features located at 55 and 110 meV seems to be temperature dependent, with a significantly higher intensity at 10 K than at 320 K.

Low frequency range: E $\leq$ 40 meV

The TEGO, BMG and their hydrogenated counterparts, H-TEGO and H-BMG spectra show the same profile in the low frequency range: a linear increase of the GDOS up to $\approx$ 20 meV, followed by a flat region up to 40 meV. As already indicated above, this [0, 40

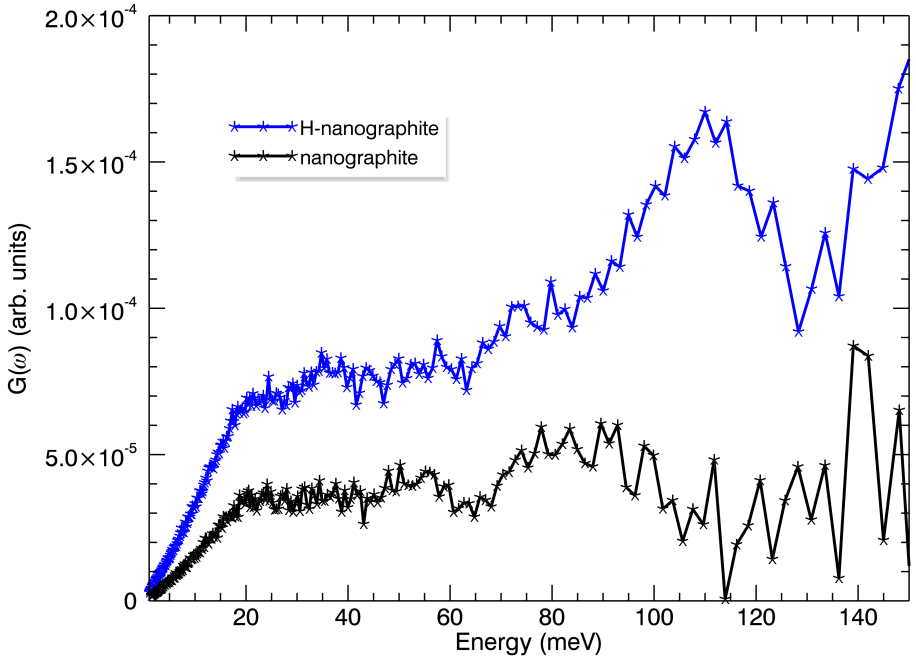

FIGURE 5.4: Experimental GDOS of nanographite and hydrogenated nano graphite measured on IN4C, at 320K and $\lambda = 2.41$ Å.

meV] is mostly temperature independent. The fact that the non-hydrogenated GDOS and the hydrogenated counterpart differ by a scaling factor indicates that the hydrogen atoms follow the movements of the carbon framework adiabatically. In this peculiar range, the dominant contributions to the GDOS arise from out-of-plane vibrations of the carbon lattice (see the dotted lines in Fig. 5.2). These long wavelength plane fluctuations bring with them the H atoms strongly bounded to the surface. The phonon modes in this range therefore contains a significant contribution from the H atoms, such that the GDOS in this range can be expressed as:

$$G(\omega) = [N_C \frac{\sigma_C}{M_C} + \alpha\ N_H \frac{\sigma_H}{M_H}] g_C(\omega) \tag{5.1}$$

with $g_C(\omega)$ the density of state per atom of the carbon framework and α a proportion factor representing the amplitude of the H displacements.

The modes in this region, implying H movements, are called **riding modes** in the following of this manuscript. Their intensity is amplified in the hydrogenated spectra due to the very large neutron cross section of hydrogen coupled to its weak mass [165], *i.e.* a very large $\frac{\sigma_H}{M_H}$ value.

According to Fig. 5.2, the H-TEGO GDOS in the riding mode part of the spectra appears temperature independent for T varying from 10 to 320 K. This indicates that

the scattered intensity follows a Bose dependence with the temperature and suggests that the signal originates mainly from phonon excitations. This simple observation gives us crucial informations:

- it excludes the presence of physisorbed molecular H_2 in the H-TEGO sample. Its presence would give rise to the appearance of an intense feature around 14.7 meV at low temperature, corresponding to the para - ortho quantum rotation for molecular H_2 [166]. A strong temperature dependence would also be observed (transition from a discrete quantum rotation spectrum at low T to a continuous classical regime at high T).
- it suggests the absence of functional groups (like methyl groups) attached to graphene planes. The latter chemical species are usually involved fast reorientations in the high temperature regime, giving rise to a quasi-elastic broadening having a strong temperature dependence. At low temperatures, these fast continuous rotations are blocked inside a potential minimum, and the group oscillates around preferential orientations. The latter oscillations show up as intense libration peaks in an energy range varying from a few meV to $\sim$ 20 or 30 meV [167, 168]. Such evolutions are not observed.

The C–H Bending mode range: E $\in$ [70, 180 meV]

The high energy H-TEGO data are dominated by intense and complex bands located around 100 and 150 meV, whose main components are highlighted by black arrows in Fig. 5.3. Their fine structure is more evident in the low temperature spectrum, due to the improved resolution in this energy range and to the reduced thermal disorder. The band centered around 100 meV is composed of three peaks, respectively located at $\approx$ 95, 105, and 115 meV. These vibrational contributions fall in the range of C- H vibrational modes of PAHs, and are therefore compatible with the presence of atomic H covalently bound to the carbon framework [169, 170]. The large capacity of TEGO and H-TEGO to capture atomic H at reactive in-plane defects through C–H covalent bonds was initially proved by μSR investigations, which highlighted also their extreme stability upon heating [84].
The C–H bending mode region of the neutron INS spectra contains therefore the spectral signature of the local environment of the captured atomic H at the surface of the TEGO and BMG. They provide an invaluable mean of probing the nature of the different in–plane atomic defects whose experimental investigation has proven very difficult

with more classical techniques (see Chap. 4). In the next paragraphs, we focus our attention on the study of these modes, using mostly the IN1-BeF and IN1-LAGRANGE spectrometer to investigate this part of the spectrum with improved resolution.

In Fig. 5.5, the neutron spectra of H-TEGO (H-Graphene), H-BMG (H-Nanographite) and coronene collected using IN1-BeF are reported. The spectrum of a commercial glassy carbon sample [171], measured using the TOSCA spectrometer at ISIS (UK) is also shown for comparison.

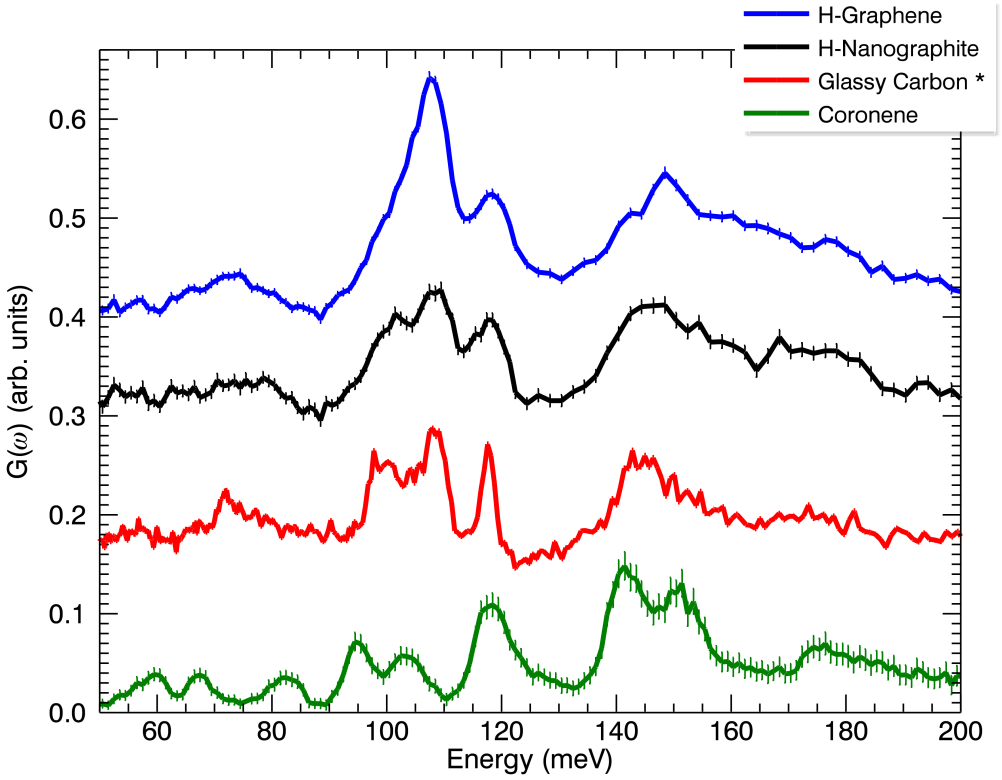

FIGURE 5.5: From top to bottom: GDOS of H-graphene (H-TEGO, in blue), H-nanographite (H-BMG, in black), glassy carbon (GC in red) and Coronene (in green). The GC spectrum was measured on TOSCA [171] and was downloaded from the INS TOSCA database [172].

An improved resolution version of the H-TEGO GDOS was obtained with the use of the graphite analyzers on IN1–Lagrange, which is shown on Fig 5.6 in an extended energy range, up to the C–H stretching modes, whose band is centered around 390 meV.

Coronene (see Fig. 5.9 is a polycyclic aromatic hydrocarbon (PAH[4]) comprising six peri-fused benzene rings, with chemical formula $C_{24}H_{12}$. Coronene is often thought as a the

[4]PAHs are hydrocarbons - organic compounds containing only carbon and hydrogen - that are composed of multiple aromatic rings.

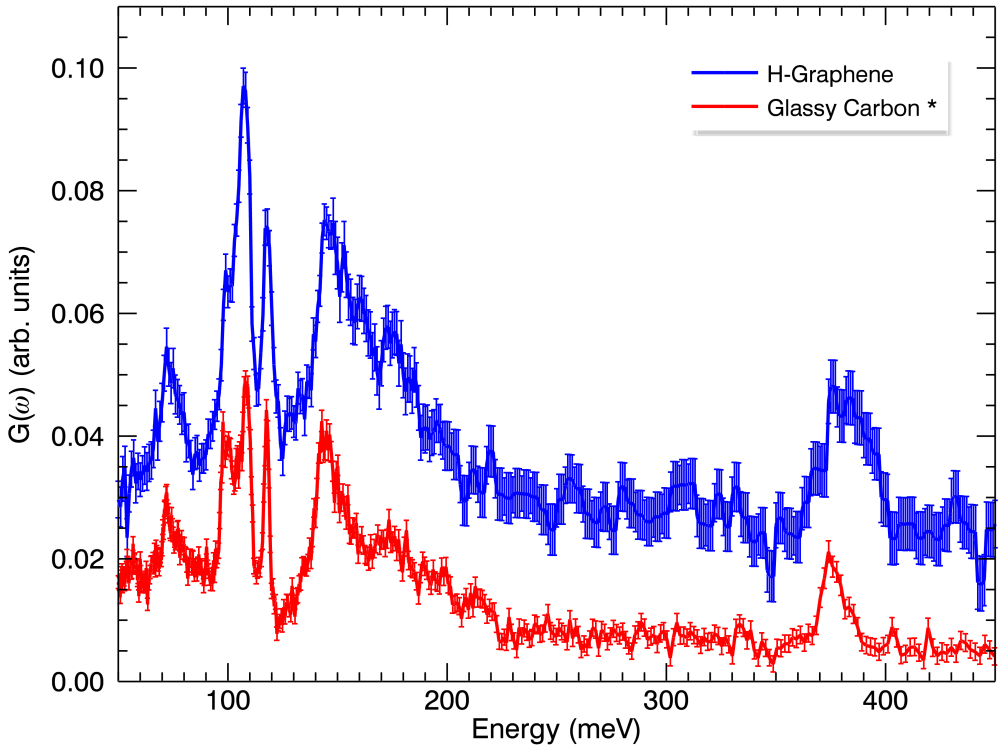

FIGURE 5.6: Inelastic neutron spectra obtained on Lagrange at 10 K on hydrogenated TEGO compared to that of GC measured on TOSCA (ISIS), taken from [171].

smallest model for graphene with H atoms bonded to C at the external edges and lying along the carbon plane, as expected for Csp^2-H bonds. Glassy carbon is a form of carbon made by heating an aromatic polymer, generally a phenolic resole or a furfurylic resin to high temperature in an inert atmosphere [173, 174]. Glassy carbon is an example of a non-graphitizing carbon: a carbon that cannot be transformed into crystalline graphite even at temperatures ≥ 3000 . Its disordered structure is known to contain mostly sp^2 carbon atoms, similar to graphite but with much smaller sheets, *and edges terminated by H atoms* [171].

All the spectra shown in Fig. 5.5 display strong similarities: they all present three groups of complex bands separated by minima located around 87 and 130 meV. In particular, the band between 90 and 130 meV (further referred to as the C–H out of plane bending region) is composed of several individual components. The other components of this band vary in position and in relative intensity from one sample to another. The high frequency band (further referred to as the C–H in plane bending region[5]) shows

[5]These denominations follow from the description of the eigenmodes calculated on the coronene molecule

an asymmetric profile, with a rather sharp low frequency side and a smoother decay at high frequency.
The coronene GDOS spectrum shows slight differences with regards to that of the other compounds. It possesses a much pronounced molecular character, with significantly more symmetric features, all being rather well separated in the GDOS spectrum, *i.e.* reflecting the increase symmetry of the molecule.
By contrast, disregarding the differences in resolution, the glassy carbon GDOS is surprisingly similar to that of the H-BMG GDOS: the C–H out-of-plane bending range is composed of 4 main components, with a maximum located at $\sim$ 108 meV, the latter intensity being slightly larger than that of the maximum intensity observed in the C–H in-plane bending range located at $\sim$ 150 meV. This suggests that the local environment of the H atoms is the same in both samples, *i.e.* reflecting the signature of the C–H bonds at the edge of the graphitic planes. This will further be confirmed by our simulations.
When compared to the latter discussed GDOS, the H-TEGO profile in the out-of-plane bending region shows a significantly increase of intensity at $\sim$ 108 meV. If one makes the assumption that the H-TEGO GDOS is composed of the GDOS originating from C–H bonds at the edge of the graphitic planes AND from C–H bonds located ON the graphitic plane, *i.e.* at the on-plane defects, then the sole contribution of the defects can be isolated by subtracting a certain quantity of the H-BMG spectrum to the H-TEGO spectrum. The difference curve is shown in Fig. 5.7. It features a well defined peaks at $\sim$ 108 meV with a broader tail around 118 meV. This feature stands as the spectral signature of the C–H bonds located at the surface of the graphene sheet.

5.2 Modeling and Simulations

For an accurate attribution of the experimental features discussed above, we have simulated the H-DOS for a large set of possible H-configurations at a graphene surface, including in-plane defects, which are expected to give intense contributions in the H-TEGO GDOS. Our interest here, is not so much to give a detailed description of each specific mode but identify the spectral signatures of each configurations to help characterizing the H local environment specific to the observed features.

Several theoretical studies have been published on the H-graphene system, especially with the aim of investigating its electronic behavior. A large majority of them consider the guest H as an *adatom*, namely an additional atom located above the graphene surface and bonded covalently to a carbon atom, breaking the local aromaticity of the carbon framework, *i.e.* forming a C-H sigma bond with the π electron of the C atom.

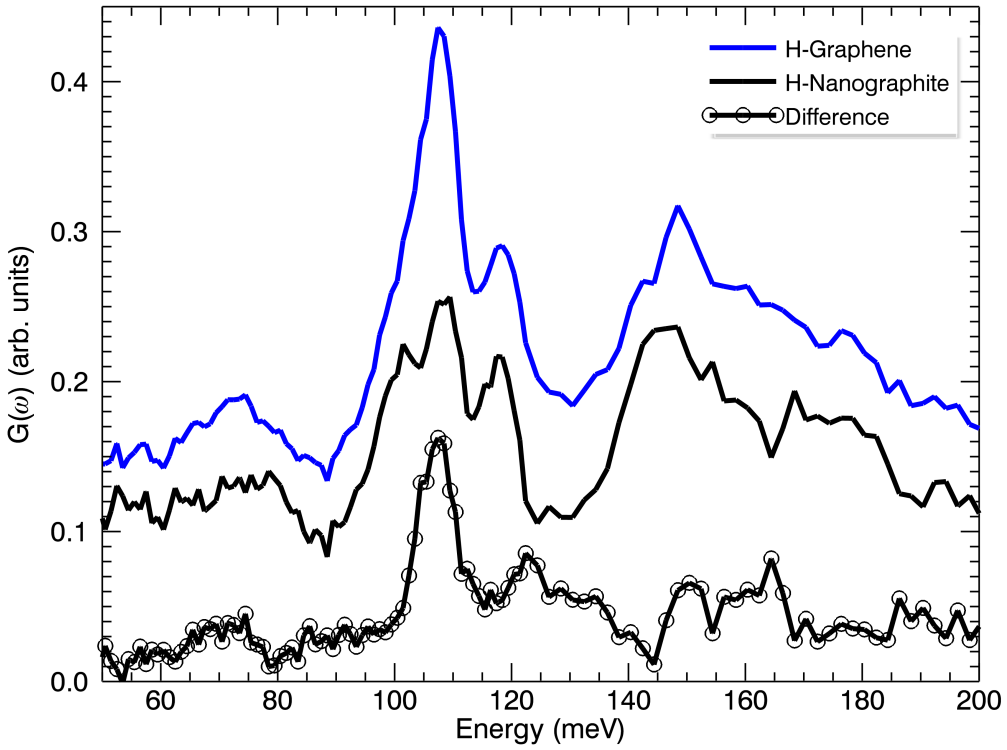

FIGURE 5.7: Difference spectrum between H-TEGO and H-nanographite from data measured on IN1–BeF. It highlights the excess of intensity at 108 meV.

A large number of papers have been published on the physicochemical properties of the hydrogen atoms bonded to the graphene surface. They concern both the thermodynamic stability properties, structure, diffusion and electronic properties of these systems composed of single H atoms, dimers or small cluster of adatoms [51, 52, 175, 176]. The Graphane 2D crystal (a completely hydrogenated graphene) has also been extensively investigated theoretically [41]. The quantity of experimental and theoretical investigations which consider explicitly hydrogen atoms located at in-plane defects, like carbon vacancy [177], is much less important. The presence of hydrogenated vacancies in TEGO cannot be disregarded, since the exfoliation of graphite oxide leads inevitably to the formation of in-plane voids, presumably rich in dangling bonds. Most likely, these radicals may be then partially or completely saturated by atomic hydrogen, by dissociation of the H_2 molecules occurring during the treatment in H_2 flux at high temperature. We have therefore incorporated different carbon atom vacancies saturated by hydrogen atoms inside our graphene models and calculated the resulting H partial density of states. We therefore created a catalogue allowing to classify the C-H bond type and local environment according to its vibrational spectrum.

A large set of hydrogen configurations at the graphene surface were accounted: from single H adatom to larger aggregates, from one Single carbon Atom Vacancy (SAV) to large in-plane voids. We have also considered the response of C-H at the external edges and tested our procedure on well-know (from experiments and literature data), Polycyclic Aromatic Hydrocarbon (PAHs), like coronene and corannulene molecules.

The partial Hydrogen Density of States (H-pDOS) was calculated for each different configuration as the Time Fourier Transform of the Velocity Auto-Correlation Function (VACF), computed from the MD *ab-initio* trajectories using the nMoldyn software (see Chap. 3). Simulations were carried out in the NVT ensemble on a graphene supercell of dimensions 14.76 (19.68) $\times$ 14.76 (19.68) $\times$ 34 Å^3 (6 or 8 periodic lengths along the basal lattice vectors $\vec{a}$ and $\vec{b}$, in order to avoid possible interactions between neighbour images), decorated with chemisorbed hydrogen atoms located at different position and in different configurations. Periodic boundary conditions were applied in the $\vec{a}$ and $\vec{b}$ directions in order to simulate a plane of extended dimension. The vacuum thickness along the $\vec{c}$ axis (out-of-plane direction) was set to 17 Å, to avoid any possible interaction with neighbour images [178].
In a first step, the input structures were relaxed until residual Hellmann-Feynman forces reach 10^{-3} eV/ Å per atom or lower. Sampling of the configuration space was carried out at temperatures between 280 and 320 K (nominal value set at 300 K), during 10 ps long trajectories. We have checked that larger supercells give the same results as those derived from the supercells described in the next section, as well as longer/shorter trajectories (20/5 ps) and lower temperatures (150 K). The above described simulation conditions allowed a good compromise between computational cost and accuracy in the energy domain of interest.

The as-obtained density of states were then convoluted with a gaussian function with varying width to account for the energy dependent instrumental resolution of the neutron spectrometers.

5.2.1 C-H at the external edges

In this section, we are interested in the signature of the C-H bonds located at the edge of the graphene plane, *i.e.* for which H are bonded to C atoms located at the external border of the plane.
We have started our numerical investigations by considering the coronene molecule $C_{24}H_{12}$, which represents the simplest one-layer graphene model with H bonded at the

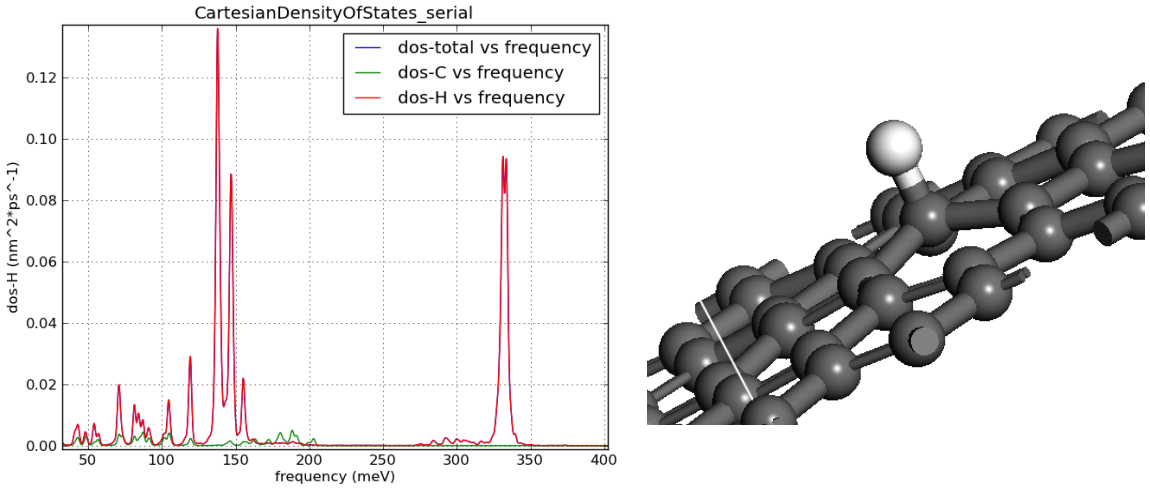

FIGURE 5.8: *Left:* Different component (coherent and incoherent) in the DOS of a H-Adatom. Energy resolution of 2%. *Right:* Image of a H-adatom. H is bonded to the C atom at the surface. The result of the broken aromaticity of the lattice is that the adjacent C is pushed up of 0.89 Å out of the plane.

C of external edges (see Fig. 5.9) and the corannulene molecule which incorporates a pentagonal ring at the center of its structure, creating a curvature (see Fig. 5.10).

Coronene has a delocalized aromatic structure, resembling a fragment of a graphite layer, with six fold symmetry, terminated with H atoms. The 12 hydrogen atoms passivate the terminal dangling bonds of the C_{24} cluster. As they are well separated from the central ring, they represent the smallest graphene-like structure with H bonded at the external edges.

Coronene displays 102 fundamental internal modes. Among them, one finds:

- Out-of-plane bending and torsional modes of the coronene ring in the energy range 90-300 cm^{-1}. These modes involve displacements of the edge carbon atoms, the latter following the global shape fluctuations of the carbon flake. We refer to these modes as the *H riding modes*.
- In-plane C-C stretching and breathing modes of the coronene rings at 1000, 1230, 1400, 1450, 1600 cm^{-1}. These are equivalent to the surface modes of a graphite layer.
- C-H bending modes: out-of-plane bending modes in the 980-1020 cm^{-1} range, and in-plane bending modes in the 1100- 1700 cm^{-1} range.

The Corannulene molecule is a bowl shaped polycyclic aromatic hydrocarbon (PAH) with chemical formula $C_{20}H_{10}$ (see Fig. 5.10). Its consists of a cyclopentane ring fused

with 5 benzene rings. The introduction of the central pentagon induces the curvature and the whole molecule is puckered in the shape of a cap so-called bucky bowl. The vibrational spectrum of this molecule has been investigated both from the experimental and theoretical point of view [179].

Our simulations were performed by considering one molecule inside a cubic box with lateral side of 20 Å and with periodic boundary conditions.
The GDOS extracted from the INS measurements and from the MD simulations are presented in Fig. 5.9 for the coronene and Fig. 5.10 for the corannulene molecules. The theoretical GDOS is found to be in excellent agreement with the data [6], both in the position of the principal features, and in their relative intensity. This very good match validates our numerical procedure that we use in the next sections of this chapter.

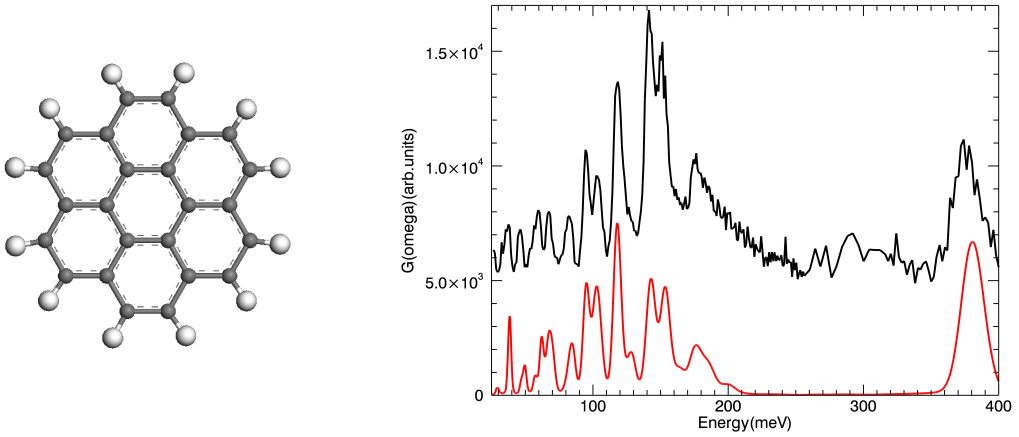

FIGURE 5.9: *Left:* The coronene molecule $C_{24}H_{12}$. *Right:* The Generalized density of states of coronene: experimental data collected on IN1BeF at 13 K on a coronene powder (black) and simulated H-pDOS (red).

Effect of increasing the fragment's dimensions

Polycyclic Aromatic (PAHs) structures of the type $C_{6n^2}H_{6n}$, with n increasing from 2 [7] to 4 have been considered as atomic models for graphene fragments with variable size, *i.e.* characterized by lateral dimensions of increasing extension [180]. The increase of the PAH molecules from $C_{24}H_{12}$ (n=2) to $C_{96}H_{24}$ (n=4) leads to a progressive evolution from a typical molecular spectrum, characterized by well-defined symmetric peaks to a

[6] and with the GDOS derived from simulations carried out on corannulene in the crystalline form, using *ab-initio* phonon calculation with the direct method approach (see [179]).
[7] n=2 corresponds to a coronene molecule

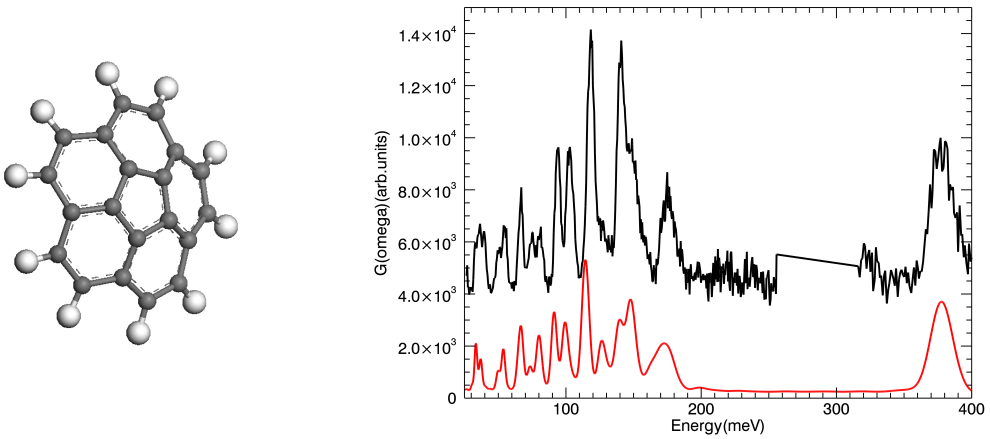

FIGURE 5.10: *Left:* The corannulene molecule $C_{20}H_{10}$. *Right:* The Generalized density of states of corannulene: experimental data collected on IN1BeF at 13 K on a corannulene powder (black) and simulated H-pDOS (red).

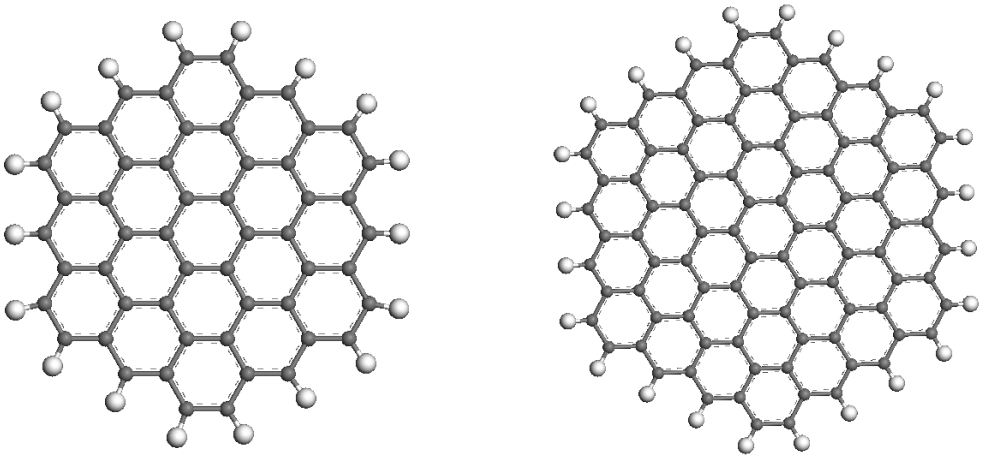

FIGURE 5.11: *Left:* The molecule of $C_{54}H_{18}$. It corresponds to a coronene molecule with an additional chain ring of C atoms. *Right:* The molecule of $C_{96}H_{24}$. It corresponds to a coronene molecule with two additional chain rings of C atoms.

spectrum presenting a more complex profiles with bands, sometimes asymmetric, separated by gaps. In particular, the gaps observed in the simulated spectra of $C_{54}H_{18}$ and $C_{96}H_{24}$ appear at $\sim$ 85 and 125 meV, *i.e.* in good correspondence with those observed in the experimental GDOS of H-TEGO, H-BMG and CG (see Fig. 5.5). It is tempting to associate the evolution of the spectra to an increased lattice-like character of the bending modes originating from the six lateral edges (of zig–zag type) of the fragments. The problem is equivalent to solving the dynamical problem of 6 coupled linear chains of limited extend. Limiting the extension implies folding the dispersions curves of the

infinite chain at many places in the 1D Brillouin zone, *i.e.* creating VHS in the GDOS. The coupling between the chains creates gaps in the dispersion scheme.

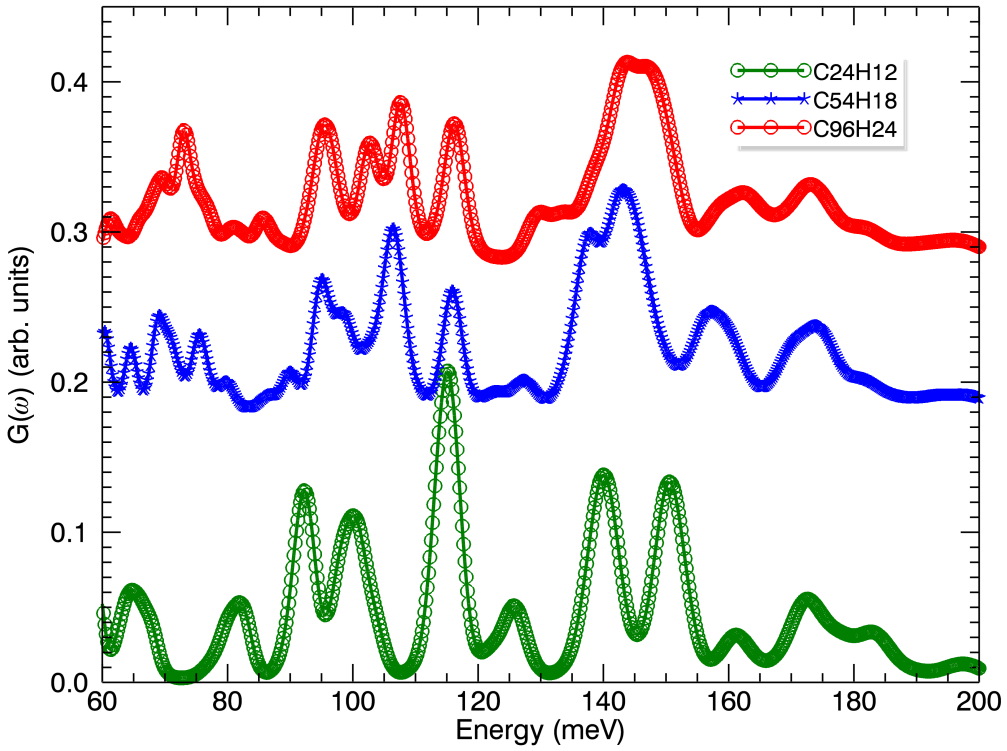

FIGURE 5.12: H-pDOS of $C_{6n^2}H_{6n}$ fragments with n=2 (green), 3 (blue) and 4 (red). The case n=2 corresponds to the coronene molecule.

It is noteworthy to note that we have mostly considered edges of zig–zag type, the molecular fragment $C_{6n^2}H_{6n}$ considered here being zig–zag terminated. On an experimental point of view, the zigzag edges have exhibited a greater stability compared to the armchair edges [181]. The H-pDOS of a PAH model molecule delimited by 6 armchair segments (as the $C_{42}H_{18}$ shown in Fig. 5.13, further referred below as the *armchair model*) are very similar to the previous spectra discussed. The gap at 85 meV is however not observed in the armchair model, as shown in Fig. 5.13. The latter observation, in contrast with the experimental GDOS, gives further weight to the hypothesis of the presence of a majority of zig-zag type of graphene edges in our BMG and TEGO samples.

5.2.2 In plane C–H

Hydrogen-graphene systems were modeled as trigonal graphene supercells decorated with chemisorbed hydrogen atoms located at different position and in different configurations.

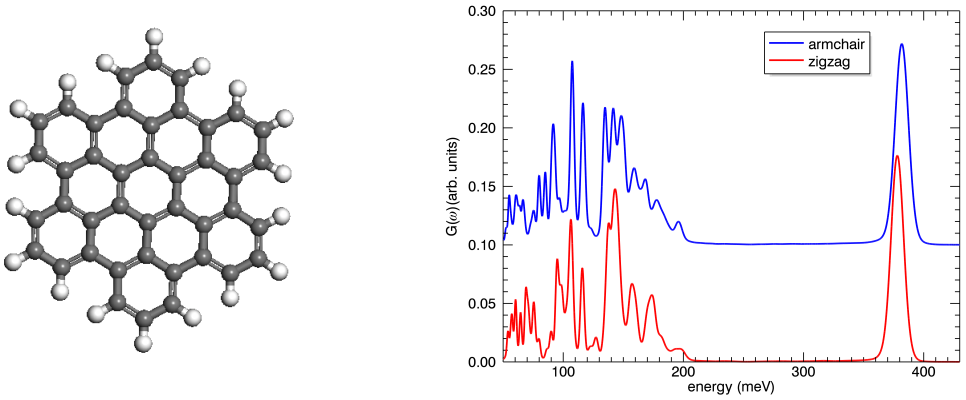

FIGURE 5.13: *Left:* A molecular fragment with a majority of C-H bonds at armchair types of edges. *Right:* The corresponding H-pDOS

We have considered two chemical scenarios for the in–plane C-H bond:

- Csp^3-H bonds: the H atom bonded onto the graphene plane changes the hybridization of its adjacent C atom from sp^2 to sp^3 and creates the covalent C–H bond.
- Csp^2-H bonds: the H atom saturates a dangling bonds at in-plane defects.

Some representations of the most significant models are illustrated in Fig. 5.14, 5.15 and 5.16.

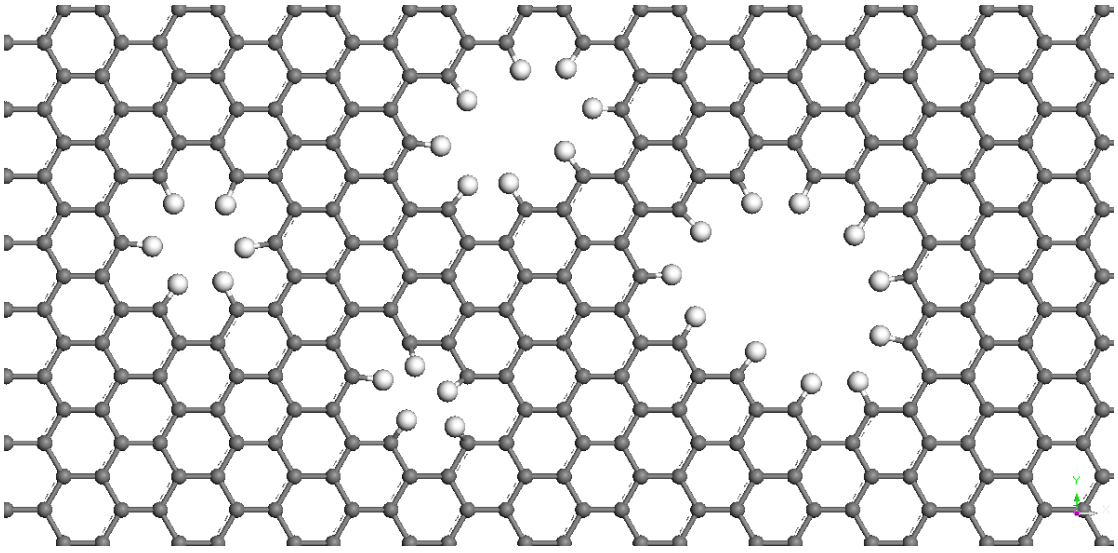

FIGURE 5.14: In-plane defects: Extended inner voids.

We have systematically considered H-saturated in-plane defects (Csp^2-H type), from a Single (carbon) Atom Vacancy (SAV) to larger inner voids at the graphitic plane (up to

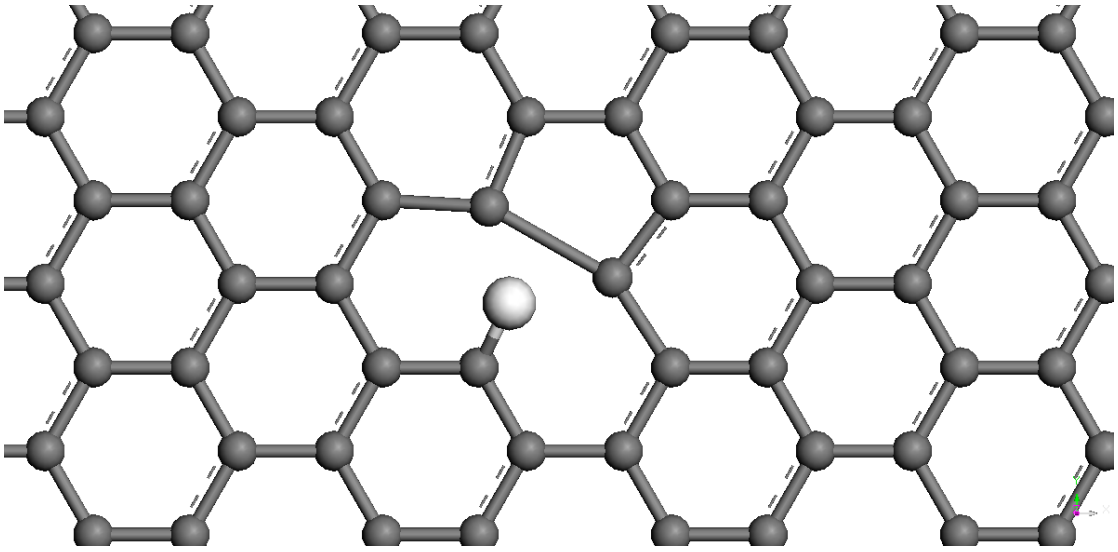

FIGURE 5.15: In-plane defects: Single Atom Vacancy.

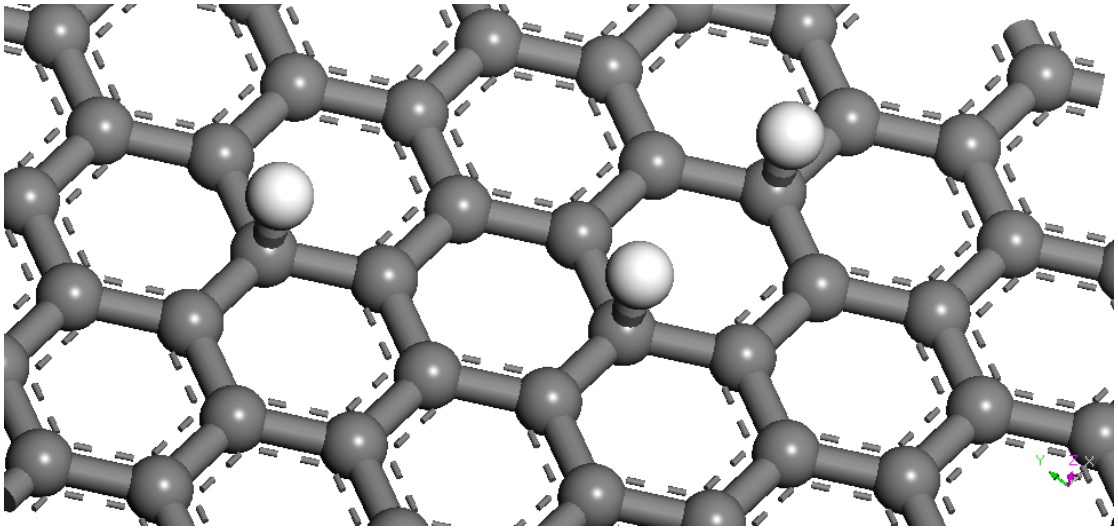

FIGURE 5.16: Adatom-like structures: Single atom and para-dimer. The structures imaged here were not allowed to fully relax: H forms a covalent bond with the π C orbital. This full sp^2 to sp^3 re-hybridization for the bonding C leads to the breakage of the local aromaticity of the plane and to a subsequent out-of-plane pulling out of the bond.

16 Å in diameter).
We have also simulated a large number of Csp^3-H configurations: single ad-atom, cis-dimers in para and ortho positions (with H adsorbed only on one side of the graphene sheet), trans-dimers in para and ortho positions (with H adsorbed on both sides of the graphene sheet in an alternated way), small clusters as cis (8) and trans (9) hexamers [176]. We also simulated the graphane lattice in both the boat and chair conformers [41].
Other models, *e.g.* with CH_2 group at an in-plane vacancy [84], *i.e.* in-plane voids in a double hydrogenated state have been simulated as well.

In the Table 5.17 we have reported a short summary of the most significative models considered for simulations in this work.

In the following subsections, the simulated partial H-DOS for each H-graphene configuration is reported and discussed in detail.

Adatom-like structures: H onto the plane with Csp^3-H bond: In Fig. 5.14, the H-DOS for some Csp^3-H configurations, from a single adatom to larger clusters obtained by increasing the dimensions of the H aggregates onto the graphene plane, are reported. The H-pDOS are rather similar from one model to another: they display predominant C-H bending components in an energy range above 138 meV, peaked around 140 meV/ 150 meV. The C-H stretching band is found around 370 meV.

Other configurations (like ortho- and meta-, cis- and trans- dimers and small 6-H clusters) have been simulated as well. They are not reported for clarity in the plot: the H-pDOS features very similar vibrational bands, located at the same the energy region (140-160 meV for the bending modes and 360-375 meV for the stretching modes).

In-plane defects: H at inner voids with Csp^2-H bond: Carbon vacancies at the graphene planes, created during the thermal exfoliation, are expected to be present in the TEGO sample. In the following, we report the H-pDOS of several H saturated graphene in-plane voids. These in-plane defects have been built by removing a certain number n of carbon atoms and saturating the residual dangling bonds with H atoms. These defects will be referred to nAV, n providing an indication of the hole extension. For $n = 1$, 2 or 3, the models are also referred to as SAV (Single Atom Vacancy), DAV (Double Atom Vacancy) and TAV (Triple Atom Vacancy).

Small nAV: The extraction of one carbon atom from the graphene plane creates a vacancy (Single Atom Vacancy) and leaves three σ dangling bonds and one unpaired π

Name	C–H bond	Description and Reference
EDGES		
Coronene	Csp^2-H	- 5.9
Corannulene	Csp^2-H	- 5.10
$C_{54}H_{18}$	Csp^2-H	zig–zag edges - 5.11
$C_{96}H_{24}$	Csp^2-H	zig–zag edges - 5.11
$C_{42}H_{18}$	Csp^2-H	armchair edges - 5.13
Small nAV		
SAV (VH)	Csp^2-H	One H atom saturating one dangling bond in a carbon vacancy 5.15
anti VH2	Csp^2-H	Two H atoms saturating two dangling bond in a carbon vacancy [177]
anti VH3	Csp^2-H	Fully saturated carbon vacancy [177]
DAV	Csp^2-H	Fully saturated di-carbon vacancy 5.15
TAV	Csp^2-H	Fully saturated tri-carbon vacancy 5.14
LARGE nAV		
"coronene"-like void	Csp^2-H	Fully saturated void (diameter 5 Å) 5.14
"ovalene"-like void	Csp^2-H	Fully saturated void (diameter 7 Å) 5.14
"big" void	Csp^2-H	Fully saturated void (diameter 12 Å) 5.14
"bigger" void	Csp^2-H	Fully saturated void (diameter 16 Å)
AD–ATOMS		
adatom	Csp^3-H	Single H atom bonded to a C onto the plane 5.16
dimer	Csp^3-H	Two H atoms bonded to C onto the plane (in para, ortho or meta positions) 5.16
cluster	Csp^3-H	Small cluster onto the plane (6 H atoms) [176]
graphane	Csp^3-H	Graphane lattice (chair and boat conformers) [41]
Double H SAV (VH2)	Csp^3-H	Two H atom saturating one dangling bond in a carbon vacancy (Double hydrogenation at the apical C) [84]
Double H "coronene"-like void	Csp^3-H	Fully saturated void (diameter 5 Å) with double hydrogenation 5.15

FIGURE 5.17: Summary of the models considered for simulations

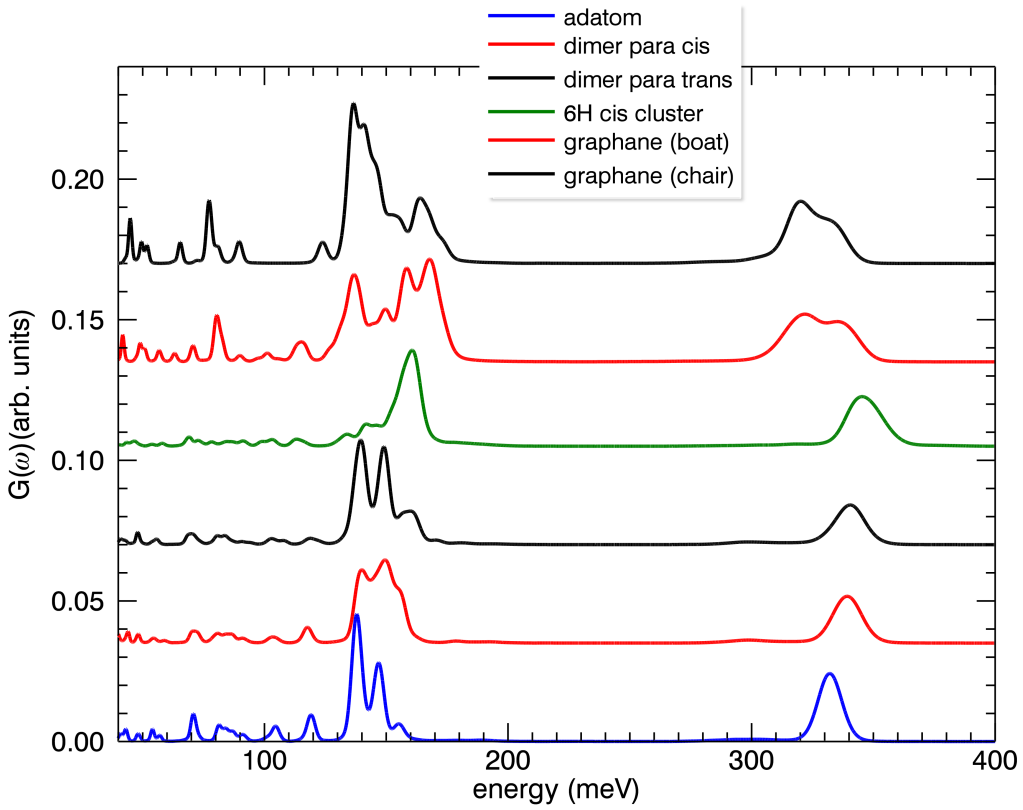

FIGURE 5.18: HDOS of different ad-atom configurations.

electron on the lattice. The σ electrons are tightly localized on the nearest C neighbours of the vacant one, while the π electron is delocalized on one of the two sub-lattices as a consequence of its the aromatic character. Therefore the vacancy (SAV) is threefold symmetric in a degenerate electronic state and undergoes a Jahn-Teller (JT) distortion, where two of the three carbon atoms above close up a pentagon by forming a weak C-C bond. There are three identical possibilities which differ in the carbon atom opposing the pentagon (apical carbon atom). The hydrogen atom binds to this apical carbon where much of the unpaired electron density resides, and forms a strong covalent bond (completely consistent with the typical value for the C–H binding energy, which is 4 eV). The carbon atom moves slightly out of the plane and correspondingly the C-H bond gets tilted, being the latter deformed with respect to a typical Csp^2-H bond. The adsorption of hydrogen atoms onto a carbon atom vacancy was investigated by first principles calculations, from the mono-hydrogenated up to the fully hydrogenated state, where six H atoms covalently bond to the vacancy. Their phase diagram shows that the most stable hydrogenated species are triply- and singly-hydrogenated species [177]. The single hydrogenation state of SAV was already observed in TEGO by μ SR spectroscopy, which evidenced the formation of CHMu (analogous to CH_2) groups at SAV [84].

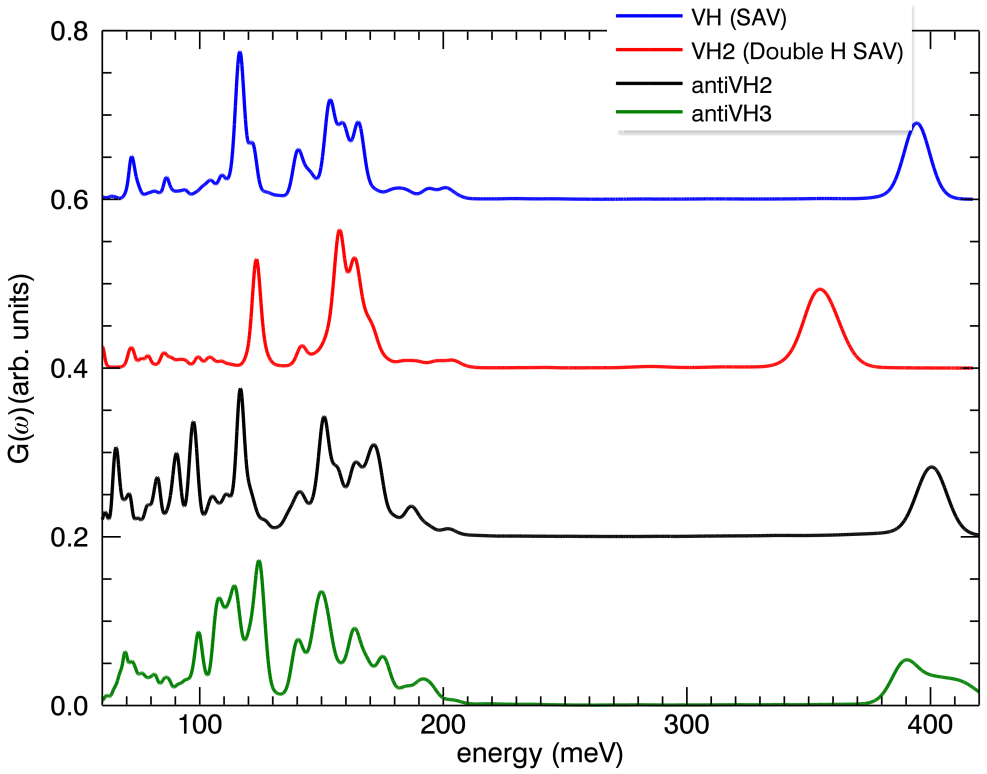

FIGURE 5.19: HDOS of different $SAVH_n$ configurations

The SAV H-pDOS, for different hydrogenation states, is shown in Fig. 5.19. Singly-hydrogenated SAV gives rise to a predominant C–H bending peak at 118 meV. The double-hydrogenation (CH_2 group bonded to the apical C in SAV) leads to a full sp^2-sp^3 re-hybridization of C valence orbitals. As a consequence the predominant features are shifted towards slightly higher energies, as observed for Csp^3-H bonds.

Large nAV We have studied the modifications induced on the H-pDOS upon increasing the dimension of the voids. In small voids (diameter below 5 Å) the C–H bonds keep (partially) their tilted out-of-plane character. This preserves the vibrational peak at 118 meV and contributes to the progressive emergency of another important vibrational line located at 108 meV, which is the main component for a 5 Å ("coronene"-like) and 7 Å ("ovalene"-like) diameter voids (see Fig. 5.22).

Larger voids, with diameter $\geq$ 12 Å , have an INS response more spread out and quite similar to the external edges' one. We have limited our simulations to voids of 20 Å in diameter (not shown), for computational cost reasons, which have indeed confirmed

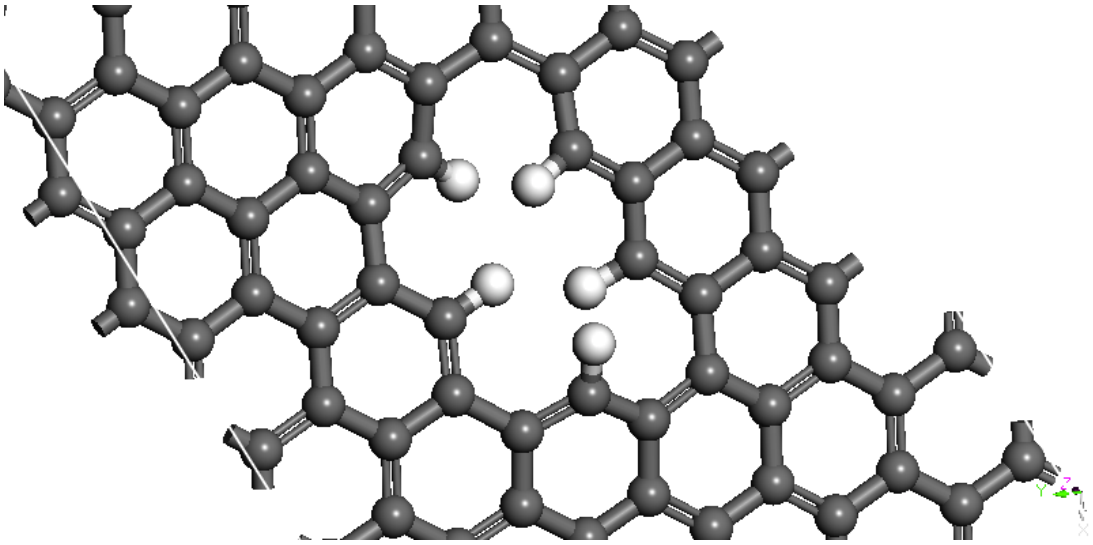

FIGURE 5.20: Image of a TAV in fully hydrogenated state.

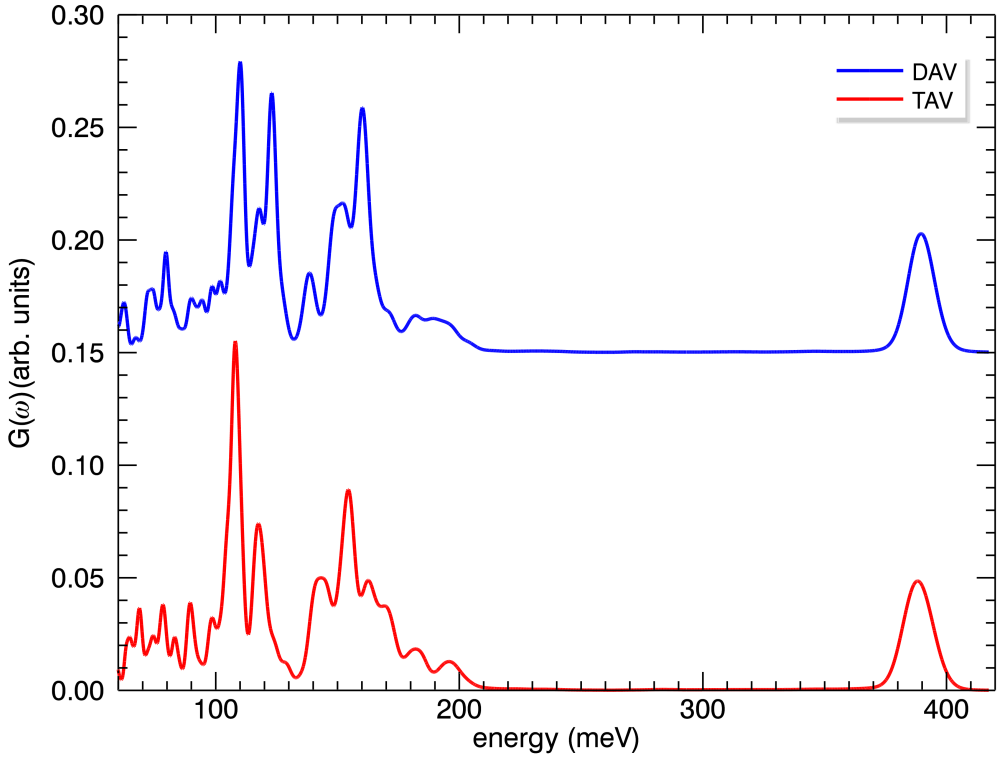

FIGURE 5.21: H-pDOS of DAV and TAV voids.

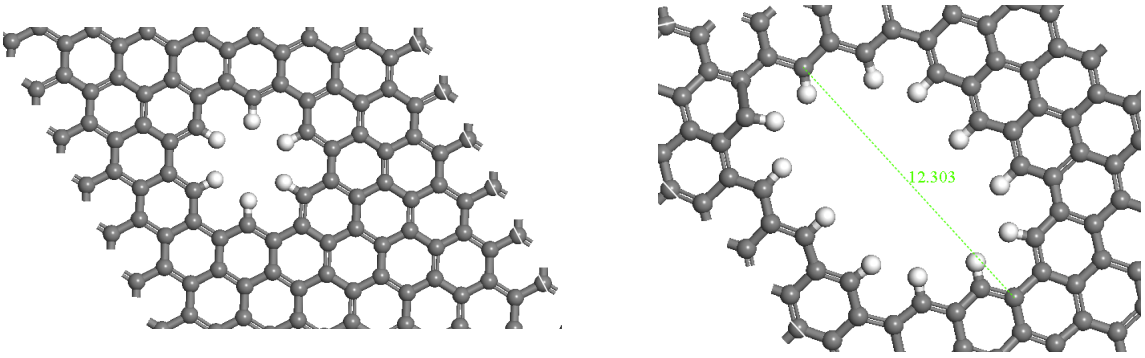

FIGURE 5.22: *Left:* Image of a coronene-like hole of 5 Å in diameter. *Right:* Image of a big hole of 12 Å in diameter.

this trend. Nano-sized and even larger carbon vacancies at the graphene planes, most likely created by the evaporation of chemical groups during the exfoliation process, are expected to fully behave as external edges [182].

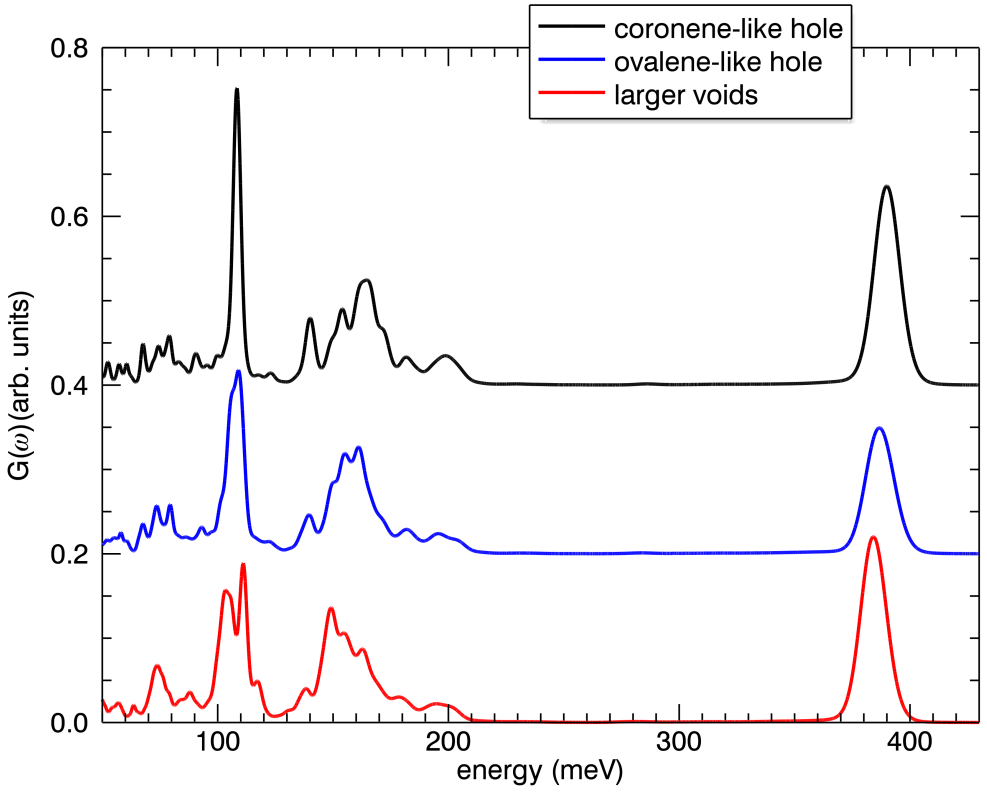

FIGURE 5.23: HDOS of voids of increasing diameter.

Finally, we would like to conclude this overview by showing the effect of the double hydrogenation on the vibrational properties of in-plane defects. In Fig. 5.24, the H-DOS

for a doubly-hydrogenated coronene-like voids is reported. Once again, due to the full sp^2-sp^3 re-hybridization, the peculiar vibrational lines appears slightly shifted towards higher frequencies.

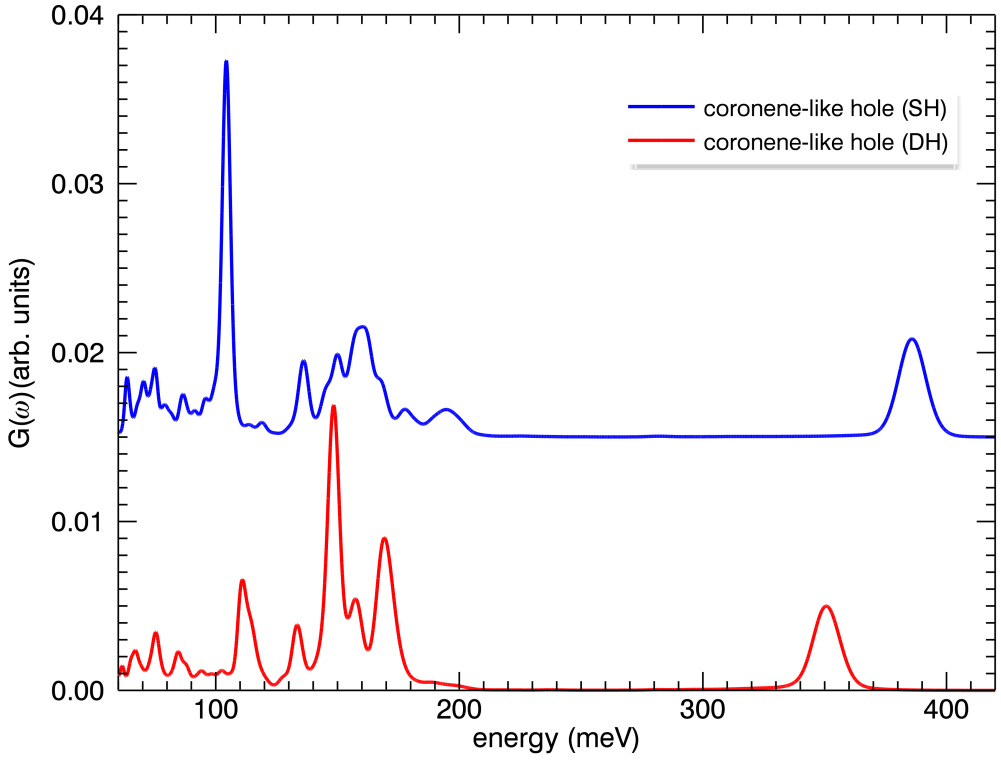

FIGURE 5.24: HDOS of coronene-like voids with single-hydrogenation compared to the same voids with double-hydrogenation.

5.3 C-H modes attribution

We already discussed in the previous sections the strong similarities between the INS spectra of H-Graphene, H-nanographite, Coronene and Glassy Carbon, especially concerning the position in frequency of the peaks. These can be attributed to common dynamical features, most likely to H bonded at the external edges. The overall profile of the $C_{96}H_{24}$ simulated GDOS, can actually account for most of the characteristic features observed in the H-nanographite (H-BMG) spectrum. This observation suggests that H atoms are essentially located at the edges of the nano–domain and that a single H saturation per edge C atoms occurs (Fig. 5.25).

However, the simulations of H at the external edges fail to reproduce the peculiar features of the H-TEGO, *e.g.* the dominant peak at 108 meV highlighted in Fig. 5.26 showing the

difference between the H-TEGO GDOS and the H-BMG GDOS. The extra dynamical features in H-TEGO, which appear as an over-intensity located in particular at the 108 meV band, have to be attributed to H covalently bonded to in-plane defects.

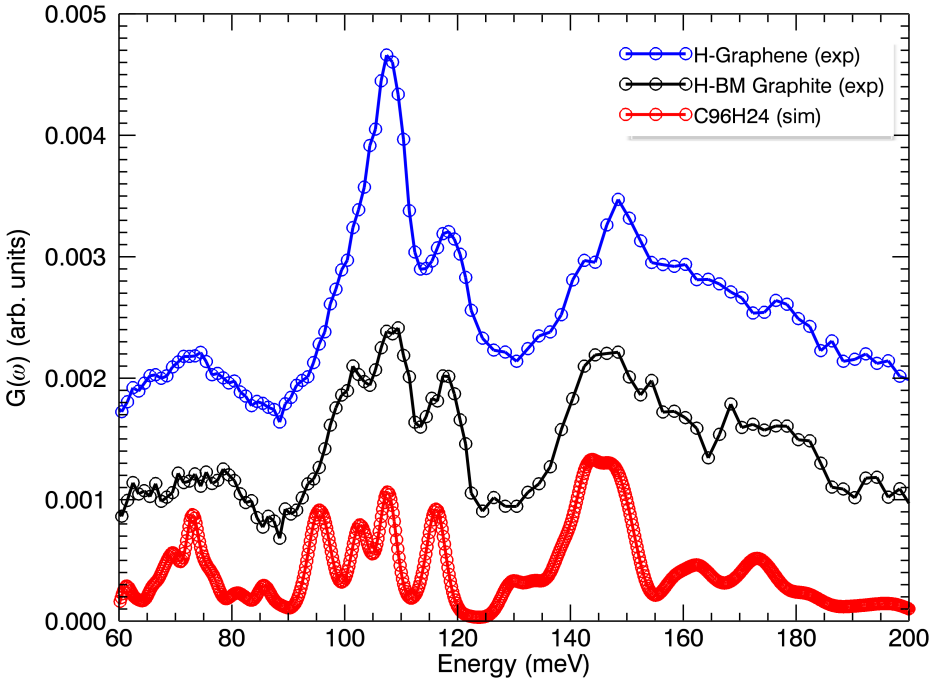

FIGURE 5.25: C–H modes attribution: contribution from C-H edges.

We have considered several linear combinations of the simulated H-pDOS in order to assign the vibrational features to specific C–H configurations and get the best agreement with the experimental data:

$$G_s(\omega) = \sum_k C_k G_k(\omega) \tag{5.2}$$

C_k therefore gives the proportion of local environment of type k present in the sample. The best agreement is obtained by considering mostly Csp^2-H configurations, in which H is located at the external edges, at the borders of in-plane voids onto the plane in the proportion of 47% (external edges) + 33% (large nAV - 5Å diameter void) + 20% (small nAV - SAV), respectively. The results are shown in Fig. 5.26 and Fig. 5.27.
nAV are in-plane defects are well expected in chemically produced graphene. They reliably play an active role in dissociating the hydrogen molecule and be easily saturated during the hydrogenation process. On the dynamical point of view, these simulated

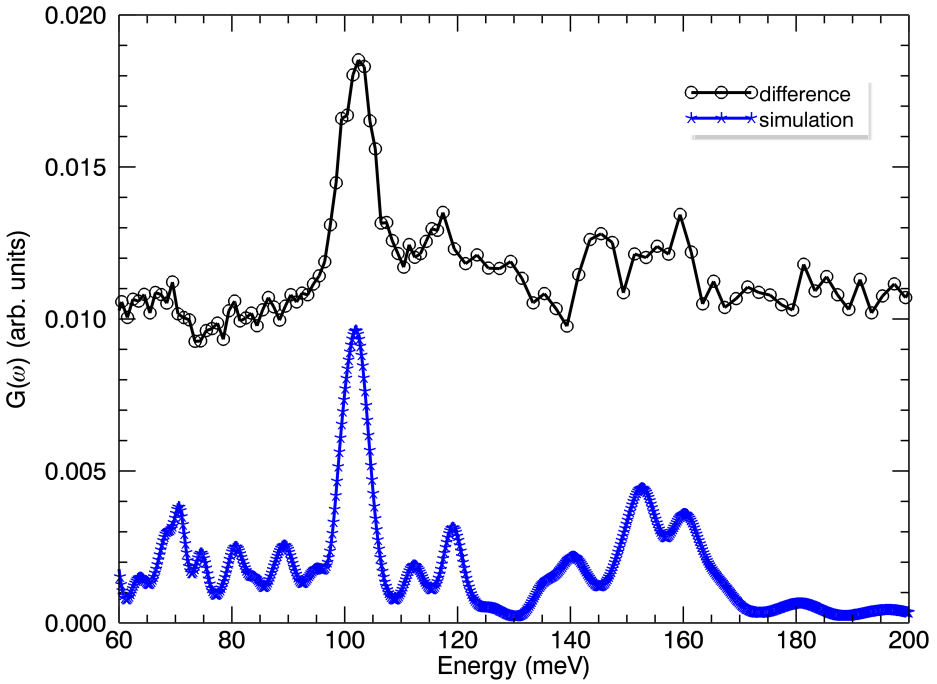

FIGURE 5.26: C–H modes attribution: contribution from C–H at in-plane voids. In black the difference spectrum between H-TEGO and H-nanographite is reported. It highlights the dynamical features peculiar of H-TEGO. The attribution has been done on the basis of *ab-initio* simulated H-DOS, carried out for several H-graphene configurations.

Csp^2-H configurations present C–H bending and stretching modes which match reasonably well the experimental features (within the energy region of interest), providing predominant features in GDOS at 108 meV and 118 meV, where the peculiar excess of intensity in H-TEGO is observed.

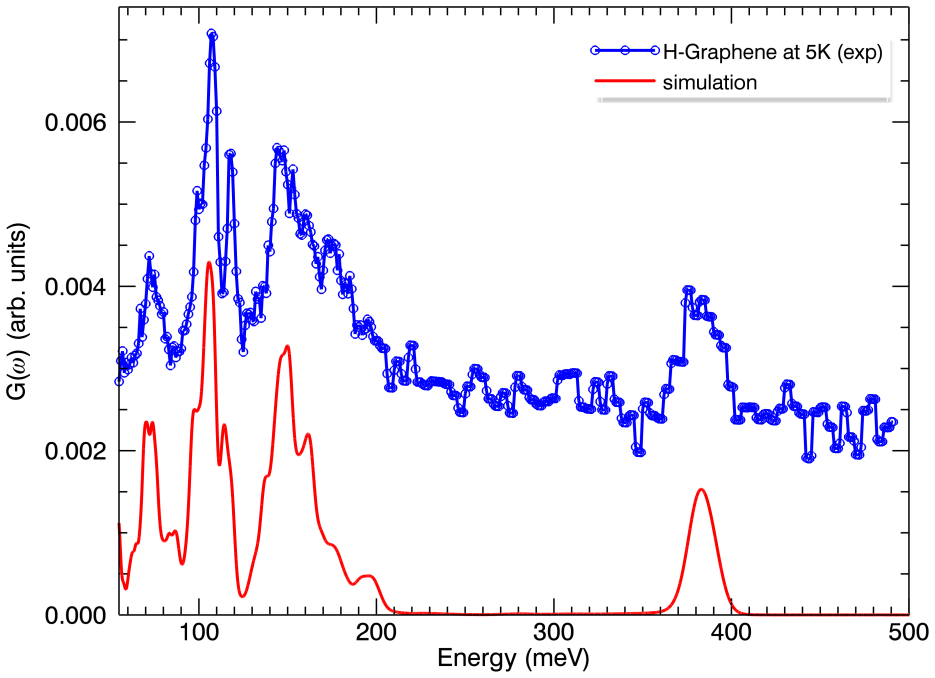

FIGURE 5.27: Attribution: contribution from C-H edges and at in-plane voids (global view)

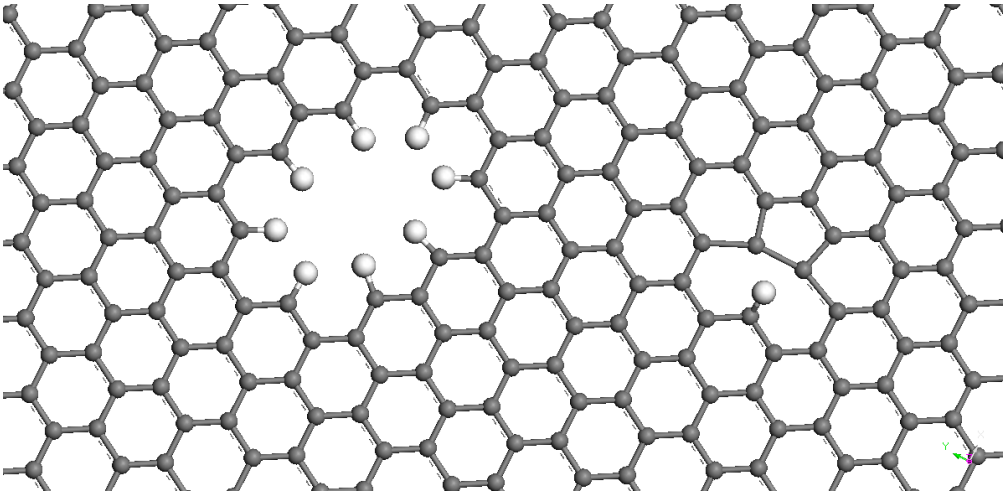

FIGURE 5.28: Hydrogenated in-plane defects in H-TEGO

5.4 Partial Conclusions

The partial conclusions of this chapter are:

- The clear increase of H chemisorbed in H-TEGO samples, as derived from the INS measurements, witnesses the effectiveness of chemically produced graphene to dissociate the H_2 molecules and induce C-H bonds. This probably arises from the presence of defects, such as (unsaturated) carbon vacancies and edges.
- The H-TEGO and H-BMG GDOS spectra shares strong similarities with those of polycyclic aromatic hydrocarbons.
- The H-BMG features have been attributed to H bonded at the external edges.
- The peculiar features in H-TEGO have been labeled on the basis of *ab-initio* simulations. They prove the presence of a large proportion of H covalently bonded on carbon atoms located inside small in–plane defects (diameter inferior to 12 Å).

Chapter 6

Evolution of the INS spectrum of Hydrogenated Graphene with temperature: a signature of atomic H diffusion?

In 2011, Prof. M. Riccó and co-authors, in the framework of the thesis work of Dr. Marcello Mazzani, a former PhD student in the Carbon Nanostructures Laboratory Group (University of Parma) [83], reported the first muon spectroscopy (μSR) investigation of chemically produced graphene. μSR is a very sensitive tool for probing local magnetic fields in condensed matter and, in low electron density materials as organic systems, allows to investigating the hydrogen state in the sample. The idea of employing μSR in the study of TEGO emerged from still open and well-debated questions regarding the possible onset of magnetism in graphene on one hand and its atomic interactions with hydrogen on the other hand. These questions are critical in the prospect of engineering new platform graphene technologies. As in the case of neutron spectroscopy, the gram-scale availability of the samples was appropriate to the large penetration depth of muons, which can easily reach ≈ 0.5 mm. In a μSR experiment, polarized positive muons are implanted into the sample and their spins start to precess. Muons decay rapidly into positrons, which are emitted preferentially in the direction of the muon spin. In the case of systems with a relatively low electron density like carbon nano–structures, the implanted muons capture an electron and form muonium (Mu), a light isotope of hydrogen, *i.e.* having a similar chemical behaviour. The μSR precession can originate either from a uniform quasi-static local magnetic field at the muon stopping site, being usually the signature of long-range magnetic order, or in a few cases, it may be due to the

dipolar interaction of the muon with an isolated magnetic nucleus, like ^{1}H. The muon spin precession observed in TEGO and H-TEGO samples was demonstrated to originate from muon-hydrogen nuclear dipolar interaction with a single proton located at a distance of 1.7 Å from the muon. This interpretation ruled out the existence of magnetic phases in defective TEGO samples. The amplitude of the observed precession (related to the muons fraction involved) correlates with the density of defects and dramatically increases after hydrogenation of the samples. The latter observation is consistent with the formation of CH-Mu groups at Single carbon Atom Vacancies, SAV (See Chap. 5 – analogous to CH_2 groups [1]), which appeared exceptionally stable up to 1250 K. Moreover the amplitude was found to increase as a function of temperature, suggesting a possible thermal activated trapping mechanism. After the muon thermalization and electron capture, a thermally activated motion like the Mu diffusion onto the graphene surface could account for the observed increase of amplitude: the more mobile Mu is at the graphene surface, the more easily it can be trapped by in-plane SAVs which act as trapping centers [84].

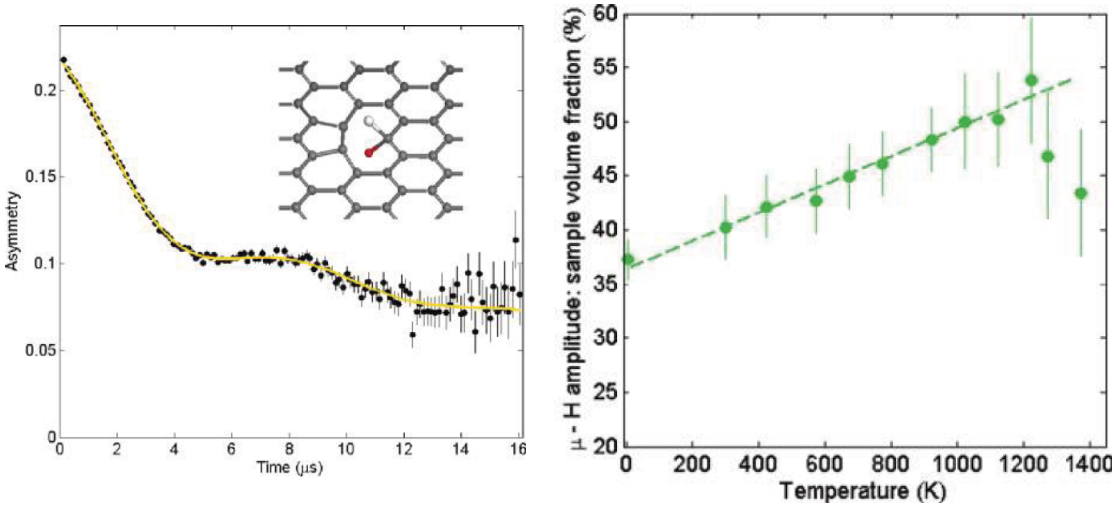

FIGURE 6.1: *Left:* Fit of the muon decay asymmetry for H-TEGO in the hypothesis of dipolar interaction between μ and nearby hydrogen atom. The fit for the hypothesis of long-range magnetism is less satisfactory in the long times region. The fitted Mu-H distance (1.70 Å) matches the inter-proton distance in a CH_2 group, with the carbon atom in sp^3 hybridization. The formation of this group at a graphene vacancy is depicted in the inset. Taken from [84]. *Right:* Temperature evolution of the muon precession amplitude. The increase with temperature suggests a thermally activated capture mechanism most likely associated with diffusion dynamics. The slight drop in amplitude observed above very high temperatures shows the exceptional thermal stability of the CHMu group, up to 1200 K. Taken from [84].

Further investigations were required to identify the precise trapping mechanism and investigate the behaviour of hydrogen in H-TEGO samples. We employed **Solid State**

[1]The theoretical model and *ab-initio* calculation were performed by Prof. O.V.Yazyev from the EPFL, in Lausanne (Switzerland)

Nuclear Magnetic Resonance ^{1}H-NMR, as a sensitive probe to slow frequency diffusive motions [85]. These measurements were performed in collaboration with Dr. P. Carretta and S. Sanna from the NMR group at the University of Pavia (Italy).
As shown in Fig. 6.2 (Left), the temperature dependence of the ^{1}H-NMR signal presents a non-trivial behaviour: the line shape evidenced two main contributions over the temperature range between 70 K and 360 K: a Gaussian component, with a T-independent width ν_0 of $\approx$ 30 kHz, and a Lorentzian component, which displays a significant broadening upon cooling, approaching $\Gamma_0 \approx$ 20 kHz below $\approx$120 K. These two features in the ^{1}H-NMR spectrum suggests the presence of two different H atomic species in the sample: one being "static", associated with the the Gaussian profile, and one being "mobile", associated with the Lorentzian lineshape. The temperature dependence of the Lorentzian width $\Gamma(T)$ is reported in Fig. 6.2 (Right). The observed narrowing of the linewidth on heating indicates the onset of a low-frequency dynamics, which modulates the local magnetic field felt by the protons. In H-TEGO, this modulation is expected to originate from the dipolar interaction between mobile ^{1}H nuclei. The fit of the temperature evolution of the correlation time τ_C to a thermally activated (Arrhenius) law ($\tau_C(T) = \tau_\infty e^{\frac{U}{k_\beta T}}$) gives an activation energy barrier for the dynamical process $U \sim 29 \pm 4$ meV and a characteristic time $\tau_\infty = 0.5 \pm 0.1$ μs. It is important to highlight that the long timescale of the measured dynamics is not compatible neither with the presence of molecular hydrogen, nor with a localized motion of a small hydrogenated group like a methyl group [167] or an hydroxyl group which could have remained attached to the graphene surface following an incomplete desorption of the functional groups during the exfoliation process.

The main results from these investigations stand in the evidence of **the mobility of hydrogen atoms chemisorbed at the surface of a graphene-like plane, associated with a surprisingly low energy barrier of about 30 meV.**

In order to get a deeper insight into the nature of the dynamics of the system and clarify the origin of these unclear and unusual phenomena, we have extended our INS investigations performed on the H-TEGO sample (already presented in Chap. 5) to the temperature dependence of the whole GDOS, from base temperature (5K) up $\approx$ 1300 K. Our approach is constituted of two steps, dividing this chapter into two parts:

1. In the first part, we present the temperature dependence of the GDOS spectra, focusing on the high-energy C–H modes, in the temperature range [5 - 300 K] using the IN1–LAGRANGE spectrometer (described in Chap. 2). It is important to remind that we already discussed in Chap. 5 the T-independence of the low energy range of the H-TEGO GDOS in this temperature range. This can be

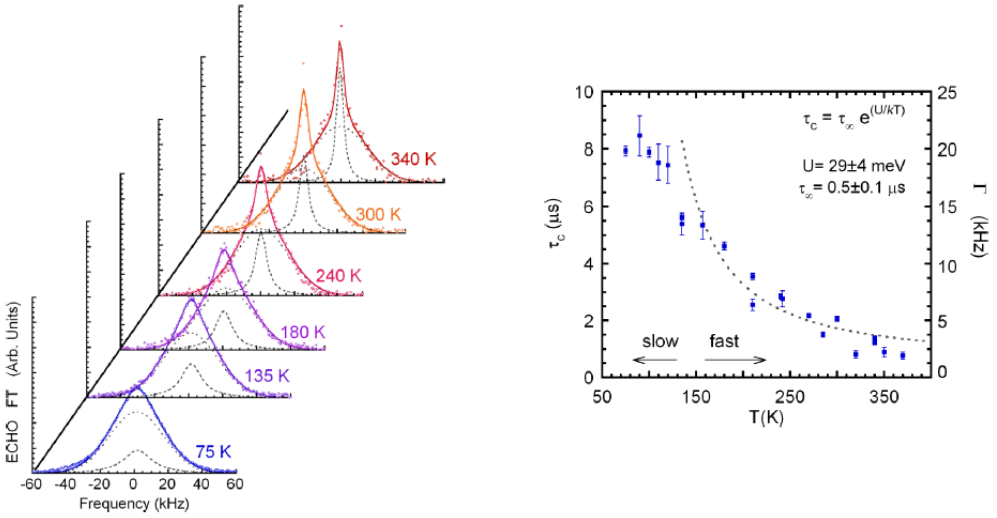

FIGURE 6.2: NMR investigation of the H-TEGO sample (Taken from [85]) –*Left:* Temperature evolution of the ^{1}H-NMR spectrum profile measured at μ_0H = 5.6 T (circles). The fit was done considering a large Gaussian contribution with a T independent (fixed) added to a Lorentzian function, whose width is temperature dependent. *Right:* Temperature dependence of the correlation time of the diffusion process probed by ^{1}H-NMR. Fitting the temperature dependence of the Lorentzian component's linewidth with a thermally activated behaviour (Arrhenius's law) yields an activation energy barrier of $U \sim 29 \pm 4$ meV.

understood that any slow in–plane diffusion process of the H atoms will not affect the riding modes, as the H atoms keep on following the graphene out-of-plane fluctuations in this region.

2. In the second part, we present the evolution of the H-TEGO GDOS from 300 K up to the 1300 K, *i.e.* up to temperatures at which the C–H bonds become unstable. The results are obtained using the IN4C spectrometer in down scattering (anti-Stokes) mode.

6.1 Temperature dependence of the C-H modes in H-TEGO

We have collected INS spectra of H-graphene (H-TEGO) at different temperatures from 5 K to 300 K. We focused on the C–H modes bending region which, as described in Chap. 5, has revealed to be very sensitive to the H local environment. Any slow dynamical process (local rearrangement or long range diffusion) of the H atoms is therefore likely to induce modifications in the bending mode region of the GDOS.

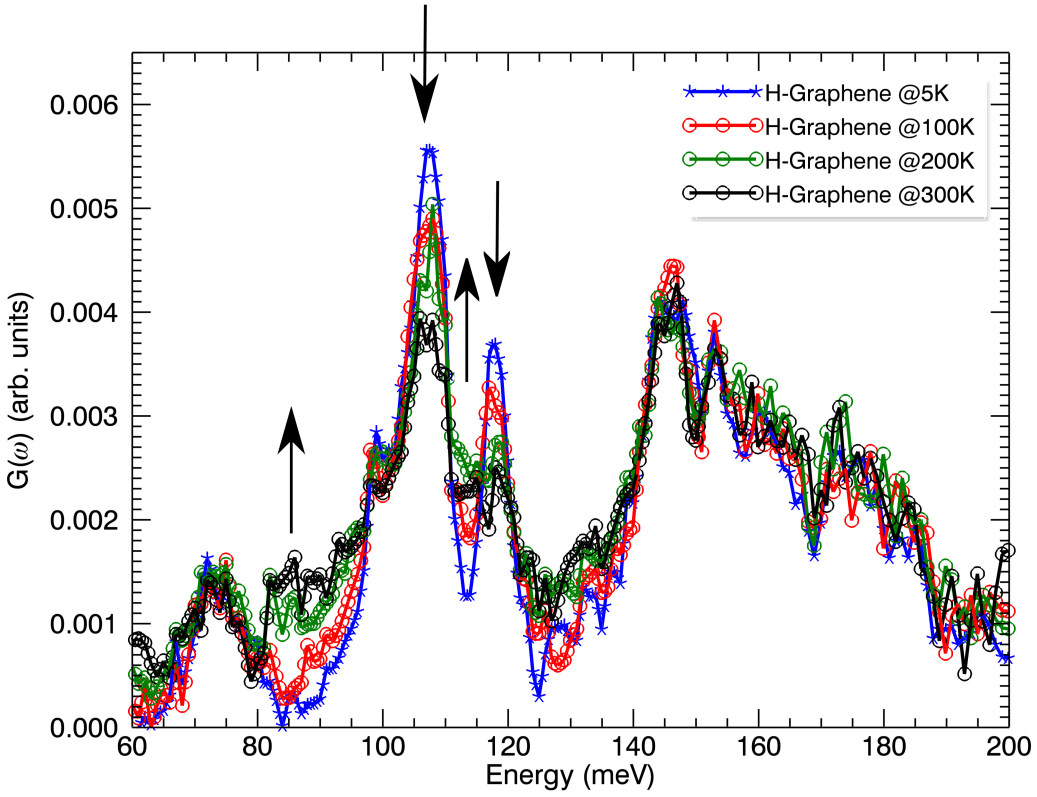

FIGURE 6.3: INS spectra of H-TEGO collected on Lagrange at different temperatures, from 5 K to 300 K.

When H-TEGO is progressively heated up (see Fig. 6.3), we observe an important and unexpected thermal evolution in the general shape of the GDOS, characterized in particular by the decrease in intensity of some C-H bending peaks in the band located around 100 meV, which is accompanied by the simultaneous appearance of some features at slightly lower energies. The intensity of the band centered around 150 meV remains constant.

In order to better isolate the T–dependent contributions from the static ones, we fitted the neutron spectra collected at different temperatures, with a linear convolution of 15 gaussians functions (Fig. 6.4). The background, positions and width of the gaussians functions are kept fixed, the only free parameter being their intensities. Our model was therefore composed of 15 free parameters, namely the integrated intensities of each single vibrational component. Among these 15 free parameters, only four clearly change with temperature: these are the intensity of the peaks located at 108 meV and 118 meV which drop with increasing T. The intensity loss is compensated by the appearance of features centered at 89 meV and 113 meV, whose intensities increase with T. The two

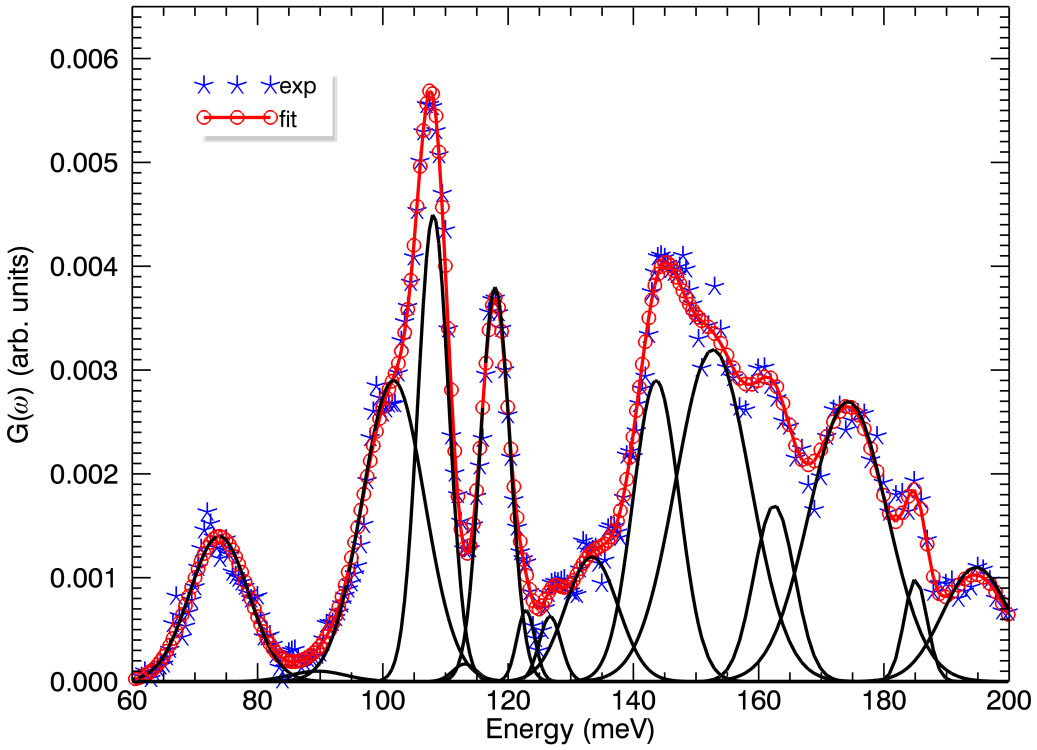

FIGURE 6.4: Lagrange data at 5 K and fitting using 15 gaussian functions.

sets of peaks located respectively at 118 and 89 meV on one hand and at 108 meV and 113 meV on the other hand seem to be coupled, the integrated intensity in the total range of the bending mode region remaining constant at all temperatures investigated. It is important to note that the GDOS transfer is not due to an enlargement of the peak, nor to a progressive softening of the low T mode's frequency.

We attribute this thermal evolution of the GDOS to a modification of the local environment of the different H populations, *i.e.* subsequently affecting their bending mode frequencies. It is important to observe that this intensity redistribution concerns essentially the peaks centered at 108 meV and 118 meV, whose contributions have clearly been attributed to H bonded at in-plane inner voids, extended and single atom vacancies, respectively (see Chap. 5, Fig. 5.26). This suggests in particular that the hydrogen located at the edges of the graphene plane have their bending modes unaffected by the temperature increase. This was checked by repeating the above described experiments on a H-BMG sample: its GDOS was observed to be essentially T independent in the C–H bending mode range. In the INS spectra, the integrated intensity of a vibrational peak centered at $\hbar\omega$ is directly proportional to the number N of H atoms participating to this eigenmode. We make therefore the assumption that the evolution of the GDOS

with temperature is due to an activated process from a ground state configuration to another state characterized by an energy difference of 2ϵ (two state model). The effect of temperature is therefore to distribute the N H atoms over the two states (below referred to as states $|+\rangle$ and $|-\rangle$ with population N_+ and N_- respectively) according to their T dependent probability [183]. The different population ratio are expressed as:

$$\frac{N_+}{N} = \frac{exp(-\frac{\epsilon}{K_\beta T})}{exp(+\frac{\epsilon}{K_\beta T}) + exp(-\frac{\epsilon}{K_\beta T})} \tag{6.1}$$

$$\frac{N_-}{N} = \frac{exp(+\frac{\epsilon}{K_\beta T})}{exp(+\frac{\epsilon}{K_\beta T}) + exp(-\frac{\epsilon}{K_\beta T})} \tag{6.2}$$

Fig. 6.5 shows the values of the integrated intensities of the peaks at 89 meV, 113 meV, 108 meV and 118 meV, measured at different temperatures ranging from 5K to 300K, together with the respective fits N± = f(T) (N_+ for the rising contributions at 89 meV and 113 meV and N_- for the dropping ones at 108 meV and 118 meV). The fit provides an energy difference between the two energy levels $2\epsilon \sim 20$ meV and 14 meV (± 4meV), for the two couples of spectral lines respectively. Surprisingly they have a value comparable to the activation energy previously extracted from ^{1}H-NMR in the same temperature range (U $\sim$ 30 meV).

In conclusion, the T dependence of the GDOS spectra suggests an activated modification of the local environment of the H atoms which are located inside the voids at the surface of the graphene plane. The energy difference between the initial state and final configuration is similar to the activated energy derived from the ^{1}H-NMR investigations. Two category of H atoms are therefore observed inside the H-TEGO sample, by INS and NMR:

1. a "static" category that we identified belonging to the C-H bonds at the edge of the graphene planes, *i.e.* characterized by a T-independent gaussian lineshape in the NMR spectrum and a "edge-like" C-H bending INS spectrum).

2. a "mobile" category, characterized by a T-dependent lorentzian lineshape in the NMR spectrum and by a "in–plane void" like INS spectrum.

6.1.1 Different scenarios

In order to shed light into the data interpretation, we proceeded to the attribution of the C-H spectral lines which appear with increasing temperature. We followed the same

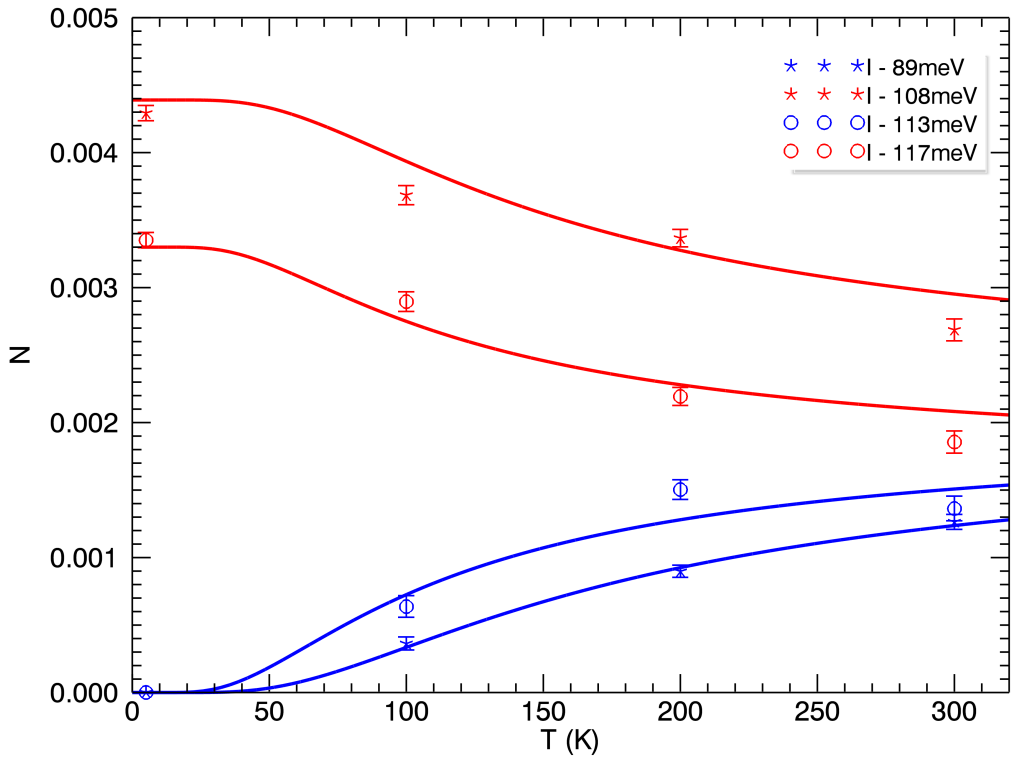

[h]

FIGURE 6.5: Integrated intensities and fit using a two–levels statistical model to describe the T dependence of the intensities.

strategy used for the data at 5 K and developed in Chap. 5: we tried to reproduce the spectra at 300 K by a statistical sum of GDOS issued from a large variety of model local environment, in order to find out the best candidates of the "final high temperature configuration" associated with the state $|+\rangle$ in the two state model.

In particular, we worked on finding possible scenarios that could locally modify the environment of H located inside the in–plane voids.
The best agreement between the data and the simulations was obtained for two models and are shown in Fig. 6.6.

Evaporation of the H from the voids to the surface: The first hypothesis we took into account was the conversion of 15% of H at in-plane defects to ad–atom configurations where the C atoms adopt a pure sp^3 hybridization. The best agreement between the experimental INS features at 300 K and our simulations (from the collection of models described in the previous Chap. 5) was found for graphane-like islands.

The vibrational spectrum reported in Fig. 6.6 has been calculated for a linear combination of H at the external edges, at single atom vacancies (SAV), extended inner voids and boat-graphane like structures in the proportion of 47% (edges): 15% (SAV): 23% (inner voids): 15% (boat-graphane). The formation of these graphane-like structures could be due to a thermally activated torsional re-arrangements of the bonds that deform locally the lattice, supporting the migration of H atoms from the defect (extended inner voids and SAV), onto the neighbouring C atoms, most likely close to the defect itself and subsequently clustering in Csp^3-H islands. In this scenario, H atoms move from the defect (Csp^2-H) and jump onto to plane (Csp^3-H). Even though this scenario fits both the INS and NMR signatures, it appears hardly possible on an energetic point of view, since it would imply breaking several C-H bonds ($\approx$ 4 eV each[2]), and creating unsaturated dangling bonds inside the voids. It should be accomplished at the cost of massive defects reconstruction, hence implying important modification on the graphene lattice, already at low temperatures. This hypothesis seems therefore very difficult to retain, the resulting difference in energy ΔE between the initial and final state being of the order of several tens of eV.

Local reorganization of H unsaturated voids: In a second step, we considered the effect of the presence of H incompletely saturated, in-plane carbon vacancies (see Fig. 6.7) on the simulated GDOS. In this case, we could easily picture the occurrence of two ideal H arrangements: H atoms can saturate dangling bonds in a packed configuration inside the voids (see Fig. 6.7 – *Left*) or they can assume a dispersed or dilute arrangement with more uniformly distributed H inside the void (see Fig. 6.7 – *Right*). In the compact configuration, the average H local environment is similarly to the completely saturated case. It is not surprising that the corresponding GDOS features a predominant peak at the same energy (108 meV), matching the experimental feature at the lowest temperature. This is not the case for the dilute configuration for which the local environment felt by each H is different. In particular,the H–H interaction is significantly reduced for this configuration compared to the compact one. The dilute model leads to a shift of the predominant peak of the GDOS to 113 meV, which fits well the position of the new emerging vibrational feature (see Fig. 6.8).
From an energetic point of view, if breaking a C–H covalent bond requires $\approx$ 4 eV and is indeed incompatible with the temperature range involved in the dynamical process observed, the difference in energy between two configurations which differ only for the

[2]This value has been calculated as [$E_{unsatvoids}$ + E_H - $E_{unsatvoids+H}$], where $E_{unsatvoids}$ is the total energy of a graphene supercell with a fully not-saturated void, *i.e.* presenting n dangling bonds, E_H is the energy of a single H atom and $E_{unsatvoids+H}$ the total energy of the graphene supercell with a $n-1$ dangling bonds and one C-H at the in-plane void.

position of one H in a partially unsaturated voids while keeping the total number of dangling bonds constant, was found to be only $\Delta E \approx 70$ meV. At the time of writing, we failed in finding an equivalent interpretation for the other set of peaks: no scenario is actually found to reproduce the loss of transfer of intensity from 118 meV to 89 meV. The peak at 118 meV is the predominant signature of the SAV in–plane defects. For this peculiar model, an H movement would induce either to be transferred to an adjacent C atom inside the void, resulting in the same configuration but rotated by 60^o, or to be transferred to an adjacent C atom on the plane, *i.e.* bringing energetics issues. Some other hypothesis have to be explored, in particular those involving short lived transition states which could lead to the local diffusion of the atom inside the void.

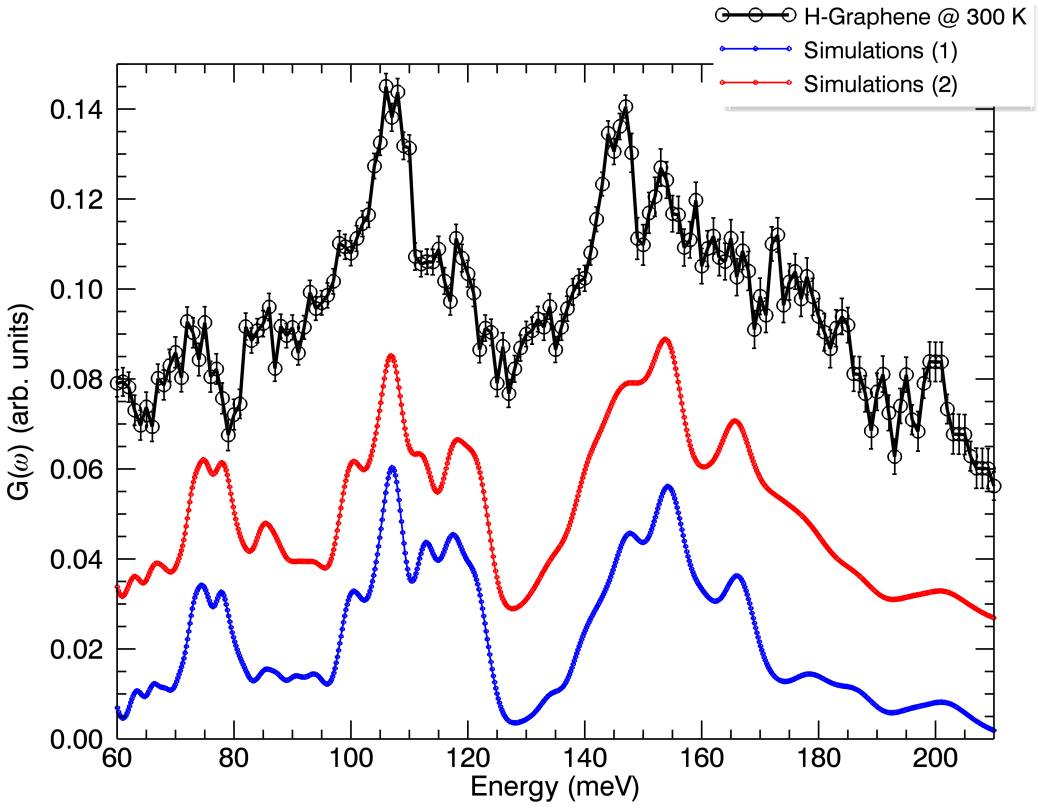

FIGURE 6.6: Comparison of the experimental INS data of H-TEGO (black circles) at 300 K with the vibrational spectrum calculated for (1) a linear combination of H at the external edges, H at single atom vacancies (SAV), H at extended inner voids in compact configuration and in H at unsaturated extended inner voids in outspread configuration, in the proportion of 47%:20%:24%:9% (blue curve). (2) a linear combination of H at the external edges, H at single atom vacancies (SAV), H at extended inner voids and in graphane-boat structure in the proportion of 47%:15%:23%:15% (red curve)

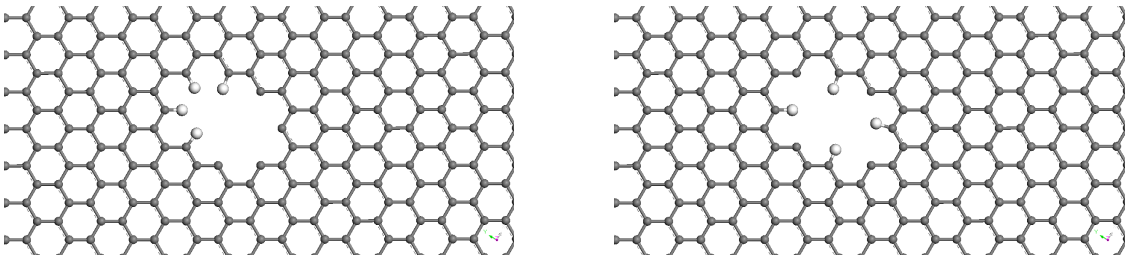

FIGURE 6.7: *Left:* In-plane defects, in the presence of unsaturated bonds: *compact* configuration. *Right:* In-plane defects, in the presence of unsaturated bonds: *dilute* configuration.

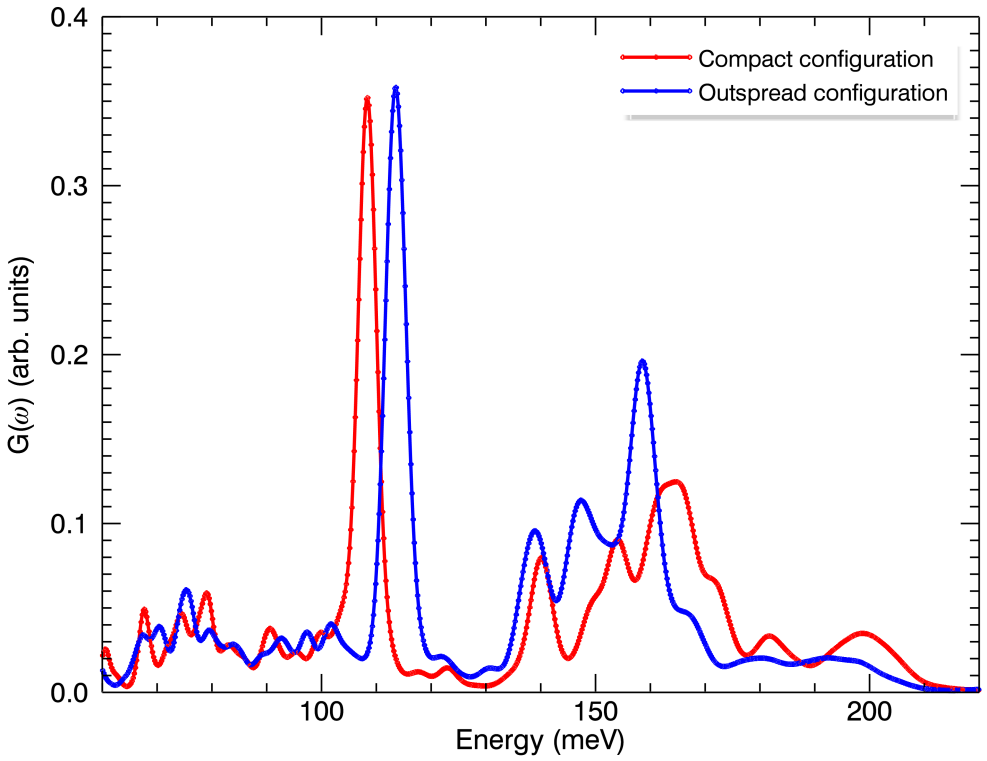

FIGURE 6.8: In-plane defects, in the presence of unsaturated bonds: GDOS of the *compact* and *dilute* (blue) configuration, as depicted in Fig. 6.7

6.1.2 Quantum tunneling at the origin of the H diffusion?

Even though the *compact to dilute* scenario is still difficult to accept from a classical point of view, due to the high energies required for *breaking* covalent C–H bonds, H jumps from one configuration to the other seem more acceptable if one considers the quantum nature of an hydrogen atom, in addition to the restricted/confined space inside the voids. In view of these considerations, the process of H jump from one carbon atom to the other could be induced through Quantum Incoherent Tunnelling. Quantum tunnelling through the interceding barrier between potential wells actually requires short distances between minima in the potential energy surface, enabling wave functions to overlap. It requires also that the mass of the particle is small [184]. Quantum effect appear unavoidable when considering the dynamics of hydrogen in a small (diameter inferior to 12 Å) in–plane voids in graphene. In this case, the energy barrier to overcome for a H transfer is not the top of the potential barrier, but the energy difference ΔE between the final and the initial states of the system. This difference in energy can be provided by thermal excitations, *i.e.* phonons of the graphene lattice, in a way similar to what is observed in the case of proton transfer in hydrogen bonded crystals, the most representative one being benzoic acid.

Several experimental techniques, including NMR and INS, have been employed in the study of the double proton transfer in benzoic acid and similar organic crystals [185]. These systems can be formally described by an asymmetric double-minimum potential (see Fig. 6.9), coupled to the crystal vibrations. At low temperatures one may restrict only to the two lowest energy eigenstates, which must be coupled to the crystalline phonons in order to obtain the relaxation. In a two double-well potential, the analysis of tunneling is a function of the proton transfer coordinate as well as of the transverse skeleton mode (phonons) coupled to the proton transfer coordinate. The probability for interchange between the two wells defines the correlation time. In general, the proton transfer motion is characterized not only by the motion of the hydrogen atom but also by the simultaneous displacement of other atoms in the molecular skeleton. This leads the system being characterized by a multi-dimensional potential energy surface (PES), which could give rise to different relaxation processes depending on the topography of the potential energy surface itself,

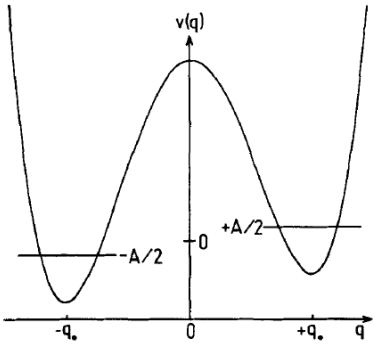

FIGURE 6.9: An asymmetric double-well potential as a function of the coordinate q, as formalized for proton transfer in benzoic acid crystals. Taken from [185].

the modes promoting proton tunneling and the specific details of the level structure and energy gaps between the proton configuration states. In the case of defective graphene, this could account for the relatively high energy barrier and long timescale, with respect to the usual ones, probed in hydrogen bond dynamics [186, 187].

The complex structure of defective graphene complicates the formal treatment, which has been developed for much simpler and well-defined cases. We have individuated and limited the configurations involved in this dynamical process to small in–plane carbon vacancies, with a diameter inferior to 12 Å) and we support the idea of a H-jump from one site to the other in not-completely saturated small in-plane voids through quantum tunneling. Quantum effects appear to us as the only mechanism able to reconcile the strength of C–H covalent bonds involved in the dynamical process to the relatively low temperatures and activation energies. This part of the work is still in progress during the writing of this manuscript.

6.2 Temperature dependence of the H-TEGO GDOS in the [300 − 1370 K] range.

We followed the temperature dependence of the complete GDOS of H-TEGO using the Thermal Neutron Time-of-Flight Spectrometer IN4C, from ambient temperature up to 1370 K. The experiment was performed in a standard furnace. In this case around 300 mg of H-TEGO powder was placed inside a quartz tube covered with a Niobium foil, in order to reach high temperatures. We have used $\lambda = 2.41$ Å as incident wavelength, in high resolution mode (Inelastic Time Focusing), as described earlier.
The generalized density of states (GDOS) of hydrogenated graphene H–TEGO, measured at different temperatures between 320 K and 1370 K is presented in Fig. 6.10. Data have been corrected from the DW factor which affects INS data by dumping the intensity[3] after proper data treatment and normalizations.
The C-H bands clearly persist up to 800 K /1100 K, although it displays a progressive broadening and loss of intensity, probably due to anharmonicity at high temperature of the bending modes. This confirms the stability of C–H bonds up to 800 K/ 1100 K. However, in the data collected at 1100 K and then at the ultimate temperature of 1370 K, we observe a non-negligible increase in the intensity of the low energy modes, corresponding to graphene collective motions while the C-H bands, especially the one around 100 meV, appear very broadened. At temperatures above 1000 K, TEGO undergoes

[3]DW-factor correction on the GDOS was performed applying interpolation to $Q \to 0$ over 5 groups, as implemented in the LAMP/IDL subroutine *interp_q*0, see Chap. 2

most likely some structural modifications, leading eventually to the irreversible detachment of H. This behavior could suggest a possible thermal evolution in the dynamical properties. The low frequency excess of intensity in this T range might reflects in–plane diffusion of the atoms.

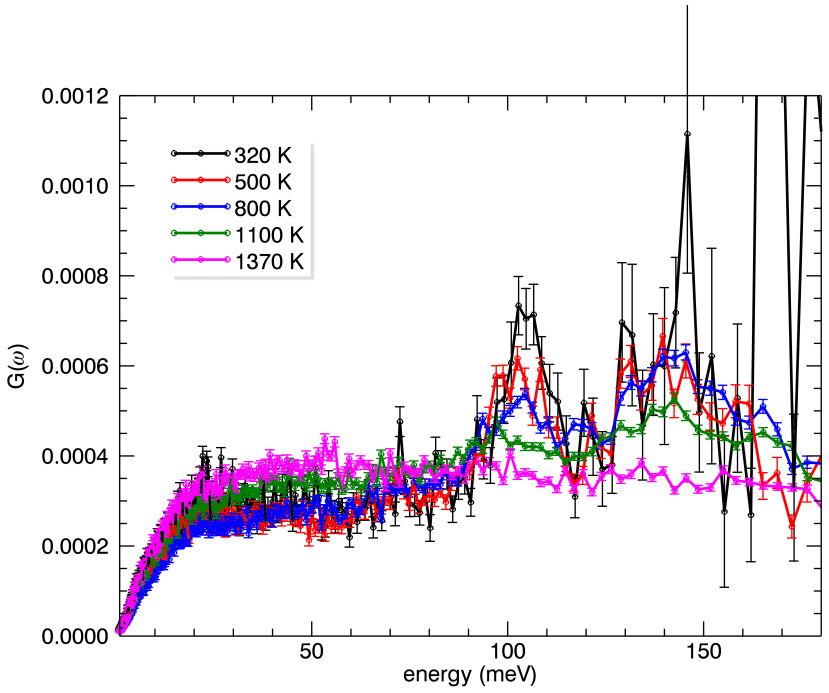

FIGURE 6.10: Inelastic neutron spectra obtained on IN4 at 320 K with incident wavelength of 2.41 Å on hydrogenated H-TEGO, at different temperatures from 320 K and 1370 K.

6.3 Partial conclusions

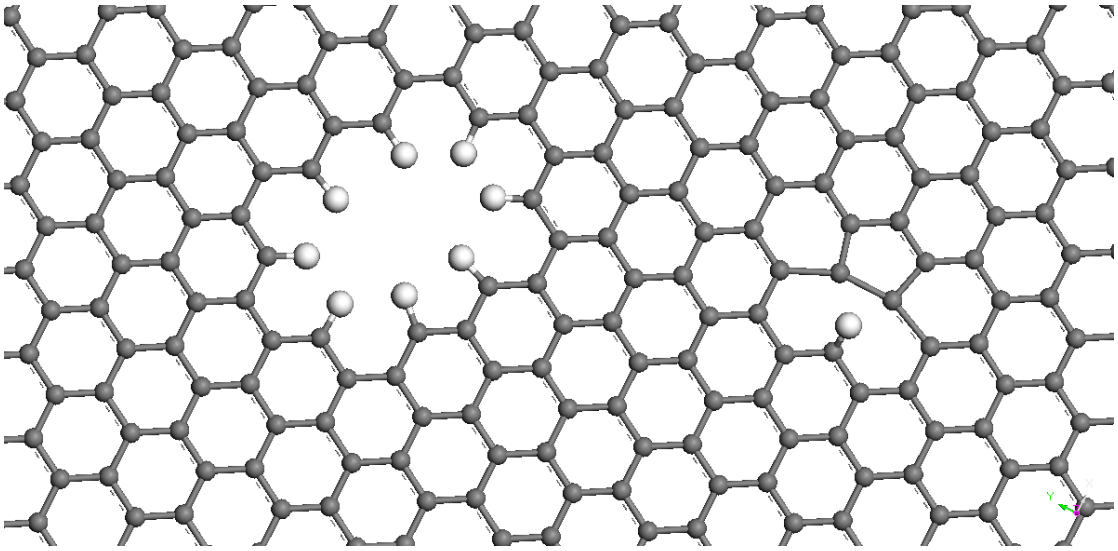

FIGURE 6.11: In-plane defects involved in the dynamical process observed

The partial conclusions of this chapter are:

- Previous μSR and ^{1}H-NMR investigations evidenced an un-expected mobility of chemisorbed H at the graphene surface. This dynamical process was found to be associated to a very small activation energy of about $\approx$ 30 meV.
- INS have evidenced a non-trivial temperature (from 5 K to 300 K) evolution of the C-H bending vibrational lines associated with an energy barrier of about $\approx$ 20 meV.
- C-H bending vibrational lines affected while increasing the temperature are associated to small in-plane defects, only. The features associated to the edges are T-independent.
- We interpret this thermal behaviour as a change in the H-local environment, occurring in partially un-saturated voids.
- The implication of quantum effects like incoherent tunnelling is proposed to account for the small energies ($\approx$ 20 meV) and timescales (μs) involved in the dynamical process
- The C–H bonds are found to be stable up to 1000 K.

Chapter 7

Nickel Decorated Graphene

7.1 Introduction

In the last years, hydrogen has been identified as a possible replacement to the current fossil fuels source for automotive applications. One of the major obstacle on the way towards the development of a hydrogen-based economy is still represented by the difficulties of efficiently storing hydrogen. In this domain, considerable interest has been stimulated by carbon nano-structures for their relatively low cost and the possibility to significantly change the nature of hydrogen bonding but also greatly reduce the weight of hydrogen storage devices using light carbon framework.
The possibility of gram scale production of graphene and its chemical functionalization have recently become possible with the development of chemical methods, as already discussed in Chap. 1. Graphene appears very attractive for gas adsorption and by consequence in the field of energy and hydrogen storage thanks to its low atomic mass and its very large specific surface area (up to 2630 m^2/ g, if one considers both sides of the graphene plane). Pure graphene, however, encounters difficulties in the hydrogenation process and the fully hydrogenated graphene (graphane), which has a highly desirable hydrogen content of 7.7 wt% H_2, can be produced only at elevated temperatures and applying high hydrogen pressure [41]. This indicates the existence of large thermodynamic barriers that have to be overcome in the hope of using graphene as solid-state hydrogen storage medium. These barriers probably originate from the high activation energy required to dissociate H_2 at the graphene surface. Several ways to enhance hydrogen sorption have been theoretically predicted and in some cases experimentally observed [16, 188]. We have shown in the previous chapters, that defects in graphene play a fundamental role in the dissociation of hydrogen molecules and act as trapping centers for atomic hydrogen [84, 85]. Adding metal atoms in the carbon framework can support

hydrogen dissociation and enhance dramatically the adsorption kinetics and capability. In this context, it has been suggested that both spillover mechanism [31] and quantum orbital interactions, like Kubas binding [30], can boost carbon nanostructures performances, *i.e.* carbon nanotubes [189], fullerenes [190] and graphene complexes [188], once decorated with (alkali, alkali-earth, transition) metal atoms and by then enabling hydrogenation under mild conditions. In particular, for Kubas interaction, the binding energy is thought to fall in the range of 15-30 kJ/mol, which is a highly desirable value for room temperature hydrogen storage applications.

In the following two Chapters (Chap. 7 and 8) we report the neutron scattering characterizations of selected metal-decorated carbon nano–structures for hydrogen storage applications. In the following sections we will discuss the structural and dynamical investigations of Nickel-decorated TEGO and its hydrogenated counterpart, while the next Chapter will be devoted to the dynamical characterizations of Metal–intercalated fullerides (A_xC_{60}, with A=Li, Na and x = 6,10,12) and their hydrogenated phases. A brief description of the systems, the chemical–physical interest and the methods will be given in each pertaining section. In particular, the experimental methods have been already discussed in the previous chapters, while the computational methods employed for the phonon calculations will be simply named and appropriate references will be given in the text for the reader interested in having more complete reviews. As a final remark, we would like to point out that this part of the work is not as consistent as the hydrogenated-TEGO section, which represents the real heart of the thesis. It is far to be an exhaustive and finished study: the intent is to give a brief overview and summarize the future prospects on these ongoing studies, as complement of the investigations already performed and cited throughout these next two chapters.

7.2 Nickel-decorated graphene

Dr. M. Gaboardi of the Carbon Nanostructures Laboratory (University of Parma) and coworkers synthesized a novel functionalized graphene decorated with mono–dispersed nickel nanoparticles of 17 nm in diameter. The samples were synthesized following an innovative synthetic approach, based on the absence of solvents and without exposing the material to oxidizing agents. This is fundamental in order to prevent undesired reactions like the oxidation of the carbon support or the nickel nanoparticles. The interaction with hydrogen has been investigated by means of Muon Spin Relaxation (μSR), dynamic pcT and BET isotherm measurements. μSR has showed that a considerable fraction of muonium (38%) is captured, indicating a strong hydrogen–graphene interaction. The locally modified graphene around the metal nanoparticle showed a larger

affinity to hydrogen (muonium) with respect to the unperturbed plane, which enhances its chemisorption. Moreover, the presence of Ni on graphene has significantly increased the amount of molecular hydrogen adsorbed at 77 K, reaching the maximum of 1.1 wt % H_2 and hence a hydrogen adsorption 51% higher than other in other common carbon based materials [26]. This is probably due to Ni–activated physisorption. Hydrogen adsorption proved to be fully reversible during numerous cycles [142].
In this section we will present a brief introduction of the synthesis procedure and some elastic and inelastic neutron measurements carried out on Ni-decorated TEGO.

7.2.1 Synthesis and characterizations

The synthetic strategy adopted for the synthesis of nickel-decorated graphene was to make a solution of graphene and the metal precursor in a solvent which solubilises the precursor in order to get an uniform impregnation of graphene and then remove the solvent.

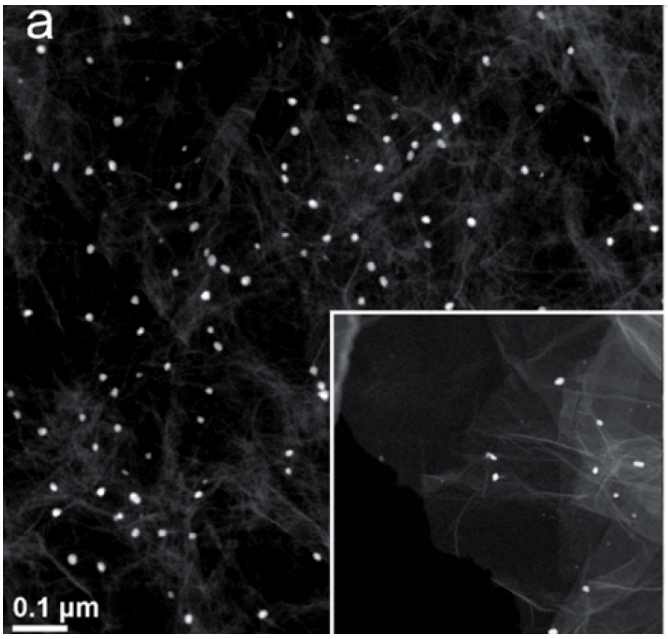

FIGURE 7.1: HAADF–STEM image of a Ni decorated TEGO flake. Ni particles show up as very bright spots in the dark field image, thanks to the higher atomic number of Ni with respect to C. In the inset HAADF–STEM image of a single layer graphene region of the sample is reported. Images from [142].

Graphene flakes were synthesized via the thermal exfoliation of graphite oxide (GO) process, as already discussed in Chap. 4. The synthesis of Ni decorated TEGO was performed by mixing TEGO with Nickel–acetylacetonate ($Ni(acac)_2$) in anhydrous tetrahydrofuran (THF) and then evacuated until the pressure was lower than 10^{-5} mbar. The synthesis vial was immersed in liquid nitrogen to condense the solvent and then ensure

the impregnation of TEGO with the metal-organic precursor. The solvent was then removed and the product was heated up to 300^{o}C in high dynamic vacuum (10^{-6} mbar), in order to thermally decompose Ni(acac)$_2$. The as-prepared Nickel decorated TEGO shows up as a uniform black powder. More details about the synthesis procedure can be found in [142].

TEM images of Ni-TEGO are reported in Fig. 7.1 and have revealed that the graphene films are decorated by nanometer-sized nickel particles. Both HR-TEM images and bulk SQuID measurements have given an average nanoparticle diameter of about 20 nm.

We performed a high neutron diffraction experiment on the two-axis diffractometer D4C at the ILL in order to provide the structural characterization of the sample. 300 mg of samples were put in a 7 mm cylindrical Vanadium cell. The wavelength used was 0.5 Å (refined value $\lambda = 0.4989$ Å), which provides a good compromise between high neutron flux and a high $Q_{max} = 23.5$ Å $^{-1}$ suitable for space Fourier transform and analysis in direct space. Measurements were performed at 20 K in order to reduce thermal vibrations and point out static disorder (see Chap. 2 for data treatment).

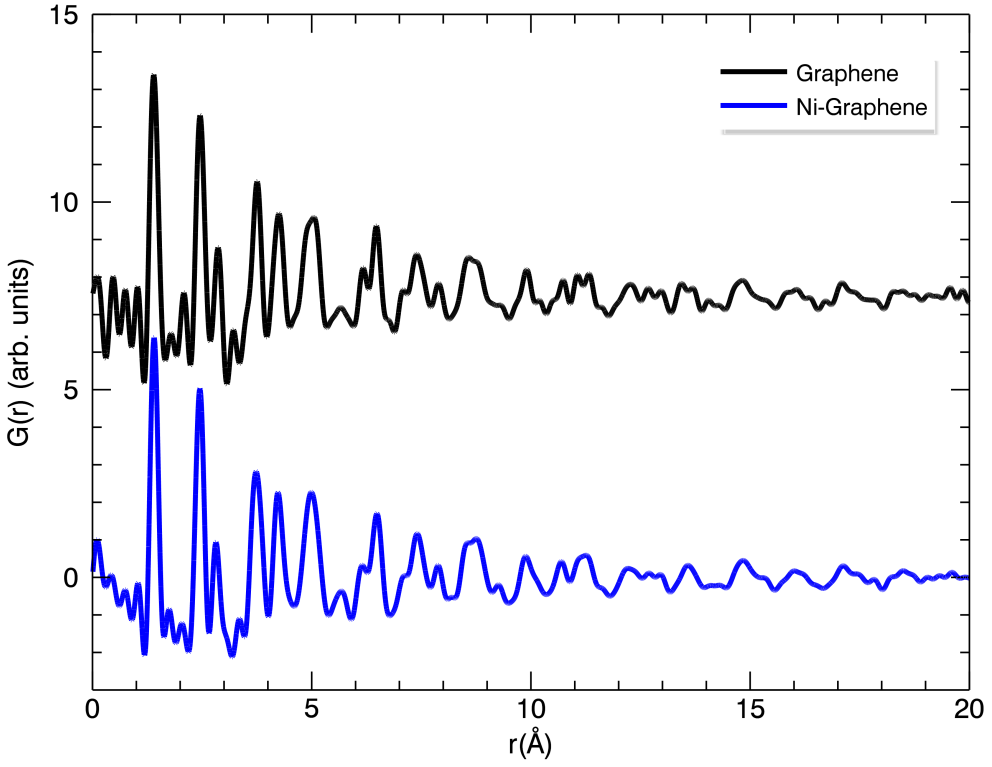

FIGURE 7.2: $G(r)$ of Ni-TEGO, from high energy diffraction data collected on D4C at the ILL ($\lambda = 0.5$ Å , $Q_{max} = 23.5$ Å $^{-1}$).

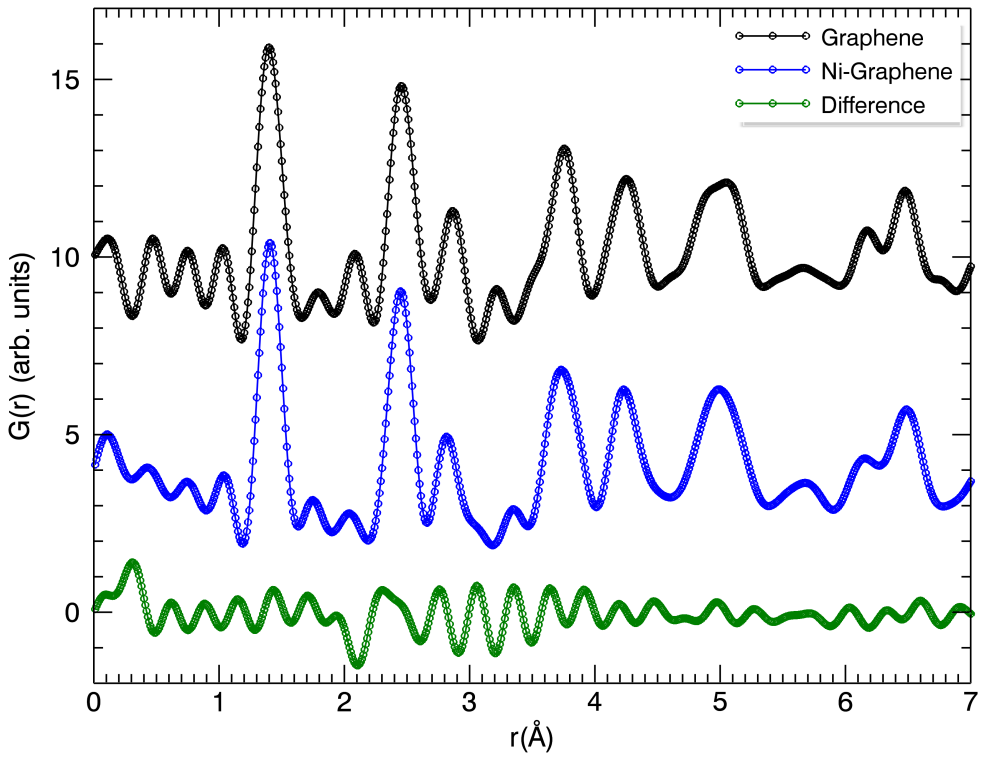

FIGURE 7.3: $G(r)$ of Ni-TEGO, TEGO and their difference for r = [0 - 7 Å].

The $G(r)$ of as-prepared graphene and Ni-decorated graphene are reported in Fig. 7.2 and Fig. 7.3 (a simple shift along the y-axis has been applied to graphene data, in order to make the plot clearer). No important dissimilarities can be evidenced in the $G(r)$s. The only differences may be noticed at [d_1 = 2.4 Å d_2 = 3.5 Å and d_3 = 4.98 Å] which represent the three first Ni-Ni distances [191] and at [d_4 = 1.7 Å d_4 = 3.0 Å and d_6 = 3.33 Å] which represent the three first Ni-C distances [192]. This suggests the chemical anchorage of the Ni-nanoparticles to the graphenic support, most likely at the defects. Despite the large coherent cross section (σ_C (Ni)= 13.3 barns), the stoichiometric quantity of metal introduced by the chemical decoration (nominal stoichiometry NiC_{80}) prevents any further information to be derived from $G(r)$.

The experimental GDOS of different TEGO and H-TEGO samples, measured on the thermal neutron time-of-flight spectrometer IN4C at the ILL (see Chap. 2) are reported in Fig. 7.4, Fig. 7.5 and Fig. 7.6. The GDOS of Ni-TEGO appears essentially featureless and very similar to the one of TEGO; a linear increase of the GDOS is observed up to ≈ 20 meV, followed by flat region up to 50 meV. It is however noteworthy to evidence the presence of some extra intensity in Ni-TEGO data. A normalized Ni-TEGO and TEGO

GDOS subtraction allows to observe the vibrational modes of Nickel, which are expected around 20 meV and 34 meV [193, 194]. The nanosized nature of the particles is well reproduced in the GDOS (green squares in Fig. 7.4): one can observe broad features and an increased intensity in the low energy part of the spectrum, as discussed in Chap. 4.

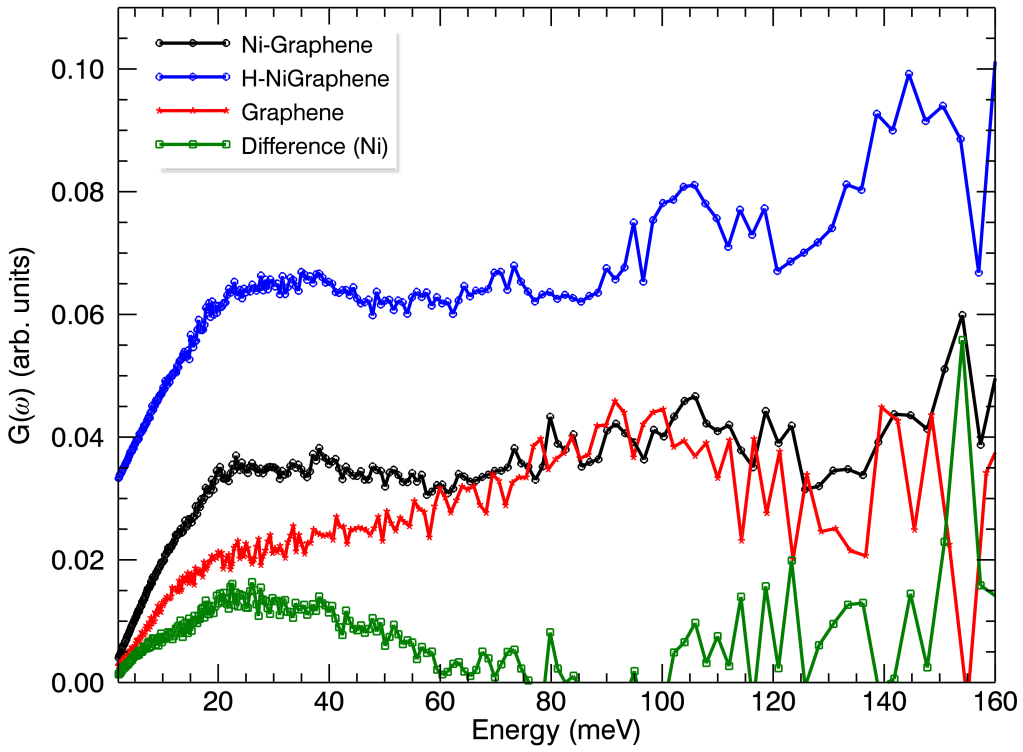

FIGURE 7.4: GDOS of as-prepared TEGO, Ni-decorated TEGO (Ni–graphene) and Ni-decorated TEGO after hydrogenation at 350^o C under 100 bar of hydrogen (H-Ni Graphene) measured on IN4C, in anti-stokes mode at 320 K (λ = 2.41 Å).

Thermal treatment in hydrogen atmosphere (350^o C and 100 bar) was performed at the EMPA Laboratory in Dübendorf, Switzerland (Energy and Hydrogen section). The hydrogenation leads to a very small enhancement in the total intensity of the GDOS, as shown in Fig. 7.5. The Ni nanoparticles seem to prevent the dissociation of H_2 and the subsequent chemisorption of atomic H. This is probably due to the fact that the nano particles saturate the defects and consequently inhibit their catalytic role in H-absorption. The extra-intensity is mainly restricted to the localized band around 150 meV, the latter being compatible with the presence of Csp^3-H bonds. The lack of H–riding modes in the [0-50 meV] range and of intense features at around 100 meV allow one to excluding the presence of Ni–H bonds, the latter being the signatures of H–chemisorption at the Ni–nanoparticle surface [195]. Moreover, no sharp features and no

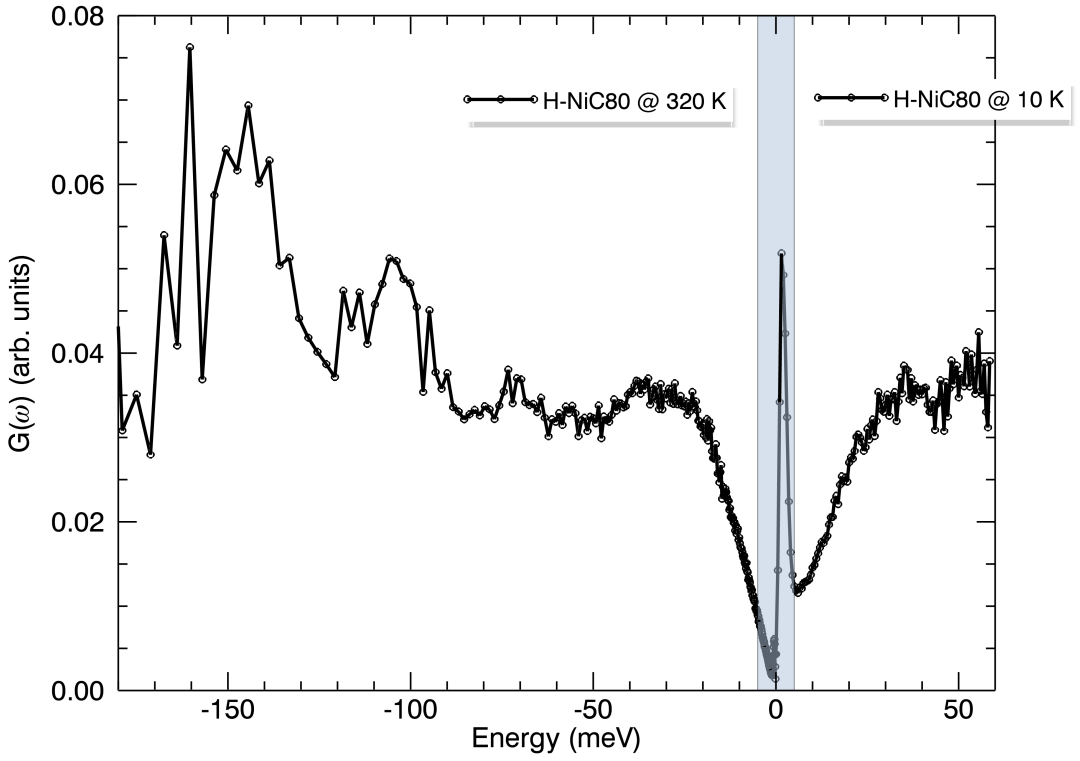

FIGURE 7.5: GDOS of Ni-decorated graphene, after hydrogenation at 350 ^{o} C under 100 bar of hydrogen: data were collected on IN4C, in anti-stokes side at 320 K (λ = 2.41 Å), shown on the left and in stokes side at 10 K (λ = 1.11Å), shown on the right. The overshadowed region represents the data affected by the presence of the elastic line.

important temperature evolution are observed in the low energy part of the spectrum (see Fig. 7.6). This fact allows to excluding the possibility of low frequency contributions from molecular hydrogen quantum rotations and quasielastic–like signal, which would originate from relaxation processes in the picosecond time scale.

In addition, BET and pcT measurements did not show any evidence of Ni catalyzed dissociation of hydrogen, neither at cryogenic temperatures (77 K) [142]. These results suggest that a further improvement of the system would be necessary to achieve the optimal conditions for hydrogen storage: either by reducing the size of the nanoparticles or even by decorating TEGO with atomic nickel. Ultimately a more precise knowledge of the morphology could help in better understanding the interaction with hydrogen itself and the chemical-physical mechanism associated with H absorption.

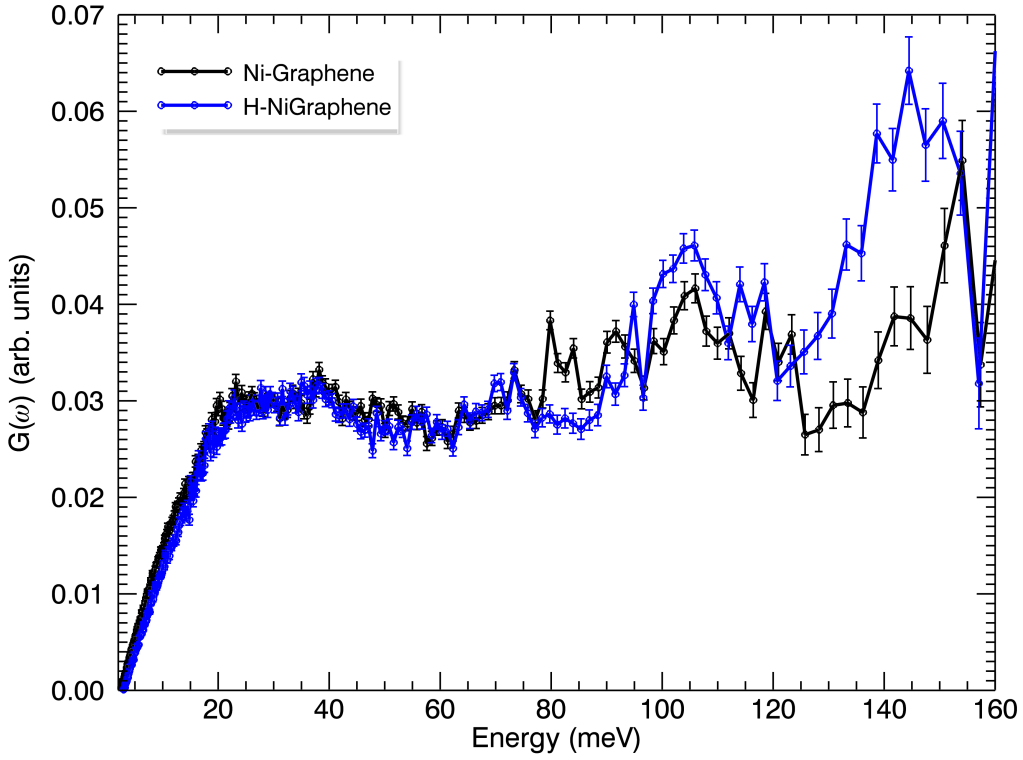

FIGURE 7.6: GDOS of Ni-decorated TEGO (Ni–Graphene) and hydrogenated Ni-decorated TEGO (H–Ni Graphene) measured on IN4C, in anti-stokes mode at 320 K (λ=2.41 Å). One can observe the absence of H–riding modes in the low–medium energy part of the spectrum and the rising of a localized band at 150 meV, which can be ascribed to C-H bending modes. The spectra were normalized to the same intensity in the [0, 40meV] range.

7.3 Partial conclusions

The principle considerations of this chapter can be summarized in the following lines:

- We have shown the NS study of Ni-decorated graphene. We have discussed the effects of the presence of the Ni-nanoparticles on the structural and dynamical properties of TEGO. We have also qualitatively discussed the hydrogenated phase on the perspective of INS.
- Contrary to what is expected, Nickel decoration of graphene seems to saturate the defects and inhibit their catalytic action in H_2 dissociation and subsequent H chemisorption.

Chapter 8

Alkali Metal-Intercalated Fullerides

8.1 Introduction

The intercalation of C_{60} with electron donors like alkali metals A results in a large class of fulleride salts with stoichiometry of the type A_xC_{60}, among which A_3C_{60} has received particular attention during the last decades for its superconducting properties [196]. In particular, lithium intercalated fullerides Li_xC_{60} display a large panel of physical properties, which are mainly due to the small Li-ion dimensions and to the partial charge transfer from the Li atoms to the buckyball. Lithium-doped fullerites behave differently depending on the amount of intercalated lithium. At high doping levels, typically for x $\geq$ 6, both diffraction and NMR clearly showed the formation of lithia clusters located in the largest interstices of the C_{60} *fcc* lattice [197]. However, as the lithium concentration decreases below x=6 the volume occupied by the lithia decreases and the efficiency of charge transfer is expected to increase [197]. Both these factors lead to a reduction of the interfullerene distance and, if two facing carbon atoms get close enough, covalent bonds can form between neighbours C_{60}, giving rise to fullerene polymerization. Li_4C_{60} is the most representative member of this family. The polymerization occurs due to the chemical pressure exerted by Coulomb interaction, leading to a 2D polymer pattern, which is characterized by the coexistence of single and double C-C bonds propagating along two orthogonal directions of the plane. Fullerene polymers can be able to sustain the light metal ion diffusion also at room temperature. Li_4C_{60} has shown important superionic conductivity properties [15] and its dynamical and structural properties have been extensively investigated by XRD [198], ND, INS and *ab-initio* phonon calculations

[199]. The fullerite class of compounds appears interesting in the field of hydrogen storage as well. It has been theoretically predicted that large quantities of hydrogen can be absorbed with useful binding energy in the so–called metal-coated "superfulleroids" [200, 201], making them attractive for technological applications. However, these "superfulleroid" structures (see Fig. 8.1) have never been observed in the solid-state, mainly because of the well-known tendency of metals to clusterize.

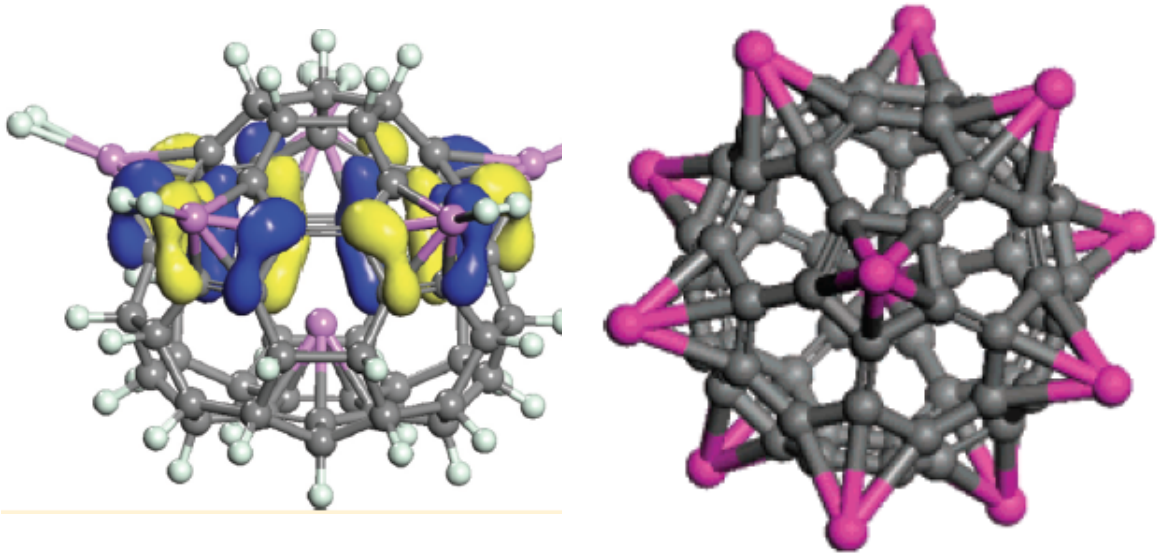

FIGURE 8.1: *Left:* Li-coated C_{60} fullerene, as predicted in [201]. *Right:* Two configurations of $Ti_{12}C_{60}$, as predicted in [200].

The intercalation of lithium and sodium in fullerene A_xC_{60}(A=Li, Na, x≥6) has proved to reversibly uptake relatively high amounts of hydrogen via a complex chemisorption mechanism. In these systems, the number of intercalated ions equals or exceeds the six-fold degeneracy of the t_{1u}-LUMO of C_{60}. In this condition, fullerene is charged with six electrons and the exceeding electrons are forced to stay on the metal cluster. It has been observed that that alkali - metal intercalated fullerenes with high stoichiometry (Li_6C_{60}, $Li_{12}C_{60}$ and $Na_{10}C_{60}$) increase their respective hydrogen storage capacities up to about 5, 4.5 and 3.5 wt% H_2 and significantly lower the desorption temperature with respect to pure C_{60} [202].

We have found that hydrogen mainly covalently binds to the C_{60} molecule in these systems, thus forming the so–called hydrofullerene ($C_{60}H_y$, y ≈ 36-48). A minority part of H_2 however reacts with a fraction of the alkali metal ion (Li or Na), leading to an alkali hydride segregated phase. From a structural point of view, the alkali clusters are localized inside the octahedral or tetrahedral voids of the *fcc* fullerite structure, while

the hydrogenated phase is characterized by the high steric hindrance of $C_{60}H_y$ (packed in a *bcc* or highly expanded *fcc* lattice), the latter allowing only few metal ions to be retained in the structure.
The interaction of A_xC_{60} compounds with hydrogen has been extensively studied thanks to the fruitful collaborations between the Carbon Nanostructures Laboratory Group in Parma (Italy), Empa - Hydrogen and Energy group, directed by Prof. Andreas Züttel in Dübendorf (Switzerland) and Dr. Chiara Milanese of the Pavia H_2 Lab in Pavia (Italy), using different experimental approaches like μSR, X-ray, in-situ neutron powder diffraction, infrared spectroscopy and pcT (pressure, composition, and temperature). Although the study of the initial and final products gave clear pictures of the sample, the intermediate hydrogenation steps are still not completely understood. Muon Spin Relaxation (μSR) on Li_6C_{60} and $Na_{10}C_{60}$ shed some light on this mechanism. In these systems, the hydrogen molecule undergoes first an initial dissociation by the intercalated and partially ionized alkali clusters. In a second step, the so–created hydrogen atoms covalently bond the C_{60}^{x-} anions. The formation of muonium adduct radicals is promoted in Li_6C_{60} and $Na_{10}C_{60}$ thanks to the presence of metal clusters, which provide suitable environment to the formation of interstitial Mu. The hydrogenation is found to be even more effective at cryogenic temperatures, indicating that the reaction between C_{60} and atomic hydrogen occurs with a very low energy barrier. On the contrary, H_2 dissociation mediated by the partially ionized alkali clusters requires high temperatures ($T > 100^oC$). This observation clarified that relatively high temperatures are required to activate the H_2 dissociation process operated by the alkali cluster, which is the only thermodynamical barrier for the H_2 absorption [35]. Moreover, it has been shown that the absorption and desorption temperatures are significantly reduced (200^oC lower) and that the amount of hydrogen absorbed is higher compared to pure C_{60}, either due to a catalytic reaction of hydrogen on the alkali metal or due to the negatively charged C_{60} [16, 34].

The use of neutron scattering is expected to help in better clarifying the hydrogenation process, either on the dynamical or the structural point of view, thanks to the high neutron sensitivity to hydrogen.

In the following section we will discuss the dynamical properties of $Li_{12}C_{60}$ and Li_6C_{60}, the hydrogenation process of $Li_{12}C_{60}$ followed by in-situ inelastic neutron scattering measurements and the neutron spectra of the hydrogenated phases of $Li_{12}C_{60}$, Li_6C_{60} and $Na_{10}C_{60}$.

8.2 Synthesis and characterization

C_{60} crystalline powder (MER, 99.9 % purity) was mixed to small pieces of lithium metal (Sigma-Aldrich, 99 % purity) in the stoichiometric ratio 1:12 or 1:6 respectively and grinded through high energy ball milling. The resulting black powder was subsequently treated in a furnace at 270^o C for 36 hours, to let them react and obtain a homogeneous phase. Laboratory Xray powder diffraction measurements have confirmed the expected *fcc* crystal structure for monomeric Li-intercalated fullerides. The air sensitivity of the samples required to handle the compounds under strict oxygen and moisture free condition (H_2O and O_2 levels under 1 ppm).

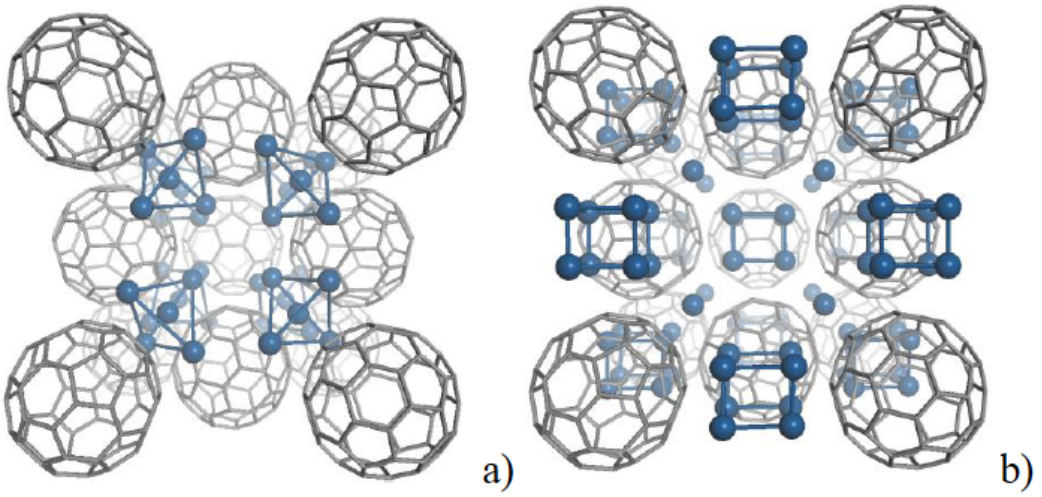

FIGURE 8.2: *Left:* The low temperature phase of $Li_{12}C_{60}$ [203]. *Right:* A graphical representation of the high temperature phase as suggested by μSR and INS experiments [204]. The frontal C_{60} has been omitted for clarity.

At low temperature (20 K), $\mathbf{Li_{12}C_{60}}$ has a monoclinic crystalline structure (space group $P21/c$ and lattice parameters a = 9.888(9) Å , b = 9.901(8) Å , c = 14.290(8) Å ,β = 89.51(6)^o), with the C_{60} molecules keeping the monomeric state. There are two different voids in this fulleride structure, corresponding respectively to the pseudo-tetrahedral (small) and the pseudo-octahedral (big) voids of the parental cubic lattice, which can accommodate the alkali atoms. The small clusters, composed of five Li atoms (with a centered tetrahedron structure) reside in the pseudo-tetrahedral voids, while the remaining two Li ions, which complete the stoichiometry, are probably delocalized in the remaining interstitial space [203]. Above 553 K the structure changes to *fcc* (space group $Fm\bar{3}m$), with the Li clusters located in the center of the octahedral voids and the C_{60} molecules characterized by rotational disorder (see Fig. 8.2).

8.3 Inelastic Neutron Scattering: $Li_{12}C_{60}$ and Li_6C_{60}

Inelastic Neutron Scattering data have been collected on IN4C at the ILL (see Chap. 2). About 300 mg of Li-intercalated fulleride powder has been sealed in a standard aluminium flat container with an indium o-ring and measured using neutron incident wavelengths of 1.11, 2.41 and 3.0 Å. Different datasets, collected at several temperatures from 10 to 320 K, have been treated according to the standard data treatment as described in Chap. 2. The signal was then converted into the generalized density of states $G(\omega)$, susceptibility $\frac{\chi(\omega)}{\omega}$ or the map $S(Q,\omega)$ and reported in the most convenient representation [205]. *Ab-initio* phonon calculations have been carried out on the $Li_{12}C_{60}$ low temperature structure in order to attribute the experimental INS features to specific normal modes in the lattice, as expected for the refined structure reported in [203].

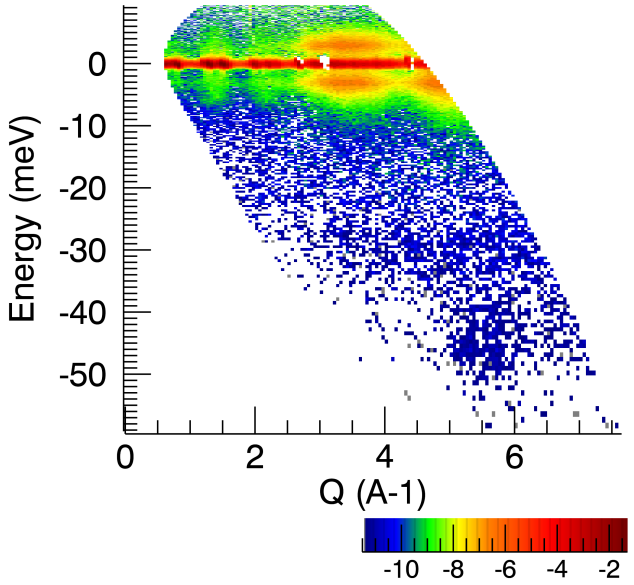

FIGURE 8.3: $S(Q,\omega)$ map of $Li_{12}C_{60}$. Data have been collected on IN4C at the ILL at 320 K and using an incident $\lambda = 2.41$ Å.

The $S(Q,\omega)$ maps of $Li_{12}C_{60}$ and Li_6C_{60} present typical features associated with the rotations of the C_{60} molecule (see Fig. 8.3 and Fig. 8.4). They appear as a diffuse lobe with a maximum located at $Q \approx 3.4$ Å^{-1} [206, 207]. The energy dependence of the signal is however much better defined in $Li_{12}C_{60}$ than in Li_6C_{60}. In Fig. 8.5 we have reported the $S(\omega)$ of $\mathbf{Li_{12}C_{60}}$, obtained from IN4C data after grouping over the entire Q-range and measured at different temperatures ($\lambda = 3.0$ Å). It is clearly identifiable a well-defined and T-indipendent libration peak, located around 3.0 meV as in pure C_{60} and indicating the absence of dynamical disorder in the investigated temperature range. No dramatic

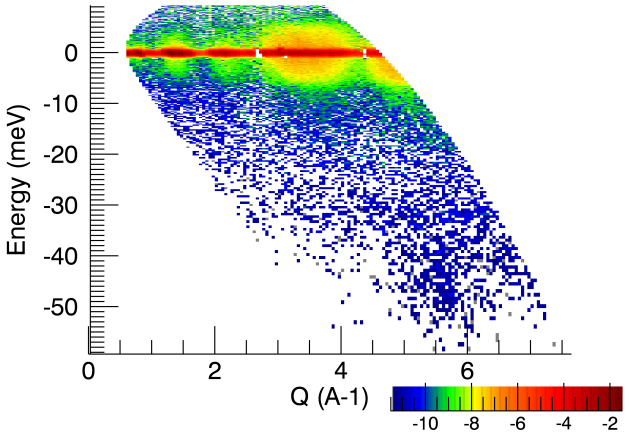

FIGURE 8.4: $S(Q,\omega)$ map of Li_6C_{60}. Data have been collected on IN4C at the ILL at 320 K and using an incident $\lambda = 2.41$ Å.

temperature-induced distortion of the lattice modes seem to occur in the [10 K - 320 K] temperature interval; however further investigations, with optimized experimental conditions for the low-energy range, are required for completing the study. Moreover, the lack of evolution of the principal C_{60} molecular modes with temperature indicates the absence of severe modification of their local environment (see Fig. 8.6, Fig. 8.7). For $\mathbf{Li_6C_{60}}$, the lack of a well–defined libration frequency and a different distribution of the intramolecular C_{60} modes suggest a possible distortion of the buckyball, *i.e.* due to the inhomogeneous character of the charge distribution, and the existence of static disorder, which broadens the libration lines and damps the lattice modes (see Fig. 8.5 and Fig. 8.6). More detailed studies, including *ab-initio* phonon calculations are required for further investigating the Li_6C_{60} dynamical and structural properties.

The theoretical $G(\omega)$ was calculated using the direct method as implemented in the software PHONON [208] on the basis of first-principles calculations. They were performed within the projector augmented wave (PAW) formalism of the Kohn - Sham density functional theory, in the generalized gradient approximation (GGA) and using the Vienna ab-initio simulation package (VASP). All electronic functions were calculated at the gamma point only and applying an energy cut-off of 450.0 eV. Following the geometry optimization, a series of single point energy (SPE) calculations, which give the Hellmann-Feynman forces were performed. The dynamical matrix for any point in reciprocal space was generated and diagonalized to compute phonon eigenmodes i with momentum $\hbar\vec{q}$ and energy $\hbar\omega(\vec{q},i)$, for a large number of $\vec{Q} = \vec{q} + \vec{G_{hkl}}$ [1] with random orientation on a dense equidistant grid. The neutron scattering lengths of the elements were taken into account to compute the phonon form factors as they are detected in an

[1] $\vec{G_{hkl}}$ represents the lattice vectors.

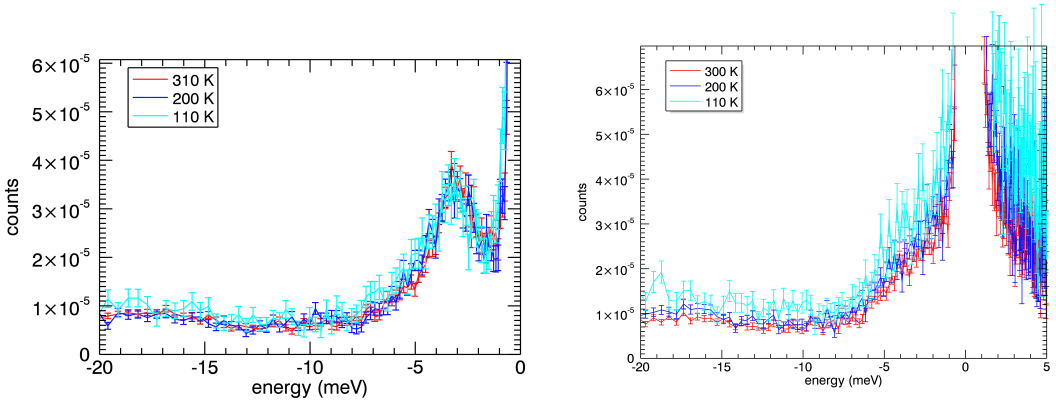

FIGURE 8.5: *Left:* $S(\omega)$ of $Li_{12}C_{60}$.
Right: $S(\omega)$ of Li_6C_{60}. Data were collected at different temperatures IN4C using $\lambda =$ 3.0 Å as incident wavelength and corrected for the Bose-population factor.

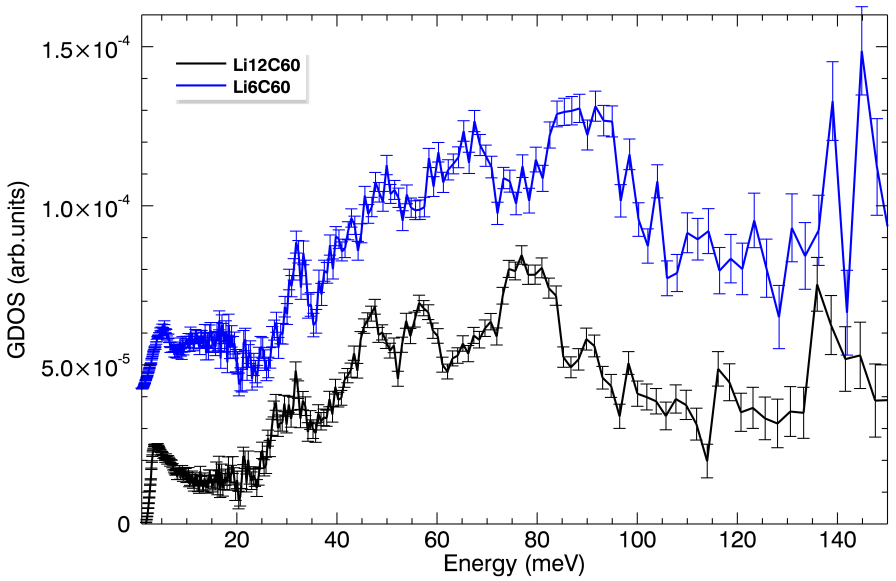

FIGURE 8.6: GDOS of Li_6C_{60} and $Li_{12}C_{60}$ measured on IN4C at 320 K and using an incident $\lambda = 2.41$ Å . The GDOS of Li_6C_{60} displays important similarities with respect to $Li_{12}C_{60}$, in particular in the Li-modes region [10-50 meV]. The clear modification of the intramolecular modes [E $\geq$40 meV] with respect to $Li_{12}C_{60}$ suggests a probable lower symmetry and the distortion of the buckyball.

INS experiment. A detailed description of the direct method for the phonon calculation is not in the intent of this chapter. The interested reader could refer to [209] and [210] or to the Phonon software manual [208] for a detailed overview.

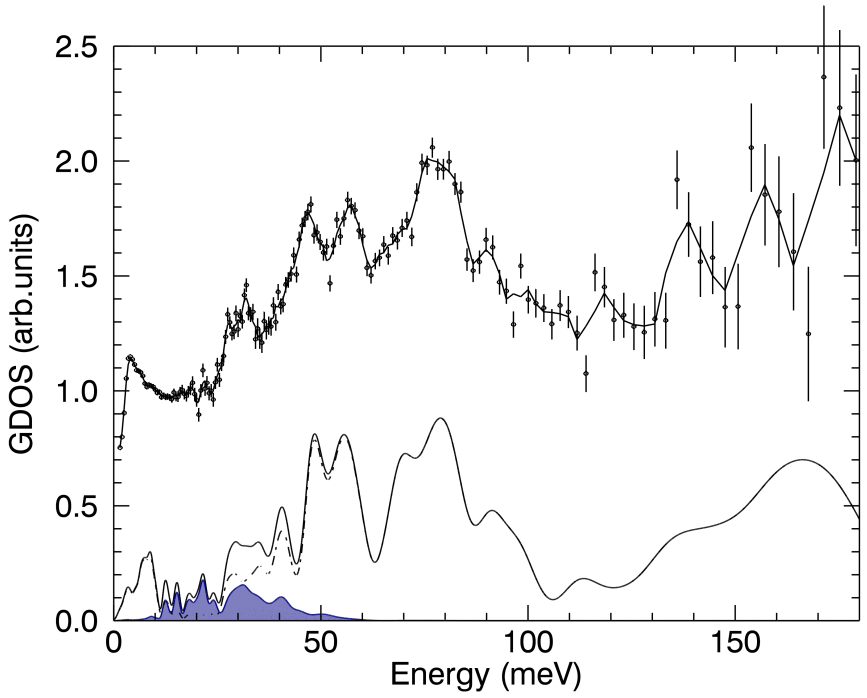

FIGURE 8.7: (top curve, black dots) $Li_{12}C_{60}$ GDOS was extracted from IN4C data at 320 K and using 2.41 Å as incident neutrons. The bottom curves show the calculated GDOS of $Li_{12}C_{60}$ (black solid line), the Carbon (black dot-dashed line) and Lithium (blue solid line and shaded blue area) partial GDOS. The theoretical spectra were convoluted with a Gaussian function having a full width at half maximum matching the energy resolution of IN4C at the experimental conditions.

Fig. 8.7 shows the Generalized Density of States (GDOS) of the $Li_{12}C_{60}$ powder sample, measured on IN4C at 320 K using 2.41 Å as neutron incident wavelength. The experimental spectrum is shown together with the results obtained from *ab-initio* lattice dynamics calculations. The GDOS displays several bands separated by gaps, typical of a molecular crystal, distributed over a wide energy range from zero to 180 meV. The $Li_{12}C_{60}$ spectrum shares strong similarities with that of pure C_{60} [206] but also significant differences, especially in the low frequency range (< 50 meV). The spectrum of C_{60} displays a band below 8 meV resulting from modes of the molecules as a whole. A ≈ 20 meV gap separates the latter band from the first C_{60} molecular mode (of Hg symmetry) at 33 meV, appearing in the GDOS as a sharp intense feature. The $Li_{12}C_{60}$ GDOS does not show a comparable lack of modes in this "gap" frequency range. By contrast, a significant intensity is observed in the 15-25 meV range and a complex feature at 27–33 meV replaces the well-defined peak at 33 meV found in pure C_{60}. The comparison

with the theoretical results allows to attribute the low frequency features extending up to 10 meV to the lattice modes involving C_{60} translations and rotations. In addition, the complex structure at 27–33 meV is very well reproduced by the simulations and mostly originates from the parent C_{60} radial modes which are split into more components due to the electronic charge redistribution at the C_{60} surface and lower symmetry of the $Li_{12}C_{60}$ crystal. Our calculations show that the partial GDOS of Li (blue area in Fig. 8.7) contributes to the total spectrum from 10 meV up to 50 meV, with several peaks in the C_{60} gap region, e.g. [10-27 meV], where no contribution from C vibrations is expected, making this frequency window a perfect probe of the Li dynamics.

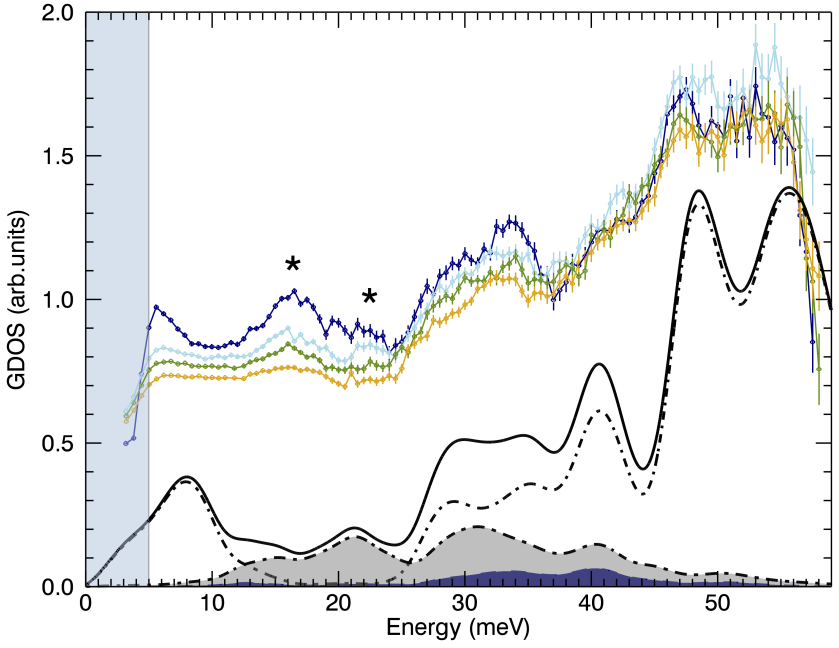

FIGURE 8.8: Generalized density of states (GDOS) of $Li_{12}C_{60}$ was derived from IN4C data collected using 1.1 Åas incident neutrons at 10, 200, 250 and 320 K. The bottom curves show the calculated total GDOS of $Li_{12}C_{60}$ (black solid line), Carbon (black dot-dashed line) and Lithium (solid line and shaded grey area) partial GDOS. The navy area within the grey area represents only the partial GDOS of Li atom at the centre of the tetrahedral cluster. The calculated spectra were convoluted with a Gaussian function having a full width at half maximum matching the energy resolution of IN4C for the specific experimental conditions.

The experimental GDOS collected at 10, 200, 250 and 320 K (Fig. 8.8) clearly show that the bands located around 15 and 22 meV drop as the temperature increases, while the other bands are essentially unaffected. The experimental INS data are compared to the spectra calculated at 10 K. Two important features are calculated at 15 and 22 meV, in good correspondence with the peaks in this range in the 10 K data. These modes are essentially related to the displacement of the lithium atoms located at the corners of

the tetrahedron, making the Li cluster, while the one in the central position contributes at larger frequencies. No new modes, nor softening seem to appear in the GDOS as a function of temperature, indicating that the Li dynamics is certainly getting significantly softer as the temperature rises. INS measurements therefore support the hypothesis of a progressive change in the dynamics of the Li atoms (probably those at the corner of the tetrahedron cluster), from an oscillating character to an over-damped character, as temperature increases. This behavior appears compatible with a progressive melting of the Li - tetrahedral clusters, which is probably at the origin of the very high ionic conductivity of this material (not shown here and still under investigation).

8.4 $Li_{12}C_{60}$: Following the hydrogenation process

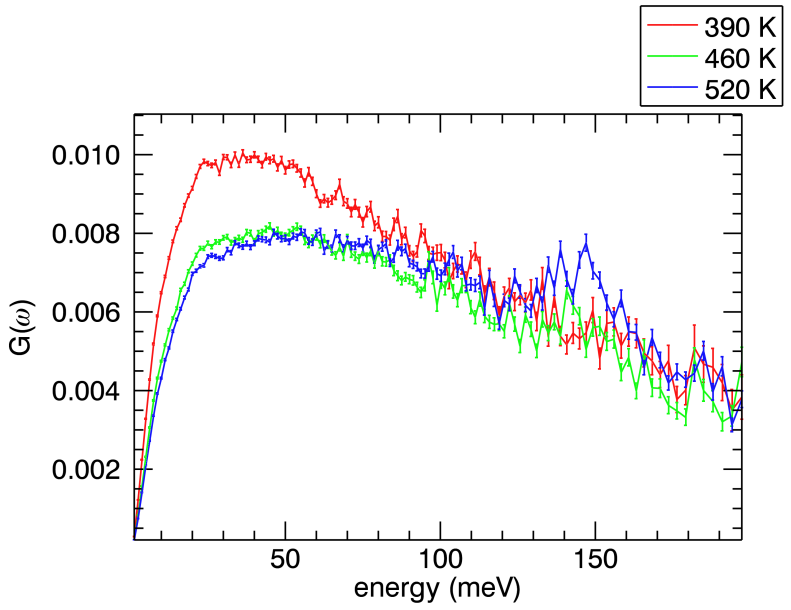

FIGURE 8.9: Hydrogenation of $Li_{12}C_{60}$ followed by INS: GDOS were collected on IN4C using $\lambda = 2.41$ Å, at different temperatures (from 300 K to 520 K) under 100 bar of H_2. Not all the temperatures have been reported for clarity.

We have followed the thermal evolution of the dynamical properties of the $Li_{12}C_{60}$ fulleride under hydrogen pressure, on the time–of–flight spectrometer IN4C. Neutron spectra in neutron-gain are expected to evidence the onset of the first states of hydrogenation and allow to distinguishing the nature and the local environment of the chemisorbed hydrogen, on the basis of different spectral responses.

The data were collected from RT to 500 K, with an incident wavelength of $\lambda = 2.41$ Å in high resolution mode. In Fig. 8.9, we report the evolution of the GDOS of $Li_{12}C_{60}$

under H_2 pressure (100 bar of H_2 have been loaded at RT, then the variation of the pressure in the sample holder has been recorded as a function of time and temperature) from RT to 520 K. Beside the signal coming from the recoil of molecular hydrogen [89], we can observe the first appearance of a peak located at 150 meV at 455 K. This is the typical frequency of C-H bending modes in hydrofullerite ($H_{36}C_{60}$) [211]. Even though $Li_{12}C_{60}$ is expected to reversibly absorb up to 5 wt% H_2 with an onset temperature of 540 K and through the partial segregation of Li-H, the signature of Li-H ($\approx$ 100 meV [212]) is not evident in this data set. It appears difficult to extract a reliable hypothesis for the hydrogenation process. Probably the experimental conditions (520 K and 100 bar of H_2) were too mild for allowing a complete hydrogenation. Further experiments on Lagrange are probably better suited for this energy range.

8.5 Inelastic Neutron Scattering on the hydrogenated phases

Hydrogenated $Li_{12}C_{60}$ and Li_6C_{60} were obtained by thermal treatment at the temperature of 350^{o}C and a H_2 pressure of 100 bar[2]. $Li_{12}C_{60}$ can reversibly absorb up to 5 wt% H_2 at the temperature of $\approx$ 270^{o}C similarly to Li_6C_{60} [213] and through the partial segregation of Li-H [16]. INS data of the $C_{60}H_x$ hydrofullerite shows that the energy regions corresponding to the intermolecular and radial intramolecular vibrations appear to be largely the same as in pure C_{60}, due to the fact that hydrogen atoms are chemically bound to the buckyball molecules. In particular, the contribution of the librational modes is slightly higher than that in pure C_{60} because of the larger librational amplitude of H atoms, which are further away from the centre of the molecule than the corresponding C atoms. Moreover INS spectra are dominated by a broad and strong band centered at $\omega \approx$155 meV, with a shoulder on the lower-energy side and a full width at half maximum of 35 meV [211].

The experimental GDOS of of $Li_6C_{60}H_y$ and $Li_{12}C_{60}H_y$ measured on IN4C are reported in Fig. 8.11 and 8.12. One can note the typical hydrofullerite features, with a very intense peak located at around 150 meV for both the samples, which is expected to originate mainly from Csp^3-H bending modes. Between 20 and 110 meV, the spectra exhibit four peaks at 25, 38, 56 and 75 meV, as well as some features at around 8 meV. For $Li_{12}C_{60}H_y$ one can observe the presence of another band located around 90 - 100 meV which can be indeed ascribed to the presence of a segregated Li-hydride phase [212].

[2]hydrogenation was carried on by Dr. Chiara Milanese of the Pavia H_2 lab (University of Pavia, Italy).

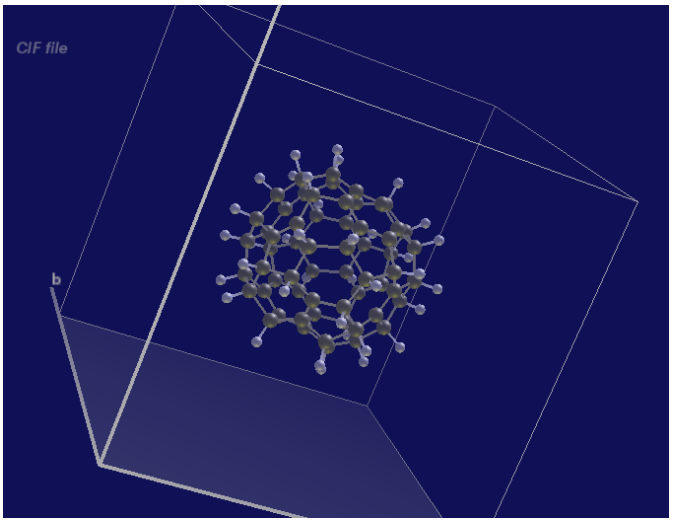

FIGURE 8.10: $C_{60}H_{36}$ molecule: the S_6 isomer (*ab-initio* optimized structure)

The hydrogenation of the C_{60} truncated icosahedron necessarily lowers the symmetry of the original molecule, because of the local distortion resulting from the sp^3 rather than sp^2 hybridization of the protonated carbons. In particular, the amount of chemisorbed hydrogen in our samples appears compatible with the formation of hydrofullerites with the $C_{60}H_{36}$ stoichiometry. There are roughly 10^{13} possible isomers of $C_{60}H_{36}$, but only four are energetically stable. The presence of various isomers depends mostly on the preparation method. These isomers, with symmetry T, T_h, D_{3d} and S_6 respectively, differ from the distribution of hexagonal - hexagonal and hexagonal - pentagonal rings bonds and hence differ from the local surface curvature [214].

The intensity and frequency of each vibrational component in the INS spectra is expected to strongly depend on the H local environment. The combination of DFT calculations and neutron spectroscopy data could allow to revealing the hydrogenation sites in Li and Na fullerides and subsequently provide structural models for the obtained hydrofullerites [215], as discussed for the case of H–TEGO in Chap. 5.

Thanks to the better resolution of the Lagrange spectrometer and the possibility to perform the data acquisition at low temperature (see Chap. 2), it has been possible to further investigate the complex structure of the C-H bending and stretching bands. We have recorded the INS spectra of $H_yLi_6C_{60}$, $H_yLi_{12}C_{60}$ and $H_yNa_{10}C_{60}$ on the Lagrange spectrometer [3].

[3]The $Na_{10}C_{60}$ compound is not discussed in this work. The amount of hydrogen absorbed is slightly inferior than for Li-intercalate compounds (around 3.5 wt % H_2). We have decided to focused our overview on Li_6C_{60} and $Li_{12}C_{60}$, which are better understood at the time of writing. Details for the interested reader can be found in [35, 216].

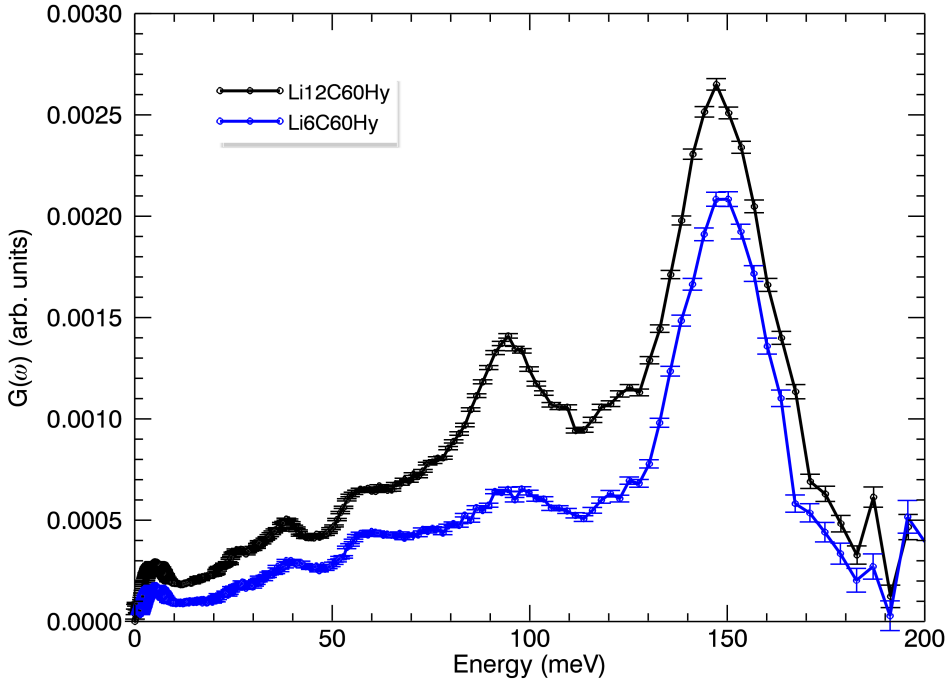

FIGURE 8.11: GDOS of $Li_6C_{60}H_y$ and $Li_{12}C_{60}H_y$ measured on IN4C at 320 K and using an incident $\lambda = 2.41$ Å .

The experimental data were recorded at 5 K to freeze the chemistry and reduce the thermal vibrations and Cu (220) and Cu (331) monochromators were used to select the incident wavelengths. The INS spectra (see Fig. 8.13) are presented together with the simulated H-pDOS for the different $C_{60}H_{36}$ isomers (see Fig. 8.14). H–pDOS have been calculated from *ab-initio* MD trajectories as described in Chap. 2. The energy transfer spanned the range from 27 meV to 500 meV, including also the stretching band, which appears located around 370 meV. The broad C-H bending band can be decomposed into three different components, located at 155, 164 and 170 meV, respectively and which constitute its fine structure. Surprisingly, this appears largely the same for all the samples measured and in good agreement with the simulations. In particular, the relative intensity of each bending line and the asymmetric shape of the stretching band, due to two adjacent peaks located at 360 and 385 meV, suggest the predominant presence of the T_h or D_{3d} hydrofullerite isomers. However, a more precise and quantitative attribution should account a probable multiphasicity and a not-homogenous hydrogenation degree of the samples.

The experimental $G(r)$ of $Li_6C_{60}D_y$, $Li_{12}C_{60}D_y$ and $Na_{10}C_{60}D_y$ measured on D4C (measured and extracted in the same experimental conditions as discussed for the other

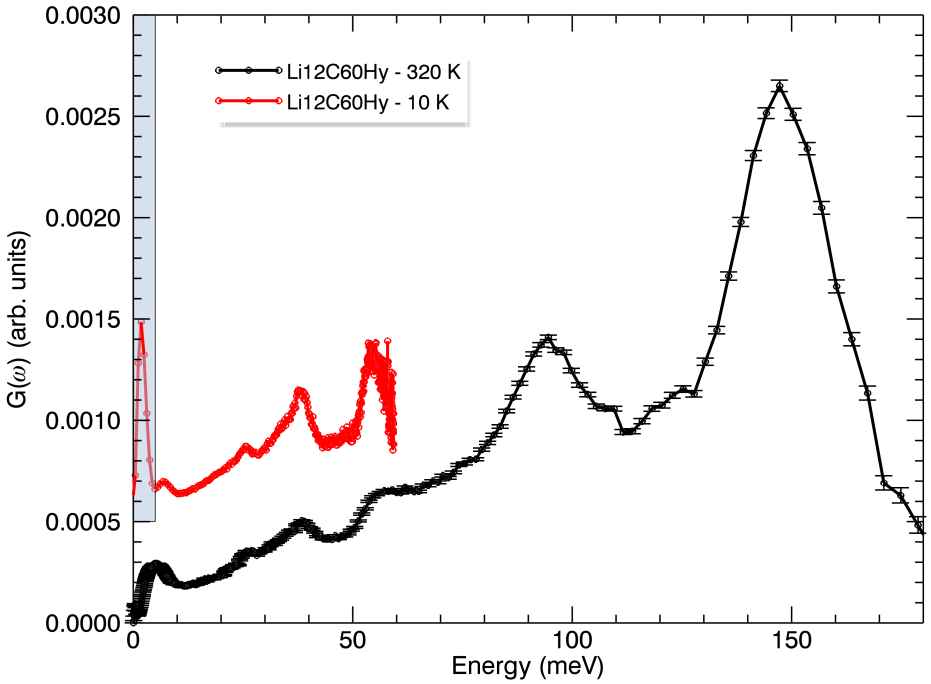

FIGURE 8.12: GDOS of the hydrogenated $Li_{12}C_{60}$ fulleride measured on IN4C at 320 K and λ=2.41 Å (black curve) and 10 K and λ = 1.11 Å (red curve). In the overshadowed region, INS data are affected by a strong contribution due to the elastic line.

samples) have been reported in Fig. 8.15. One can clearly observe a first peak at 1.10 Å corresponding to C-H(D) bond lengths and a second one at around 1.5 Å due to the first C-C distance. A more accurate data analysis, including modelization and structural refinements (in progress at this time) could allow to extracting more accurate informations about the interatomic distances and atomic arrangements. Ultimately, the combination of INS, modelization and PDF analysis, could allow to revealing the hydrogenation sites in Li- and Na-fullerides and subsequently, provide structural models for the obtained hydrofullerites.

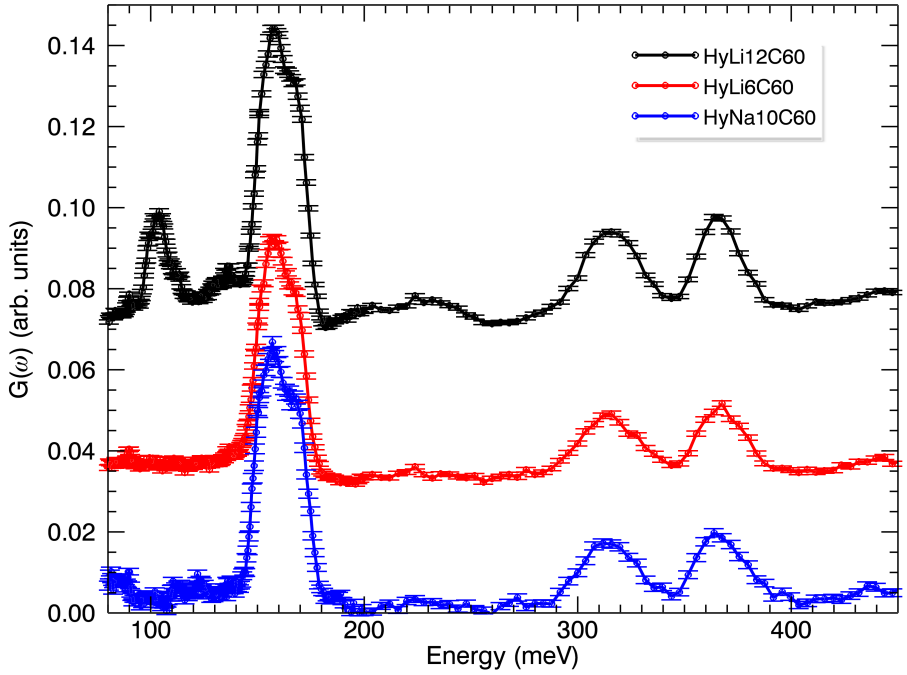

FIGURE 8.13: The hydrogenated fullerides $Li_6C_{60}H_y$, $Li_{12}C_{60}H_y$ and $Na_{10}C_{60}H_y$ measured on Lagrange at 5 K, using Cu(220) to monochromatize the incident beam. The peak around 310 meV is most likely the second-order of the strong C-H bending peak.

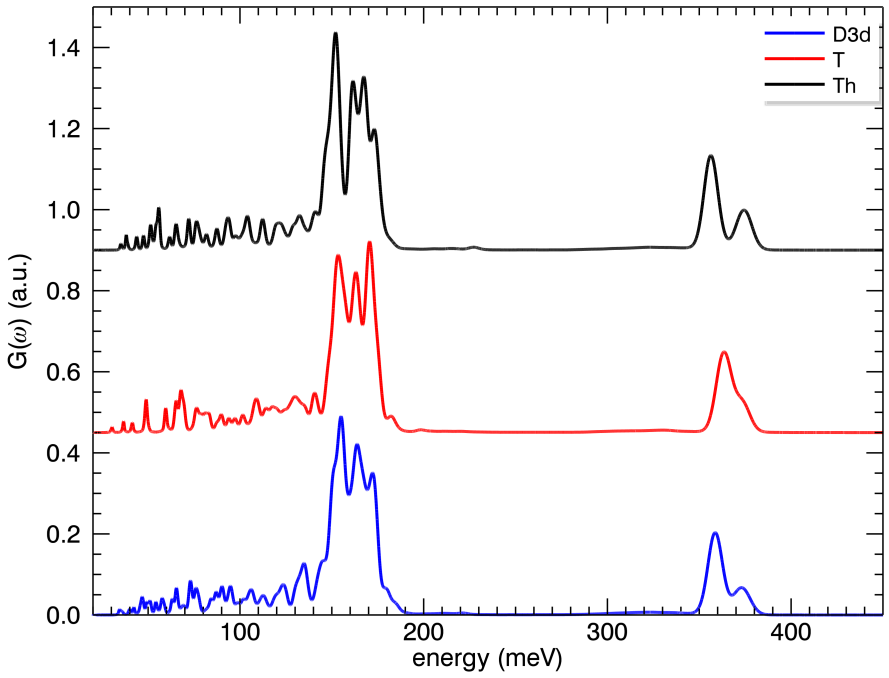

FIGURE 8.14: H-pDOS of the most stable $C_{60}H_{36}$ isomers T, T_h, D_{3d} simulated through *ab–initio* MD simulations. $S6$ has not been reported here since its spectrum appears very similar to T, but less-structured.

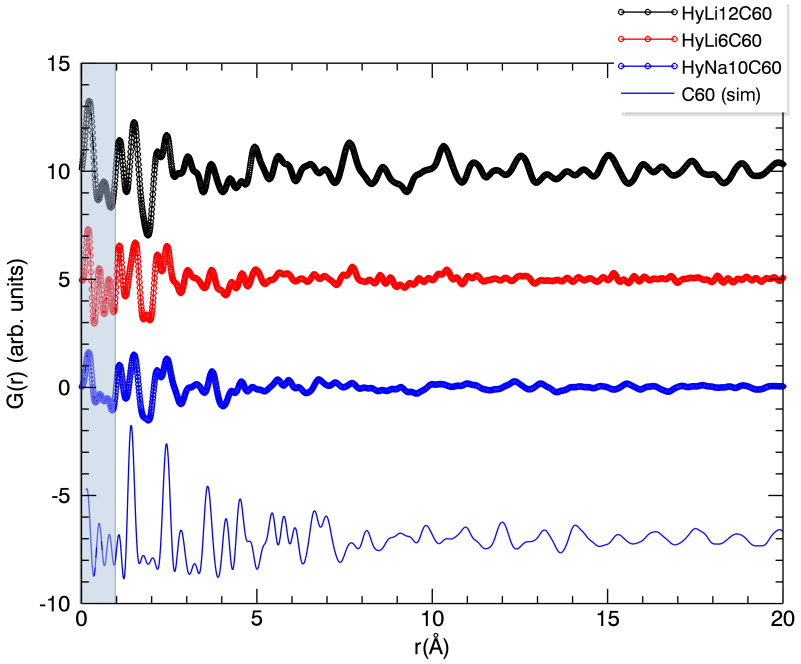

FIGURE 8.15: $G(r)$ of $Li_6C_{60}D_y$, $Li_{12}C_{60}D_y$ and $Na_{10}C_{60}D_y$ extracted from high energy diffraction data collected on D4C

8.6 Partial conclusions

The principle considerations of this chapter can be summarized in the following lines:

- We have presented the INS characterization of the Li-intercalated fullerides $Li_{12}C_{60}$ and Li_6C_{60} and in particular we have discussed the modification on the C_{60} dynamics induced by the presence of the intercalates. In $Li_{12}C_{60}$, the experimental features have been attributed with the help of *ab-initio* phonon calculations.
- The Li dynamics in $Li_{12}C_{60}$ has been probed by INS, revealing an internal Li cluster rearrangement above 150 K.
- We have presented an overview on the hydrogenated phases of $Li_{12}C_{60}$, Li_6C_{60} and $Na_{10}C_{60}$. The main vibrational features have been ascribed to the formation of hydrofullerite and the specific assignment has been done with the help of *ab-initio* simulations.
- A more complete study, including the synchronous combination of INS, diffraction/PDF analysis and *ab-initio* simulations are required for getting a deeper insight into the dynamical and structural properties of these metal-decorated carbon nanostructures. Ultimately this could help unravelling the hydrogen interactions underlying the absorption mechanism.

Chapter 9

Conclusions and Perspectives

The aim of this PhD project was the use of neutron scattering and DFT simulations to understand the specific chemical state of hydrogen adsorbed at some selected carbon nanostructures, in particular chemically synthesized defective graphene and alkali doped fullerides. The strategy was to extend the work previously carried out at the Carbon Nanostructures Laboratory (CNL) in Parma, to the neutron scattering perspective. This experimental technique stands as a natural probe for investigating hydrogenous materials and for providing a very deep insight into the hydrogen behavior, thanks to the high neutrons' sensitivity to hydrogen.

The thesis is organized in two parts:

- Chapters 4, 5 , 6 and 7 are focused on the study of *Thermal Exfoliated Graphite Oxide* (TEGO) based compounds.
- *Alkali-metals fullerides* A_xC_{60} (with A=Li and Na and x=6,10,12) are discussed in Chapter 8. This latter part stands as a complement to former studies conducted using several techniques within the CNL.

The INS spectra of $Li_{12}C_{60}$ and Li_6C_{60} reveal a significantly different phonon pattern. In particular the energy profile of the intense libration peak in the spectra suggests a lower symmetry of the Li_6C_{60} phase with respect to $Li_{12}C_{60}$. A non–homogeneous charge distribution at the cage surface or the presence of static merohedral disorders, similar to the bulk C_{60} compound, can be at the origin of this symmetry reduction. The temperature evolution of the $Li_{12}C_{60}$ spectra is in agreement with the μSR derived scenario of a T-dependent structural rearrangement of the Li-clusters inside the fullerene network. The hydrogenated phases of Li_6C_{60}, $Li_{12}C_{60}$ and $Na_{10}C_{60}$ display common features in

the high frequency range of the spectra, which stand as the vibrational signatures of hydrofullerites. Our combined INS and DFT analysis suggests the predominant presence of the T_h/D_{3d} hydrofullerene isomers in our samples.

The most significant part of the thesis was devoted to the study of TEGO–based compounds. The study of hydrogenated graphene, with muon spin spectroscopy μSR and ^{1}H-NMR, has clearly revealed its capacity to capture hydrogen. Two types of H atoms attached to the carbon framework were identified, one being static and one mobile, giving specific signatures in the NMR spectrum. Our studies have showed that Neutron Spectroscopy combined to DFT simulations, allowed to efficiently characterize the surface state of graphene. The INS investigations confirmed the presence of H atoms covalently bonded to C atoms in various positions onto the graphene planes. The *ab-initio*–based assignment of the C–H vibrational lines in the bending modes region, allowed to precisely individuate these configurations: some H atoms are located at the edge of the carbon framework, while the others are localized into defects on top of its surface. The temperature dependence of the spectral lines revealed an activated evolution of the surface H dynamics, with a relatively small energy barrier in agreement with that derived from NMR. We interpret this phenomenon as a quantum tunneling effect, occurring in partially saturated in-plane defects. The theoretical and experimental framework set up within these pioneering studies have to be continued and completed, including data collection with improved resolution and smaller temperature steps, from base temperature up to temperatures above 1000 K, where the complete detachment of H from the carbon network occurs. In addition, an appropriate theoretical formalization, accounting for the presence of defects in graphene and adapted to the case of the Single Atom Vacancy, is lacking at the moment. We hope that the present experimental evidence of the surprising mobility of H atoms at low temperature, will motivate such theoretical developments. Linking these observations to approaches of astrochemical relevance might shed light on the influence of the quantum nature of H on space chemistry.

Contrary to what we expected, our investigations reveal that the decoration of graphene with Nickel nanoparticles reduces the storage capacity of the modified hosts. This suggests that the Nickel nanoparticles passivate the defects, inhibiting their catalytic action in H_2 dissociation and subsequent H chemisorption. Further investigations are required to understand this peculiar inter-relation. This is of upmost importance in order to improve the H storage capacity of this system. At the moment, the storage capacity of H in graphene is insufficient and far to be usable in any device.

As a final conclusion, we would like to underline another important point relative to this work. The use of neutron spectroscopy not only reveals the presence of defects at the graphene surface but most important, it also provides an experimental solution to detect and characterize them qualitatively and quantitatively. This is of major importance in the graphene industry so as to monitor the process of this material with a controlled amount of defects. Moreover the anomalous behavior in temperature opens fascinating prospects, linked to the application of the methodology here discussed to other hydrogen–graphene systems, *i.e.* where H is bonded onto the plane, in Csp^3–H type configurations. For that, one should consider reconstructed planes or limit in-plane defects and apply H directly under atomic form.

This thesis has provided a statistical understanding of the structure of TEGO and has proved that the mobility of hydrogen is strongly linked to its local environment. Ultimately it has helped to provide a deeper understanding of the interaction between hydrogen and the carbon nanostructures, which appears of great fundamental and technological importance.

Appendix A

VASP

Some of the VASP INCAR files, used for the *ab-initio simulations* performed for H-graphene analysis. For more specific details, refer to the VASP user guide [217].

$system = Geometry Optimisation
NELMIN = 5 # it specifies the minimum number of electronic self-consistent steps.
EDIFF = 1E-4 # it specifies the global break condition for the electronic SC-loop.
EDIFFG = -1E-3 # it defines the break condition for the ionic relaxation loop
PREC = Accurate
IBRION = 2 # this parameter determines how the ions are updated and moved (conjugate-gradient algorithm)
ISIF = 2 # it controls whether the stress tensor is calculated (it does not allow any change in cell volume and shape)
NSW = 1500 # it defines the maximum number of ionic steps
LCHARG= .FALSE.
ISMEAR = 0; SIGMA=0.1 # it determines how the partial occupancies are set for each wavefunction (Gaussian smearing)

$system = Molecular Dynamics (setting for thermalisation)
ALGO = V # it specify the electronic minimisation algorithm (RMM-DIIS). Recommended for large MD runs
MAXMIX = 40
IBRION = 0
NSW = 2000
it specifies the length of the trajectory SMASS = -1 # it determines frequency of coupling to heat bath: Canonical (NVT ensemble) MD with temperature scaling to 300 K every 2 steps

NBLOCK = 2
POTIM = 1.0 # this is the time step in fs
TEBEG = 300
ISYM = 0
LREAL =.TRUE.
LCHARG =.FALSE.
NELMIN = 4
PREC = LOW
ISTART = 0 or 1
ISMEAR = 0; SIGMA=0.1

$system = Molecular Dynamics (setting for trajectories production)
ALGO = V
MAXMIX = 40
IBRION = 0
EDIFF = 1E-02
NSW = 10000
NBLOCK = 1
POTIM = 1.0
TEBEG = 300
ISYM = 0
SMASS = 0.001 # Canonical (NVT ensemble) MD with Nose thermostat
LREAL =.TRUE.
LCHARG =.FALSE.
NELMIN = 4
PREC = LOW
ISTART = 0
ISMEAR = 0; SIGMA=0.1

Appendix B

INS: Data Treatment

B.1 EXAMPLE 1: Data treatment for TOF-data (IN4)

```
rdset,PROPOSAL='proposalnumber' ;
; Vanadium ;
w58 = rdrun(51341) & w58 = normalise(w58) & w58 = in4strip(w58,\w,\bad)
; Li12C60(AEK) m=366.42 mg 0.5-0.25-3.75
;-------------------------------------------------------------------------------
;  320K -  2.41 A  - High T High lambda
; -> Extensive energy range for the GDOS on anti-Stokes side - "Low" Q
;-------------------------------------------------------------------------------
; 320K $\lambda$=2.4\AA HR (2.4_ELP_280_TF10 BC2 phase 26)
; High T, High lambda
; Extensive energy range for the GDOS on anti-Stokes side - Low Q
a='68909>68922' ; numors
w1=rdopr(a) \& w1=normalise(w1) \& w1=in4strip(w1,\/wide,\/bad) ; Reads data,
normalizes to Monitor1, removes small angle and bad detector
; empty cell
b='68929>68931'
t=0.85 ; transmission coefficient
w9=rdopr(b) \& w9=normalise(w9) \& w9=in4strip(w9,/wide,/bad)
w1=w1-t*w9 \& e1=sqrt(e1^2.+(t*e9)^2) ; remove the empty can
w2=corr_tof(w1,/b,propb=0.9, \/det) ; Subtracts a flat background
in each detector, found using a moving filter and corrects for
energy-variation of detector efficiency - \frame corrects for frameoverlap
w3=sumbank(w2) ; Averages intensities coming from detectors at same
```

```
scattering angle
w5=total(w3,1) \& x5=4*!pi*sin(x5*!pi/360.)/3 ; diffraction pattern in Q
w4 = vnorm(w3,w58,min = 322,max = 335)  ; Corrects for angle-variation
of detector efficiency (Vanadium normalization)
w19 = w4
w20 = t2e(w19) ; from tof to energy
w21=reb(w20, de=0.01)   ; rebid in energy with step de
w22 = sqw_rebin(w21,dq=0.10,emin=-20,\/swap) ; S(Q,w) map
w26=regular(w22) ; transform S(Q,w) on a regular grid
w23 = sgroup(w21,1)                          ; S(w)
w27=kis(w23, emin=-200, t=320.) ; Susceptibility - p23[11] should be 320 K
w24 = gdos(w23,emin=-200,emax=-0.1, /inv, elim=0.001)      ; GDOS
w24 = reb(w24,de=.1) ; rebin
w25 = w24 & x25 = -x24
;-------------------------------------------------------------------------------
; 10 K - 1.1 A - Low T
; ->  Good resolution at "Intermediate-High" Energies on Stokes side - High Q
;-------------------------------------------------------------------------------
; 10K l=1.11A (1.11A_ELP100_ETF)
a='69074>69079'
w1=rdopr(a) & w1=normalise(w1) & w1=in4strip(w1,/wide,/bad)
; empty cell 0.5-0.5
b='69062>69064'
t=0.85
w9=rdopr(b) & w9=normalise(w9) & w9=in4strip(w9,/wide,/bad)
w1=w1-t*w9 & e1=sqrt(e1^2.+(t*e9)^2)
w2=corr_tof(w1,/b,propb=0.5, /det)
w3=sumbank(w2)
w4 = vnorm(w3,w58,min = 322,max = 335)
w40 = w4
w41 = t2e(w40)
w42 = sqw_rebin(w41,dq=0.10,emin=-20,/swap)
w43 = sgroup(w41,1)
w44 = gdos(w43,emin = -200,lim=0.004)
w44 = reb(w44,de=.1)
```

B.2 EXAMPLE 1: Data treatment for LAGRANGE data

```
RDSET,PATH='/net/serdon/illdata/processed/133/in1/exp_7-04-125/processed
/HGrapheneAFH/',/raw
w50=read_column('Correction_factor_Cu220revised_LAMPascii.txt')
SETMANIP,/raw
;Sample 5K
;
SETMANIP,/raw
RDSET,inst='in1';,PATH='/Users/rols/Manips-neutrons/GRAPHENE/LAG_2013/
rawdata'
RDSET,PROPOSAL='exp_7-04-125',/raw
w1=rdrun(7002) ; Cu 220 1
w1=w1/n1 & x1=x1 & e1=e1/n1 & n1[*] = 1.0
w2=rdrun(7003) ; Cu 220 2
w2=w2/n2 & x2=x2 & e2=e2/n2 & n2[*] = 1.0
w3=rdrun(7004) ; Cu 220 3
w3=w3/n3 & x3=x3 & e3=e3/n3 & n3[*] = 1.0
w4=rdrun(7005) ; Cu 220 1
w4=w4/n4 & x4=x4 & e4=e4/n4 & n4[*] = 1.0
w5=rdrun(7006) ; Cu 220 2
w5=w5/n5 & x5=x5 & e5=e5/n5 & n5[*] = 1.0
w6=rdrun(7007) ; Cu 220 3
w6=w6/n6 & x6=x6 & e6=e6/n6 & n6[*] = 1.0
w1=0.5*(w1+w4) & e1=0.5*sqrt(e1^2+e4^2)
w2=0.5*(w2+w5) & e2=0.5*sqrt(e2^2+e5^2)
w3=0.5*(w3+w6) & e3=0.5*sqrt(e3^2+e6^2)
;
w7=[w1,w2,w3] & x7=[x1,x2,x3] & e7=[e1,e2,e3] & n7=[n1,n2,n3]
;Substract empty cell - load in w45!
;RDSET,PATH='/Users/rols/Manips-neutrons/GRAPHENE/LAG_2013/
Empty_Lagrange+cell/'
RDSET,PATH='/net/serdon/illdata/processed/133/in1/exp_7-04-125/
processed/Empty_Lagrange+cell/'
w45=rdopr('6572>6574')
w45=w45/n45 & x45=x45 & e45=e45/n45 & n45[*] = 1.0
w46=interpol(w45,x45,x7) & x46=x7 & e46=interpol(e45,x45,x7) &
n46=interpol(n45,x45,x7)
w21=w7-w46 & x21=x7 & e21=sqrt(e7^2+e46^2)
```

```
w8=w21
;water correction factor: load in w50!
w55=interpol(w50,x50,x8) & x55=x8 & e55=interpol(e50,x50,x8)
;& n55=interpol(n50,x50,x8)
;Correction of data
w9=w8*w55 & x9=x8 & e9=e8*w55
;
w10=w9 & x10=x9-4.; sample Cu220 5K
;
;Sample 100K
;
RDSET,inst='in1';,PATH='/Users/rols/Manips-neutrons/GRAPHENE/
LAG_2013/rawdata'
RDSET,PROPOSAL='exp_7-04-125',/raw
w1=rdrun(7012) ; Cu 220 1
w1=w1/n1 & x1=x1 & e1=e1/n1 & n1[*] = 1.0
w2=rdrun(7013) ; Cu 220 2
w2=w2/n2 & x2=x2 & e2=e2/n2 & n2[*] = 1.0
w3=rdrun(7014) ; Cu 220 3
w3=w3/n3 & x3=x3 & e3=e3/n3 & n3[*] = 1.0
w4=rdrun(7015) ; Cu 220 1
w4=w4/n4 & x4=x4 & e4=e4/n4 & n4[*] = 1.0
w5=rdrun(7016) ; Cu 220 2
w5=w5/n5 & x5=x5 & e5=e5/n5 & n5[*] = 1.0
;w6=rdrun(7014) ; Cu 220 3
;w6=w6/n6 & x6=x6 & e6=e6/n6 & n6[*] = 1.0
w1=0.5*(w1+w4) & e1=0.5*sqrt(e1^2+e4^2)
w2=0.5*(w2+w5) & e2=0.5*sqrt(e2^2+e5^2)
;w3=0.5*(w3+w6) & e3=0.5*sqrt(e3^2+e6^2)
;
w7=[w1,w2,w3] & x7=[x1,x2,x3] & e7=[e1,e2,e3] & n7=[n1,n2,n3]
;Substract empty cell - load in w45!
RDSET,PATH='/net/serdon/illdata/processed/133/in1/exp_7-04-125/
processed/Empty_Lagrange+cell/'
;RDSET,PATH='/Users/rols/Manips-neutrons/GRAPHENE/LAG_2013/
Empty_Lagrange+cell/'
w45=rdopr('6572>6574')
w45=w45/n45 & x45=x45 & e45=e45/n45 & n45[*] = 1.0
w46=interpol(w45,x45,x7) & x46=x7 & e46=interpol(e45,x45,x7)
```

```
& n46=interpol(n45,x45,x7)
w21=w7-w46 & x21=x7 & e21=sqrt(e7^2+e46^2)
w8=w21
;water correction factor: load in w50!
w55=interpol(w50,x50,x8) & x55=x8 & e55=interpol(e50,x50,x8)
;& n55=interpol(n50,x50,x8)
;Correction of data
w9=w8*w55 & x9=x8 & e9=e8*w55
;
w13=w9 & x13=x9-4. ; sample Cu220 100K
;
;Sample 200K
;
RDSET,inst='in1';,PATH='/Users/rols/Manips-neutrons/GRAPHENE/
LAG_2013/rawdata'
RDSET,PROPOSAL='exp_7-04-125',/raw
w1=rdrun(7019) ; Cu 220 1
w1=w1/n1 & x1=x1 & e1=e1/n1 & n1[*] = 1.0
w2=rdrun(7020) ; Cu 220 2
w2=w2/n2 & x2=x2 & e2=e2/n2 & n2[*] = 1.0
w3=rdrun(7021) ; Cu 220 3
w3=w3/n3 & x3=x3 & e3=e3/n3 & n3[*] = 1.0
w4=rdrun(7022) ; Cu 220 1
w4=w4/n4 & x4=x4 & e4=e4/n4 & n4[*] = 1.0
w5=rdrun(7023) ; Cu 220 2
w5=w5/n5 & x5=x5 & e5=e5/n5 & n5[*] = 1.0
w6=rdrun(7024) ; Cu 220 3
w6=w6/n6 & x6=x6 & e6=e6/n6 & n6[*] = 1.0
w1=0.5*(w1+w4) & e1=0.5*sqrt(e1^2+e4^2)
w2=0.5*(w2+w5) & e2=0.5*sqrt(e2^2+e5^2)
w3=0.5*(w3+w6) & e3=0.5*sqrt(e3^2+e6^2)
;
w7=[w1,w2,w3] & x7=[x1,x2,x3] & e7=[e1,e2,e3] & n7=[n1,n2,n3]
;Substract empty cell - load in w45!
RDSET,PATH='/net/serdon/illdata/processed/133/in1/exp_7-04-125/
processed/Empty_Lagrange+cell/'
;RDSET,PATH='/Users/rols/Manips-neutrons/GRAPHENE/LAG_2013/
Empty_Lagrange+cell/'
w45=rdopr('6572>6574')
```

```
w45=w45/n45 & x45=x45 & e45=e45/n45 & n45[*] = 1.0
w46=interpol(w45,x45,x7) & x46=x7 & e46=interpol(e45,x45,x7)
& n46=interpol(n45,x45,x7)
w21=w7-w46 & x21=x7 & e21=sqrt(e7^2+e46^2)
w8=w21
;water correction factor: load in w50!
w55=interpol(w50,x50,x8) & x55=x8 & e55=interpol(e50,x50,x8)
;& n55=interpol(n50,x50,x8)
;Correction of data
w9=w8*w55 & x9=x8 & e9=e8*w55
;
w15=w9 & x15=x9-4. ; sample Cu220 200K
;
;Sample 300K
;
RDSET,inst='in1';,PATH='/Users/rols/Manips-neutrons/GRAPHENE
/LAG_2013/rawdata'
RDSET,PROPOSAL='exp_7-04-125',/raw
w1=rdrun(7027) ; Cu 220 1
w1=w1/n1 & x1=x1 & e1=e1/n1 & n1[*] = 1.0
w2=rdrun(7028) ; Cu 220 2
w2=w2/n2 & x2=x2 & e2=e2/n2 & n2[*] = 1.0
w3=rdrun(7029) ; Cu 220 3
w3=w3/n3 & x3=x3 & e3=e3/n3 & n3[*] = 1.0
w4=rdrun(7030) ; Cu 220 1
w4=w4/n4 & x4=x4 & e4=e4/n4 & n4[*] = 1.0
w5=rdrun(7031) ; Cu 220 2
w5=w5/n5 & x5=x5 & e5=e5/n5 & n5[*] = 1.0
w6=rdrun(7032) ; Cu 220 3
w6=w6/n6 & x6=x6 & e6=e6/n6 & n6[*] = 1.0
w1=0.5*(w1+w4) & e1=0.5*sqrt(e1^2+e4^2)
w2=0.5*(w2+w5) & e2=0.5*sqrt(e2^2+e5^2)
w3=0.5*(w3+w6) & e3=0.5*sqrt(e3^2+e6^2)
;
w7=[w1,w2,w3] & x7=[x1,x2,x3] & e7=[e1,e2,e3] & n7=[n1,n2,n3]
;Substract empty cell - load in w45!
RDSET,PATH='/net/serdon/illdata/processed/133/in1/exp_7-04-125
/processed/Empty_Lagrange+cell/'
;RDSET,PATH='/Users/rols/Manips-neutrons/GRAPHENE/LAG_2013/
```

```
Empty_Lagrange+cell/'
w45=rdopr('6572>6574')
w45=w45/n45 & x45=x45 & e45=e45/n45 & n45[*] = 1.0
w46=interpol(w45,x45,x7) & x46=x7 & e46=interpol(e45,x45,x7)
& n46=interpol(n45,x45,x7)
w21=w7-w46 & x21=x7 & e21=sqrt(e7^2+e46^2)
w8=w21
;water correction factor: load in w50!
w55=interpol(w50,x50,x8) & x55=x8 & e55=interpol(e50,x50,x8)
;& n55=interpol(n50,x50,x8)
;Correction of data
w9=w8*w55 & x9=x8 & e9=e8*w55
;
w17=w9 & x17=x9-4. ; sample Cu220 300K
;-------------------------------------------------------------
;Rebin to de=1.
;-------------
e=1.
w30=reb(w10,de=1.,/force)
w31=reb(w13,de=1.,/force)
w32=reb(w15,de=1.,/force)
w33=reb(w17,de=1.,/force)
;-------------
;OUTPUT
;-------------
output,w30,'HgrapheneAFH_5K.dat' & print,'Data for AFH
@ 5K saved in file HgrapheneAFH_5K.dat'
output,w31,'HgrapheneAFH_100K.dat' & print,'Data for AFH
@ 100K saved in file HgrapheneAFH_100K.dat'
output,w32,'HgrapheneAFH_200K.dat' & print,'Data for AFH
@ 200K saved in file HgrapheneAFH_200K.dat'
output,w33,'HgrapheneAFH_300K.dat' & print,'Data for AFH
@ 300K saved in file HgrapheneAFH_300K.dat'
;-------------
SAVESESSION
; NOTE: multiphonon and Debye-Waller corrections are not
included in this .prox file
```

Bibliography

[1] Hassan Raza (Ed.). Graphene nanoelectronics. Technical Report XXIII, Metrology, Synthesis, Properties and Applications Series: NanoScience and Technology, 2012.

[2] F. Schedin, A. K. Geim, S. V. Morozov, and K. S. Novoselov. Detection of individual gas molecules adsorbed on graphene. *Nature Materials*, 6:652–655, 2007.

[3] A. Krueger. New carbon materials: Biological applications of functionalized nanodiamond materials. *Chem. Eur. J.*, 14:1382–1390, 2008.

[4] L. Schlapbach and A. Züttel. Hydrogen-storage materials for mobile applications. *Nature*, 414:353–358, 2001.

[5] M. F, Yu, O. Lourie, M. J. Dyer, K. Moloni, T. F. Kelly, and R. S. Ruoff. Strength and breaking mechanism of multiwalled carbon nanotubes under tensile load. *Science*, 287(637), 2000.

[6] K. S. Novoselov, A. K. Geim, S. V. Morozov, D. Jiang, Y. Zhang, S. V. Dubonos, I. V. Grigorieva, and A. A. Firsov. Electric field effect in atomically thin carbon films. *Science*, 306(5696):666–669, 2004.

[7] H. W. Kroto. C_{60} : Buckminsterfullerene, the celestial sphere that fell to earth. *Angew. Chem. Int. Ed. Engl.*, 31:111–129, 1992.

[8] W. I. F. David, R. M. Ibberson, J. C. Matthewman, K. Prassides, T. J. S. Dennis, J. P. Hare, and H. W. Kroto. Crystal structure and bonding of ordered C_{60}. *Nature*, 353:147–149, 1991.

[9] J. R. Olson, K. A. Topp, and R. O. Pohl. Specific heat and thermal conductivity of solid fullerenes. *Science*, 19(259):5098, 1993.

[10] H. Schober, A. Tölle, B. Renker, R. Heid, and F. Gompf. Microscopic dynamics of AC_{60} compounds in the plastic, polymer, and dimer phases investigated by inelastic neutron scattering. *Phys. Rev. B*, 56:5937–5950, Sep 1997. doi: 10.

1103/PhysRevB.56.5937. URL http://link.aps.org/doi/10.1103/PhysRevB.56.5937.

[11] P. A Heiney, G. BM Vaughan, J. E Fischer, N. Coustel, D. E Cox, J. RD Copley, DA Neumann, WA Kamitakahara, K. M Creegan, D. M Cox, et al. Discontinuous volume change at the orientational-ordering transition in solid C_{60}. *Physical Review B*, 45(8):4544, 1992.

[12] S. Liu, Y. J. Lu, M. M. Kappes, and J. A. Ibers. The structure of the C_{60} molecule: X-Ray crystal structure determination of a twin at 110 K. *Science*, 254(5030):408–410, 1991.

[13] Q. Zhu, O. Zhou, N. Coustel, G. B. M. Vaughan, J. P. McCauley, W. J. Romanow, J. E. Fischer, and A. B. Smith. X-ray diffaction evidence for nonstoichiometric Rubidium-C_{60} intercalation compounds. *Science*, 254(5031):545–548, 1991.

[14] S. P. Kelty, C. C. Chen, and C. M. Lieber. Superconductivity at 30 K in caesium-doped C_{60}. *Nature*, 352:223–225, 1991.

[15] M. Riccó, M. Belli, M. Mazzani, D. Pontiroli, D. Quintavalle, A. Janossy, and G. Csanyi. Superionic conductivity in the Li_4C_{60} fulleride polymer. *Physical review letters*, 102(14):145901, 2009.

[16] Ph. Mauron, M. Gaboardi, A. Remhof, A. Bliersbach, D. Sheptyakov, M. Aramini, G. Vlahopoulou, F. Giglio, D. Pontiroli, M. Riccó, and A. Zuttel. Hydrogen sorption in $Li_{12}C_{60}$. *J.Phys.Chem.C*, 117(44):22598–22602, 2013.

[17] A. K. Geim and K. S. Novoselov. The rise of graphene. *Nature Materials*, 6: 183–191, 2007.

[18] N. D. Mermin. Crystalline order in two dimensions. *Phys. Rev.*, 176(250), 1968.

[19] A. Fasolino, J. H. Los, and M. I. Katsnelson. Intrinsic ripples in graphene. *Nature Materials*, 6(858-861), 2007.

[20] J. C. Meyer, A. K. Geim, M. I. Katsnelson, K. S. Novoselov, T. J. Booth, and S. Roth. The structure of suspended graphene sheets. *Nature*, 446:60–63, 2007.

[21] URL http://graphene-flagship.eu/?page_id=34.

[22] H. Alloul. *Introduction to the Physics of Electrons in Solids*. Springer, 2007.

[23] A. Y Ganin, Y. Takabayashi, P. Jeglič, D. Arčon, A. Potočnik, P. J Baker, Y. Ohishi, M. T McDonald, M. D Tzirakis, A. McLennan, et al. Polymorphism control of superconductivity and magnetism in Cs_3C_{60} close to the Mott transition. *Nature*, 466(7303):221–225, 2010.

[24] M. S. Dresselhaus, G. Dresselhaus, and P. C. Eklund. *Science of Fullerenes and Carbon Nanotubes: Their Properties and Applications*. Academic Press, Mar 1996.

[25] K. Prassides and H. Alloul. *Fullerene-Based Materials: Structures and Properties*. Springer-Verlag, 2004.

[26] A. Zuttel, P. Sudan, Ph, Mauron, T. Kiyobayashi, Ch, Emmenegger, and L. Schlapbach. Hydrogen storage in carbon nanostructures. *International Journal of Hydrogen Energy*, 27(2):203–212, 2002.

[27] A. C. Dillon, K. M. Joned, T. A. Bekkedahl, C. H. Klang, D. S. Bethune, and M. J. Heben. Storage of hydrogen in sigle-walled carbon nanotubes. *Nature*, 386: 377–379, 1997.

[28] R. Ströbel, J. Garche, P. T. Moseley, L. Jörissenb, and G. Wolf. Hydrogen storage by carbon materials. *Journal of Power Sources*, 159(2):781–801, Sep 2006.

[29] URL http://energy.gov.

[30] G. J. Kubas. Metal-dihydrogen and σ-bond coordination: the consummate extension of the dewar-chatt-duncanson model for metal-olefin π bonding. *J. Organomet. Chem*, 635:37–68, 2001.

[31] A. Singh, M. Ribas, and B. Yakobson. H-spillover through the catalyst saturation: An ab initio thermodynamics study. *ACS Nano*, 3:1657–1662, 2009.

[32] X. Ming Liu, Y. Tang, En Shi Xu, T. C. Fitzgibbons, G. S. Larsen, H. R. Gutierrez, Huan-Hsiung Tseng, Ming-Sheng Yu, Cheng-Si Tsao, J. V. Badding, et al. Evidence for ambient-temperature reversible catalytic hydrogenation in Pt-doped carbons. *Nano letters*, 13(1):137–141, 2012.

[33] C. S, Tsao, Y. Liu, H. Y, Chuang, A. Lueking, S. H, and Chen. Hydrogen spillover effect of pt-doped activated carbon studied by inelastic neutron scattering. *J. Phys. Chem. Lett.*, 2:2322–2325, 2011.

[34] Ph, Mauron, A. Remhof, A. Bliersbach, A. Borgschulte, A. Zuttel, D. Sheptyakov, M. Gaboardi, M. Choucair, D. Pontiroli, M. Aramini, and M. Riccó. Reversible hydrogen absorption in sodium intercalated fullerenes. *International Journal of Hydrogen Energy*, 37(19):14307–14314, 2012.

[35] M. Aramini, M. Gaboardi, G. Vlahopoulou, D. Pontiroli, C. Cavallari, C. Milanese, and M. Riccó. Muon spin relaxation reveals the hydrogen storage mechanism in light alkali metal fullerides. *Carbon*, (doi: http://dx.doi.org/10.1016/j.carbon.2013.09.063), 2013.

[36] M. Gaboardi. *Hydrogen storage in light alkali-cluster intercalated fullerides*. PhD thesis, Physics - University of Parma (Italy), 2014.

[37] M. Aramini. *The Hydrogen Storage in Alkali-Transition metal Fullerides*. PhD thesis, Science and Technology of Innovative Materials - University of Parma (Italy), 2014.

[38] R. J. Olsen, M. Beckner, M. B. Stone, P. Pfeifer, C. Wexler, and H. Taub. Quantum excitation spectrum of hydrogen adsorbed in nanoporous carbons observed by inelastic neutron scattering. *Carbon*, 58(46-58), 2013.

[39] K. Itoh, Y. Miyahara, S. Orimo, H. Fujii, T. Kamiyama, and T. Fukunaga. T he local structure of hydrogen storage nanocrystalline graphite by neutron scattering. *Journal of Alloys and Compounds*, 356-357:608–611, 2003.

[40] Z. Q. Li, C. J. Lu, Z. P. Xia, Y. Zhou, and Z. Luo. X-ray diffraction patterns of graphite and turbostratic carbon. *Carbon*, 45:1686–1695, 2007.

[41] J. O. Sofo, A. S. Chaudhari, and G. D. Barber. Graphane: A two-dimensional hydrocarbon. *Phys. Rev. B*, 75:153401, 2007.

[42] O. V. Yazyev and L. Helm. Defect-induced magnetism in graphene. *Phys. Rev. B*, 75(125408), 2007.

[43] D. Soriano, F. Munoz-Rojas, J. Fernandez-Rossier, and J. J. Palacios. Hydrogenated graphene nanoribbons for spintronics. *Phys. Rev. B*, 81(16):165409, 2010.

[44] W. Han, R. K. Kawakami, M. Gmitra, and J. Fabian. Graphene spintronics. *Nature Nanotechnology*, 9:794–807, 2014.

[45] L. Hornekaer, E. Rauls, W. Xu, Z. Sljivancanin, R. Otero, I. Stensgaard, E. Laegsgaard, B. Hammer, and F. Besenbacher. Clustering of chemisorbed H(D) atoms on the graphite (0001) surface due to preferential sticking. *Phys. Rev. Lett.*, 97 (186102), 2006.

[46] A. Andree, M. Le, Lay, T. Zecho, and J. Küper. Pair formation and clustering of D on the basal plane of graphite. *Chemical Physics Letters*, 425:99–104, 2006.

[47] R. Martinazzo and G. F. Tantardini. Quantum study of Eley-Rideal reaction and collision induced desorption of hydrogen atoms on a graphite surface. H-physisorbed case. *J. Chem. Phys.*, 124(124703), 2006.

[48] L. Horneaer, Z. Sljivancanin, W. Xu, R. Otero, E. Rauls, I. Stensgaard, E. Laegsgaard, B. Hammer, and F. Besenbacher. Metastable structures and recombination pathways for atomic hydrogen on the graphite (0001) surface. *Phys. Rev. Lett.*, 96(156104), 2006.

[49] L. Boschman, G. Reitsma, S. Cazaux, T. Schlathölter, R. Hoekstra, M. Spaans, and O. Gonzalez-Magana. Hydrogenation of PAH cations: a first step towards H_2 formation. *The Astrophysical Journal Letters*, 761(1):33–38, 2012.

[50] E. Rauls and L. Hornekaer. Catalyzed routes to molecular hydrogen formation and hydrogen addition reactions on neutral polycyclic aromatic hydrocarbon under interstellar conditions. *The Astrophysical Journal*, 679:531–536, 2008.

[51] Y. Lin, F. Ding, and B. I. Yakobson. Hydrogen storage by spillover on graphene as a phase nucleation process. *Phys. Rev. B*, 78:041402(R), 2008.

[52] C. P. Herrero and R. Ramirez. Vibrational properties and diffusion of hydrogen on graphene. *Phys. Rev. B*, 79:115429, 2009.

[53] L. Hornekaer, A. Baurichter, V. V. Petrunin, D. Field, and A. C. Luntz. Importance of surface morphology in interstellar H_2 formation. *Science*, 302(1943), 2003.

[54] M. Hirama, T. Tokosumi, T. Ishida, and J. Aihara. Possible molecular hydrogen formation mediated by the inner and outer carbon atoms of typical PAH cations. *Chemical Physics*, 305:307–316, 2004.

[55] H. M. Cuppen and L. Horneaer. Kinetic Monte Carlo studies of hydrogen abstraction from graphite. *J. Chem. Phys.*, 128(174707), 2008.

[56] S. Casolo, O. M. Lovvik, R. Martinazzo, and G. F. Tantardini. Understanding adsorption of hydrogen atoms on graphene. *J. Chem. Phys*, 130(054704), 2009.

[57] M. Bonfanti, R. Martinazzo, G. F. Tantardini, and A. Ponti. Physisorption and diffusion of hydrogen atoms on graphite from correlated calculations on the H-Coronene model system. *J.Phys.Chem.C*, 111:5825–5829, 2007.

[58] A. H. Castro, Neto, F. Guinea, N. M. R. Peres, K. S. Novoselov, and A. K. Geim. The electronic properties of graphene. *Rev. Mod. Phys.*, 81:109–162, 2009.

[59] A. R. Akhmerov and C. W. J. Beenakker. Detection of valley polarization in graphene by a superconducting contact. *Phys. Rev. Lett.*, 98(157003), 2007.

[60] A. A. Balandin, S. Ghosh, W. Bao, I. Calizo, D. Teweldebrhan, F. Miao, and C. N. Lau. Superior thermal conductivity of single-layer graphene. *Nano Letters*, 8(3): 902–907, 2008.

[61] K. I. Bolotin, K. J. Sikes, Z. Jianga, M. Klimac, G. Fudenberg, J. Honec, P. Kim, and H. L. Stormer. Ultrahigh electron mobility in suspended graphene. *Solid State Communications*, 146:351–355, 2008.

[62] C. W. J. Beenakker. Specular andreev reflection in graphene. *Phys. Rev. Lett.*, 97 (067007), 2006.

[63] K. S. Novoselov, A. K. Geim, S. V. Morozov, D. Jiang, M. I. Katsnelson, I. V. Grigorieva, S. V. Dubonos, and A. A. Firsov. Two-dimensional gas of massless dirac fermions in graphene. *Nature*, 438:197–200, 2005.

[64] A. K. Geim. Graphene: Status and prospects. *Science*, 324:1530–1534, 2009.

[65] K. S. Novoselov, V. I. Falko, L. Colombo, P. R. Gellert, M. G. Schwab, and K. Kim. A roadmap for graphene. *Nature*, 490:192–200, 2012.

[66] K. S. Novoselov, D. Jiang, F. Schedin, T. J. Booth, V. V. Khotkevich, S. V. Morozov, and A. K. Geim. Two-dimensional atomic crystals. *Proc. Natl Acad. Sci. USA*, 102:10451–10453, 2005.

[67] P. W. Sutter, J. I, Flege, and E. A. Sutter. Epitaxial graphene on ruthenium. *Nature Materials*, 7:406–411, 2008.

[68] K. R. Paton and J. N. Coleman. Scalable production of large quantities of defect-free few-layer graphene by shear exfoliation in liquids. *Nature Materials*, 13:624–630, 2014.

[69] M. Choucair, P. Thordarson, and J. A. Stride. Gram-scale production of graphene based on solvothermal synthesis and sonication. *Nature Nanotechnology*, 4:30–33, 2009.

[70] S. Park and R. S. Ruoff. Chemical methods for the production of graphenes. *Nature Nanotechnology*, 4:217–224, 2009.

[71] P. Mahanandia, F. Simon, G. Heinrich, and K. K. Nanda. An electrochemical method for the synthesis of few layer graphene sheets for high temperature applications. *Chem Commun (Camb)*, 50(35):4613–5, 2014.

[72] X. Li, G. Zhang, X. Bai, X. Sun, X. Wang, E. Wang, and H. Dai. Highly conducting graphene sheets and langmuir–blodgett films. *Nature Nanotechnology*, 3:538 – 542, 2008.

[73] A. Hashimoto, K. Suenaga, A. Gloter, K. Urita, and S. Iijima. Direct evidence for atomic defects in graphene layers. *Nature*, 430:870–873, 2004.

[74] F. Banhart, J. Kotakoski, and A. V. Krasheninnikov. Structural defects in graphene. *ACS Nano*, 5(1):26–41, 2011.

[75] H. Terrones, R. Lv, M. Terrones, and M. S. Dresselhaus. The role of defects and doping in 2d graphene sheets and 1d nanoribbons. *Rep. Prog. Phys*, 75:062501, 2012.

[76] C. P. Ewels, M. I. Heggie, and P. R. Briddon. Adatoms and nanoengineering of carbon. *Chemical Physics Letters*, 351:178–182, 2002.

[77] K. Nakada, M. Fujita, G. Dresselhaus, and M. S. Dresselhaus. Edge state in graphene ribbons: Nanometer size effect and edge shape dependence. *Phys. Rev. B*, 54(17954), 1996.

[78] T. Enoki, S. Fujii, and K. Takai. Zigzag and armchair edges in graphene. *Carbon*, 50(9):3141–3145, 2012.

[79] M. Fujita, K. Wakabayashi, K. Nakada, and K. Kusakabe. Peculiar localized state at zigzag graphite edge. *J. Phys. Soc. Jpn.*, 65:1920–1923, 1996.

[80] J. Kausteklis, P. Cevc, D. Arcon, L. Nasi, D. Pontiroli, M. Mazzani, and M. Riccó. Electron paramagnetic resonance study of nanostructured graphite. *Phys. Rev. B*, 84(125406), 2011.

[81] L. R. Radovic and B. Bockrath. On the chemical nature of graphene edges: Origin of stability and potential for magnetism in carbon materials. *J. Am. Chem. Soc.*, 127:5917–5927, 2005.

[82] R. Balog, B. Jørgensen, L. Nilsson, M. Andersen, E. Rienks, M. Bianchi, M. Fanetti, E. Lægsgaard, A. Baraldi, S. Lizzit, et al. Bandgap opening in graphene induced by patterned hydrogen adsorption. *Nature materials*, 9(4):315–319, 2010.

[83] M. Mazzani. *Muons and Hydrogen in Graphene*. PhD thesis, Science and Technology of Innovative Materials - University of Parma (Italy), 2011.

[84] M. Riccó, D. Pontiroli, M. Mazzani, M. Choucair, J. A. Stride, and O. V. Yazyev. Muons probe strong hydrogen interactions with defective graphene. *Nano Lett.*, 11(11):4919–4922, 2011.

[85] D. Pontiroli, M. Aramini, M. Gaboardi, M. Mazzani, S. Sanna, F. Caracciolo, P. Carretta, C. Cavallari, S. Rols, R. Tatti, L. Aversa, R. Verucchi, and M. Riccó. Tracking the hydrogen motion in defective graphene. *J.Phys.Chem.C*, 118(13): 7110–7116, 2014.

[86] A. J. Ramirez-Cuesta, M. O. Jones, and W. I. F. David. Neutron scattering and hydrogen storage. *Materials Today*, 12(11):54–61, 2009.

[87] D. A. Neumann. Neutron scattering and hydrogenous materials. *Materials Today*, 9(1-2):34–41, 2006.

[88] G. L. Squires. *Introduction to the Theory of Thermal Neutron Scattering*. Dover books on physics. Dover Publications, 1978. ISBN 9780486694474.

[89] S. W. Lovesey. *Theory of neutron scattering from condensed matter*. Number vol. 1 in International series of monographs on physics. Clarendon Press, 1984. ISBN 9780198520177.

[90] N. W. Ashcroft and N. D. Mermin. *Solid state physics*. Science: Physics. Saunders College, 1976. ISBN 9780030493461.

[91] A. A. Maradudin, G. H. Weiss, and E. W. Montroll. *Theory of lattice dynamics in the harmonic approximation*. Academic Press, New York, 1963.

[92] C. Bousige, S. Rols, J. Cambedouzou, B. Verberck, S. Pekker, E. Pellegrini, and P. Launois. Lattice dynamics of a rotor-stator molecular crystal: Fullerene-cubane $C_{60}{\cdot}C_8H_8$. *Phys. Rev. B*, 82:195413, Nov 2010. doi: 10.1103/PhysRevB.82.195413.

[93] Valeri Petkov. Nanostructure by high-energy x-ray diffraction. *Materials Today*, 11(11):28–38, 2008.

[94] H. E. Fischer, G. J. Cuello, P. Palleau, D. Feltin, A. C. Barnes, Y. S. Badyal, and J. M. Simonson. D4c: A very high precision diffractometer for disordered materials. *Applied Physics A*, 74(1):s160–s162, 2002. ISSN 0947-8396. doi: 10.1007/s003390101087.

[95] H. H Paalman and C. J. Pings. Numerical evaluation of x-ray absorption factors for cylindrical samples and annular sample cells. *Journal of Applied Physics*, 33 (8):2635–2639, 1962.

[96] I. A. Blech and B. L. Averbach. Multiple scattering of neutrons in vanadium and copper. *Physical Review*, 137(4A):A1113, 1965.

[97] J. L. Yarnell, M. J. Katz, R. G. Wenzel, and S. H. Koenig. Structure factor and radial distribution function for liquid argon at 85 k. *Physical Review A*, 7(6):2130, 1973.

[98] URL https://www.ill.eu/instruments-support/instruments-groups/instruments/in4c/description/instrument-layout/.

[99] H. Mutka. Coupled time and space focusing for time-of-flight inelastic scattering. *Nuclear Instruments and Methods in Physics Research Section A: Accelerators, Spectrometers, Detectors and Associated Equipment*, 338(1):144–150, 1994.

[100] A. Ivanov, M. Jimenéz-Ruiz, and J. Kulda. In1-lagrange–the new ill instrument to explore vibration dynamics of complex materials. In *Journal of Physics: Conference Series*, volume 554, page 012001. IOP Publishing, 2014.

[101] D. Sholl and J. A. Steckel. *Density Functional Theory: A Practical Introduction.* John Wiley and Sons, Inc., 2009.

[102] R. G. Parr and W. Yang. *Density-Functional Theory of Atoms and Molecules.* OUP, Oxford,, 1989.

[103] J. Callaway and N. H. March. Density functional methods: Theory and applications. *Solid State Physics*, 1984.

[104] A. D. Becke. Perspective: Fifty years of density-functional theory in chemical physics. *J. Chem. Phys.*, 140(18A301), 2014.

[105] P. Hohenberg and W. Kohn. Inhomogeneous electron gas. *Phys. Rev.*, 136(864B), 1964.

[106] W. Kohn and L. J. Sham. Self-consistent equations including exchange and correlation effects. *Phys. Rev.*, 140(A1133), 1965.

[107] D. M. Ceperley and B. J. Alder. Ground state of the electron gas by a stochastic method. *Phys. Rev. Lett.*, 45:566, 1980.

[108] J. P. Perdew, K. Burke, and M. Ernzerhof. Generalized gradient approximation made simple. *Phys. Rev. Lett.*, 77:3865, 1996.

[109] J. P. Perdew, J. A. Chevary, S. H. Vosko, K. A. Jackson, M. R. Pederson, D. J. Singh, and C. Fiolhais. Atoms, molecules, solids, and surfaces: Applications of the generalized gradient approximation for exchange and correlation. *Phys. Rev. B*, 48:4978, 1993.

[110] C. Lee, W. Yang, and R. G. Parr. Development of the colle-salvetti correlation-energy formula into a functional of the electron density. *Phys. Rev. B*, 37:785, 1988.

[111] J. P. Perdew. Density-functional approximation for the correlation energy of the inhomogeneous electron gas. *Phys. Rev. B*, 33:8822–24, 1986.

[112] D. Vanderbilt. Soft self-consistent pseudopotentials in a generalized eigenvalue formalism. *Phys. Rev. B (R)*, 40(11):7892–7896, 1990.

[113] P. E. Blöchl. Projector augmented-wave method. *Phys. Rev. B*, 50:17953, 1994.

[114] G. Kresse and D. Joubert. From ultrasoft pseudopotentials to the projector augmented-wave method. *Phys. Rev. B*, 59:1758, 1999.

[115] URL http://www.vasp.at.

[116] URL http://www.castep.org.

[117] H. J. Monkhorst and J. D. Pack. Special points for brillouin-zone integrations. *Phys. Rev. B*, 13:5188, 1976.

[118] J. D. Pack and H. J. Monkhorst. Special points for brillouin-zone integrations - a reply. *Phys. Rev. B*, 16:1748, 1977.

[119] R. Car and M. Parrinello. Unified approach for molecular dynamics and density-functional theory. *Phys. Rev. Lett.*, 55(22):2471–2474, 1985.

[120] M. Johnson, N. Malikova, M. Plazanet, (Eds, and). Jdn 18 : Neutrons et simulations. http://www.sfn.asso.fr/JDN/JDN18, 2010.

[121] K. Hermansson, G. C. Lie, and E. Clementi. On velocity scaling in molecular dynamics simulations. *J. Comp. Chem.*, 9(3):200–203, 1988.

[122] J. P. M. Berendsen, H. J. C. Postma, W. F. van, Gunsteren, A. DiNola, and J. R. Haak. Molecular-dynamics with coupling to an external bath. *J. Chem. Phys.*, 81 (8):3684–3690, 1985.

[123] S. Nose. A unified formulation of the constant temperature molecular-dynamics methods. *J. Chem. Phys.*, 81(1):511–519, 1984.

[124] W. G. Hoover. Canonical dynamics: Equilibrium phase-space distributions. *Phys. Rev. A*, 31(3):1695–1697, 1985.

[125] K. Kunc and E. Tosatti. "direct" evaluation of the inverse dielectric matrix in semiconductors. *Phys. Rev. B (R)*, 29:7045, 1984.

[126] M. Cococcioni, S. de, and Gironcoli. Linear response approach to the calculation of the effective interaction parameters in the LDA+U method. *Phys. Rev. B*, 71 (035105), 2005.

[127] R. P. Feynman. Forces in molecules. *Phys. Rev. B*, 56:340, 1939.

[128] AIP Conf. Proc, editor. *Calculation of phonon dispersion curves by the direct method*, volume 121, 1999.

[129] V. Calandrini, E. Pellegrini, P. Calligari, K. Hinsen1, and G. R. Kneller. nmoldyn - interfacing spectroscopic experiments, molecular dynamics simulations and models for time correlation functions. *Collection SFN*, pages 201–232, 2011.

[130] V. Calandrini, P. Calligari, K. Hinsen, and G. R. Kneller. *nMOLDYN: User's Guide*.

[131] S. Stankovich, D. A. Dikin, R. D. Piner, K. A. Kohlhaas, A. Kleinhammes, Y. Jia, Y. Wu, S. T. Nguyen, and R. S. Ruoff. Synthesis of graphene-based nanosheets via chemical reduction of exfoliated graphite oxide. *Carbon*, 45(7):1558–1565, 2007.

[132] B. C. Brodie. On the atomic weight of graphite. *Esq., F.R.S., Pres. C.S.,*, 1859.

[133] L. Staudenmaier. Verfahren zur darstellung der graphitsäure. *Berichte der deutschen chemischen Gesellschaf*, 31(2):1481–1487, 1898.

[134] W. Gao, L. B. Alemany, L. Ci, and P. M. Ajayan. New insights into the structure and reduction of graphite oxide. *Nature Chemistry*, 1:403–408, 2009.

[135] C. Gómez-Navarro, R. T. Weitz, A. M. Bittner, M. Scolari, A. Mews, M. Burghard, and K. Kern. Electronic transport properties of individual chemically reduced graphene oxide sheets. *Nano letters*, 7(11):3499–3503, 2007.

[136] H. He, J. Klinowski, M. Forster, and A. Lerf. A new structural model for graphite oxide. *Chemical Physics Letters*, 287(1-2):53–56, 1998.

[137] T. Szabó, O. Berkesi, P. Forgó, K. Josepovits, Y. Sanakis, D. Petridis, and I. Dékány. Evolution of surface functional groups in a series of progressively oxidized graphite oxides. *Chemistry of materials*, 18(11):2740–2749, 2006.

[138] D. R. Dreyer, S. Park, C. W. Bielawski, and R. S. Ruoff. The chemistry of graphene oxide. *Chemical Society Reviews*, 39:228–240, 2010.

[139] K. A. Mkhoyan, A. W. Contryman, J. Silcox, D. A. Stewart, G. Eda, C. Mattevi, S. Miller, and M. Chhowalla. Atomic and electronic structure of graphene-oxide. *Nano Letters*, 9(3):1058–1063, 2009.

[140] URL https://www.youtube.com/watch?v=bl45J6iw3tE.

[141] Y. Hernandez, V. Nicolosi, M. Lotya, F. M. Blighe, Z. Sun, S. De, IT McGovern, B. Holland, M. Byrne, Y. K. Gun'Ko, et al. High-yield production of graphene by liquid-phase exfoliation of graphite. *Nature nanotechnology*, 3(9):563–568, 2008.

[142] M. Gaboardi, A. Bliersbach, G. Bertoni, M. Aramini, G. Vlahopoulou, D. Pontiroli, Ph, Mauron, G. Magnani, G. Salviati, A. Zuttel, and M. Riccó. Decoration of graphene with nickel nanoparticles: study of the interaction with hydrogen. *J. Mater. Chem. A*, (DOI: 10.1039/c3ta14127f), 2014.

[143] URL http://www.ill.eu/instruments-support/instruments-groups/instruments/d2b.

[144] URL http://www.esrf.eu/UsersAndScience/Experiments/StructMaterials/ID15.

[145] J. I. Langford and A. J. C. Wilson. Scherrer after sixty years: A survey and some new results in the determination of crystallite size. *J.Appl.Cryst.*, 11:102–113, 1978.

[146] P. Scherrer. Bestimmung der grösse und der inneren struktur von kolloidteilchen mittels röntgenstrahlen. *Nachr. Ges. Wiss. Göttingen*, 26:98–100, 1918.

[147] B. E. Warren. X-ray diffraction in random layer lattices. *Phys. Rev.*, 59(9):693–698, 1941.

[148] J. Biscoe and B. E. Warren. An x-ray study of carbon black. *Journal of Applied Physics*, 13:364–371, 1942.

[149] M. Leoni. Diffraction analysis of layer disorder. *Z. Kristallogr.*, 223:561–568, 2008.

[150] A. P. Hammersley. FIT2D V9.129 reference manual. *ESRF - Internal Report*, 1998.

[151] URL http://www.diffpy.org/doc/pdfgetx3/.

[152] C. L. Farrow, P. Juhas, J. W. Liu, D. Bryndin, E. S. Boǎnd zin, J. Bloch, Th, Proffen, and S. J. L. Billinge. Pdffit2 and pdfgui: computer programs for studying nanostructure in crystals. *J. Phys.: Condens. Matter*, 19(335219), 2007.

[153] R. L. McGreevy. Reverse monte carlo modelling. *J. Phys.: Condens. Matter*, 13: R877, 2001.

[154] M. Riccó, M. Aramini, M. Mazzani, D. Pontiroli, M. Gaboardi, and O. V. Yazyev. Muons probe magnetism and hydrogen interaction in graphene. *Physica Scripta*, 88(6), 2013.

[155] S. J. Kerber, J. J. Bruckner, K. Wozniak, S. Seal, S. Hardcastle, and T. L. Barr. The nature of hydrogen in x-ray photoelectron spectroscopy: General patterns from hydroxides to hydrogen bonding. *J. Vac. Sci. Technol. A - Vacuum Surfaces and Films*, 14(3):1314–1320, 1996.

[156] A. C. Ferrari, J. C. Meyer, V. Scardaci, C. Casiraghi, M. Lazzeri, F. Mauri, S. Piscanec, D. Jiang, K. S. Novoselov, S. Roth, and A. K. Geim. Raman spectrum of graphene and graphene layers. *Phys. Rev. Lett.*, 96(187401), 2006.

[157] A. C. Ferrari. Raman spectroscopy of graphene and graphite: Disorder, electron–phonon coupling, doping and nonadiabatic effects. *Solid State Communications*, 143(1-2):47–57, 2007.

[158] A. Eckmann, A. Felten, A. Mishchenko, L. Britnell, R. Krupke, K. S. Novoselov, and C. Casiraghi. Probing the nature of defects in graphene by raman spectroscopy. *Nano Letters*, 12(8):3925–3930, 2012.

[159] L. G. Cancado, A. Jorio, E. H. Martins, Ferreira, F. Stavale, C. A. Achete, R. B. Capaz, M. V. O. Moutinho, A. Lombardo, T. Kulmala, and A. C. Ferrari. Quantifying defects in graphene via raman spectroscopy at different excitation energies. *Phys. Chem. Chem. Phys.*, 9:1276–1291, 2007.

[160] R. Nicklow, N. Wakabayashi, and H. G. Smith. Lattice dynamics of pyrolytic graphite. *Phys. Rev. B*, 5(12):4951–4962, 1972.

[161] R. J. Nemanich and S. A. Solin. First- and second-order raman scattering from finite-size crystals of graphite. *Phys. Rev. B*, 20(2):392–401, 1979.

[162] G. Dolling and B. N. Brockhouse. Lattice vibrations in pyrolitic graphite. *Phys. Rev.*, 128(3):1120–1123, 1962.

[163] L. Saviot, C. H. Netting, D. B. Murray, S. Rols, A. Mermet, A. L. Papa, C. Pighini, D. Aymes, and N. Millot. Inelastic neutron scattering due to acoustic vibrations confined in nanoparticles: Theory and experiment. *Phys. Rev. B*, 78:245426, Dec 2008.

[164] L. Van Hove. The occurrence of singularities in the elastic frequency distribution of a crystal. *Phys. Rev.*, 89(1189), 1953.

[165] P. C. H. Mitchell, A. J. Ramirez-Cuesta, S. F. Parker, J. Tomkinson, and D. Thompsett. Hydrogen spillover on carbon-supported metal catalysts studied by inelastic neutron scattering. surface vibrational states and hydrogen riding modes. *J. Phys. Chem. B*, 107:6838–6845, 2003.

[166] A. J. Horsewill, K. S. Panesar, S. Rols, M. R. Johnson, Y. Murata, K. Komatsu, S. Mamone, A. Danquigny, F. Cuda, S. Maltsev, M. C. Grossel, M. Carravetta, and M. H. Levitt. Quantum translator-rotator: Inelastic neutron scattering of dihydrogen molecules trapped inside anisotropic fullerene cages. *Phys. Rev. Lett.*, 102(013001), 2009.

[167] E. Stanik, G. Majera, S. Orimo, T. Ichikawa, and H. Fujii. Nuclear-magnetic-resonance measurements of the hydrogen dynamics in nanocrystalline graphite. *J. Appl. Phys.*, 98(044302), 2005.

[168] M. Bee, H. Jobic, and C. Sourisseau. Neutron scattering study of methyl group reorientations in trimethyloxosulphonioum iodide, $(CH_3)_3SOI$. *J. Phys. C: Solid State Phys.*, 18(31):5771, 1985.

[169] P. C. H. Mitchell, A. J. Ramirez-Cuesta, S. F. Parker, and J. Tomkinson. Inelastic neutron scattering in spectroscopic studies of hydrogen on carbon-supported catalysts-experimental spectra and computed spectra of model systems. *Journal of Molecular Structure*, 651–653:781–785, 2003.

[170] P. Papanek, W. A. Kamitakahara, P. Zhou, and J. E. Fischer. Neutron scattering studies of disordered carbon anode materials. *J. Phys.: Condens. Matter*, 13: 8287–8301, 2001.

[171] S. F. Parker, S. Imberti, S. K. Callear, and P. W. Albers. Structural and spectroscopic studies of a commercial glassy carbon. *Chemical Physics*, 427(0):44 – 48, 2013.

[172] URL http://wwwisis2.isis.rl.ac.uk/INSdatabase/Theindex.asp.

[173] J. C. Lewis, B. Redfern, and F. C. Cowlard. Vitreous carbon as a crucible material for semiconductors. *Solid-State Electronics*, 6(3):251 – IN4, 1963.

[174] F. C. Cowlard and J. C. Lewis. Vitreous carbon — a new form of carbon. *Journal of Materials Science*, 2(6):507–512, 1967. URL http://dx.doi.org/10.1007/BF00752216.

[175] S. Sakong and P. Kratzer. Hydrogen vibrational modes on graphene and relaxation of the C–H stretch excitation from first-principles calculations. *J. Chem. Phys.*, 133:054505, 2010.

[176] Z. Sljivancanin, M. Andersen, L. Horneaer, and B. Hammer. Structure and stability of small H clusters on graphene. *Phys. Rev. B*, 83:205426, 2011.

[177] M. Casartelli, S. Casolo, G. F. Tantardini, and R. Martinazzo. Structure and stability of hydrogenated carbon atom vacancies in graphene. *Carbon*, 77:165–174, 2014.

[178] X. Wu and X. C. Zeng. Periodic graphene nanobuds. *Nano Lett.*, 9(1):250–256, 2009.

[179] R. Le, Parc, P. Hermet, S. Rols, D. Maurin, L. Alvarez, A. Ivanov, M. Quimby, C. G. Hanley, L. T. Scott, J. L, and Bantignies. New insights on vibrational dynamics of corannulene. *J.Phys.Chem.C*, 116:25089–25096, 2012.

[180] C. Cavallari, D. Pontiroli, M. Jiménez-Ruiz, A. Ivanov, M. Mazzani, M. Gaboardi, M. Aramini, M. Brunelli, M. Riccó, and S. Rols. Hydrogen on graphene investigated by inelastic neutron scattering. *Journal of Physics: Conference Series*, 554: 012009, 2014.

[181] C. O. Girit, J. C. Meyer, R. Erni, M. D. Rossell, C. Kisielowski, L. Yang, C. H, Park, M. F. Crommie, M. L. Cohen, S. G. Louie, and A. Zettl. Graphene at the edge: Stability and dynamics. *Science*, 323(5922):1705–1708, 2009.

[182] A. Allouche and Y. Ferro. Dissociative adsorption of small molecules at vacancies on the graphite (0001) surface. *Carbon*, 44:3320–3327, 2006.

[183] Frederick and Reif. *Fundamentals of Statistical and Thermal Physics*. McGraw-Hill Science/Engineering/Math, 1965.

[184] A. J. Horsewill. Quantum tunnelling in the hydrogen bond. *Progress in Nuclear Magnetic Resonance Spectroscopy*, 52:170–196, 2007.

[185] J. l. Skinners and H. P. Trommsdorff. Proton transfer in benzoic acid crystals: A chemical spin-boson problem. theoretical analysis of nuclear magnetic resonance, neutron scattering, and optical experiments. *J. Chem. Phys*, 89(2):897–907, 1988.

[186] A. J. Horsewill, C. J. McGloin, H. P. Trommsdorff, and M. R. Johnson. Proton tunnelling in the hydrogen bonds of halogen-substituted derivatives of benzoic acid studied by NMR relaxometry: the case of large energy asymmetry. *Chem. Phys.*, 291:41–52, 2003.

[187] A. J. Horsewill. How quantum tunnelling can contribute to proton transfer at biologically relevant temperatures. *J. Phys. Org. Chem.*, 23:580–585, 2010.

[188] H. Lee, J. Ihm, M. L. Cohen, and S. G. Louie. Calcium-decorated graphene-based nanostructures for hydrogen storage. *Nano Lett.*, 10(793-798), 2010.

[189] T. Yildirim and S. Ciraci. Titanium-decorated carbon nanotubes as a potential high-capacity hydrogen storage medium. *Phys. Rev. Lett*, 94:175501, 2005.

[190] K. R. S. Chandrakumar and S. K. Ghosh. Alkali-metal-induced enhancement of hydrogen adsorption in C_{60} fullerene: an ab initio study. *Nano Lett.*, 8:13–19, 2008.

[191] R. W. G. Wyckoff. *Crystal Structures 1*, volume 7-83. Interscience Publishers, New York, New York, 1963.

[192] L. Cronin, C. L. Higgitt, R. Karch, and R. N. Perutz. Rapid intermolecular carbon–fluorine bond activation of pentafluoropyridine at nickel(0): Comparative reactivity of fluorinated arene and fluorinated pyridine derivatives. *Organometallics*, 16: 4920–4928, 1997.

[193] R. J. Birgeneau, J. Cordes, G. Dolling, and A. D. B. Woods. Normal modes of vibration in nickel. *Phys. Rev.*, 136(5A):A1359–A1365, Nov 1964.

[194] M. Kresch, O. Delaire, R. Stevens, J. Y. Y. Lin, and B. Fultz. Neutron scattering measurements of phonons in nickel at elevated temperatures. *Phys. Rev. B*, 75 (10):104301, Mar 2007.

[195] V. E. Antonov, V. K. Fedotov, B. A. Gnesin, G. Grosse, A. S. Ivanov, A. I. Kolesnikov, and F. E. Wagner. Anisotropy in the inelastic neutron scattering from fcc niH. *Europhys. Lett.*, 51(2):140–146, 200.

[196] K. Holczer and R. L. Whetten. Superconducting and normal state properties of the A_3C_{60} compounds. *Carbon*, 30(8):1261–1276, 1992.

[197] M. Riccó, T. Shiroka, M. Belli, D. Pontiroli, M. Pagliari, G. Ruani, D. Palles, and S. Margadonna. Unusual polymerization in the Li_4C_{60} fulleride. *Phys. Rev. B*, 72:155437, 2005.

[198] S. Margadonna, D. Pontiroli, M. Belli, T. Shiroka, M. Ricco, and M. Brunelli. Li_4C_{60}: A polymeric fulleride with a two-dimensional architecture and mixed interfullerene bonding motifs. *Journal of the American Chemical Society*, 126(46): 15032–15033, 2004.

[199] D. Pontiroli, M. Aramini, M. Gaboardi, M. Mazzani, M. Riccó, C. Cavallari, E. Suard, M. R. Johnson, D. Richard, and S. Rols. Structure and dynamics of the fullerene polymer Li_4C_{60} studied with neutron scattering. *to be submitted*, 2015.

[200] Q. Sun, Q. Wang, P. Jena, and Y. Kawazoe. Clustering of Ti on a C_{60} surface and its effect on hydrogen storage. *J. Am. Chem. Soc.*, 127:14582–14583, 2005.

[201] Q. Wang and P. Jena. Density functional theory study of the interaction of hydrogen with Li_6C_{60}. *J. Phys. Chem. Lett.*, 3:1084–1088, 2012.

[202] Dmitry V Schur, Svetlana Yu Zaginaichenko, Aleksandr F Savenko, Vyacheslav A Bogolepov, Nina S Anikina, AD Zolotarenko, Zinaida A Matysina, T Nejat Veziroglu, and Natalia E Skryabina. Experimental evaluation of total hydrogen capacity for fullerite C_{60}. *international journal of hydrogen energy*, 36(1):1143–1151, 2011.

[203] F. Giglio, D. Pontiroli, M. Gaboardi, M. Aramini, C. Cavallari, M. Brunelli, P. Galinetto, C. Milanese, and M. Riccó. $Li_{12}C_{60}$: A lithium clusters intercalated fulleride. *Chemical Physics Letters*, 609:155–160, 2014.

[204] M. Gaboardi, C. Cavallari, G. Magnani, D. Pontiroli, S. Rols, and M. Riccó. Hydrogen storage mechanism and lithium dynamics in $Li_{12}C_{60}$ studied by μSR. *Submitted*, 2015.

[205] S. Rols, S. Petit, J. Combet, et, F. Leclercq-Hugeux, (Eds, and). *JDN 16 - Diffusion Inélastique des Neutrons pour l'Étude des Excitations dans la Matiére Condensée*. 2008.

[206] S. Rols, C. Bousige, J. Cambedouzou, P. Launois, J.L. Sauvajol, H. Schober, V.N. Agafonov, V.A. Davydov, and J. Ollivier. Unravelling low lying phonons and vibrations of carbon nanostructures: The contribution of inelastic and quasi-elastic neutron scattering. *European Physical Journal-Special Topics*, 213(1):77, 2012.

[207] H. Schober and S. Rols. Les excitations dans la matière condensée : vibrations et phonons. *Collection SFN*, 10:3–136, 2010.

[208] K. Parlinski. software phonon. *Http://wolf.ifj.edu.pl/phonon/*, 2008.

[209] K. Parlinski. Phonons calculated from first-principles. *Collection SFN*, 12:161–166, 2011.

[210] K. Parlinski. First-principle lattice dynamics and thermodynamics of crystals. *Journal of Physics: Conference Series*, 92:012009, 2007.

[211] A. I. Kolesnikov, V. E. Antonov, I. O. Bashkin, G. Grosse, A. P. Moravsky, A. Yu, Muzychka, E. G. Ponyatovsky, and F. E. Wagner. Neutron spectroscopy of C_{60} fullerite hydrogenated under high pressure; evidence for interstitial molecular hydrogen. *J. Phys.: Condens. Matter*, 9:2831–2838, 1997.

[212] J. Boronat, C. Cazorla, D. Colognesi, and M. Zoppi. Quantum hydrogen vibrational dynamics in LiH: Neutron-scattering measurements and variational monte carlo simulations. *Phys. Rev. B*, 69(174302), 2004.

[213] J. A Teprovich Jr, M. S Wellons, R. Lascola, S.J. Hwang, P. A. Ward, R. N. Compton, and R. Zidan. Synthesis and characterization of a lithium-doped fullerane $Li_xC_{60}H_y$ for reversible hydrogen storage. *Nano Lett.*, 12(2):582–589, 2012.

[214] K. P. Meletov, S. Assimopoulos, G. A. Kourouklis, and I. O. Bashkin. Phase transitions in hydrofullerene $C_{60}H_{36}$ studied by luminescence and raman spectroscopy at pressure up to 12gpa. *Physics of the Solid State*, 2002.

[215] L. E. Hall, D. R. McKenzie, R. L. Davis, M. I. Aitalla, and A. M. Vassallo. Structural determination of the hydrofullerene $C_{60}D_{36}$ by neutron diffraction. *Acta Cryst.*, B54:345–350, 1998.

[216] T. Yildirim, O. Zhou, J.E. Fischer, N. Bykovetz, R.A. Strongin, M.A. Cichy, Smith III A.B., C.L. Lin, and R. Jelinek. Intercalation of sodium heteroclusters into the C_{60} lattice. *Nature*, 360(6404):568–571, 1992.

[217] G. Kresse, M. Marsman, and J. Furthmuller. *Vasp: User Guide*. Computational Materials Physics (Faculty of Physics - Universitat Wien), http://cms.mpi.univie.ac.at/vasp/vasp/vasp.html.